ČESKÉ VYSKOKÉ UČENÍ TECHNICKÉ V PRAZE

FAKULTA ELEKTROTECHNICKÁ

Supravodiče pre aplikácie v elektroenergetike

Habilitačná práca

29.5.2020 Mgr.Bc. Michal Chudý, PhD.

Abstrakt

Je známym faktom, že vysokoteplotné supravodiče sú materiály, ktoré sú schopné zvýšiť výkon a efektívnosť elektrických zariadení. Širokospektrálna adopcia týchto materiálov v energetike by mala nesporne obrovský impakt na efektívnosť a znamenala by obrovské úspory v spotrebe elektrickej energie. Najjednoduchšie riešenia spočívajú vo vybraných aplikáciách v nahradení klasických cievok cievkami vyrobených s vysokoteplotnej supravodivej pásky. Avšak v reálne existujú vážne bariéry vo širokospektrálnom využívaní supravodičov ako aj vysokoteplotných supravodičov (hlavne YBCO = Ytrium Barium Copper Oxide, BSCOO =Bismuth Strontium Calcium Copper Oxide) ktorým sa venuje táto práca. Hlavným problémom však nie je potreba chladenia na kryogenické teploty ale stále príliš vysoká cena supravodivých materiálov a priveľa technických špecifickostí, ktoré by mohli znamenať kazovosť zariadení hlavne pri vysokoteplotných supravodičoch. Navyše pri aplikáciách so striedavým prúdom vykazujú aj supravodiče nenulové straty. Z tohto dôvodu treba pristupovať veľmi opatrne k aplikáciám kde sú supravodiče vystavené striedavým magnetickým poliam. Vysokoteplotné supravodiče sú dostupné hlavne ako supravodivé pásky a vyznačujú vysokou mierou magnetickej anizotropie. Magnetické pole pôsobiace kolmo na plochu pásky dokáže spôsobiť pomerne výrazné straty. Dizajn supravodivých zariadení je preto mimoriadne dôležitý aby sa v čo najväčšej miere predišlo zníženiu výkonu supravodiča priamym pôsobením magnetického poľa. Kapacita vedenia prúdu musí byť preto otestovaná aj pre najhorší prípad veľkosti a smeru magnetického poľa, aby sa predišlo prípadnému prepáleniu supravodiča vplyvom preťaženia v danom zariadení. Táto práca sa venuje využitiu vysokoteplotných supravodičov v rôznych aplikáciách v elektroenergetike. Konkrétnejšie aplikáciám vysokoteplotných supravodičov budúcich fúznych reaktoroch, elektrických generátoroch a to hlavne vo veterných turbínach ale tiež v supravodivých rotačníkoch na uskladňovanie energie.

Obsah

1. Úvod

Táto habilitačná práca sa venuje problematike vysokoteplotných supravodičov a ich aplikácií v elektroenergetike. Nakoľko sa jedná o veľmi širokú tému, v práca sa sústreďuje hlavne na aplikácie v termojadrovej fúzii a v produkcii energie z vetra. Okrajovo sa však venuje aj iným témam. Práca pozostáva z trinástich karentových publikácii a dvoch publikácii z medzinárodných konferencií. Tieto publikácie sú zoradené a opísané takým spôsobom aby na seba logicky nadväzovali a vysvetlili čitateľovi danú problematiku v chronologicky členených častiach. Prezentované výsledky majú zásadný impakt na fungovanie a možnosť aplikácie vysokoteplotných supravodičov do spomínaných aplikácií v elektroenergetike. V úvode tejto práce je vysvetlená podstata mikroštruktúry vysokoteplotných supravodičov. Je to hlavne elementárna teória pinningu na ktorej závisí drvivá väčšina vlastností vysokoteplotných supravodičov. Je nutné poznať podstatu pinningu, aby bolo možné správne pochopiť a interpretovať výsledky prezentovaných experimentov, preto sú základy teórie pinningu uvedené hneď v úvodnej kapitole. Prvý set predložených prác sa venuje štúdiu anizotropie vysokoteplotných supravodivých pások a to hlavne z pohľadu mikroskopickej štruktúry materiálov. Druhý set publikácii sa tiež venuje anizotropii, avšak štúdie sa už viac zaoberajú makroskopickými dôsledkami a výslednými charakteristikami supravodičov. Tretia skupina publikácií je následne venovaná štúdiu supravodivých cievok ako najelementárnejších supravodivých zariadení v generátoroch elektrickej energie prípadne v motoroch. Následne je štvrtá časť venovaná priamo fungovaniu týchto zariadení ako aj celých systémov založených na vysokoteplotných supravodičoch. Teda v práci sú vysokoteplotné supravodiče študované od mikroskopických problémov supravodivých materiálov až po vlastnosti celých systémov aplikácii založených na vysokoteplotných supravodičoch. analyzuje vlastnosti je prirodzený jav v týchto materiáloch spôsobená rozličnou silou pinningu podľa smeru magnetického poľa. Znamená obrovskú variáciu vo vlastnostiach a preto je táto časť práce nesmierne dôležitá. Ako úvod tejto práce je venovaný aj teórii pinningu aby v ďalšej časti sa práca zameriava na supravodivé materiály a ich použitie v konkrétnych aplikáciách v energetike.

1.1 Vysokoteplotné supravodiče a supravodivé pásky

Vysokoteplotné supravodiče boli objavené Alexom Müllerom a Georgom Bednorzom v roku 1986 keď spozorovali supravodivé vlastnosti Ba-La-Cu-O systému v teplotách v akých dovtedy supravodivosť nebola pozorovaná [1]. Týmto počinom sa ihneď otvorila nová oblasť výskumu. Kritické teploty vysokoteplotných supravodičov boli behom niekoľkých rokov zvýšené z pôvodných ~ 40 K v Ba-La -

Cu-O až na 153 K v Hg-Ba-Ca-Cu-O – avšak toto bolo namerané pod vysokým tlakom. Všetky tieto vysokoteplotné supravodiče boli založené na CU-O vrstvách a preto dostali názov kupráty. Avšak v roku 2008 bola skupinou H. Hosona [2] objavená nová rodina vysokoteplotných supravodičov založená na železe.

Materiál s najväčším potenciálom je aktuálne Y-Ba-Cu-O tzv. YBCO alebo Y123 . Preto sa v tejto práci budeme dominantne venovať hlavne tomuto materiálu. Kryštalická štruktúra tohto materiálu je zobrazená na Obr. 1. Kryštál YBCO má vrstvovitú štruktúru a patrí do skupiny Perkovskite. Kritická teplota tohto materiálu je ~92 K. Kryštál YBCO má výrazné anizotropné vlastnosti čo sa týka supravodivosti nakoľko supravodivé vlastnosti sú silné v rovine *ab*, ale supravodivosť po osi *c* je rádovo slabšia.

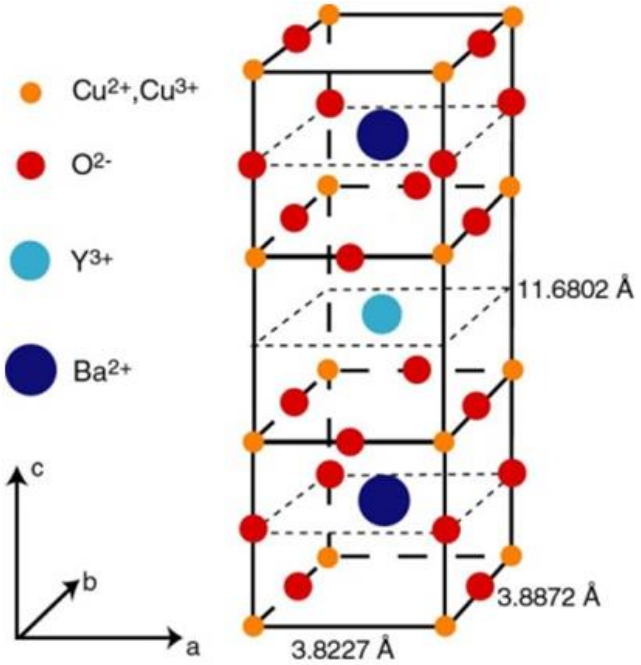

Obr. 1: Perkovskite štruktúra kryštálu YBCO.

Z dôvodu tejto anizotropie je výroba vodičov tzv. pások z tohto materiálu pomerne náročná. Prvá generácia vysokoteplotných supravodivých pások bola vyhotovená z materiálu Bi – Sr-Ca-Cu-O tzv. BSCCO, ktorého kryštály sa vedia pomerne dobre epitaxiálne usporiadať jednoduchým valcovaním v plášti. Nevýhodou tohto procesu je vysoká cena nakoľko ako plášť sa najvhodnejšie ukázalo striebro a nakoniec BSCCO má pomerne zlé výkonové charakteristiky v magnetickom poly. YBCO si oproti BSCCO ponecháva veľmi dobré supravodivé vlastnosti aj v magnetických poliach kde BSCCO už takmer nie je supravodivé. Avšak epitaxiálne usporiadanie kryštálov YBCO je oveľa náročnejšie ako v prípade BSCCO. Bolo Vyvinutých niekoľko metód ako naniesť vrstvu YBCO v správnom smere tak, aby supravodivosť supravodivej pásky bola najvýraznejšia v pozdĺžnom smere. YBCO pásky sa nazývajú

druhou generáciou supravodivých pások alebo aj „coated conductors“. Metódam výroby výkonných supravodivých pások sa venuje množstvo publikácií napr. [3][4] a je niekoľko svetových producentov YBCO komerčných supravodivých pások, ktorí svoje technologické postupy neustále vylepšujú. Všetky metódy výroby týchto pások však majú spoločné, že páska sa musí skladá z viacerých vrstiev, ktoré zabezpečia správne uloženie kryštálov YBCO v supravodivej vrstve. Názorný príklad supravodivej pásky druhej generácie je na Obr. 2.

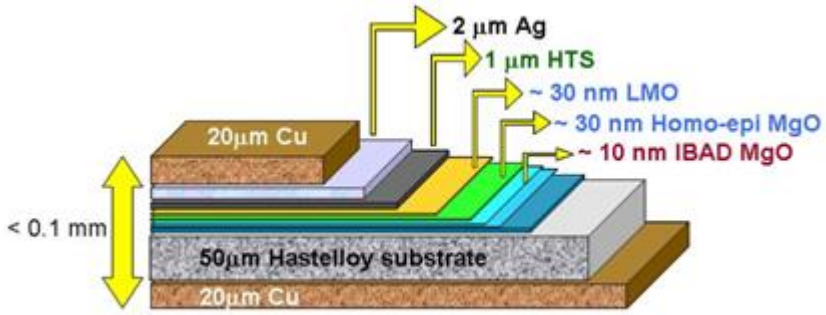

Obr. 2: Príklad supravodivej pásky druhej generácie (SuperPower).

1.2 Pinning

Objavenie vysokoteplotných supravodičov viedlo k okamžitému skúmaniu javu, tzv. “flux pinningu”. Ako je dobre známe, vysokoteplotné supravodiče sú supravodičmi druhého druhu. Toto znamená že v supravodivom stave fungujú spolu s čiastočne penetrovaným magnetickým polom. Supravodivé vlastnosti sa prejavujú až po horné hraničné magnetické pole. ktoré sa označuje B_{c2} . Pričom $B_{c2} = \kappa\sqrt{2}B_c$, kde B_c sa označuje termodynamické kritické pole a κ je Ginzburg-Landau (GL) parameter. Vysokoteplotné supravodiče teda operujú v tomto stave koexistencie kuprových párov schopných viesť elektrický prúd bez straty a magnetického poľa, ktoré svojím pohybom v princípe produkuje napätie. Toto napätie je zapríčinené Lorentzovou silou na magnetické prúdnice. (podľa Maxwell-Faradayovej rovnice). Akékoľvek detegované napätie znamená že transport elektrického prúdu už nie je bezstratový a je diskutabilné ďalej hovoriť o supravodivom stave danej látky.

Avšak pridanie mikro defektov do štruktúry supravodivej látky zmenší priemernú voľnú dráhu nosičov náboja, čo má za následok zvýšenie Ginzburg-Landau (GL) parametra κ a aj magnetického poľa B.

Hoci tento mechanizmus bol podrobne opísaný v teórii Ginzburg-Landaua pre nízkoteplotné supravodiče, je veľmi pravdepodobné že funguje obdobne aj pre vysokoteplotné supravodiče. Tieto mikro defekty sa o fyzike supravodičov označujú ako pinningové centrá. Pinningové centrá sú alebo z nesupravodivého materiálu alebo ich GL parameter κ je oveľa vyšší ako ten okolitých zŕn či kryštálov supravodiča. Práve pinningové centrá sú zodpovedné za existenciu supravodivých prúdov v

“zmiešanom stave supravodičov 2 druhu” kde koexistujú supravodivé a nesupravodivé časti materiálu. Magnetické prúdy sú totiž priťahované týmito defektmi a pokiaľ sú tieto defekty dosť silné, dokážu zabrániť tejto prúdnici v pohybe, takže sa na supravodiči netvorí žiadne napätie a prúd ide bez strát i v zmiešanom stave. Supravodič sa snaží každý magnetický tok vo vnútri odtieniť. Robí to prostredníctvom vytvorenia supravodivých vírov okolo každej prúdnice magnetického poľa. Tieto víry sa nazývajú Abrikosove výry a sú opísané nasledujúcou rovnicou.[5]

$$B_v = \frac{\phi_0}{2\pi\lambda^2} \begin{cases} \ln\left(\frac{\lambda}{r}\right) & \text{if } \xi < r \ll \lambda \\ \left(\frac{\pi\lambda}{2r}\right)^{\frac{1}{2}} e^{\frac{-r}{\lambda}} & \text{if } r \gg \lambda \end{cases}$$

Kde:
B_v – magnetické pole, ξ – Koherenčná dĺžka supravodiča, λ – Londonova penetračná hĺbka, r- polomer, ϕ_0 – magnetický tok,

Náčrt Abrikosovho víru je ilustrovaný na Obrázku 1. A Takže supravodič dokáže viesť prúd bez akýchkoľvek strát a teda bez akéhokoľvek napätia pokiaľ sú tieto víry stabilne fixované. V momente, keď Lorentzova sila prekoná silu pinningového centra, víry sa pustia do pohybu a v supravodiči sa začne tvoriť napätie. Toto znamená porušenie supravodivého stavu daného materiálu. Sila pinningu silne závisí od typu a množstva pinningových centier v supravodiči. Keďže schopnosť supravodiča viesť bezstratovo elektrický prúd primárne závisí na vlastnostiach pinningových centier, fyzika pinningu a štúdium výroby efektívnych pinnningových centier je jedným z kľúčových výskumov v oblasti supravodivosti, ktorý vedie k zlepšovaniu vlastností supravodičov.

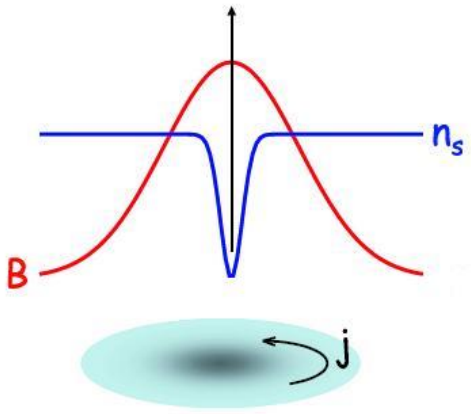

Obr. 1: Náčrt Abrikosovho víru, j = hustota elektrického prúdu, B – magnetické pole, n_s – hustota Kuprových párov.

1.3 Aplikácie supravodivých pások druhej generácie

Už niekoľko rokov sa hovorí o komerčných aplikáciách vysokoteplotných supravodivých pások. Avšak na klasickom trhu sa supravodiče zatiaľ nemôžu presadiť kvôli cene, ktorá je o niekoľko rádov vyššia ako štandardné riešenie z tradičných materiálov. Šancu však majú v špeciálnych zariadeniach od

ktorých sa vyžadujú vlastnosti, ktoré nie je vôbec, alebo len veľmi ťažko možné dosiahnuť bez supravodičov. V mnohých takýchto zariadeniach sa dnes už používajú nízkoteplotné supravodiče chladené primárne tekutým héliom (MRI zobrazovanie, magnety v urýchľovači LHC v CERNE, Maglev vlaky atď.). Ďalšou dôležitou aplikáciou supravodičov je termojadrová fúzia. Je jasné, že bez supravodičov tieto zariadenia nedokážu vyprodukovať dostatočné magnetické pole, aby termojadrová fúzia dokázala vyprodukovať viac energie ako by bolo spotrebované v magnetoch tokamaku alebo stellatora. Aktuálne najväčší výskumný projekt zaoberajúci sa termojadrovou fúziou – ITER (International Thermonuclear Experinmental Reactor) počíta so všetkými magnetmi vyrobenými so supravodičov. Konkrétne nízkoteplotných supravodičov NbTi, Nb_3Sn. Už nasledujúca generácia termojadrového reaktoru, ktorá by mala byť posledným krokom demonštrácie komerčne dostupného zariadenia tzv. DEMO by už mala fungovať na báze magnetov z vysokoteplotných supravodičov. Najhorúcejším kandidátom na aplikácie v DEMOe sú supravodivé pásky druhej generácie a ako supravodivý materiál sa uvažuje teda YBCO. Výzvou, ktorou sa zaoberá časť tejto práce je radiácia z fúznej reakcie, ktorá môže ovplyvniť supravodivé vlastnosti inštalovaných magnetov. Uvažovaná fúzna reakcia pre ITER ako aj pre DEMO bude s najväčšou pravdepodobnosťou deutérium (D) s tríciom (T):

$$^{2}_{1}D + ^{3}_{1}T = ^{4}_{2}He + ^{1}_{0}n + 17.6\ MeV$$

Kde trícium bude produkované priamo v reaktore reakciami:

$$^{1}_{0}n + ^{6}_{3}Li = ^{4}_{2}He + ^{3}_{1}T$$

$$^{1}_{0}n + ^{7}_{3}Li = ^{4}_{2}He + ^{3}_{1}T + ^{1}_{0}n$$

Z tohto je jasné, že rádioaktívne žiarenie na časti reaktoru spôsobujú hlavne toky neutrónov z fúznej reakcie. Tieto toky sú však dôležité pre tvorbu trícia ako aj zber energie. Preto sa tieto časti reaktoru budú snažiť absorbovať čo najväčšiu časť žiarenia a intenzity dopadajúce na oblasť supravodivých magnetov budú značne zredukované. Je však nesmierne dôležité preskúmať vplyv týchto tokov na supravodivé vlastnosti YBCO pások. Avšak je dôležité si uvedomiť, že pinning je jedným z najdôležitejších faktorov, ktorý ovplyvňuje supravodivé vlastnosti supravodičov druhej generácie. Hoci je väčšina predložených článkov v tejto práci venovaná termojadrovej fúzii, poznatky z mikroštruktúry supravodičov sú veľmi dobre aplikovateľné aj v ďalších oblastiach energetiky spomenutých neskorších kapitolách tejto práce. Keďže pinningové centrá sú v podstate defekty v štruktúre supravodiča, ktoré sú nesupravodivé alebo slabšie supravodivé, defekty spôsobené radiáciou nemusia mať negatívne dôsledky na supravodivý materiál. Presnejšie ak defekty spôsobené neutrónmi (klasifikované ako rýchle neutróny) majú určitú veľkosť, môžu byť veľmi efektívnymi pinningovými centrami a mať za následok zvýšenie výkonu supravodičov. Avšak neutróny pri reakciách

s atómami supravodiča môžu vytvoriť ťažšie a nestabilné izotopy, ktoré môžu znamenať zmenu vlastností supravodiča. Tento jav sa nazýva Izotopový efekt a pozorovaný je hlavne znížením kritickej teploty supravodiča. Znamená samozrejme aj to, že supravodič sa stane rádioaktívnym.

Avšak so supravodičmi sa v energetike v budúcnosti počíta aj pri výrobe generátorov a to hlavne tam, kde je potreba znížiť hmotnosť generátora pri zachovaní výkonu. Toto je prípad napr. veterných turbín montovaných v šelfových moriach. Táto aplikácia je motiváciou pre experimenty predložených publikácií tejto práce. Supravodiče ponúkajú viacero možností uskladňovania energie ako napríklad SMES (Superconducting Magnetic Energy Storage) alebo rotačníky, ktorým venujeme pozornosť aj v tejto práci. Ďalšou veľkou skupinou aplikácií sú supravodivé káble. Avšak tie sú samostatným výskumným smerom a ako súčasť tejto práce neboli vykonané žiadne experimentálne merania v tejto oblasti.

2. Zoznam prezentovaných vedeckých prác

1. M. Eisterer, R. Fuger, **M. Chudy**, F. Hengstberger and H.W. Weber, "Neutron irradiation of coated conductors", Supercond. Sci. Technol. 23, 014009, 2010.

2. **M. Chudy**, M. Eisterer, H.W. Weber, "Asymmetric angular dependence of *J*c in coated conductors prior to and after fast neutron irradiation", Physica C 470, pp. 1300-1303, 2010.

3. **M. Chudy**, R. Fuger, M. Eisterer, H.W. Weber, "Characterization of commercial YBCO coated conductors after neutron irradiation", IEEE Trans. Appl.Sup. 21, 3, 3162 - 3165, 2011.

4. J. Veterníková, **M. Chudy**, M. Eisterer, H.W. Weber, V. Slugeň, S. Sojak, M. Petriska, " Application of positron annihilation spectroscopy for measurement of irradiated samples $YBa_2Cu_3O_{7-\delta}$" , Journal of Fusion Energy, 31 (2012) 1 pp 89-95.

5. **M. Chudy**, J. Veterníková, V. Slugeň, S. Sojak, M. Petriska, M.Eisterer, H.W. Weber, " Point defects in $YBa_2Cu_3O_{7-\delta}$ studied by positron annihilation spectroscopy", Supercond. Sci. Technol. 25, 075017 (5pp), 2012.

6. **M Chudy**, Z Zhong, M Eisterer and T Coombs, „ *n*-Values of commercial YBCO tapes before and after irradiation by fast neutrons“, *Supercond. Sci. Technol.* ***28*** *035008*

7. **M. Chudy**, S. C. Hopkins, M. Woźniak, B. A. Glowacki, M. Eisterer, H.W. Weber, " Full angular critical current characteristics of coated conductors using a two-axis high current goniometer", Supercond. Sci. Technol. 24 **,**075018 (5pp), 2011.

8. Min Zhang, YiRan Chen, **Michal Chudy**,Jae-Ho Kim, Sastry Pamidi, Weijia Yuan and T A Coombs," Study of 2G high temperature superconducting coils: determination of critical current", J. Appl. Phys.111, 083902, 2012.

9. **M. Chudy**, Y. Chen, Min Zhang, T A Coombs, "Anisotropy of 2G HTS racetrack coils in external magnetic fields" Supercond. Sci. Technol. 26, 075015(7pp), 2013.

10. Y. Chen, M. Zhang, **M. Chudy**, K. Matsuda, T. Coombs, "Complex Study of Transport ACLoss in Various 2G HTS Racetrack Coils" , Physica C 487,31–36, 2013.

11. Y Chen,Min Zhang, **M Chudy**, W Wang, Z Zhong, Z Huang and T Coombs, "*Theoretical and experimental magnetization loss comparison between IBAD coils and RABiTS coils",* IEEE Trans. Appl.Sup. **23**. 8201504, 2013.

12. **M. Chudy**, Y. Chen, M. Zhang, M. Baghdadi, J. Lalk, T. Pretorius, and T. Coombs, "Power Losses of 2G HTS Coils Measured in External Magnetic DC and Ripple Fields", IEEE Trans. Appl.Sup. 24**,** 1, 8200606, 2014.

13. Min Zhang, **M. Chudy**, Wei Wang, Y. Chen, Z. Huang, Z. Zhong, M. Baghdadi, J. Kvitkovic, S. V. Pamidi, and T.A. Coombs, " AC loss estimation of HTS armature windings for electric machines"

14. Z. Huang, W. Xian, Min Zhang, **M. Chudy**, Y. Chen, Z. Zhong, M. Baghdadi, Wei Wang, F. Spaven, K. Matsuda and T.A. Coombs, "Control and operation of a high temperature superconducting synchronous motor" IEEE Trans. Appl.Sup. 23, 5200204, 2013.

15. **Michal Chudy**, Lynette Herbst, Jörg Lalk, "Wind farms associated with flywheel energy storage Plants", IEEE PES Innovative Smart Grid Technologies Conference Europe, 2015-January (January)

3. Komentáre k prezentovaným vedecký prácam

Táto habilitačná práca je súhrnom výsledkov z viacerých oblastí aplikácie supravodičov v elektroenergetike. Predložená habilitačná práca je súborom vedeckých publikácií publikovaných vo vedeckých časopisoch a v zborníkoch vedeckých konferencií.

3.1 Anizotropia supravodivých pások druhej generácie a ich reakcia na neutrónové žiarenie

Publikácia č.1: Neutron irradiation of coated conductors

Publikácia sa zaoberá efektom neutrónového ožiarenia supravodivého materiálu – v tomto prípade YBCO. Je to veľká téma, ktorej sa a Atominstitute vo Viedni venuje už niekoľko desiatok rokov a za ten čas si toto laboratórium vyslúžilo povesť svetového lídra v tejto problematike napr.[6]–[8]. Aj táto publikácia pochádza práve z tohto laboratória. Je to jedna z najkomplexnejších publikácií o efekte ožiarenia YBCO materiálu. Postupné ožiarenie viacerých typov supravodivých pások druhej generácie

bolo vykonané na TRIGA Mark reaktore II vo Viedni (TU Wien, Atominstitut). Ožiarenie bolo vykonané pri niektorých vzorkách až v 4 postupných krokoch až po intenzitu $2x10^{22}$ m^{-2} rýchlych neutrónov. Intenzita predpokladaná na 20 rokov prevádzky DEMOa je $1x10^{22}$ m^{-2} takže $2x10^{22}$ m^{-2} zodpovedá 40 rokom prevádzky. Pomalé a termálne neutróny nie sú v týchto intenzitách zarátané lebo je nepravdepodobné, že v oblasti magnetov by sa nachádzali a vo viacerých publikáciách bol študovaný ich vplyv a bol vyhodnotený ako minimálny až zanedbateľný [9].

Je známym faktom, že pri ožarovaní neutrónmi sa znižuje kritická teplota. Vzorky MODRAB, PLDYSZ a MOCVDMgO mali pred ožiarením kritické teploty 90.6 K, 88.5 K a 89.1 K. Všetkým trom vzorkám sa kritická teplota z pôvodných približne znížila približne o 2 stupne pri intenzite $1x10^{22}$ m^{-2} rýchlych neutrónov. Čo je dôležité, šírka prechodu do normálneho stavu sa nezvýšila. Meranie kritickej teploty prebehlo aj pod vplyvom magnetického poľa až do 15 T pri usporiadaní kde magnetické pole H bolo rovnobežné s osou c H‖c (viď Obr. 1). Dve vzorky si zachovali podobný priebeh pred aj po ožiarení avšak vzorka MODRAB si výrazne po ožiarení polepšila vo vyšších magnetických poliach.

Nosnou časťou článku sú merania kritických prúdov, resp. kritických prúdových hustôt. Tie boli namerané až pre 4 intenzity ožiarenia rýchlymi neutrónmi, pre teploty 10 K, 50 K, 64 K 77 K a pre magnetické polia kde H‖c a H‖ab. Z výsledkov je jasné, že ožiarenie do $1x10^{22}$ m^{-2} rýchlych neutrónov zvýšilo kritické prúdy pre dominantný smer H‖c pre všetky teploty. Toto je veľmi významný výsledok tejto publikácie ako aj celého výskumného smeru štúdia ožarovania supravodičov neutrónmi. V nedominantnom smere H‖ab sa vlastnosti po ožiarení mierne zhoršili, prípadne ostali len málo zmenené. Významným prínosom články je rozanalyzovanie tvz. granulového efektu v supravodičoch. Kritické prúdy v supravodiči môžu byť obmedzené alebo prechodom medzi jednotlivými časticami supravodiča - kryštálmi, zhlukmi kryštálov (granulami) alebo priamo v kryštály. Ožiarenie rýchlymi neutrónmi zlepšuje supravodivé vlastnosti pokiaľ je kritický prúd v supravodiči limitovaný priamo v kryštály. Vďaka ožiareniu je možné lepšie rozlíšiť tieto módu nakoľko k zlepšeniu vlastností nedochádza pokiaľ je prúd limitovaný prechodmi medzi kryštálmi.

V poslednej časti článku sú prezentované výsledky meraní kritických prúdov pod rôznymi veľkosťami a uhlami magnetického poľa. Práve tento typ charakterizácie supravodičov je nesmierne dôležitý nakoľko supravodivé pásky sú mimoriadne anizotropické a presný uhol magnetického poľa veľmi výrazne ovplyvňuje ich vlastnosti ako pred tak aj po ožiarení. Ožiarenie navyše obvykle mení priebeh anizotropie a v mnohých prípadoch je anizotropia ožiarením mierne potlačená.

Publikácia č.2: Asymmetric angular dependence of *J*c in coated conductors prior to and after fast neutron irradiation

Problém anizotropného správania vysokoteplotných supravodičov a teda aj materiálu YBCO a supravodivých pások druhej generácie bol už rozobratý a zaoberala sa ním aj publikácia č.1. V tomto článku sa dôkladne rozoberá problém anizotropie konkrétnej komerčnej supravodivej pásky druhej generácie od firmy SuperPower pred a po ožiarení rýchlymi neutrónmi. Jedná sa o pásku kde je supravodivá vrstva nanášaná metódou tzv. Metal Organic Chemical Vapour Deposition (MOCVD). Táto komerčná páska patrila svojho času výkonom a správaním sa v magnetických poliach k jednej z najvýkonnejších. Problematikou však bola anizotropia a maximálny výkon , ktorý nebol nameraný pri smere magnetického poľa H‖c ale s odchýlkou približne 2 stupne. Toto by mohlo znamenať problém pre určité aplikácie a preto sa článok týmto javom zaoberá a snaží sa vysvetliť fyzikálny dôvod tejto odchýlky. Odchýlka je študovaná taktiež po ožiarení tokom rýchlych neutrónov.

V tejto štúdii boli vykonané merania kritických prúdov a prúdových hustôt pod rôznymi uhlami a veľkosťami magnetického poľa a v teplotách 50, 64 ,77 K. Uhlové rozlíšenie meraní bolo 1 stupeň. Štúdia sa zameriava hlavne na polohu hlavného píku pri H‖c a aj na polohu menšieho píku pri H‖ab. Hlavne menší pík očividne mení svoju polohu pri zmene veľkosti magnetického poľa a podobný hoci jemnejší priebeh pohybu bol zaznamenaný aj pri hlavnom píku pri H‖c. Pohyb píkov bol následne sledovaný aj po ožiarení rýchlymi neutrónmi. Rýchlymi neutrónmi sa však pomerne výrazne zmenil priebeh kritického prúdu v závislosti od uhla magnetického poľa. Toto je veľmi dobre pozorovateľné pre teplote 64 K. Hoci anizotropia po ožiarení bola výrazne potlačená, pri hlavnom píku H‖c sa utvorili akési ramená a hlboké minimá v kritickom prúde už niekoľko stupňov od píku. Taktiež priebehy n hodnôt (exponentu pri prechode U v závislosti od I pri prechode so supravodivého stavu do normálneho) sa začali správať úplne inak po ako pred ožiarením.

Z meraní z Hallovou sondou sa zistilo, že supravodivá plocha kryštálov ab je nanesená o po 2 stupňovým uhlom vzhľadom na rovinu supravodivej pásky. Toto vychýlenie môže byť zodpovedné za veľkú časť spomínaných javov. Toto vychýlenie je spôsobené pravdepodobne metódou MOCVD, kde sa supravodivá vrstva musí nanášať pod určitým uhlom. Z výsledkov charakteristiky vlastností prezentovaných v tejto práci a taktiež v iných štúdiách však nie je úplne jasné či daná odchýlka je nevýhodou alebo výhodou pre aplikácie supravodivých pások druhej generácie.

Publikácia č.3: Characterization of commercial YBCO coated conductors after neutron irradiation

Táto publikácia sa hlbšie zaoberá charakterom pinningových centier vytvorených ožiarením rýchlymi neutrónmi. Článok analyzuje pinningové centrá vytvorené po ožiarení komerčných supravodivých pások druhej generácie podobne ako pri predchádzajúcich publikáciách. Tento krát sa jedná opäť o supravodivú pásku od firmy SuperPower kde je supravodivá vrstva YBCO nanesená metódou MOCVD

na IBAD (Ion Beam assisted Depossition) Mgo podložnej vrstve. Druhá vzorka je of firmy Bruker a tá má supravodivú vrstvu v hrúbke až 2.5 µm nanesenú metódou PLD (Pulsed Laser Deposition) a podložná vrstva je nanesená taktiež metódou IBAD, ale sa skladá z Ytria stabilizovaným ZrO. (YSZ template).

Podľa známej publikácie od Blattera a kol. [10] existuje formula, podľa ktorej sa dá uhlová anizotropia transformovať do izotopického problému a grafu, kde kritický prúd závisí iba od veľkosti magnetického poľa a nie jeho smeru. Táto publikácia obsahuje formulu, podľa ktorej sa YBCO anizotropná charakteristika pretransformuje na izotropnú. Táto formula (anisotropic scalling) je vytvorená detailným štúdiom štruktúry a vlastností kryštálov YBCO. Funguje pri náhodne rozložených pinningových centrách , ktoré nezvýhodňujú pinning v žiadnom smere. Vďaka tejto vlastnosti je daná formula silným nástrojom na rozlíšenie náhodne rozložených a korelovaných pinningových centier. Podľa charakteristiky ožiarenia vzoriek rýchlymi neutrónmi je jasné, že defekty v sledovaných vzorkách musia byť úplne náhodné. Je to z dôvodu, že boli ožiarené v centre experimentálneho reaktora TRIGA MARK 2 vo Viedni, kde sú toku neutrónov so všetkých smerov.

Avšak prekvapujúco formula pre „anisotropic scalling“ nefunguje pre študované pinningové centrá. Tento jav si však vyžaduje hlbšiu štúdiu. Ak je formula pre „anisotropic scalling“ správna potom by to znamenalo, že pinningové centrá vytvorené rýchlymi neutrónmi interagujú s inými korelovanými už existujúcimi pinningovými centrami. Ďalšou možnosťou je neplatnosť formuly pre „anisotropic scalling“ pre pásky druhej generácie vyrobených spomenutými metódami, keďže aj pred ožiarením táto formula nefungovala na 100 percent. Článok sa zaoberá aj ožiarením supravodiča termálnymi neutrónmi. Hoci termálne neutróny samé o sebe nedokážu svojou energiou poškodiť kryštalickú mriežku YBCO a tým vytvoriť pinningové centrum, dokážu aktivovať prvky v supravodivej páske, ktoré sa následne stanú β žiaričmi. Keďže je dobre známe, že β žiarenie dokáže vytvoriť efektívne pinningové centrá[11] je jasné že tento sekundárny jav môže zlepšiť vlastnosti supravodiča aj po zdanlivo neúčinnom ožiarení termálnymi neutrónmi. Avšak pri pozorovaných tokoch termálnych neutrónov bol tento jav pozorovaný len minimálne a bol zhodnotený ako zanedbateľný.

Publikácia č.4: Positron annihilation lifetime spectroscopy study of neutron irradiated high temperature superconductors Y Ba_2 Cu_3 $O_{7-\delta}$ for application in fusion facilities

Do ďalšieho štúdia pinningových centier v surpavodivých páskach druhej generácie boli zapojené aj sofistikované metódy z defektoskopie. Presnejšie, študovanie defektov pomocou pozitrónovej anihilačnej analýzy. Kvôli štruktúre pásky a prítomnosti viacerých nesupravodivých stabilizačných vrstiev, pre tento experiment boli pripravené špeciálne vzorky tzv.. „bulky“ YBCO, ktoré boli štruktúrou

identické supravodivej vrstve použitej v supravodivej páske. Hoci páska obsahuje iné pole pinningových centier ako bulk, je úplne oprávnené uvažovať, že mechanizmus vytvorenia defektov po ožiarení rýchlymi neutrónmi je identický pri páske ako pri bulku.

Táto publikácia obsahuje podrobný opis aparatúry a princípu pozitrónovej anihilačnej analýzy.

Namerané hodnoty na vzorkách ukázali, že pozitrónová anihilačná spektroskopia je veľmi účinný spôsob štúdia malých pinningových centier na úrovni mono alebo bi-atomárnych vakancií v kryštalických mriežkach. Metóda je neefektívna na pozorovanie veľkých pinningových centier rozmerov aj niekoľko nm.

Publikácia č. 5 Point defects in $YBa_2Cu_3O_{7-\delta}$ studied by positron annihilation spectroscopy

Táto publikácia sa zaoberá hlbokou analýzou výsledkov z experimentu detailne opísaného v predošlej publikácii č.4.

Keďže predchádzajúce publikácie sa venovali „veľkým“ pinningovým centrám tu sa zameriavame na bodové pinningové centrá, ktoré sa tiež vytvárajú pri ožiarení rýchlymi neutrónmi. Avšak ich význam a efektivita pri zvyšovaní kritických prúdov nie je taká výrazná v porovnaní s „veľkými“ pinningovými centrami v rozmeroch rádovo niekoľko nm.

Avšak aj mono alebo bi vakancie v kryštalickej mriežke YBCO môžu byť efektívnymi pinningovými centrami.

Supravodivé YBCO bulky boli ožiarené v dvoch stupňoch na toky $1x10^{21}$ a $6x10^{21}$ m^{-2} a následne zohriate na teplotu 250 °C po dobu 4h. Podľa očakávania sa kritické prúdy pribúdajúcim vplyvom žiarenia zvyšovali. Tie boli namerané na VSM (Vibrating Sample Magnetometer). Taktiež podľa predpokladu sa kritický prúd znížil po zohriatí vzorky. Toto je známy fakt, keďže bodové defekty kryštalickej mriežky sa pri zohriatí a následnom ochladení dokážu zaceliť. Bárium vakancie a Cu-O bi - vakancie boli identifikované ako hlavné efektívne bodové defekty a teda aj pinningové centrá. Ich hustota však nie je úplne úmerná intenzite ožiarenia. Hustota týchto bodových defektov je až o celý rád vyššia ako koncentrácia dobre známych „veľkých“ pinningových centier. Tento pomer sa však znižuje ďalším ožarovaním.

V štúdii bolo použité aj zariadenie SQUID (*superconducting* quantum interference device) na meranie kritických prúdov ako aj kritickej teploty. Hlavným výstupom publikácie sú presné hodnoty hustôt bodových defektov a ich vplyv na supravodivé parametere vzoriek. Bol preukázaný prekvapujúci a neočakávaný vplyv bodových pinningových centier na kritické prúdy a kritické prúdové hustoty pričom vplyv na kritickú teplotu si ponechali “veľké” pinningové centrá.

Publikácia č. 6 *n*-Values of commercial YBCO tapes before and after irradiation by fast neutrons

Jedná sa o jednu z najhodnotnejších teoretických publikácií analyzujúcich pinning v supravodivých páskach po ožiarení rýchlymi neutrónmi. Význam publikácie je zvýraznený tým, že obsahuje množstvo unikátnych experimentálnych dát opisujúcich závislosti n-hodnôt od teploty, veľkosti a uhla externého magnetického poľa na rôzne druhy komerčných supravodivých pások druhej generácie. N hodnota reprezentuje homogenitu supravodiča ako aj termálne aktivovaný depinning. Vzťah reprezentujúci n hodnotu pri prechode so supravodivého do normálneho stavu je nasledovný:

$$\frac{V}{V_c} = \left(\frac{I}{I_c}\right)^n$$

Hoci je to dôležitou charakteristikou supravodiča, kvalitných článkov analyzujúcich práve tento parameter je veľmi málo. n hodnoty sú pritom kľúčové pre mnohé aplikácie, nakoľko príliš vysoké hodnoty znamenajú obrovské riziko poškodenia supravodivého zariadenia pri prekročení maximálnych prúdových hodnôt, kde supravodič extrémne rýchlo prejde zo supravodivého do normálneho stavu. Príliš malé n hodnoty zase znamenajú príliš nízke využitie potenciálu supravodiča a zbytočné zníženie prirodzeného prúdu v supravodiči.

V článku sú analyzované opäť komerčné supravodivé pásky druhej generácie a to: SuperPower(2008) 4 mm, SuperPower(2012) 4 mm, SuperPower(2012) 12 mm, AMSC 4 mm , AMSC 12 mm, SHSC 4 mm. teda táto štúdia sa zaoberá aj páskami širokými 12 mm a nielen štandardnými 4mm širokými páskami. V štúdii sú prezentované dáta n hodnôt pod rôznymi uhlami a veľkosťami magnetického poľa až to 15 T. Plné uhlové profily n-hodnôt sú až do 6 T. Všetky hodnoty boli merané pre teploty od 50 K – 85 K.

Z prezentovaných výsledkov vidno, že novšie a výkonnejšie pásky majú o niečo vyššie n hodnoty. Keďže publikácia obsahuje pomerne veľké množstvo dát, bolo ich možné hlbšie analyzovať a dobudovať aj teóriu v oblasti termálnej aktivácie magnetických vírov a plazenie vírov (flux creep). Efekt uniformity, čo bol faktor v minulosti pokladaný ako jeden zo základných pôvodcov exponenciálneho charakteru prechodu a teda n hodnoty, bol úplne vylúčený ako faktor akokoľvek ovplyvňujúci n hodnoty vo vyšších poliach kde je prúd limitovaný zrnami (granulami) YBCO. Taktiež bol tento faktor spochybnený pri experimente s ožiarením a je otázkou či vôbec zohráva nejakú rolu, alebo je to len pozostatok zo starších publikácií a opatrnosť vo vyjadreniach v tých novších ktorá zatiaľ bráni aby bol tento faktor úplne vylúčený. Ani táto štúdia však nedokáže tento faktor úplne vylúčiť a to hlavne pri malých externých poliach, avšak potvrdiť sa ho nepodarilo nikde.

Celkovo sa dá pozorovať istá úmernosť medzi n hodnotami a kritickými prúdmi. To sa dá vysvetliť medzi koreláciou medzi n-hodnotami a pinningovou energiou čo je v súlade s teóriou prezentovanou

v článku od Y. Yeshurun, a kol. [12]. Avšak v pri výsledkoch meraní je bola pozorovaná i opačná korelácia n hodnôt s pinningovou energiou (alebo kritickým prúdom nakoľko sú úmerné). Takáto inverzná korelácia už bola pozorovaná a vysvetlená schodovitými čiarami magnetického toku. Tie sa tvoria v prípade vysokej hustoty periodických pinningových centier. Takéto centrá sú napríklad štruktúrne-vnútorné pinningové centrá YBCO kryštálov tvorene CU-O vrstvami (intrinsic pinning). V prípade ožiarenia pravdepodobne nastala nejaká zmena-interakcia s pinningovými centrami vytvorenými ožiarením (netreba zabúdať ani na veľké množstvo bodových pinningových centier spomínaných v publikáciách č. 4 a 5) ktorá umožnila vytvorenie schodových čiar magnetického toku. Toto však nastalo iba pri teplotách 64 K a 50 K. Tento výsledok je mimoriadne významný a znamená posun štúdiu plazyvých magnetických tokov a objasnení exponenciálneho charakteru prechodu medzi supravodivým a prirodzeným stavom.

3.2 Charakteristika supravodivých cievok pre energetiku

Supravodivé generátory majú potenciál najmä v morských verených turbínach kde ďalšie zvyšovanie výkonu je limitované kvôli veľkej hmotnosti generátora umiestneného na stožiari. Supravodivé generátory a motory majú potenciál napríklad v letectve, kde je nutnosť nízkej hmotnosti zariadení.
V predchádzajúce časti boli venované hlavne materiálom a supravodivým páskam druhej generácie. V tejto kapitole budú prezentované už najjednoduchšie zariadenia vyrobené zo supravodivých pások druhej generácie, ktorými sú cievky. Keďže cievky sú elementárne prvky mnohých zariadení ako základné prvky motorov a generátorov, štúdium vlastností cievok je extrémne dôležité pre ďalší krok smerom k aplikáciám supravodičov.

Publikácia č. 7: Full angular critical current characteristics of coated conductors using a two-axis high current goniometer

Táto publikácia sa stále venuje problematike pinningu avšak namerané výsledky majú impakt na vývoj supravodivých motorov a generátorov. Vzorkami sú opäť supravodivé pásky druhej generácie od SuperPower a AMSC hrubými 4mm. Pre aplikácie v energetike a hlavne v rotačných zariadeniach ako sú motory a generátory, cievky na seba navzájom pôsobia magnetickými poľami rôznych smerov. Preto poznať správanie sa pásky pod rôznymi uhlami v smere tvz. maximálnej Lorentzovej sily, ktorá bola spomínaná v predchádzajúcich publikáciách nemusí stačiť. Preto bol zostrojený goniometer ktorým sa dajú vzorky charakterizovať pod každým smerom magnetického poľa. Zostrojenie tohto zariadenia bolo pomerne náročné a opis zariadenia je významnou časťou publikácie. Pre názornejšiu

predstavu je na Obr. 4 ukázaná vzorka nainštalovaná pre charakterizáciu v goniometri. Na Obr. 4 je goniometer v už spomínanej polohe s maximálnou Lorentzovou silou, avšak uhol θ zabezpečuje rotáciu mimo maximálnej Lorentzovej sily.

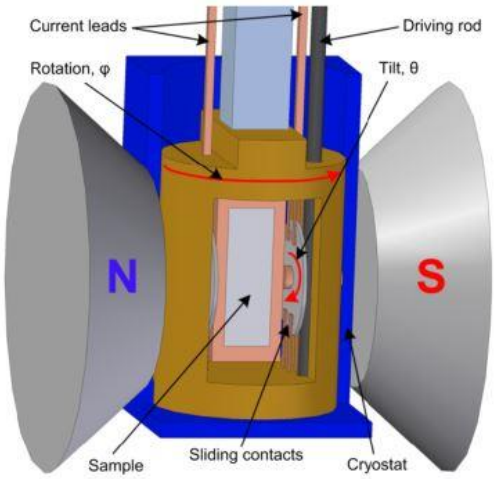

Obr. 4. Náčrt goniometra na charakterizáciu supravodivých pások.

Merania sú prevedené v tekutom dusíku a teda v teplote približne 77 K. Magnetické polia, dosiahnuteľné na magnete goniometra boli do veľkosti poľa 500 mT a výsledky meraní sú uvedené v publikácii. Pri SuperPower páske boli opäť pozorované zaujímavé posuny píkov a teraz sa dalo aj podľa jednoduchých geometrických výpočtov ukázať uhlové posunutie supravodivých ab vrstiev oproti ploche pásky.

Publikácia č. 8: Study of 2G high temperature superconducting coils: determination of critical current

Supravodivé cievky vyrobené zo supravodivých pások druhej generácie sú zaujímavým prvkom pre mnohé aplikácie. Ich štúdium je extrémne zaujímavé vďaka anizotropii supravodivých pások. V cievke sa tvorí komplexné magnetické pole pôsobiace na každý závit cievky inou intenzitou a pod iným uhlom. Ak je cievka vystavená pôsobeniu externého magnetického poľa, jej vlastnosti sa môžu znova radikálne meniť a dokonca môže nastať aj navýšenie výkonu. Toto správanie sa v magnetickom poli ako aj vo vlastnom poli sa dá dnes namodelovať vysoko sofistikovanými simulačnými technikami. Používa sa hlavne program COMSOL [13], ktorý pracuje s metódou konečných prvkov (finite element) a používa už známy vzťah exponenciálneho prechodu so supravodivého stavu do normálneho inak nazývaný aj EJ exponenciálny zákon. (publikácia č.6. ,exponent je n hodnota)

V tejto publikácii sa pracuje s dvoma kruhovými cievkami (pancake coil) ktoré poli vyrobené so supravodivých pások SuperPower a AMSC. Obe cievky mali 40 závitov a vnútorný priemer 59 mm.

Pre obe cievky bol vytvorený model v programe COMSOL Ako jedna z hlavných vstupných premenných pre tento model sú výsledky meraní kritických prúdov a n hodnôt pri rôznych smeroch magnetického poľa. Hlavne pri konfigurácii s maximálnou Lorentzovou silou. (Boli prezentované v článkoch predstavených v častiach 3.1 a 3.2).

Platnosť modelu bola overená aj experimentom s veľmi dobrou zhodou. Z experimentov a simulácii je dobre známym faktom, že najvnútornejší závit cievky je zaťažený najviac a prechádza do normálneho stavu skôr ako ostatné závity. Preto je kritický prúd cievky limitovaný najčastejšie práve týmto závitom. Všeobecne sa pokladá za kritické kritérium bezpečnej prevádzky supravodivej cievky zhotovenej z 2G supravodivých pások 100 μV/m. Avšak zostrojeným modelom bolo ukázané že pri tomto kritickom napätí v cievke je napätie na najvnútornejšom závite až do hodnoty 2000 μV/m čo už znamená výrazné prehrievanie tejto časti cievky a páska v tomto závite už takmer vôbec neoperuje v supravodivom stave alebo na jeho úplnej hranici. Takmer polovica celkového napätia cievky je produkovaná práve v tomto najvnútornejšom závite. Dlhodobá ale aj kratšia prevádzka na týchto hraničných hodnotách môže viesť k trvalému poškodeniu cievky. Preto je v tejto štúdii navrhnuté nové kritické napäťové kritérium, ktorého hodnota je 20 μV/m a zabezpečilo by trvalú bezpečnú prevádzku cievky pokiaľ sa napätie udrží na tejto hodnote. Návrh tohto kritéria je hlavným a najdôležitejším výstupom tejto publikácie. Význam tohto nového kritéria potvrdzuje fakt, že toto je najcitovanejší článok so všetkých článkov predložených v tejto práci.

Publikácia č. 9: Anisotropy of 2G HTS racetrack coils in external magnetic fields

Kapitola 3.1 bola do značnej miery venovaná anizotropii supravodivých pások druhej generácie a meraniam kritických prúdov pod rôznymi uhlami pokrývajúcimi aj 180 °. V tejto publikácii bol vykonaný takmer identický experiment uhlových meraní až na ten rozdiel , že vzorkou nebola samostatná páska, ale celá cievka.

Nakoľko vytvoriť homogénne externé magnetické pole na takejto veľkej ploche je pomerne náročné plus sily ktoré v istých smeroch pôsobia na cievku môžu byť značne veľké, zostrojenie spoľahlivej meracej aparatúry bola obrovská výzva. Schéma meracej aparatúry je zobrazená na Obr.5

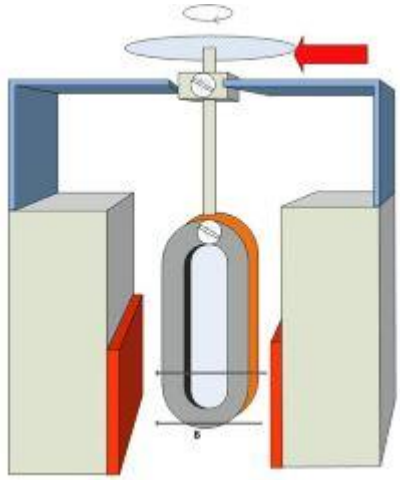

Obr.5: Meracia aparatúra na charakteristiku cievok pod rôznymi uhlami externého magnetického poľa.

Vzorkami boli dve cievky v tvare ovalu (racetrack coils) vyrobené z pások od SuperPower a AMSC. Práve cievky takéhoto tvaru sú najvhodnejšími kandidátmi na aplikácie v supravodivých generátoroch/motoroch[14].

V článku sa nachádzajú výsledky meraní pri teplote 77 K (teplota tekutého dusíka) v externom poli do 120 mT. Vyššie polia nebolo možné namerať kvôli vysokým magnetickým silám pôsobiacim na cievku pod prúdom. Výsledky sú rozanalyzované a namerané charakteristiky vysvetlené na základe anizotropie samotných pások. Výsledky meraní sú analyzované aj na základe simulácií v programe COMSOL. Celkovo táto publikácia dáva veľmi dobrú informáciu o správaní sa cievok v magnetickom poli a ich najvhodnejšom geometrickom usporiadaní pre prípadné aplikácie v energetike.

3.3 Straty v supravodivých cievkach pri striedavom prúde

Straty v supravodičoch druhého druhu a teda aj vo vysokoteplotných supravodičoch pri napojení na striedavý prúd sú známym a pomerne dobre preštudovaným javom. [15], [16]. Principiálne je za týmto javom už spomínaný pinning, ktorý bráni zmene magnetického toku v supravodiči. Hoci toto je veľmi efektívne pri jednosmernom prúde, pri prúde kde neustále dochádza k zmene smeru prúdu a teda i magnetického toku môže táto vlastnosť pôsobiť aj kontraproduktívne. V každom prípade sú tieto straty v supravodičoch rádovo nižšie ako v bežných vodičoch, avšak tento jav si vyžaduje hlbšie štúdium.

Publikácia 10: Complex Study of Transport AC Loss in Various 2G HTS Racetrack Coils

Existuje pomerne veľa publikácii venujúcim sa stratám v supravodivých páskach druhej generácie[17], [18]. Táto publikácia sa však zaoberá stratami v supravodivých cievkach vyrobených z pások druhej

generácie. Tieto straty sú kľúčové pri dizajne supravodivých zariadení ako aj ich chladiacich systémov, keďže tie musia tieto straty vyrovnávať aby sa nezvyšovala teplota prevádzky supravodičov. Existuje viacero možností ako elektrickou metódou určiť striedavé straty pri supravodivých cievkach. Napríklad metóda "critical state" opísaná v článku [19] J.R. Clemom a kol. Napríklad E. Pardo a kol.[20] použili metódu minimálnej variácie magnetickej energie. Potom F. Grilli Ashworth vyvinuli model založený na krajných elementoch aby stanovili straty vo cievkach z vysokoteplotných supravodičov [21].
V tejto publikácii sú však striedavé straty v cievkach stanovené zjednodušenou metódou podľa [22]. Vzorkami boli identické cievky ako boli použité v publikácii č.9. Merania strát boli prevedené v tekutom dusíku a teda pri teplote približne 77 K a pri frekvenciách 20, 50 a 100 Hz. Namerané hodnoty boli následne porovnané s nasimulovanými dátami z programu COMSOL. Simulácie a uskutočnené merania ukázali dobrú zhodu v hodnotách. Zaujímavým výstupom publikácie je experimentálne zistenie, že podložná magnetická vrstva v supravodivej páske (substrate) zvyšuje straty v supravodivej cievke. Keďže AMS páska je vyrobená použitím práve takejto vrstvy, produkuje aj vyššie straty pri striedavom prúde.

Publikácia 11: *Theoretical and experimental magnetization loss comparison between IBAD coils and RABiTS coils*

V tejto publikácii je hlbšie rozobratý rozdiel medzi cievkou vyrobenou z pásky s magnetickým a nemagnetickým substrátom (substrate), ktorý bol načrtnutý v publikácii č.10. V tejto práci sa však straty pri striedavom prúde merali štandardnou metódou s pomocnými cievkami (pick up coils). Nakoľko cievky charakterizované v predchádzajúcej štúdii sú vyrobené jedna z pásky na magnetickom a druha na nemagnetickom substráte , vzorky nebolo nutné meniť a boli ideálnymi kandidátmi pre túto štúdiu.
Merania boli vykonané v tekutom dusíku (77 K) pre frekvencie 10, 50 a 100 Hz. Hoci frekvencia teoreticky na stratu v supravodiči nevplýva. (nakoľko sa obvykle vyjadruje vo W na jeden cyklus) avšak existujú javy ktoré sú aktívne iba pri vyšších frekvenciách a môžu straty ovplyvniť. K experimentálnym meraniam boli znova pridané aj simulácie z programu COMSOL.
Z analýzy nameraných výsledkov a simulácií vyplýva že magnetizačné straty sú oveľa vyššie v cievke s feromagnetickým substrátom. Ten prehlbuje prenikanie magnetického poľa do cievky a zvyšuje magnetický tok v danom preniknutom regióne. Avšak feromagnetické straty v samotnom substráte sa ukázali ako bezvýznamné okrem veľmi malých magnitúd polí kde substrát ešte nie je saturovaný. Zo zistení štúdie však vyplýva, že v súvislosti so zachovaním čo najnižších magnetických strát cievky je dôležité zachovať všetky materiály v substráte supravodivej pásky nemagnetické.

Publikácia 12: Power Losses of 2G HTS Coils Measured in External Magnetic DC and Ripple Fields

Motiváciou tejto štúdie je priama aplikácia vysokoteplotných supravodičov vo veterných turbínach. Existuje niekoľko konceptuálnych štúdií podporujúcich túto myšlienku ako napr. [23]. Podstatou aplikácie supravodičov je aktuálny trend bezprevodovkových veterných turbín s viacpólovým generátorom. Táto architektúra má nesporné výhody v oblasti poruchovosti nakoľko porucha prevodovky je pomerne častá a veľmi časovo i finančne náročná na odstránenie [24]. Znamená však vyššiu hmotnosť generátora umiestneného na stožiari. V prípade vysokovýkonných veterných turbín inštalovaných v šelfových oblastiach morí by bolo kvôli vysokej hmotnosti nesmierne náročné zostrojiť bezprevodovkovú veternú turbínu s výkonom vyšším ako 10 MW. Tuto je práve priestor pre vysokoteplotné supravodiče, ktoré by dokázali znížiť hmotnosť 10 MW viacpólového generátora až na 1/3 pôvodnej hmotnosti. Tento koncept má však mnoho ekonomických a technických výziev. Medzi nimi sú napríklad aj straty v supravodivom rotore pri oscilácii magnetického poľa, ktoré sa deje v rotačných zariadeniach. V ideálnom prípade je cievka v rotore generátora vystavená vždy konštantnému magnetickému poľu. Avšak v reálne toto pole mierne osciluje a navyše pri nekonštantnej rýchlosti otáčania veternej turbíny sú tieto oscilácie dokonca s nekonštantnou frekvenciou.

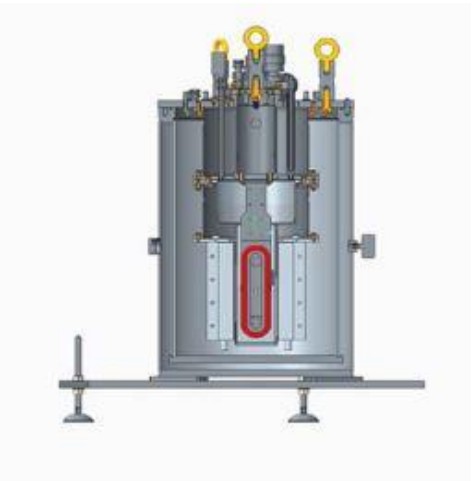

Obr.6: Schéma experimentálneho kalorimetrického zariadenia na meranie strát v supravodivých cievkach.

Pre simulovanie takýchto podmienok na určenie strát v supravodivých cievkach bolo špeciálne pre túto štúdiu navrhnuté a skonštruované experimentálne meracie zariadenie. Zariadenie pracuje na princípe kalorimetrickej metódy [25]. Jeho schéma je na Obr.6. Zariadenie bolo autormi článku kompletne navrhnuté a vyrobené na Univerzite v Cambridge. Kalorimetrická hodnota je založená na princípe merania objemu vyparenéhо tekutého dusíka z odizolovanej nádoby kalorimetra, v ktorej je nainštalovaná meraná supravodivá cievka.

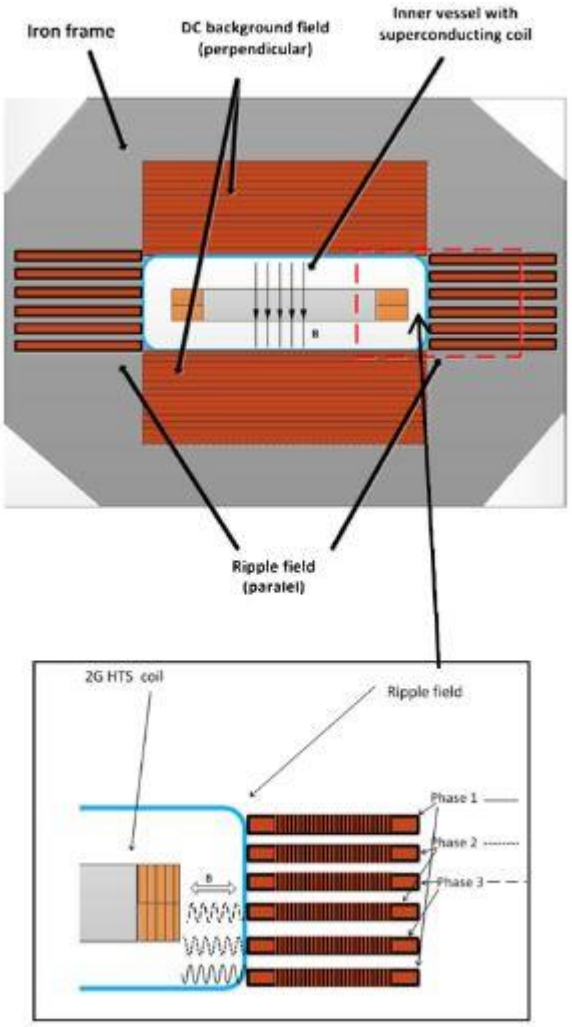

Obr.7: Schéma magnetickúch polí v kalorimetri.

Najväčšou výhodou kalorimetrickej metódy je , že straty v cievkach sa dajú merať pod akýmikoľvek externými magnetickými poľami. Toto nie je vždy možné pri elektrických metódach a v tejto v tejto štúdii sa táto výhoda aj naplno využila, kde na cievku pôsobilo externé magnetické pole paralelne na pole cievky ako aj krížne oscilujúce magnetické pole. (Obr.7)

V prvej časti publikácie bola funkčnosť zariadenia a metódy overená porovnaním s meraniami vykonanými klasickou elektrickou metódou. Hoci kalorimetrická metóda sa ukázala menej presná a to hlavne pri veľmi malých stratách, jej funkčnosť a platnosť bola úspešne overená.

Na straty bola charakterizovaná oválna cievka zostrojená zo supravodivej pásky SuperPower. V prvom kroku bola cievka napájaná striedavým prúdom a nachádzala sa v homogénnom magnetickom poli až do 200 mT. Všetko samozrejme prebiehalo v tekutom dusíku a teda pri teplote 77 K. Meraná cievka bola napájaná striedavým prúdom až po 30 A nakoľko kritický prúd bez akéhokoľvek externého poľa tejto cievky bol 36.3 A. V druhom kroku bola meraná cievka napájaná jednosmerným prúdom (25 A,30 A, 35 A) avšak bolo vytvorené premenlivé externé magické pole až do 200 mT v píku. V poslednom prípade bola cievka napájaná jednosmerným prúdom a boli aplikované premenlivé magnetické polia v dvoch smeroch. Avšak sa ukázalo, že krížna magnetická vlna s amplitúdou 30 mT nemala žiaden vplyv na výsledné straty.

V tejto publikácii bolo demonštrované zariadenie vhodné na simulovanie podmienok v reálnych generátoroch a vyčíslenie strát v supravodivých cievkach. Časovo premenné externé magnetické pole môže v supravodivej cievke spôsobiť značné straty čo bolo aj ukázané a namerané. Krížne pole danej amplitúdy ako aj bolo predpokladané nemalo na straty nijaký vplyv. Toto by sa však mohlo zmeniť v prípade iného usporiadania cievky.

3.4 Supravodivé motory/generátory a iné aplikácie

Publikácia 13: AC loss estimation of HTS armature windings for electric machines

Je dôležité si uvedomiť, že väčšina konceptuálnych myšlienok supravodivých motorov/generátorov sa venuje hlavne supravodivému rotoru. [26]. Je to hlavne kvôli stratám v supravodčoch pri aplikovanom striedavom prúde, ktorému bola venovaná predchádzajúca sekcia. Rotor sa väčšinou vie zaobísť s rovnako nabitými cievkami alebo dokonca aj permanentnými magnetmi. V tejto publikácii sa však analyzuje prípad motora/generátora , ktorý bude mať supravodivý aj stator. Tento koncept môže byť zaujímavý aj napriek stratám v supravodičoch pri striedavom prúde. Totiž ak je supravodivý len rotor, chladené a nechladené časti motora/generátora musia byť nejakým spôsobom fyzicky oddelené. Toto oddelenie nie je triviálne nakoľko ide o termoizoláciu v komplikovanom elektronickom zariadení. Takto je samozrejme medzera medzi rotorom a statorom zväčšená, čo má za následok zoslabnutie magnetického poľa a teda zníženie výkonu zariadenia. Ak by bolo celé zariadenie supravodivé a pracovalo by na rovnakej teplote, tomuto dôsledku by sa dalo predísť.

V tejto štúdii je rozšírený a zdokonalený COMSOL FEM model predstavený v publikácii č.8. K modelu sú pridané časti cievok so statora. Model je následne validovaný a porovnaný z experimentálnymi dátami. V ďalšej časti sa venuje stanoveniu striedavých strát v statore zariadenia pomocou vytvoreného modelu. Posledná časť štúdie sa venuje analýze súvislosti medzi výkonom samotnej supravodivej pásky druhej generácie a výslednými striedavými stratami v cievke.

Publikované dáta v štúdii sú na výsledkom počítačovej simulácie. Na základe týchto výsledkov je jasné že straty v statore sú pomerne významné. Je tu však navrhnuté i riešenie , ktorým je lepšie rozdistribuovanie cievok s menším počtom závitov. Toto riešenie však má negatívny vplyv na výslednú cenu zariadenia.

Z obrázkov prezentovaných v tejto predloženej publikácii je jasné že model poskytuje pomerne spoľahlivé dáta. Transportné straty v statore boli poctivo spočítané a bolo navrhnuté riešenie ich zníženia.

Publikácia 14: Control and operation of a high temperature superconducting synchronous motor

Táto práca sa venuje opisu a testovej prevádzke supravodivého motora skonštruovaného autormi na ústave inžinierstva na Univerzite v Cambridge. Tento motor má stator zložený so 75 supravodivých

bulkov vyrobených z YBCO materiálu priamo na ústave. Magnetizácia bulkov pre prevádzku motora navrhnutá pulzovou magnetizáciou [27] v cievkach nad štruktúrou motora. Práve magnetizácia bulkov aby pracovali ako permanentné magnety je veľmi problematickým procesom a obrovskou výzvou pri dizajne supravodivých motorov/generátorov. Študovaný motor je celý ponorený do vane s tekutým dusíkom a teda pracuje pri teplote 77 K. V statore sa nachádza 6 oválnych medených cievok avšak pre účely tejto štúdie boli dve cievky v statore vymenené za AMSC oválne supravodivé cievky vyrobené z pások druhej generácie ktoré už boli spomínané, opísané a charakterizované v predchádzajúcich predložených publikáciách. Týmto spôsobom je možné porovnať prúdovú charakteristiku v supravodivých a nesupravodivých cievkach. Tá aj bola v tejto štúdii nameraná a porovnaná. Hlavným cieľom tejto štúdie však bolo navrhnúť algoritmus na kontrolu a prevádzku takto modifikovaného motora. Na tento účel bola použitá aplikácia Simulink a program bol následne nahratý do invertora motora. Pri štarte motora frekvencia stúpa z 0 Hz to 5 Hz rýchlosťou 0.05 Hz/s. Napätie na statore stúpa z 12 V na 15.3 V. Prúdy v cievkach boli nastavené na maximálne hodnoty 5 A v medených a 10 A v supravodivých. Tu je však možné výkon cievok ešte značne zvýšiť avšak na tento test to postačovalo a prihliadalo sa na straty pri striedavom prúde, ktoré mali byť zachované na minime. Pri takýchto prúdoch sú udržané na zanedbateľnej úrovni.

Publikácia 15: Wind farms associated with flywheel energy storage Plants

Táto publikácia sa zaoberá teoretickým modelom aplikácie supravodivých zariadení do elektrizačnej sústavy. Nejedná sa tento krát o generátor nakoľko ten by sa v rámci elektrizačnej sústavy javil v modely ako úplne štandardný generátor. Táto štúdia sa preto zameria na systém v ktorom sa nachádzajú supravodivé rotačníky (flywheels) [28] za účelom uskladnenia elektrickej energie. V sieti je zapojený aj určitý počet veterných turbín a sú známe rýchlosti vetra z historických pozorovaní.
Štúdia bola situovaná na konkrétnu lokalitu v Juhoafrickej republike. V modely boli brané do úvahy ako technické tak I ekonomické parametre a cena jedného supravodivého rotačníka bola stanovená o jeden rád vyššia ako cena veternej turbíny. Bol navrhnutý ostrovný systém pozostávajúci s veterných turbín a supravodivých rotačníkov. Toto je však iba akademický príklad nakoľko rotačníky strácajú svoj zmysel regulovania napätia pokiaľ sú súčasťou menšieho ostrovného systému. Navyše sa podľa zostrojeného modelu ukázal daný koncept ako veľmi neefektívny. V ďalšej časti je preto namodelovaný hybridný systém, kde je priame spojenie s elektrizačnou sústavou. V tomto systéme sa ďalej uvažuje o fixnom počte veterných turbín a najefektívnejším počtom supravodivých rotačníkov.
Hoci inštalácia supravodivých rotačníkov vyzerá ako neštandardné riešenie, v určitých prípadoch môže byť veľmi užitočné keď dokáže plniť úlohu ako energetického úložiska tak I regulačného prvku v sieti.

Zostavený model ukázal efektívnu konfiguráciu systému s pozostávajúceho s veterných generátorov a rotačníkov zapojených do elektrizačnej sústavy. Primerané riešenie si však musí počkať na zvýšenie úložnej kapacity supravodivých rotačníkov. Toto zlepšenie je vzhľadom na rýchly vývoj a zlepšovanie sa vlastností supravodičov oprávnené očakávať v najbližších rokoch.

4. Závery a prínosy práce

Súbor predložených prác sa do hĺbky zaoberá aplikáciou supravodičov v elektroenergetike. Práca sa sústreďuje na hlavne na materiál YBCO, čo je aktuálne pokladané za najperspektívnejší materiál vo vysokoteplotnej supravodivosti.

Práca koncipovaná od elementárnej fyziky supravodičov, ktorá je aplikovaná do najjednoduchších vysokoteplotných supravodivých vodičov a to sú supravodivé pásky. Neskôr sa prechádza od charakterizácie daných pások až k najjednoduchším elektrotechnickým zariadeniam zostrojených z týchto pások a teda cievkam. Od cievok je v potom pozornosť plynulo presunutá supravodivým motorom/generátorom a nakoniec je v práci prezentovaný model so skutočnou supravodivou aplikáciou v energetike.

Prvá skupina predložených publikácií je venovaná zvyšovaniu výkonu supravodivých materiálov so zameraním na YBCO supravodivé pásky druhej generácie. Táto časť je najkomplexnejšia a venuje sa ako fyzike vo vnútri materiálu. Ako je vysvetlené hneď v úvode práce, „flux pinning“ je práve tým javom, ktorý zabezpečuje vysoký výkon supravodičov. Preto je tomuto javu venovaná veľká pozornosť v každej z predložených publikácií. Predložené články sa intenzívne venujú zvyšovaniu výkonu vytváraním pinningových centier ožiarením rýchlymi neutrónmi. Články s touto problematikou vznikli na technickej Univerzite vo Viedni v Atomistitute , ktorý disponuje vlastným experimentálnym reaktorom.

V druhej časti sa postupne prechádza od charakteristiky mikroskopickej štruktúry kk charakteristike elementárneho supravodivého vodiča a teda supravodivej pásky vzhľadom na jej aplikáciu do supravodivých cievok. Toto je kľúčové pre aplikácie v energetike. Experimenty v tejto časti boli vykonané v Atominstitute vo Viedni alebo aj na ústave materiálov a metalurgie na Univerzite v Cambridge. V tejto časti sú charakterizované aj supravodivé cievky. Ich vlastnosti samozrejme vyplývajú z charakteristiky supravodivej pásky z ktorej sú vyrobené. Experimenty v tejto časti boli vykonané na ústave inžinierstva na Univerzite v Cambridge. Z tejto charakteristiky je blízko k stratám v supravodivých cievkach pri striedavom prúde. Táto časť charakterizácie cievok je však natoľko dôležitá a rozsiahla, že si zaslúži vlastnú kapitolu. Experimenty boli tiež vykonané

ústave inžinierstva na Univerzite v Cambridge. Kde boli pre účel týchto štúdií vyrobené nové experimentálne zariadenia.

Posledná časť tejto práce je venovaná supravodivým generátorom/motorom a teda praktickým problémom pri aplikácii supravodičov. Alebo aj modelovým prípadom aplikácie supravodivých zariadení. Okrem supravodivého motora, ktorý bol skutočne zostrojený sú však výsledky prezentované v tejto časti hlavne výsledkom počítačového modelovania.

Z práce je zjavné , že vysokoteplotné supravodiče majú svoje miesto vo viacerých aplikáciách v elektroenergetike. V akom rozsahu budú využívané ukáže ďalší vývoj a progres v ich vlastnostiach a v každom prípade aj cena. Tá je zatiaľ jedným z hlavných problémov pri masovej aplikácii supravodičov v energetike.

5. Literatúra

[1] K. A. Bednorz, J. G.; Müller, "Possible high Tc superconductivity in the Ba-La-Cu-O system," *Zeitschrift für Phys. B*, vol. Vol. 64, pp. 189–193, 1986.

[2] H. Takahashi, K. Igawa, K. Arii, Y. Kamihara, M. Hirano, and H. Hosono, "Superconductivity At 43 K In An Iron-based Layered Compound LaO1-xFxFeAs," *Nature*, vol. 453, no. 7193, pp. 376–378, 2008.

[3] M. Igarashi *et al.*, "Remarkable progress in fabricating RE123 coated conductors by IBAD/PLD technique at Fujikura," *J. Phys. Conf. Ser.*, vol. 234, no. 2, p. 22016, 2010.

[4] A. Usoskin *et al.*, "Large area YBCO-coated stainless steel tapes with high critical currents," *IEEE Transactions on Applied Superconductivity*, vol. 13, no. 2. pp. 2452–2457, 2003.

[5] Cesnak and Takács, *Supravodivosť*. Alfa, 1979.

[6] S. Tönies, A. Vostner, and H. W. Weber, "Determination of inter- and intragranular currents in high temperature superconducting tapes and coated conductors," *J. Appl. Phys.*, vol. 92, no. 5, pp. 2628–2633, Aug. 2002.

[7] M. Eisterer, "Improvement of critical current densities by fission tracks in U-doped high temperature superconductors," *Supercond. Sci. Technol.*, vol. 1001, no. 10, pp. 1001–1005, 1998.

[8] M. Eisterer *et al.*, "Neutron irradiation of SmFeAsO $_{1-x}$ F $_{x}$," *Supercond. Sci. Technol.*, vol. 22, no. 6, p. 65015, 2009.

[9] F. M. Sauerzopf, H. P. Wiesinger, W. Kritscha, H. W. Weber, G. W. Crabtree, and J. Z. Liu, "Neutron-irradiation effects on critical current densities in single-crystalline YBa2Cu3O7-," *Phys. Rev. B*, vol. 43, no. 4, pp. 3091–3100, Feb. 1991.

[10] G. Blatter, V. B. Geshkenbein, and A. I. Larkin, "From isotropic to anisotropic superconductors: A scaling approach," *Phys. Rev. Lett.*, vol. 68, no. 6, pp. 875–878, Feb. 1992.

[11] J. Giapintzakis *et al.*, “Production and identification of flux-pinning defects by electron irradiation in YBCO single crystals,” *Phys. Rev. B*, vol. 45, no. 18, pp. 10677–10683, 1992.

[12] Y. Yeshurun, A. P. Malozemoff, and A. Shaulov, “Magnetic relaxation in high-temperature superconductors,” *Rev. Mod. Phys.*, vol. 68, no. 3, pp. 911–949, 1996.

[13] “www.comsol.com.” .

[14] Y. Jiang, R. Pei, and Z. Hong, “Design of an HTS motor,” *J. Phys. Conf. Ser.*, vol. 97, no. 1, p. 12123, 2008.

[15] P. H. Melville, “A.C. loss and related effects in type II superconductors,” *Adv. Phys.*, vol. 21, no. 92, pp. 647–689, Jul. 1972.

[16] M. R. Halse, “AC face field losses in a type II superconductor,” *J. Phys. D. Appl. Phys.*, vol. 3, no. 5, pp. 717–720, 2002.

[17] N. Amemiya *et al.*, “AC loss reduction of YBCO coated conductors by multifilamentary structure,” *Supercond. Sci. Technol.*, vol. 17, no. 12, pp. 1464–1471, 2004.

[18] F. Gömöry, M. Vojenčiak, E. Pardo, M. Solovyov, and J. Šouc, “AC losses in coated conductors,” *Supercond. Sci. Technol.*, vol. 23, no. 3, p. 34012, 2010.

[19] J. R. Clem, J. H. Claassen, and Y. Mawatari, “AC losses in a finite Z stack using an anisotropic homogeneous-medium approximation,” *Supercond. Sci. Technol.*, vol. 20, no. 12, pp. 1130–1139, 2007.

[20] E. Pardo, J. Šouc, and J. Kováč, “AC loss in ReBCO pancake coils and stacks of them: modelling and measurement,” *Supercond. Sci. Technol.*, vol. 25, no. 3, p. 35003, 2012.

[21] F Grilli and S P Ashworth, “Measuring transport AC losses in YBCO-coated conductor coils,” *Supercond. Sci. Technol.*, vol. 20, no. 8, p. 794, 2007.

[22] S. P. Ashworth and M. Suenaga, “Experimental determination of the losses produced by the interaction of AC magnetic fields and transport currents in HTS tapes,” *Phys. C Supercond.*, vol. 329, no. 3, pp. 149–159, 2000.

[23] A. B. Abrahamsen *et al.*, “Superconducting wind turbine generators,” *Supercond. Sci. Technol.*, vol. 23, no. 3, p. 34019, 2010.

[24] D. Robb, “The gearbox challenge–The role of bearings in gearbox failure,” *Wind. Mon. Mag.*, vol. Nov., pp. 55–60, 2005.

[25] N. Magnusson and S. Hörnfeldt, “Calorimetric apparatus for alternating current loss measurements on high-temperature superconductors,” *Rev. Sci. Instrum.*, vol. 69, no. 9, pp. 3320–3325, Sep. 1998.

[26] H. W. Neumüller *et al.*, “Advances in and prospects for development of high-temperature superconductor rotating machines at Siemens,” *Supercond. Sci. Technol.*, vol. 19, no. 3, p. S114, 2006.

[27] U. Mizutani, T. Oka, Y. Itoh, Y. Yanagi, M. Yoshikawa, and H. Ikuta, “Pulsed-field magnetization applied to high-Tc superconductors,” *Appl. Supercond.*, vol. 6, no. 2, pp. 235–246, 1998.

[28] J. Lee, S. Jeong, Y. H. Han, and B. J. Park, “Concept of Cold Energy Storage for Superconducting Flywheel Energy Storage System,” *IEEE Transactions on Applied Superconductivity*, vol. 21, no. 3. pp. 2221–2224, 2011.

6. Prílohy

Neutron irradiation of coated conductors

2010 Supercond. Sci. Technol. 23 014009

(http://iopscience.iop.org/0953-2048/23/1/014009)

Supercond. Sci. Technol. **23** (2010) 014009 (6pp) doi:10.1088/0953-2048/23/1/014009

Neutron irradiation of coated conductors

M Eisterer, R Fuger, M Chudy, F Hengstberger and H W Weber

Atominstitut, Vienna University of Technology, Stadionallee 2, 1020 Vienna, Austria

E-mail: eisterer@ati.ac.at

Received 31 July 2009, in final form 25 August 2009
Published 9 December 2009
Online at stacks.iop.org/SUST/23/014009

Abstract
Various commercial coated conductors were irradiated with fast neutrons in order to introduce randomly distributed, uncorrelated defects which increase the critical current density, J_c, in a wide temperature and field range. The J_c-anisotropy is significantly reduced and the angular dependence of J_c does not obey the anisotropic scaling approach. These defects enhance the irreversibility line in not fully optimized tapes, but they do not in state-of-the-art conductors. Neutron irradiation provides a clear distinction between the low field region, where J_c is limited by the grain boundaries, and the high field region, where depinning leads to dissipation.

(Some figures in this article are in colour only in the electronic version)

1. Introduction

Neutron irradiation is certainly not practical for improving the properties of long length commercial superconductors, but a very efficient tool for benchmarking and investigating flux pinning. It helps in understanding vortex physics [1–3] and limitations of the current flow [4–6]. Efficient pinning centers are introduced, whose size perfectly matches the coherence length of $YBa_2Cu_3O_{7-\delta}$ (YBCO). They improve the critical currents, if the density of defects was originally too small, but diminish them, if the total defect concentration becomes too high. Although the resulting defect structure is not perfectly well defined, since only the density of the largest defects, the collision cascades, is known [7] and many smaller defects of unknown density are produced [8], it is clearly established that all defects are randomly distributed and uncorrelated, i.e., without a preferred orientation. It is particularly interesting to study the interplay of these defects with the correlated disorder usually present in coated conductors or thin films [9–11]. In the present study, the effect of neutron irradiation on commercial coated conductors was investigated. Similarities and differences in differently produced tapes will be presented in the following in order to provide a comprehensive picture of neutron irradiation of this class of materials. We do not aim at comparing the properties of the unirradiated samples, since they were supplied at different times and the rapid development during the past few years would not allow a useful comparison between the different production routes. The different stages of optimization turned out to be the main source of differences in the radiation response of the investigated tapes.

2. Experimental details

Three different types of commercial YBCO tapes were studied. The first type of samples (denoted as MODRAB in the following) was prepared by metal organic deposition (MOD) on a RABITS template. The second series of samples (PLDYSZ) is based on an IBAD (ion beam assisted deposition) YSZ (yttrium stabilized zirconia) template. The superconducting layer was prepared by pulsed laser deposition (PLD). The third series (MOCVDMgO) had IBAD MgO templates with the YBCO layer made by metal organic chemical vapor deposition (MOCVD). The MODRAB samples were irradiated to higher fluences (4×10^{21} and 10^{22} m^{-2}) than the PLDYSZ and MOCVDMgO samples (2×10^{21} m^{-2}). All samples were characterized by four probe transport prior to and after irradiation by fast neutrons. The transport measurements were made under helium gas flow up to fields of 15 T. The samples were measured in different fields and temperatures and also rotated in the magnetic field under the maximum Lorentz force configuration ($J \perp H$). The current was continuously ramped until an abort criterion was reached. The critical current was defined by the 1 μV cm^{-1} criterion. Indium pressed contacts are most suitable for our experiments because of their low resistivity, reliability and removability, which is important for the irradiation process. The transition temperature (T_c) and the irreversibility lines were measured with a constant current of 10 mA, while the temperature was slowly decreased at fixed applied fields. T_c and T_{irr} were evaluated at 0.1 μV cm^{-1}. Only the data presented in figures 3 and 4 were measured in a vibrating sample magnetometer (VSM) at 10 K, while ramping the field at 0.6 T min^{-1}. All

samples were checked by magnetoscanning [12] to ensure homogeneous properties.

The samples were irradiated in the central irradiation facility of the TRIGA MARK II reactor in Vienna at a power of 250 kW (thermal/fast neutron flux density: $6/7.6 \times 10^{16}$ m^{-2} s^{-1}). The samples were sealed into a quartz tube to avoid contact between the samples and the cooling water in the reactor. The quartz tubes were put into aluminum containers, which were filled with water and placed at the correct irradiation position. The temperature during irradiation did not exceed 60 °C. All fluences refer to fast neutrons ($E > 0.1$ meV), the corresponding thermal neutron fluences ($E < 0.55$ eV) were smaller by a factor of 1.27 [13]. Neutron irradiation creates a wide spectrum of defects in the superconductor by elastic collisions of the neutrons with the atoms. Depending on the kinetic energy transferred from the neutron to the primary recoil atom, point defects or larger defect structures appear. In an avalanche-like process a huge number of atoms can be displaced, leading to local melting of the crystal lattice. The result is a spherical region of amorphous material with a mean diameter of about 3–6 nm [7]. While fast neutrons ($E > 0.1$ meV) transfer sufficient energy to the primary recoil atom to produce collision cascades, thermal neutrons ($E < 0.55$ eV) do not lead to defects in the material because their energy is below the displacement threshold. Epithermal neutrons (in the keV range) lead to the formation of point defects and point defect clusters. The density of collision cascades after irradiation to 10^{22} m^{-2} is about [7] 5×10^{22} m^{-3}, which corresponds to a mean distance between two cascades of 27 nm, the lattice parameter of the flux line lattice at 3.2 T.

3. Results and discussion

3.1. Transition temperature

The transition temperature of the MODRAB samples was 90.6 K, of the PLDYSZ 88.5 K and of the MOCVDMgO 89.1 K. Neutron irradiation decreases the transition temperature, T_c, which is ascribed to enhanced impurity scattering caused by the introduced defects. Non-magnetic impurities do not reduce T_c in isotropic s-wave superconductors, but in anisotropic and d-wave superconductors [14, 15]. The effect is comparatively small at the chosen fluences. We find a linear decrease with neutron fluence by around 2×10^{-22} K m^2 (2 K at a fluence of 10^{22} m^{-2}), which is around half that found in single crystals [2, 16]. The transitions normally do not broaden after irradiation to these neutron fluences.

3.2. Irreversibility line

The irreversibility lines ($H \parallel c$) of the samples are compared in figure 1. The PLDYSZ and MOCVDMgO samples behave almost identically, the irreversibility fields of the MODRAB samples are lower (except near T_c), but shift close to the values of the other samples after irradiation to 10^{22} m^{-2}. The latter do not change significantly in the accessible field range, since the moderate decrease in T_c, which somewhat decreases B_{irr} at high temperatures, is counterbalanced by a slight steepening of the irreversibility line. We note that neutron irradiation cannot improve the irreversibility line of state-of-the-art coated conductors and that all samples behave similarly after irradiation. It seems that the MODRAB samples have a comparatively low density of pinning efficient defects, which is increased by the irradiation, thus enhancing B_{irr}. The irreversibility line becomes quite insensitive to the defect concentration at high defect densities, which could indicate an upper limit for B_{irr} [17].

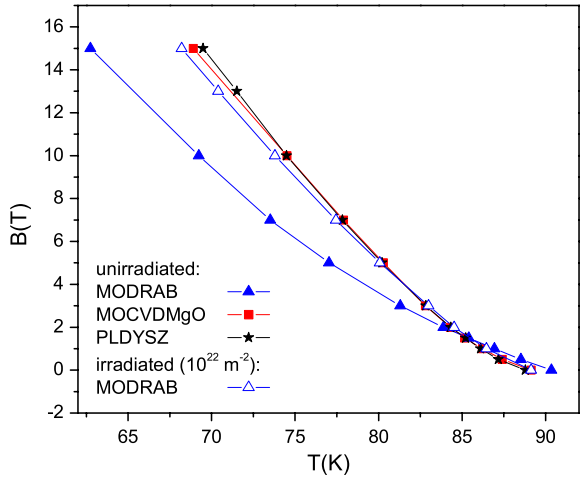

Figure 1. The irreversibility fields ($H \parallel c$) of the PLDYSZ and MOCVDMgO samples are nearly identical and higher than those of the MODRAB sample. All irreversibility lines become similar after neutron irradiation, since only that of the MODRAB sample is changed significantly.

The irradiation has no beneficial effect on the irreversibility line for the other main field orientation ($H \parallel ab$) and we observe no significant effect (MODRAB) or a slight degradation (other samples). The variation of the intrinsic pinning potential is on the length scale of the c-axis lattice parameter (equivalent to a very high density of pinning centers) and presumably much more efficient than the cascades due to its correlated two dimensional character.

3.3. Critical currents

Depending on field, temperature, fluence, and the original defect structure, the irradiation will enhance or decrease the critical currents. The strongest increase was observed in the sample with the weakest as grown pinning structure (MODRAB). The corresponding data at 77, 64, and 50 K are presented in figure 2 for both main field orientations. The critical currents decrease at low magnetic fields after irradiation, which is discussed in detail in the next section. $J_c(B)$ becomes flatter after the irradiation at low and intermediate fields, which leads to a crossover and an enhancement at intermediate and high fields. The flattening manifests itself in a smaller exponent α of the power-law $J_c \propto B^{-\alpha}$, which is a reasonable approximation for the field dependence of J_c at intermediate fields. Note that the crossover field between the enhancement and degradation of J_c is generally higher for the field parallel to the ab planes

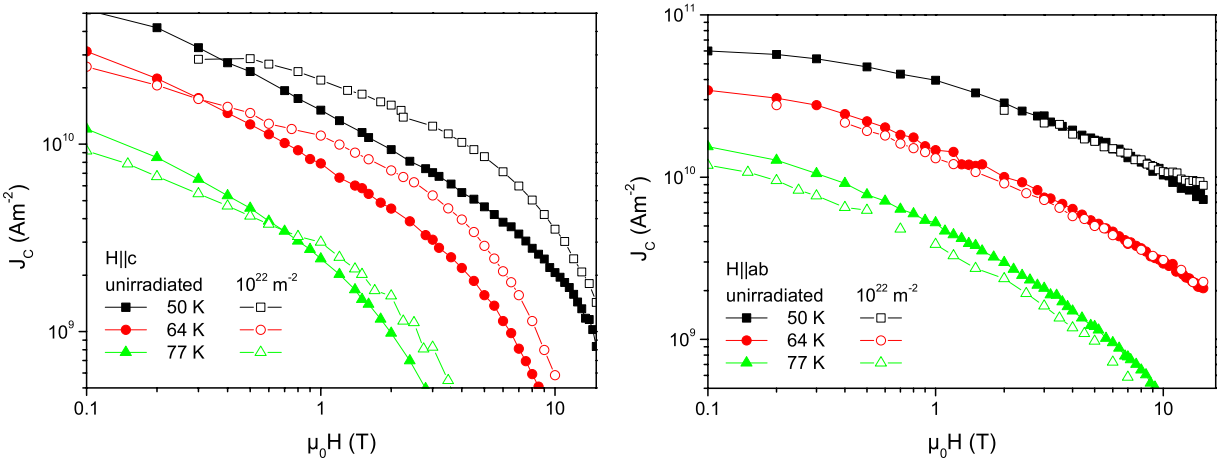

Figure 2. Neutron irradiation enhances the critical current densities in a large field and temperature range, but decreases them at low fields or close to T_c. The positive effect is larger if the field is oriented perpendicular to the tape (left panel) than in the parallel orientation (right panel).

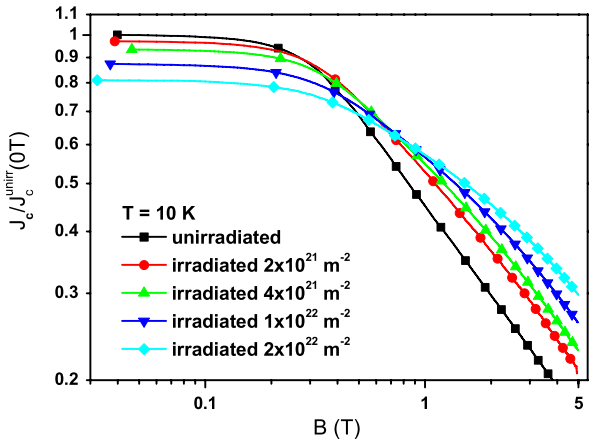

Figure 3. Crossover in $J_c(B)$ between the irradiated and the unirradiated state after sequential irradiation (sample MODRAB).

(right panel in figure 2), where an enhancement is found only at high fields and low temperatures. The currents degrade in the whole field range at 77 K. The (relative) enhancement is more pronounced at low temperatures for both orientations, which is in contrast to earlier findings on single crystals [8, 16]. This is a consequence of the competition between pinning and thermal energy, which reduces the efficiency of comparatively small defects at high temperatures. The collision cascades are obviously the largest pinning centers in single crystals, but this does not seem to be the case in coated conductors, where a large number and variety of linear and planar defects exists [9], which are more efficient than the cascades at high temperatures. In addition, neutron irradiation also introduces smaller defects, which are efficient only at low temperatures.

The other types of samples (PLDYSZ, MOCVDMgO) behave qualitatively similarly but data are available only for a fluence of 2×10^{21} m^{-2} so far. A similar reduction of J_c at low fields turns to an enhancement at comparable crossover fields, which hardly depend on the neutron fluence (see figure 3). The field dependence becomes weaker again at intermediate field, which reduces α. Only at high fields, the hardly changed irreversibility field causes a difference to the MODRAB samples. While the relative enhancement diverges for $H \parallel c$ at the originally lower irreversibility fields in the MODRAB samples, the $J_c(B)$ curves merge again near the hardly changed irreversibility fields in the PLDSZ and MOCVDMgO samples. At high temperatures, where the irreversibility field is slightly reduced due to the decrease of T_c, even a second crossover is observed, and J_c is only enhanced at intermediate fields.

3.4. Granularity effects

The crossover in the field dependence $J_c(B)$ between the unirradiated state and the irradiated state (figure 3) is a feature that is generally observed on conductors grown by physical as well as chemical deposition. The twofold effect of the irradiation on the current transport indicates that two regimes must be separated: a high field region (>1 T), which benefits from the additional pinning centers, and a low field domain, where a different mechanism causes a J_c-depression. This is explained by considering the specific nature of current transport in a granular medium, i.e., the critical current density in the grains $J_{c,G}$ has to be distinguished from the grain boundary critical current density $J_{c,GB}$ flowing across the sample. Numerous experiments on bicrystals [18] showed that, depending on the grain boundary misorientation angle, the current transport is controlled by $J_{c,GB}$ at low fields, whereas at fields in the Tesla range $J_{c,G}$ limits the current transport. Although it is not fully established that the behavior of a single well-defined grain boundary is representative for the complex grain boundary network of a coated conductor [19, 20], the current limitation by the grains and an increase of $J_{c,G}$ after irradiation are straightforward explanations for the observed J_c improvement in high fields. Further evidence for this scenario is provided by neutron irradiation of YBCO thin films grown on single-crystalline substrates, which can be regarded as single macroscopic grains and thus serve as a model system for the individual microscopic grains in a coated conductor.

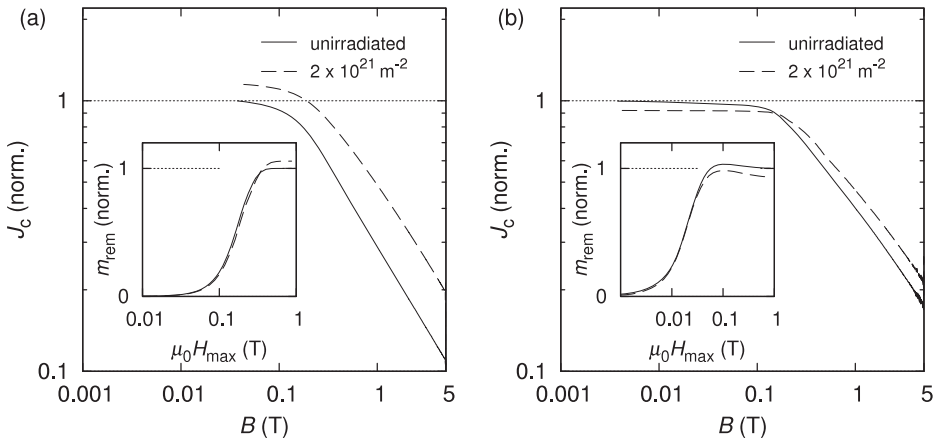

Figure 4. Comparison of the effect of neutron irradiation on samples grown on single-crystalline (a) and poly-crystalline (b) substrates. The critical current density in the single-crystalline sample is enhanced in the entire field range, while the granular sample exhibits a crossover at about the same field as state-of-the-art coated conductors. The inset shows that the remnant moment of the granular sample decreases when the grain boundary currents are saturated and the flux penetrates the grains. (Data are normalized to the unirradiated state.)

These films show, in agreement with the above assumption of an increase in $J_{c,G}$, enhanced critical current densities in the entire field range (cf figure 4(a) and [21]), if the temperature is not too close to the superconducting transition temperature, i.e., when the (moderate) reduction of T_c after irradiation is negligible. The fact that the J_c decrease occurs at rather low fields, where $J_{c,GB}$ is dominant in the bicrystal experiments, suggests that the grain boundary network is responsible for this effect. Two different but not mutually exclusive mechanisms are able to explain the reduction of $J_{c,GB}$. First, it is important to notice, that the density of the irradiation defects is too low to reduce the cross-section for current transport significantly. But the defects are mobile during the irradiation and the grain boundaries represent natural barriers for their movement, which causes the defects to accumulate—the grain boundaries deteriorate after irradiation. This effect has, however, only an impact on the overall J_c, if the current transport is limited by the grain boundaries. Hence, the crossover indicates the transition between the low field regime, which is dominated by the grain boundary network, and the high field regime, controlled by the properties of the grains.

Another explanation for the J_c reduction at low fields is based on the field exerted by the intra-granular shielding currents on the grain boundaries: If $J_{c,G}$ is larger than $J_{c,GB}$, additional flux remains trapped in the grains after a change of the external applied field and the circulating currents in the grain generate an additional field at the grain boundaries. Thus, the enhancement of $J_{c,G}$ by the irradiation, which is responsible for the J_c improvement at high fields, increases the grain boundary field and thereby reduces the field dependent $J_{c,GB}$ at low applied fields. An experimental test is provided by a method similar to [22], where the remnant magnetic moment m_{rem} of the sample is assessed after applying successively larger fields H_{max}. If $J_{c,GB}$ is smaller than $J_{c,G}$, flux will initially penetrate along the grain boundaries. After the grain boundary network has saturated and additional flux is trapped only in the grains, $m_{rem}(H_{max})$ decreases as the intra-grain currents increase the field at the grain boundary[1]. The expected behavior of $m_{rem}(H_{max})$ is clearly evident in samples grown at an early stage of optimization (figure 4(b)) to the granular substrate and thus carry a rather low $J_{c,GB}$ [21]. Despite the smaller J_c of this sample, the crossover occurs at fields comparable to state-of-the-art coated conductors. Although the two proposed mechanisms are different, they do not exclude each other, but rely on the same argument: a transition between grain boundary to grain controlled current transport leading to a crossover in $J_c(B)$ between the irradiated and the unirradiated state. It should further be noted that the complexity of the grain boundary network does not allow one to draw clear distinctions and the crossover indicates only approximately the transition from one regime to the other.

3.5. Angular dependence of J_c

The angular dependence of the critical current in the MODRAB sample at 64 K and 3 T is presented in figure 5. The pronounced peak at 0° either comes from intrinsic pinning by the periodic variation of the order parameter along the *c*-axis, or from correlated defects, such as stacking faults. There is hardly any trace of a peak at 90° in the unirradiated tape. This indicates that the density of *c*-axis correlated defects is small. The random, uncorrelated disorder introduced by the neutrons reduces the I_c-anisotropy, $\gamma_{I_c} = I_c^{max}/I_c^{min}$, from 2.7 to 1.3 at a fluence of 10^{22} m^{-2}. The latter is considerably smaller than the I_c-anisotropy in a thin film with a claimed (intrinsic or effective) anisotropy of only [10] 1.5, obtained by a scaling analysis $J_c(\theta)$ [10] on the basis of the anisotropic scaling approach by Blatter *et al* [23]. Such a small intrinsic anisotropy can be excluded in the present sample, since the anisotropy of

[1] Note, that the contribution of the currents in the grains to m_{rem} is not significant, because $m \propto r^3$, where r is the radius, which is a few millimeters for the sample and more than a hundred times less for a single grain. Thus, the dominating component of the total magnetic moment stems from the currents flowing across the grain boundaries in all samples except those with high-angle grain boundaries, which makes a direct assessment of $J_{c,G}$ and $J_{c,GB}$ (as for example in [4]) impossible.

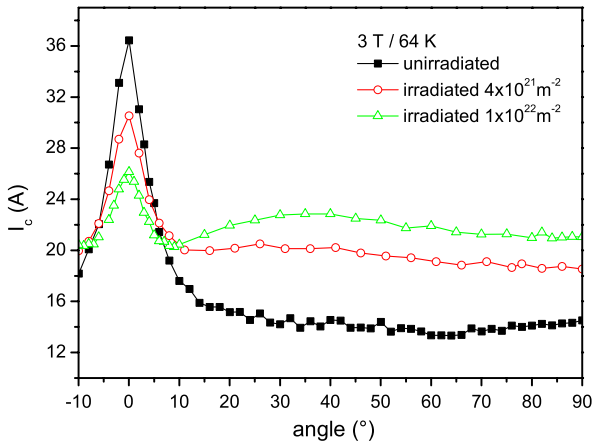

Figure 5. The irradiation reduces the J_c-anisotropy (sample MODRAB). The minimum in J_c appears near 9°, where the currents are hardly changed by the introduced defects.

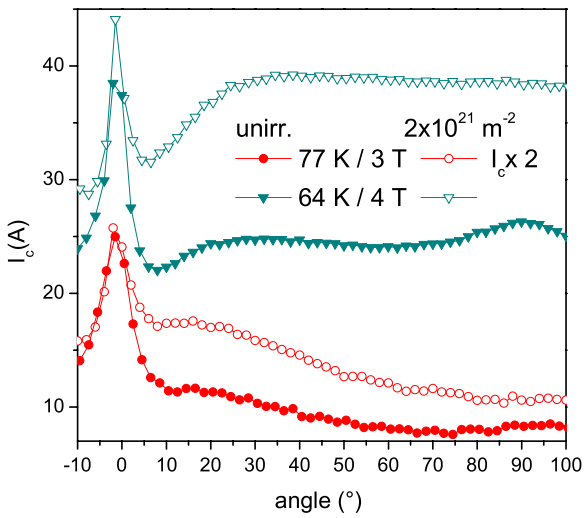

Figure 6. The peak at 90° indicates the presence of c-axis correlated defects in the MOCVDMgO sample. It disappears after neutron irradiation, the minimum at ∼9° is amplified.

the irreversibility fields is much higher and not significantly altered by the irradiation. The shape of $J_c(\theta)$ in the irradiated state is extremely interesting. The peak at 0° is followed by a minimum at about 9° and another broad maximum centered at around ∼35°. Note that this behavior was induced by the addition of random, uncorrelated disorder and is hardly compatible with the anisotropic scaling approach, although this model assumes such a defect structure, but with weak instead of strong pinning defects. This is not unexpected, since the scaling of J_c is based on single-vortex weak-collective pinning [23] which predicts extremely small currents and is obviously not applicable to 'high-J_c' coated conductors.

The MOCVDMgO samples contain c-axis correlated defects, as indicated by the peak at around 90° shown in figure 6. This peak disappears after irradiation and the currents hardly change between 25° and 90° at 64 K and 4 T, in contradiction to the anisotropic scaling approach. The minimum, again at about 9°, which was present in these samples also before irradiation, is amplified. Only the intrinsic pinning remains practically unaffected.

At higher fields (not shown in figure 6), a minimum occurs at 90°, which is an obvious consequence of the small irreversibility field in this orientation. The ratio of the irreversibility fields in the main field orientations is consistent with anisotropic scaling and with expectations for the intrinsic anisotropy ($B^{ab}_{irr}/B^{c}_{irr} \sim 4$) and seems to represent a much more reliable estimate for the intrinsic anisotropy (the scaling of fields is independent of pinning models) than the angular dependence of J_c, since this approach does not work for the relevant pinning centers in coated conductors.

3.6. Coated conductors for fusion magnets

Powerful magnets will be needed to confine the plasma of future fusion power plants. The use of high temperature superconductors instead of Nb_3Sn would allow operation at higher temperatures and/or fields, which would reduce the cooling requirements and could also result in a more compact and cheaper design. However, only first concepts for fusion magnets made of coated conductors are being developed at present. Cables with a current capability in the ten kA range are needed and the strands have to be somehow twisted [24] in order to reduce ac losses. Electrical, mechanical, and thermal stabilization of such wires and quench detection/protection will be demanding issues. Apart from these technological issues, the superconducting properties have to fulfil two basic requirements. The critical current densities must be comparatively high, since the superconducting volume fraction of a coated conductor is low (typically 1–2%) and they must not degrade during operation in a hard radiation environment (fast neutrons). A rough estimate of the required intrinsic critical current density leads to about 2.5×10^9 A m^{-2} (5×10^9 A m^{-2}) at about 12 T (14 T) [25], assuming the overall current density of the actual ITER (DEMO) cable design for the toroidal field (TF) coils or the central solenoid (CS). These values are certainly achievable with present conductors, but define the operation temperature. Cooling with liquid nitrogen would be favorable, but is possible only above 64 K (at low pressure). Figure 7 demonstrates that this seems feasible (although not at 77 K) with present conductors (MOCVDMgO) if the field is aligned with the ab planes. The magnetic field in the fusion coils will be close to this orientation, but, depending on the cable and coil design, orthogonal components will occur. In the other limiting case ($H \parallel c$), the performance currently fails significantly. Since the currents drop quickly at small misalignment angles (figures 5 and 6), further conductor development seems mandatory in order to reach the required current densities at these high temperatures. The field in the poloidal field (PF) coils is much smaller (up to about 6 T in ITER and 9 T in DEMO), which is also highlighted in figure 7. Even these requirements seem to be demanding at 77 K or for $H \parallel c$. The expected life time fluence (fast neutrons) at the main fusion magnets (PF, CS) is around 2×10^{22} m^{-2} and might be even higher in future fusion power plants. Since the currents at 77 K already degrade at a fluence of 10^{22} m^{-2}, radiation resistance is an important issue for the application of coated conductors in fusion magnets, at least at elevated temperatures.

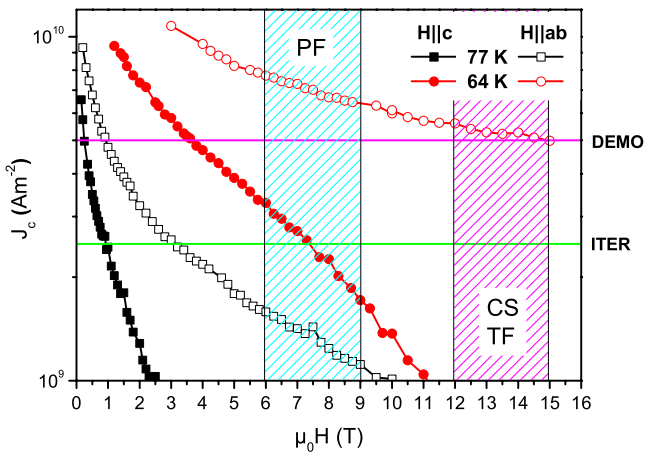

Figure 7. Commercial state-of-the-art conductors fulfil the requirements of fusion magnets on J_c at 64 K, a temperature, where liquid nitrogen (at low pressure) can be used as a coolant, if the magnetic field is parallel to the *ab* planes. For the other main field orientation as well as at 77 K the performance is still too low.

4. Conclusions

The influence of fast neutron irradiation on differently fabricated coated conductors was found to be similar. The critical currents decrease at low magnetic fields, where intergranular currents set the upper limit for loss free current flow. This decrease can be understood either by a slight degradation of the grain boundaries, or by the increasing shielding currents within the grains, which generate an additional field at the grain boundaries.

The irradiation enhances J_c at intermediate and high magnetic fields, where the macroscopic current is limited by pinning, which is improved by the additional pinning centers. Although these pinning centers are uncorrelated, the angular dependence of J_c does not obey anisotropic scaling. This is a direct consequence of the pinning strength of these defects, which cannot be considered as weak, as assumed in the scaling approach. Since this should be true for any relevant pinning centers in these 'high-J_c' conductors, anisotropic scaling based on weak-collective single-vortex pinning is not applicable.

The irreversibility line in the best available YBCO coated conductors seems to be close to optimum, because a higher concentration of strong defects does not lead to further improvements.

Acknowledgments

This work, supported by the European Communities under the contract of Association between EURATOM/OEAW was partly carried out within the framework of the European Fusion Development Agreement. The views and opinions expressed herein do not necessarily reflect those of the European Commission. One of us (MC) wishes to acknowledge financial support through the NESPA project.

References

[1] Meier-Hirmer R, Küpfer H and Scheurer H 1985 *Phys. Rev.* B **31** 183
[2] Werner M, Sauerzopf F M, Weber H W and Wisniewski A 2000 *Phys. Rev.* B **61** 14795
[3] Zehetmayer M, Eisterer M, Jun J, Kazakov S M, Karpinski J, Birajdar B, Eibl O and Weber H W 2004 *Phys. Rev.* B **69** 054510
[4] Tönies S, Vostner A and Weber H W 2002 *J. Appl. Phys.* **92** 2628
[5] Eisterer M *et al* 2006 *Supercond. Sci. Technol.* **19** S530
[6] Eisterer M, Müller R, Schöppl R, Weber H W, Soltanian S and Dou S X 2007 *Supercond. Sci. Technol.* **20** 117
[7] Frischherz M C, Kirk M A, Zhang J P and Weber H W 1993 *Phil. Mag.* A **67** 1347
[8] Sauerzopf F M 1998 *Phys. Rev.* B **57** 10959
[9] Foltyn S R, Civale L, MacManus-Driscoll J L, Jia Q X, Maiorov B, Wang H and Maley M 2007 *Nat. Mater.* **6** 631
[10] Gutierrez J *et al* 2007 *Nat. Mater.* **6** 367
[11] Chen Z, Kametani F, Chen Y, Xie Y, Selvamanickam V and Larbalestier D C 2009 *Supercond. Sci. Technol.* **22** 055013
[12] Fuger R, Hengstberger F, Eisterer M and Weber H W 2007 *IEEE Trans. Appl. Supercond.* **17** 3753
[13] Weber H W, Böck H, Unfried E and Greenwood L R 1986 *J. Nucl. Mater.* **137** 236
[14] Millis A J, Sachdev S and Varma C M 1988 *Phys. Rev.* B **37** 4975
[15] Radtke R J, Levin K, Schüttler H-B and Norman M R 1993 *Phys. Rev.* B **48** 653
[16] Sauerzopf F M, Wiesinger H P, Kritscha W, Weber H W, Crabtree G W and Liu J Z 1991 *Phys. Rev.* B **43** 3091
[17] Figueras J, Puig T, Obradors X, Kwok W K, Paulius L, Crabtree G W and Deutscher G 2006 *Nat. Phys.* **2** 402
[18] Hilgenkamp H and Mannhart J 2002 *Rev. Mod. Phys.* **74** 485
[19] Feldmann D M, Holesinger T G, Feenstra R and Larbalestier D C 2008 *J. Am. Ceram. Soc.* **91** 1869
[20] Durrell J H and Rutter N A 2009 *Supercond. Sci. Technol.* **22** 013001
[21] Hengstberger F, Eisterer M, Weber H W, Kursumovic A and MacManus-Driscoll J L 2007 *IEEE Trans. Appl. Supercond.* **17** 3549
[22] Müller K-H, Andrikidis C, Liu H K and Dou S X 1994 *Phys. Rev.* B **50** 10218
[23] Blatter G, Geshkenbein V B and Larkin A I 1992 *Phys. Rev. Lett.* **68** 875
[24] Goldacker W, Frank A, Kudymow A, Heller R, Kling A, Terzieva S and Schmidt C 2009 *Supercond. Sci. Technol.* **22** 034003
[25] Fuger R, Eisterer M and Weber H W 2009 *IEEE Trans. Appl. Supercond.* **19** 1532

Physica C 470 (2010) 1300–1303

Contents lists available at ScienceDirect

Physica C

journal homepage: www.elsevier.com/locate/physc

Asymmetric angular dependence of J_c in coated conductors prior to and after fast neutron irradiation

M. Chudy *, M. Eisterer, H.W. Weber

Vienna University of Technology, Atominstitut, Stadionallee 2, 1020 Vienna, Austria

ARTICLE INFO

Article history:
Available online 15 May 2010

Keywords:
Coated conductors
Neutron irradiation
Asymmetry
Peak shift

ABSTRACT

Angular dependent measurements of J_c were performed on a commercial coated conductor (SuperPower) consisting of a 1 μm thick YBCO layer grown on a MgO IBAD buffer layer. An asymmetric behavior of the angular dependence of J_c ($J_c(\Phi)$) was found with a changing distance between the two peaks at different temperatures and applied magnetic fields. One peak always occurs when the field is oriented parallel to the tape surface, the other smaller peak is located in the perpendicular orientation at high fields, but slightly shifted (by up to 10°) at 77 K and low magnetic fields. This peak shift, the overall $J_c(\Phi)$ asymmetry and the influence of fast neutron irradiation on $J_c(\Phi)$ are discussed. The spherical defects, introduced by collisions of fast neutrons with the lattice atoms, are randomly distributed, add to the as-grown defect structure and change the critical current anisotropy by altering both peaks.

1. Introduction

The fabrication of coated conductors (CC) significantly improved during the last years. Recently, the first HTS devices (coils and cables) were put into operation. The lengths of CC increased up to around one kilometer and the critical currents are higher and more uniform over the whole length of the conductors. (In 2008 the longest wire length of 1311 m was produced by SuperPower with a minimum I_c of 153 A [1].) It is very important for future applications of coated conductors to obtain high critical currents at all orientations of the magnetic field, because the intrinsic anisotropy of YBCO is a considerable complication for the design of HTS devices. It is therefore a challenge to reduce the strong anisotropy of YBCO CC. In addition, the excellent performance for $H \parallel ab$ field should not be degraded. We present a comparative study of the angular dependent critical current densities in commercial YBCO CC before and after irradiation with fast neutrons. We will show that the asymmetric behavior of $J_c(\Phi)$ is very similar to results on thin films, where the *ab* planes were tilted with respect to the sample surface. The position of the maxima in the two main field orientations and their changes as well as changes in the overall symmetry of $J_c(\Phi)$ after irradiation to different fast neutron fluences will be also discussed.

2. Experimental

Our commercially available samples, state-of-the-art coated conductor from SuperPower, are based on an IBAD MgO template with the YBCO layer made by metal organic chemical vapor deposition (MOCVD). They were characterized before irradiation and then sequentially irradiated to fast neutron fluences of 4×10^{21} m^{-2} and 1×10^{22} m^{-2}. The tapes are 4 mm wide, the thickness of the YBCO layer is 1 μm, and they are completely coated with a copper stabilizer. The transport measurements were made on approximately 26 mm long pieces by the standard four-probe technique with a voltage criterion of 1 μV/cm. The sample was rotated in magnetic fields of up to 6 T under the maximum Lorentz force configuration. A helium flow gas cryostat with a split coil and a rotating sample holder were used for our experiments. This setup allows us to measure $J_c(\Phi)$'s at variable temperatures and currents of up to 150 A. Some of our initial measurements were made in a setup based on a 1.4 T electromagnet with liquid nitrogen as a coolant. The irradiation was made in the central irradiation facility of the TRIGA MARK II research reactor in Vienna at a power of 250 kW. The temperature during irradiation did not exceed 60 °C. The type of artificial defect induced by neutron irradiation strongly depends on the kinetic energy of neutrons. High energy neutrons produce spherical defects of amorphous material with a diameter of a few nm (so called collision cascades), point defects and clusters of point defects are created also by neutrons with lower energies [2]. All fluences refer to fast neutrons with energies $E_n > 0.1$ MeV. The samples were irradiated sequential by, first step to a fluence of 4×10^{21} m^{-2}, then remeasured, and then irradiated again to a fluence of 1×10^{22} m^{-2}.

3. Results and discussion

The angular dependence of the critical current density $J_c(\Phi)$ at 77 K and 700 m T is shown in Fig. 1, where two peaks are observed.

* Corresponding author. Tel.: +43 1 588 01 14149; fax: +43 1 588 01 14199.
E-mail address: mchudy@ati.ac.at (M. Chudy).

0921-4534/$ - see front matter © 2010 Elsevier B.V. All rights reserved.
doi:10.1016/j.physc.2010.05.098

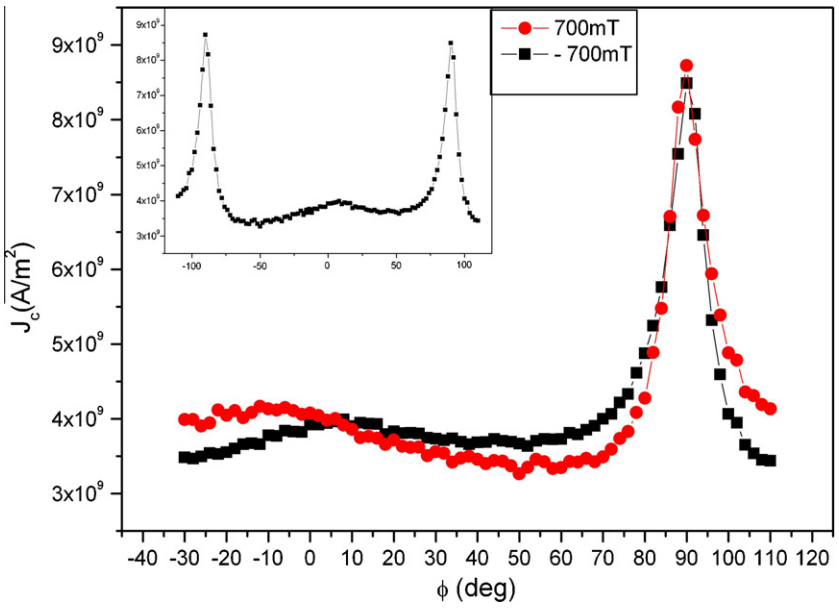

Fig. 1. Angular dependence of $J_c(\Phi)$. The angular scale refers to the sample surface. The tape was measured twice, once in a field of 700 m T and then in the reversed field. The insert represents both measurements on a single angular scale covering ≈240°.

The first is the *ab peak* at $\Phi = 90°$(90° $\iff$ $H \parallel$ sample surface) and the other less pronounced is located at an interval $\Phi \approx \langle -20°, 20°\rangle$(0° $\iff$ $H \perp$ sample surface) – the *second peak*. Both of them have an asymmetric shape and the overall $J_c(\Phi)$ follows a $J_c(\Phi) = J_c(\Phi + 180°)$ periodicity, but not a $J_c(\Phi) = J_c(-\Phi)$ symmetry. The broken symmetry of $J_c(\Phi)$ implies the existence of some geometrical effects and/or the presence of correlated pinning centers, which are not aligned with the main crystallographic directions [3]. Asymmetric $J_c(\Phi)$'s were often reported [3–6], e.g. by Maiorov et al., who cut two different bridges into the same tape [3]. The *ab* planes were tilted from the sample surface by an angle Ψ in *y* orientation (Fig. 2). One bridge was cut in *y* and the other in *x* orientation. Although both bridges were measured, the $J_c(\Phi)$ asymmetry was found only in one bridge, namely that cut in *x* orientation. The other bridge showed a symmetric $J_c(\Phi)$ and lower absolute values of J_c. Wang [4] also observed an asymmetric $J_c(\Phi)$ curve similar to ours in thin films with tilted *ab* planes. Common to all those measurements was the fact, that the *ab peak* was not observed at $\Phi = 90°$, but at a different angle $\Phi = (90° - \Psi)$. At high magnetic fields the peak was positioned precisely at $\Phi = (90° - \Psi)$ and shifted to lower angles with decreasing field. A possible explanation of this *ab peak* shift was given by Silhanek et al. [7] as being caused by a misalignment between the externally applied magnetic field H and the internal field B. Granularity effects [8,9] were discussed as well. However, we did not observe any change in the position of the *ab peak* within the accuracy of our experimental setup (±0.5°). High resolution $J_c(\Phi)$ measurements were done (Fig. 3) with a sensitive Hall probe to determine the magnetic field orientation with maximal accuracy. (The Hall probe was tested for offset voltage and linearity at different temperatures.) The magnetic field orientation was calculated from the Hall voltage using: $\Phi = a\ cos(U_{Hall}/U_{Hmax})$. As shown in Fig. 3, no shift of the *ab peak* is found at any field and temperature. These measurements were done with a 0.5° resolution and all deviations of the *ab peak* absolute angular position are within accuracy of 0.5° + 1° (estimated misalignment between the Hall probe and the sample due to mounting ⩽1°). Therefore, the *ab* planes are aligned parallel, or almost parallel to the sample surface [3,5], because the *ab peak* was always found, when the field was aligned parallel to the sample surface under our experimental conditions (*B*,*T*).

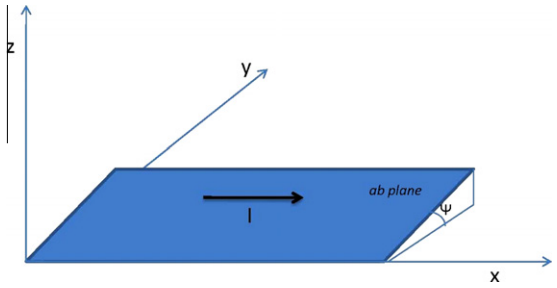

Fig. 2. Sketch of the *ab* planes tilted from the sample surface.

A different situation was found in the case of the *second peak*. This peak was fixed at the same position and rather symmetric at lower temperatures (64 K, 50 K), where the magnetic field was always above 3 T. According to the Hall probe its position was always exactly perpendicular to the sample surface (±0.5° due to the angular resolution) in these measurements. However, at 77 K the *second peak* is strongly asymmetric and its maximum occurs out of the tape normal ($\Phi = 0°$), e.g. at $\Phi = -5°$ at 1 T. At lower fields (Fig. 1) the peak shifts even more, but at high fields it almost aligns ($\Phi = 0°$), e.g. 5 T, as well as at lower temperatures. One reason for the angular variation of $J_c(\Phi)$ is the electronic mass anisotropy of YBCO. A useful approach to describe this effect is the anisotropic scaling approach by Blatter et al. [10]. Accordingly J_c systematically increases with Φ, if pinning is only due to random defects. The *second peak* cannot be described by this model, except by assuming correlated pinning. Natural candidates for *c*-axis correlated pinning centers are twin planes [11–13] or edge and screw dislocations [14,15]. The *second peak* probably results from a combination of them [16].

The asymmetric $J_c(\Phi)$ behavior and the shift of the *second peak* in a tape, in which the YBCO planes do not break the symmetry, remain an open issue. Possible candidates for this effect are the Lorentz force acting on the tape during the measurement, differing barriers to surface entry for flux lines at the two interfaces [17] or correlated pinning centers, which are not oriented perpendicular to the tape surface and which are dominant only at certain

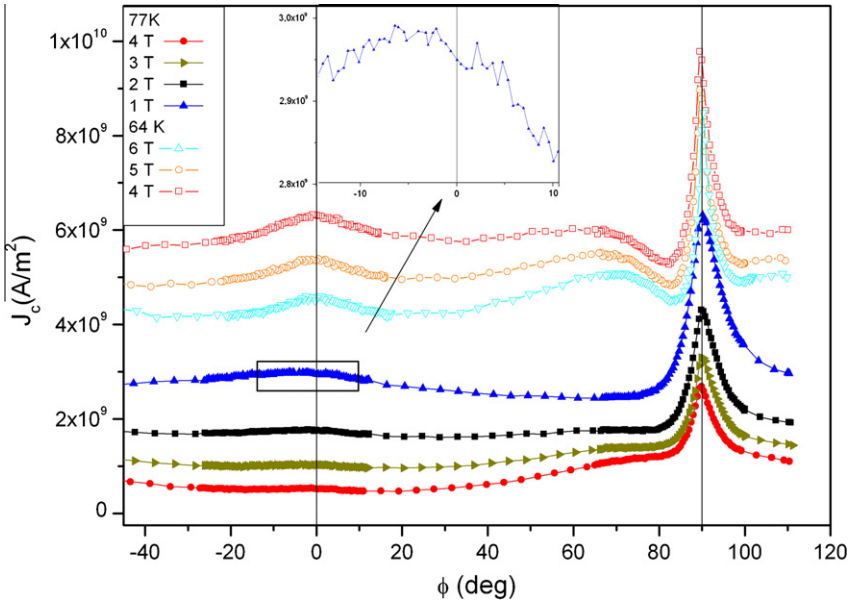

Fig. 3. $J_c(\Phi)$ at 77 K and 64 K in fields up to 6 T.

fields and temperatures. None of these effects can be completely excluded. The Lorentz force on the tape during the measurement may cause the difference of the $J_c(\Phi)$'s at reversed magnetic fields, since the tape is either pressed towards the sample holder and or into the opposite direction. This could strain the tape differently and lead to the observed behavior of $J_c(\Phi)$. However, many measurements using the same setup and the same sample holder, leading to the same mechanical loads, were done on different CC and no asymmetry has been observed [18].

Differing surface barriers causing asymmetric $J_c(\Phi)$'s were observed in PLD thin films [17]. However, this mechanism was found only in PLD films up to now and the most important outcome was a significant difference in J_c upon reversing the current (or field), which is not observed in our case (Fig. 1).

The last option is rather more general and based on changing pinning mechanisms at low magnetic fields as well as the loss of pinning efficiency due to thermal activation at high temperatures. The n-value is defined from the current–voltage curve in the transition region between thermally assisted flux flow and flux flow by a power law

$$E = E_c\left(\frac{I}{I_c}\right)^n,$$

where the n-value is the exponent n and E_c is the voltage criterion for I_c. The values of J_c and the n-values are not completely independent. Strong arguments for a functional dependence within one pinning regime were found by Civale et al. [19]. Indications for different pinning mechanisms are shown in Fig. 4, where the n-values of the $J_c(\Phi)$ measurements change behavior near $\Phi = 90°$.

We can exclude the above-mentioned explanation of the *ab peak* shift due to H and B competition, because the shift of the second peak should be more pronounced at low external magnetic

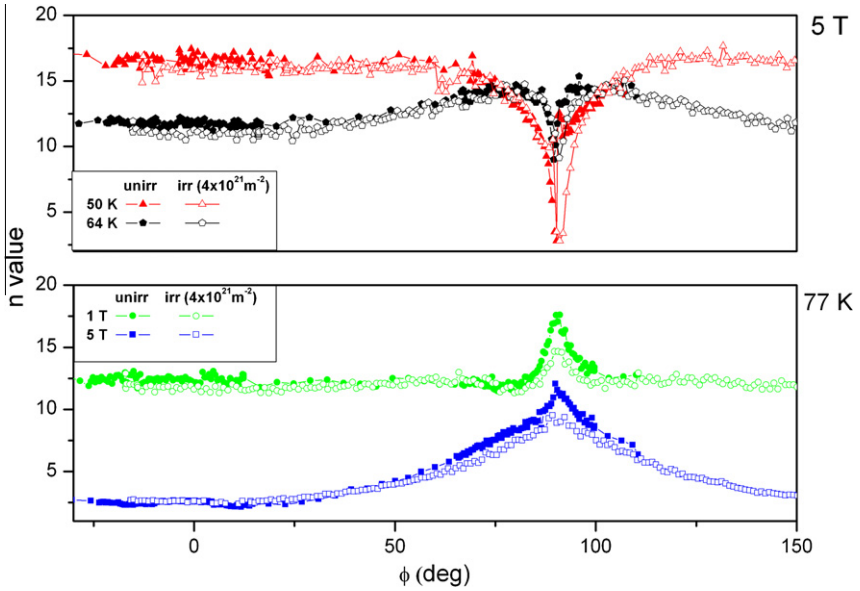

Fig. 4. n-Values obtained from $J_c(\Phi)$ measurements before and after irradiation.

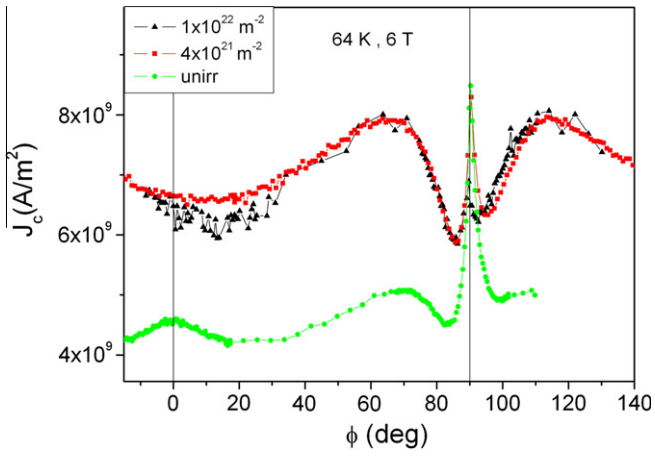

Fig. 5. Comparison of $J_c(\Phi)$ prior to and after irradiation to different fluences at 64 K and 6 T.

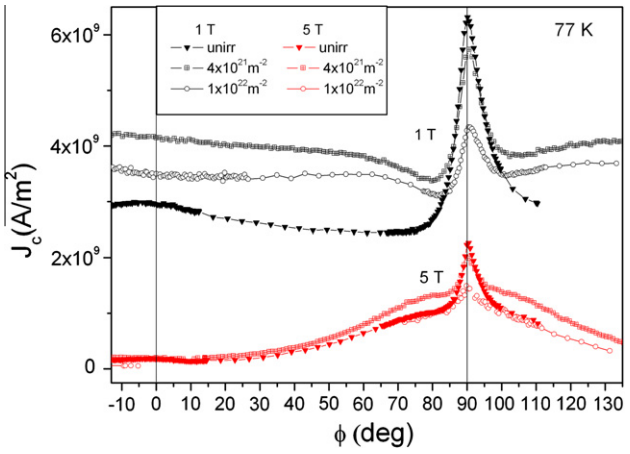

Fig. 6. Comparison of $J_c(\Phi)$ prior to and after irradiation to different fluences at 77 K and 5 T, 1 T.

fields H and high currents, but at 64 K or 50 K, where the currents are relatively high, no shift is observed, whereas it occurs at 77 K, where the currents and the self field are small. Also the same positions of the peak at smaller fields and relatively high currents (e.g. $I \approx 30$ A at 64 K, 3 T) and in high fields and small currents (e.g. $I \approx 0.1$ A at 77 K and 6 T) are in contradiction to this model.

To further investigate the pinning mechanism, the samples are irradiated by fast neutrons. The resulting plots are shown in Figs. 5 and 6. We note an overall improvement of $J_c(\Phi)$ and also a strong reduction of the $J_c(\Phi)$ anisotropy. The most interesting results refer to the position of the *ab* and of the *second peak*. The *ab peak* remains on its position at $\Phi = 90°$ at all fields and temperatures. On the other hand, the *second peak* disappears and is replaced by a local $J_c(\Phi)$ minimum at 64 K. At 77 K the $J_c(\Phi)$ curve is rather flat in this angular range. The $J_c(\Phi)$ asymmetry survives all irradiation steps. The surrounding of the *ab peak* remains asymmetric in all measurements. Because of the introduction of randomly distributed pinning centers by the irradiation, the asymmetry is suppressed in some regions of $J_c(\Phi)$, and features like shoulders close to $H \parallel ab$ (e.g. at 65° and 115° in Fig. 5) are created and seem to be symmetric. Similar shoulders in YBCO tapes were reported [20], but their origin could not be satisfactorily explained yet.

4. Conclusions

State-of-the-art coated conductors from SuperPower were investigated. Angular resolved transport measurements show an asymmetry of the $J_c(\Phi)$ curves similar to that observed in thin films containing tilted *ab* planes with respect to the tape surface. A highly sensitive Hall probe was employed to determine the orientation of the *ab* planes in the CC. The *ab peak* was always at $\Phi = 90°$, i.e. parallel to the sample surface. Beside this asymmetry also a shift of the *second peak* was observed. This shift occurs at 77 K and low fields. The peak occurs at $\Phi = 0°$ at high fields and at all temperatures. We investigated the $J_c(\Phi)$ asymmetry also after irradiation to fast neutron fluences of up to 1×10^{22} m^{-2}. The asymmetry of $J_c(\Phi)$ remained after all irradiation steps, but mainly in the angular range close to the *ab peak*.

Acknowledgements

This work was supported by the NESPA Project (Nano Engineered Superconductors for Power Applications) of the European Union. I wish to thank T.D. Withnell for his assistance in preparing the experimental setup and also for his valuable advice regarding the measuring technique.

References

[1] V. Selvamanickam, Y. Chen, X. Xiong, Y.Y. Xie, M. Marchevsky, A. Rar, Y. Qiao, R.M. Schmidt, A. Knoll, K.P. Lenseth, C.S. Weber, IEEE Trans. Appl. Supercond. 19 (2009) 3225.
[2] F.M. Sauerzopf, H.P. Wiesinger, W. Kritscha, H.W. Weber, G.W. Crabtree, J.Z. Liu, Phys. Rev. B 43 (1991) 3091.
[3] B. Maiorov, B.J. Gibbons, S. Kreiskott, V. Matias, T.G. Holesinger, L. Civale, Appl. Phys. Lett. 86 (2005) 13204.
[4] Z.L. Wang, D.H. Lowndes, D.K. Christen, D.M. Kroeger, C.E. Klabunde, D.P. Norton, Physica C 252 (1995) 125.
[5] Z. Chen, F. Kametani, Y. Chen, Y. Xie, V. Selvamanickam, D.C. Larbalestier, Supercond. Sci. Technol. 22 (2009) 055013.
[6] T.G. Holesinger, B. Maiorov, O. Ugurlu, L. Civale, Y. Chen, X. Xiong, Y. Xie, V. Selvamanickam, Supercond. Sci. Technol. 22 (2009) 045025.
[7] A.V. Silhanek, L. Civale, M.A. Avila, Phys. Rev. B 65 (2002) 174525.
[8] M.J. Hogg, F. Kahlmann, Z.H. Barber, J.E. Evetts, Supercond. Sci. Technol. 14 (2001) 647.
[9] K.R. Schöppl, H.W. Weber, J.H. Durrell, Physica C 460 (2007) 1188.
[10] G. Blatter, V.B. Geshkenbein, A.I. Larkin, Phys. Rev. Lett. 68 (1992) 875.
[11] A.A. Zhukov, H. Küpfer, H. Claus, H. Wühl, M. Kläser, G. Müller-Vogt, Phys. Rev. B 52 (1995) R9871.
[12] M. Oussena, P.A.J. de Groot, K. Deligiannis, A.V. Volkozub, R. Gagnon, L. Taillefer, Phys. Rev. Lett. 76 (1996) 2559.
[13] A.A. Zhukov, G.K. Perkins, J.V. Thomas, A.D. Caplin, H. Küpfer, T. Wolf, Phys. Rev. B 56 (1997) 3481.
[14] B. Dam, J.M. Huijbregtse, F.C. Klaassen, R.C.F. van der Geest, G. Doornhos, J.H. Rector, A.M. Testa, S. Freisem, J.C. Martínez, B. Stäuble-Pümpin, R. Griessen, Nature (London) 399 (1999) 439.
[15] A. Diaz, L. Mechin, P. Berghuis, J.E. Evetts, Phys. Rev. Lett. 80 (1998) 3855.
[16] L. Civale, B. Maiorov, A. Serquis, J.O. Willis, J.Y. Coulter, H. Wang, Q.X. Jia, P.N. Arendt, J.L. MacManus-Driscoll, M.P. Maley, S.R. Foltyn, Appl. Phys. Lett. 84 (2004) 2121.
[17] S.A. Harrington, J.L. MacManus-Driscoll, J.H. Durrell, Appl. Phys. Lett. 95 (2009) 022518.
[18] R. Fuger, M. Eisterer, F. Hengstberger, H.W. Weber, Physica C 468 (2008) 1647.
[19] L. Civale, B. Maiorov, J.L. MacManus-Driscoll, H. Wang, T.G. Holesinger, S.R. Foltyn, A. Serquis, P.N. Arendt, IEEE Trans. Appl. Supercond. 15 (2005) 2808.
[20] K. Matsumoto, T. Horide, A. Ichinose, S. Horii, Y. Yoshida, M. Mukaida, Jpn. J. Appl. Phys. 44 (2005) 246.

Characterization of Commercial YBCO Coated Conductors After Neutron Irradiation

M. Chudy, R. Fuger, M. Eisterer, and H. W. Weber

***Abstract*—In view of the significant progress in coated conductor processing technologies, a wide variety of applications have become feasible. One of them is the design of superconducting magnets for fusion devices operating in the liquid nitrogen temperature range. In this case, the material has to withstand a significant fluence of fast neutrons. Samples of the latest generation of coated conductors provided by commercial suppliers were sequentially irradiated in a fission reactor and characterized by magnetic and direct transport measurements. Angular resolved transport measurements were performed and interesting changes in $J_c(\varphi)$ were observed. In addition, the effects of thermal neutron irradiation on coated conductors are presented. The most important outcome for applications, the dependence of J_c on the neutron fluence, is discussed in the last part.**

***Index Terms*—Angular anisotropy, coated conductors, neutron irradiation, thermal neutrons, YBCO.**

I. Introduction

INTEREST in neutron irradiation of coated conductors has two main reasons. The first one is related to nuclear fusion, where coated conductors are candidate magnet materials to be employed in future fusion power plants. The second is more academic and connected to research on flux pinning and its possible enhancement. In this paper, the effect of neutron irradiation on coated conductors is presented and discussed. Neutron irradiation introduces additional pinning centers into the superconductor, which influence the critical current density, J_c and the $J_c(\varphi)$ anisotropy. Both of these aspects are discussed in this paper.

II. Equipment

The TRIGA MARK II Reactor in Vienna was used for the irradiations. Two irradiation facilities of the reactor were employed: CIF (Central Irradiation Facility) and a reflector irradiation tube. The neutron fluences at a full power (250 kW) are listed in Table I.

TABLE I
Neutron Fluences at Irradiation Facilities of the Triga Mark II Reactor

250 kW	Thermal neutrons E < 0.55 eV	Fast neutrons E > 0.1 MeV
CIF [1]	6.1×10^{16} n/m^2.s	7.6×10^{16} n/m^2.s
Ref. irr. tube [2]	1.73×10^{16} n/m^2.s	4×10^{15} n/m^2.s

Transport and magnetic measurements were performed to assess the critical current densities (or critical currents). A helium gas flow cryostat with a split coil and a rotating sample holder was employed. The transport measurements were made using approximately 26 mm long and 4 mm wide samples by the standard four-probe technique with a voltage criterion of 1 μV/cm. The samples were rotated in magnetic fields of up to 6 T under maximum Lorentz force configuration. This set-up allows us to measure $J_c(\varphi)$ at variable temperatures and currents of up to 150 A. The magnetic measurements were made in a MagLab VSM of Oxford Instruments, which allows magnetic measurements up to 5 T in the temperature range from 1.5 to 350 K. The vertical oscillation of the sample is typically between 0.5 and 1.5 mm at a frequency of 55 Hz. All measurements were made with $B \parallel c$. The samples used for magnetic measurements were approximately 4 mm long and 4 mm wide.

III. Samples

Two types of commercially available YBCO coated conductors were used. Both of them were 4 mm wide tapes stabilized by copper. The first is the 2nd generation HTS tape from SuperPower, which is made by MOCVD (metal organic chemical vapor deposition) on an IBAD MgO template [3]. The YBCO layer is 1 μm thick. The second sample from EHTS (European High Temperature Superconductor—presently: Bruker) consists of a 2.5 μm thick YBCO layer prepared by high-rate pulsed laser deposition (HR-PLD) on an yttria-stabilized ZrO (YSZ) template. The template was deposited by ion-beam assisted-deposition (IBAD) [4]. The 4 mm long samples for magnetic characterization in VSM were sequentially irradiated in the CIF to the following fast neutron fluences: 2×10^{21} m^{-2}, 4×10^{21} m^{-2}, 1×10^{22} m^{-2}, 1.3×10^{22} m^{-2} and also 2×10^{22} m^{-2}. 1×10^{22} m^{-2} corresponds to the expected neutron fluence at the magnet location over the whole ITER lifetime [5]. After each step, a series of magnetic measurements was performed in the VSM. The longer samples (26 mm) for angular resolved transport measurements were irradiated up to a fluence of 2×10^{21} m^{-2}.

Manuscript received August 02, 2010; accepted January 07, 2011. Date of publication February 28, 2011; date of current version May 27, 2011. This work was supported by NESPA Nano Engineered Superconductors for Power Applications.

M. Chudy, M. Eisterer, and H. W. Weber are with Vienna University of Technology-Atominstitut, Stadionallee 2, 1020 Vienna, Austria (e-mail: mchudy@ati.ac.at; eisterer@ati.ac.at; weber@ati.ac.at).

R. Fuger was with Vienna University of Technology-Atominstitut, Stadionallee 2, 1020 Vienna, Austria. He is now with the Research Institute of Superconductor Science and Systems, Kyushu University, Fukuoka 812–8581, Japan (e-mail: rene.fuger@super.ees.kyushu-u.ac.jp).

Color versions of one or more of the figures in this paper are available online at http://ieeexplore.ieee.org.

Digital Object Identifier 10.1109/TASC.2011.2108631

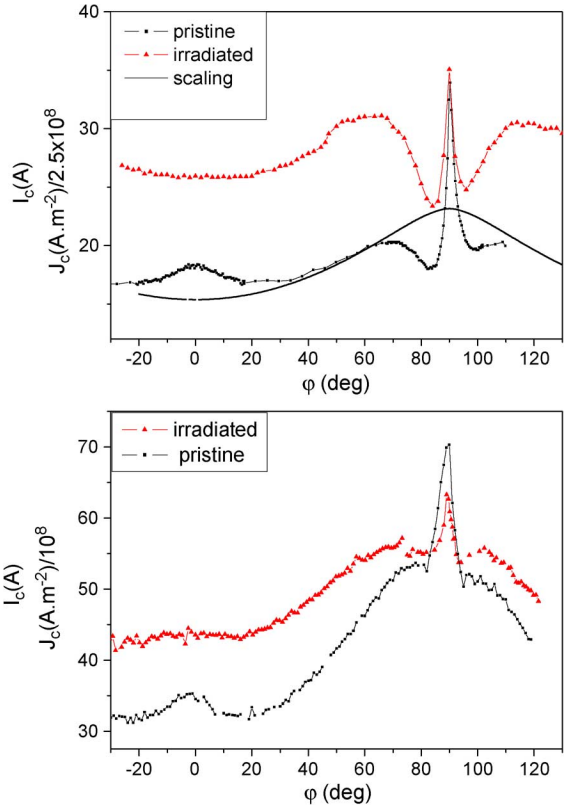

Fig. 1. Critical currents at 64 K, 6 T, top: SuperPower CC before and after irradiation to 2×10^{21} m^{-2}, bottom: EHTS.

IV. Angular Resolved Measurements

It is well known, that irradiation by fast neutrons introduces effective pinning sites into high temperature superconductors, which enhance the critical current densities [6]–[8]. The introduced defects are randomly distributed within the volume of the superconductor. The irradiation process in the CIF does fully satisfy the conditions for homogeneous irradiation. The samples from both manufacturers were irradiated to a fast neutron fluence of 2×10^{21} m^{-2} and transport measurements in the 6 T set-up were made (Fig. 1). Despite of the same irradiation conditions and the same J_c measurement method, the changes in the angular anisotropy of these similar coated conductors are rather different. In both cases, "shoulders" are created on both sides of the ab peak (90°). They are much more pronounced in the SuperPower tape. The origin of these shoulders and the difference between these tapes need to be discussed. The anisotropic scaling approach [9] is a powerful tool, which allows studying the $J_c(\varphi)$ angular anisotropy within collective pinning theory [10] and distinguishing between correlated or uncorrelated pinning in various angular intervals. Due to the observed asymmetry in the pristine SuperPower tape [11], the scaling of this tape is rather complicated, but still possible with rough approximations and in a limited angular range. We employ a $J_c(H,\varphi) \rightarrow J_c(H\varepsilon(\varphi))$ transformation, where $\varepsilon(\varphi) = [\cos^2(\varphi) + \gamma^{-2}\sin^2(\varphi)]^{1/2}$, $\gamma = 5$. $J_c(H\varepsilon(\varphi))$ was approximated by a double exponential function: $y = A1 * \exp(-x/t1) + A2 * \exp(-x/t2) + y_0$ The scaling curve is shown in Fig. 1.—top (solid black line). The good match of the shape of the scaling curve with $J_c(\varphi)$ shows that J_c between 20° and 70° of the pristine sample is caused by the

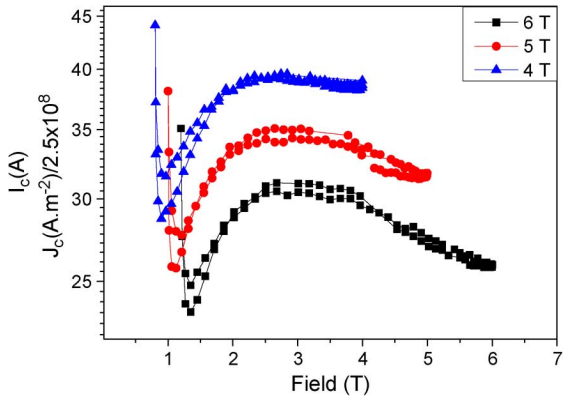

Fig. 2. $J_c(H(\varphi))$, $\gamma = 5$, transformations of irradiated SuperPower tape at 64 K.

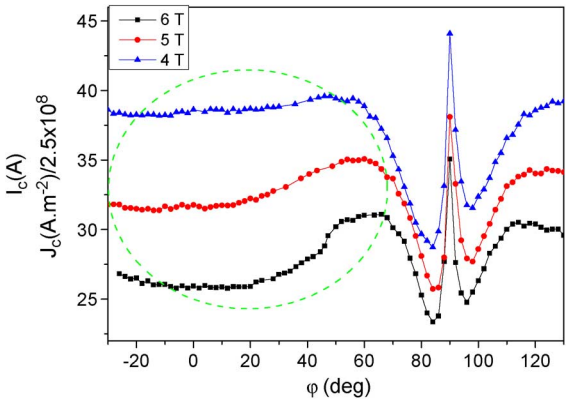

Fig. 3. SuperPower coated conductor at 64 K and after irradiation to a fast neutron fluence of 2×10^{21} m^{-2}.

mass anisotropy of YBCO and random pinning centers in the tape. The change of $J_c(\varphi)$ towards the minima beside the ab peak is probably caused by a different depinning mechanism. Both peaks are caused by correlated pinning centers introduced by the fabrication method, which cannot be described by the scaling approach.

The shoulders and minima are even more pronounced after irradiation (Fig. 1). The shape of the $J_c(\varphi)$ curve at 6 T, except near the ab peak, corresponds quite well to the shape of the scaling curve. This would be expected by introducing random pinning centers by neutron irradiation. Unexpectedly, the $J_c(\varphi)$ curves of the SuperPower tape after irradiation do not obey the anisotropic scaling approach at all (Fig. 2). The $J_c(H\varepsilon(\varphi))$ scaling curves do not collapse at any point and make an approximation by any function impossible.

The reason is shown in the Fig. 3. Since the shapes of $J_c(\varphi)$ at various external magnetic fields are different (missing local minima near $\varphi = 0°$), scaling does not work.

The efficiency of the random pinning centers introduced by neutron irradiation is varying not only with magnetic field, but also with the orientation of the field. This either contradicts the paper by Blatter *et al.* [9] and collective pinning theory or the pinning introduced by neutron irradiation is not completely random, which would contradict results reported in several papers [6], [12]. Most likely, the random pinning centers introduced by neutron irradiation together with the existing pinning centers create an "interacting" pinning structure, where both

TABLE II
MAXIMUM ENERGY OF β PARTICLES OF SELECTED ISOTOPES

Isotope	Max energy (keV)	Probability per decay
Ag 110m	530	0.305
W 187	626.7	0.587
	1312.5	0.251
	687	0.055
	694.1	0.035
Co 58	475 (positron)	0.201

types of pinning centers play a role for pinning vortices. Thus, those "interacting pinning centers" are more effective at different fields (angles) and temperatures than both types would be separately, without any interaction, by a simple addition. A similar pinning mechanism was already reported by Maiorov *et al.* [13].

V. INFLUENCE OF THERMAL NEUTRONS

Irradiation of coated conductors by thermal neutrons can address two issues. First, it could lead to an explanation of the different reaction of two similar types of CC reported in Fig. 1 to the irradiation. The second is of relevance for employing a fission reactor for simulating fusion neutron spectra, which do not contain thermal neutrons.

It is well known that only neutrons above certain energy will lead to defects, which are effective pinning centers. Most studies were done on single crystals [6]. The main difference between single crystals and CC lies in the layered structure of a CC, which might be activated by (mainly) thermal neutrons and emit secondary radiation, possibly creating pinning. Since the architecture of the tapes is different [3], [4], irradiation could lead to differences. Gamma radiation is not relevant, as only very small changes in the superconducting properties were observed [14]. We will focus on β radiation, which was studied on YBCO single crystals and reported by J. Giapintzakis *et al.* [15]. According to their results, the threshold energy of β particles for producing pinning centers is between 400 and 600 keV. The corresponding β emitters for the SuperPower tape are listed in Table II. Silver is present in EHTS as well, but the amount is lower. Thermal neutrons have very high cross sections to create these isotopes.

The sample was irradiated in the reflector irradiation facility to the thermal neutrons fluence of 7×10^{20} m^{-2}. The resulting $J_c(\varphi)$ is compared to that of the pristine sample and to a sample irradiated to a fast neutron fluence of 2×10^{21} m^{-2} (Fig. 4). Clearly, the influence of thermal neutron irradiation is neglible. The fluence of β radiation in the SuperPower tape is estimated to be $10^{13} - 10^{15}$ m^{-2} resulting from 7×10^{20} m^{-2} thermal neutrons. During this experiment about 1.63×10^{20} m^{-2} fast neutrons were also present. Even this small fast neutron fluence is significantly higher than the expected β fluence. Many β particles could have even lower energies than the threshold value (400–600 keV) because of the β decay character (neutrino emission). Therefore, the expected effective fluence of β particles is insufficient for creating the pinning centers in this way.

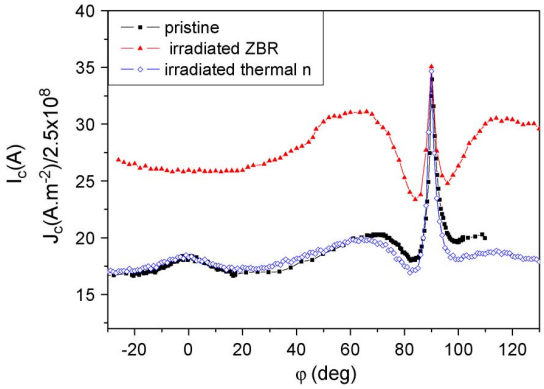

Fig. 4. J_c of a SuperPower tape at 64 K, 6 T, unirradiated, irradiated by fast neutrons, irradiated by thermal neutrons.

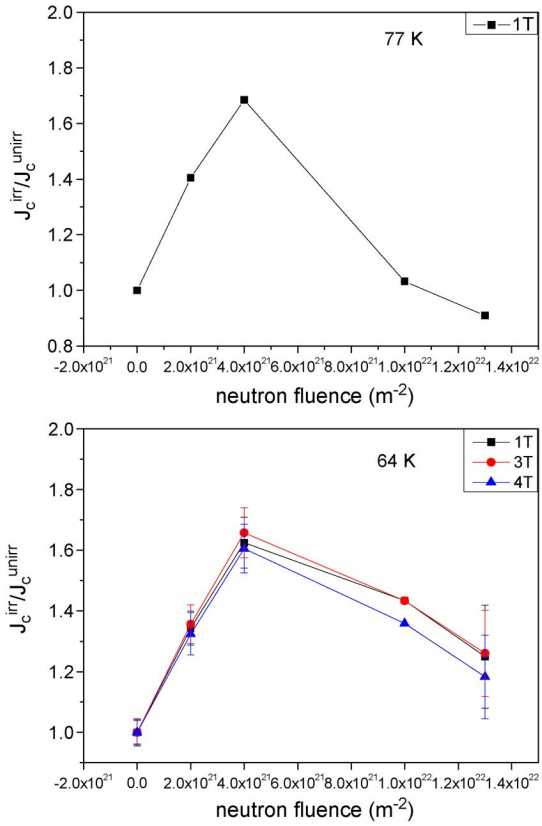

Fig. 5. Relative J_c variation after different irradiation steps of the SuperPower tape.

VI. J_c AS A FUNCTION OF FAST NEUTRON FLUENCE

Neutron irradiation might change the properties of high temperature superconductors employed in future fusion reactors. Therefore, it is crucial to know the variation of J_c as a function of neutron fluence. The samples were sequentially irradiated (up to a fluence of 1.3×10^{22} m^{-2}) and measured in the VSM for B $\|$ c and at temperatures of 64 and 77 K, which is the liquid nitrogen range. As reference magnetic fields for all J_c evaluations 1 T at 77 K and 1, 3, 4 T at 64 K were chosen. Additional samples were measured at each irradiation step and average values were calculated to increase the accuracy of the results. The results with normalized J_c s (to the J_c of the pristine sample) at 77 K and 64 K are shown in Fig. 5. At both temperatures, the maximum of J_c occurs at a fast neutron fluence of 4×10^{21} m^{-2}.

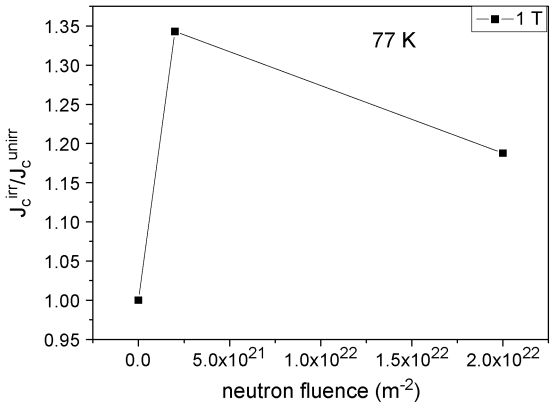

Fig. 6. Relative J_c at 77 K and 1 T for the EHTS coated conductor.

After this point the J_c is reduced. The maximal irradiation level at 77 K caused a J_c reduction below 1. However, the fluence of 1.3×10^{22} m^{-2} exceeds the estimated ITER lifetime fluence [5]. All normalized J_c s at 64 K were above 1.

The EHTS coated conductor (Fig. 6) was irradiated to a fluence of 2×10^{22} m^{-2}. Since the relative J_c was still higher at this high fluence than in the case of the unirradiated sample, we conclude, that this coated conductor will withstand higher fluences without degradation. The main reason could be the lower density of pinning centers in the unirradiated superconductor.

VII. Conclusion

We irradiated two similar types of coated conductor in a fission reactor, in order to the study the influence of irradiation relevant for possible future fusion applications. The changes in the $J_c(\varphi)$ angular anisotropy were discussed as an effect of the addition of randomly distributed pinning centers to the existing pinning lattice ("interacting pinning centers"), i.e. the neutron induced pinning centers interact also with the original pinning sites.

Since the neutron spectrum of a fusion reactor does not contain fast neutrons only, the effect of thermal and epithermal neutrons on coated conductors was investigated. No influence was found by these low energy neutrons, since the number of pinning centers created by thermal neutrons or secondary radiation is negligible compared to the density of defects created by fast neutrons. This provides additional evidence for the suitability of a fission reactor for the simulation of fusion neutrons at the magnet location. Secondary β radiation cannot explain the different shapes of $J_c(\varphi)$ in these CC. The influence of the fast neutron fluence on J_c was presented in the Section VI. Whereas fluences of up to 4×10^{21} m^{-2} improved J_c, higher fluences start reducing J_c. However, both types of CC show still better J_c after irradiation to the ITER lifetime fluence than without irradiation.

References

[1] H. W. Weber, H. Böck, E. Unfried, and L. R. Greenwood, "Neutron dosimetry and damage calculations for the TRIGA MARK-II reactor in Vienna," *J. Nucl. Mater.*, vol. 137, no. 3, pp. 236–240, Feb. 1986.

[2] General Atomic, "Calculated fluxes and cross sections for TRIGA reactors," 1963.

[3] [Online]. Available: http://www.superpowerinc.com/system/files/SP_2G+Wire+Spec+Sheet_for+web_0509.pdfAug. 2, 2010

[4] A. Usoskin, L. Kirchhoff, J. Knoke, B. Prause, A. Rutt, V. Selskij, and D. E. Farrell, "Processing of long-length YBCO coated conductors based on stainless steel tapes," *IEEE Trans. Appl. Supercond.*, vol. 17, no. 2, pp. 3235–3238, Jun. 2007.

[5] Design description document of magnets IDM number: ITER_D_22HV5L.

[6] F. M. Sauerzopf, H. P. Wiesinger, W. Kritscha, H. W. Weber, G. W. Crabtree, and J. Z. Liu, "Neutron-irradiation effects on critical current densities in single cristaline YBCO," *Phys. Rev. B*, vol. 43, p. 3091, 1991.

[7] H. W. Weber, H. P. Wiesinger, W. Kritscha, and F. M. Sauerzopf, "Critical currents in neutron irradiated YBCO and BISCCO single crystals," *Supercond. Sci. Technol.*, vol. 4, pp. S103–S105, 1991.

[8] M. Okada and T. Kawakubo*, Radiation Effects and Defects in Solids*, vol. 108, no. 2–4, pp. 137–144, Sep. 1989.

[9] G. Blatter, V. B. Geshkenbein, and A. I. Larkin, "From isotropic to anisotropic superconductors: A scaling approach," *Phys. Rev. Lett.*, vol. 68, p. 875, 1992.

[10] A. I. Larkin and Y. Ovchinnikov, "Pinning in type II superconductors," *J. Low Temp.Phys.*, vol. 34, pp. 409–428, Nov. 1979.

[11] M. Chudy, M. Eisterer, and H. W. Weber, "Asymmetric angular dependence of J_c in coated conductors prior to and after fast neutron irradiation," *Physica C*, no. 20, pp. 1300–1303, Nov. 2010.

[12] M. C. Frischherz, M. A. Kirk, J. Farmer, and H. W. Weber, "Defect cascades produced by neutron irradiation in in YBCO superconductors," in *7th Int. Workshop Critical Currents Supercond., Alpbach, Tyrol/Austria*, Jan. 1994, pp. 24–27, submitted for publication.

[13] B. Maiorov, S. A. Baily, H. Zhou, O. Ugurlu, J. A. Kennison, P. C. Dowden, T. G. Holesinger, S. R. Foltyn, and L. Civale, "Synergetic combination of different types of defect to optimize pinning landscape using $BaZrO_3$-doped $YBa^2Cu_3O_7$," *Nature Mater.*, vol. 8, pp. 398–404, 2009.

[14] H. Ozkan, B. A. Albiss, N. Hamdan, and A. Menard, "Effect of gamma irradiation and silver doping on YBCO superconductors," *J. Supercond.*, vol. 7, pp. 885–888, 1994.

[15] J. Giapintzakis, W. C. Lee, J. P. Rice, D. M. Ginsberg, and I. M. Robertson, "Production and identification of flux-pinning defects by electron irradiation in YBCO single crystals," *Phys. Rev. B*, vol. 45, no. 18, pp. 10677–10683, 1992.

J Fusion Energ
DOI 10.1007/s10894-011-9436-x

ORIGINAL RESEARCH

Positron Annihilation Lifetime Spectroscopy Study of Neutron Irradiated High Temperature Superconductors $YBa_2Cu_3O_{7-\delta}$ for Application in Fusion Facilities

J. Veterníková · M. Chudý · V. Slugeň · M. Eisterer · H. W. Weber · S. Sojak · M. Petriska · R. Hinca · J. Degmová · V. Sabelová

Abstract This study focuses on the crystallographic defects introduced by neutron irradiation and the resulting changes of the superconducting properties in the high temperature superconductor $YBa_2Cu_3O_{7-\delta}$. This material is considered to be most promising for magnet systems in future fusion reactors. Two different bulk samples, pure non-doped $YBa_2Cu_3O_{7-\delta}$ (YBCO) and multi-seed $YBa_2Cu_3O_{7-\delta}$ doped by platinum (MS2F) were studied prior to and after irradiation in the TRIGA MARK II reactor in Vienna. Neutron irradiation is responsible for a significant enhancement of the critical current densities as well as for a reduction in critical temperature. The accumulation of small open volume defects (<0.5 nm) partially causes those changes. These defects were studied by positron annihilation lifetime spectroscopy at room temperature. A high concentration of Cu–O di-vacancies was found in both samples, which increased with neutron fluence. The defect concentration was significantly reduced after a heat treatment.

Keywords $YBa_2Cu_3O_{7-\delta}$ · Fast neutron irradiation · Positron annihilation spectroscopy · Critical current density

J. Veterníková (✉) · V. Slugeň · S. Sojak · M. Petriska · R. Hinca · J. Degmová · V. Sabelová
Department of Nuclear Physics and Technology, Faculty of Electrical Engineering and Information Technology, Slovak University of Technology, Ilkovičova 3, 812 19 Bratislava, Slovak Republic
e-mail: jana.veternikova@stuba.sk

M. Chudý · M. Eisterer · H. W. Weber
Vienna University of Technology—Atominstitut, Stadionallee 2, 1020 Vienna, Austria

Introduction

Recent research and development of fusion reactors are focused on the material resistance to high neutron and thermal loads. Although the emphasis is currently placed on the construction of ITER, progress with further concepts (DEMO, PROTO, etc.) is also being made. High temperature superconductors (HTS) are promising candidates for the construction of the magnet systems in the DEMO reactor [1]. The relatively high critical temperature (T_c) of these materials enables a significant reduction of cooling costs. The most promising HTS material according to the recent research is $YBa_2Cu_3O_{7-\delta}$ (Perovskite structure) with a critical temperature of about 92 K. This material is outstanding because of high critical current densities at high fields and elevated temperatures.

Its superconducting properties can be further improved by optimization of flux pinning [2], which is an important phenomenon in all technical superconductors. Defects as twin boundaries, dislocations, voids and precipitates are responsible for the high critical currents [3]. Therefore, defects introduced by fast neutron irradiation can be effective pinning sites [4, 5] and significantly improve the superconducting properties of $YBa_2Cu_3O_{7-\delta}$ [6]. Nevertheless, the microstructure is damaged and the mechanical properties are reduced.

In fusion facilities like DEMO, fast neutrons (up to $\sim$14 MeV) produced during nuclear reactions can form defects in structural materials due to atomic displacements. According to Ref. [7], the most radiation loaded materials in fusion reactors are situated at the inner wall (Fig. 1) within the inboard blanket and the shielding, but the superconductors are also exposed to a significant fast neutron flux density of $\sim 8 \times 10^{12}$ m^{-2} s^{-1} (see Fig. 2) [8]. Estimated neutron fluence during projected lifetime of ITER operating at 1.5GW and 1 MW m^{-2} neutron loading is close to about 2.5×10^{22} MW^{-1} m^{-2} [8].

Published online: 09 June 2011

High temperature superconductors are relatively new materials, for which the irradiation behavior is not yet very well defined. The larger defects—spherical amorphous objects with a diameter of a few nm (1–5) can be examined by TEM [10]. However, the presence of smaller defects (e.g. mono-vacancies and di-vacancies with 10 times smaller diameters) has not yet been studied, although they can also contribute to flux pinning [11].

Small pinning sites are characteristic for their mobility. They are attracted by large defects and can also recombine [12, 13]. The introduced defects cause disorder in the Cu–O sublattice, which is the main reason for the T_c reduction.

In this paper, these small defects are investigated by positron annihilation lifetime spectroscopy (PALS). The samples were irradiated in a research reactor up to a fast neutron fluence of 6×10^{21} m^{-2} (E > 0.1 MeV). The influence of the defect accumulation on the superconducting properties was investigated.

Experiments

Samples

Two differently prepared samples of $YBa_2Cu_3O_{7-\delta}$ (Perovskite structure) were studied in terms of radiation stability, denoted as:

i) YBCO—sintered bulk without texture (2 h at 950°C), 1.7 mm thick, radius—19–19.5 mm, total mass—2.14 g, density of the final bulk—4.235 g/cm^3.
ii) MS2F—multi seed bulk with a total mass of 1.28 g, average thickness ~0.75 mm, radius—20 mm.

The MS2F sample was manufactured by the "melt texture growth" [14] process from a powder mixture of the oxides Y_2O_3, BaO and CuO. The process can be described by 1 and 2 [15].

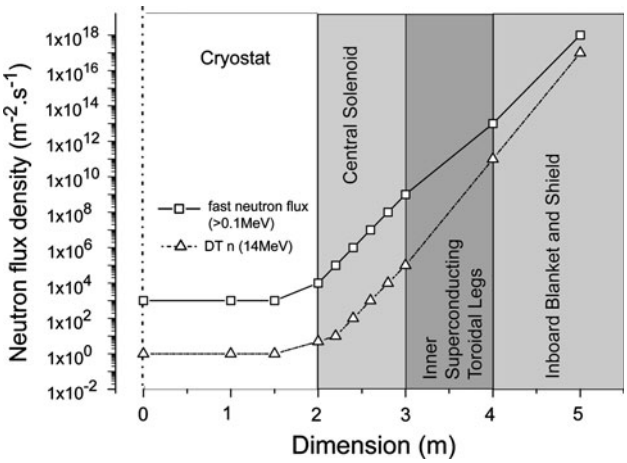

Fig. 2 Estimated neutron flux within inboard part of fusion reactor [8]

$$Y_2O_3 + (BaO + CuO)_{Liquid} \xrightarrow{1000^{\circ}C} Y_2BaCuO_5 \quad (1)$$

$$Y_2BaCuO_5 + (3BaCuO2 + 2CuO)_{Liquid} \xrightarrow{1000^{\circ}C} 2YBa_2Cu_3O_5 \quad (2)$$

MS2F is composed of two different yttrium compounds, ~70% Y-123 and ~30% Y-211 (Y_2BaCuO_5) with the additional element platinum Pt (0.1%). MS2F contained two seeds with a distance of 10.1 mm from each other (see Fig. 3). Its density is 5.274 g/cm^3.

The superconducting magnet system of fusion reactors will be constructed from coated conductors, which have a thin superconducting layer of only about 1 µm. However, PALS requires a larger amount of superconducting material. Therefore, bulk materials were investigated.

Irradiation

The investigated samples were irradiated in the TRIGA MARK II reactor in Vienna. The reactor power was

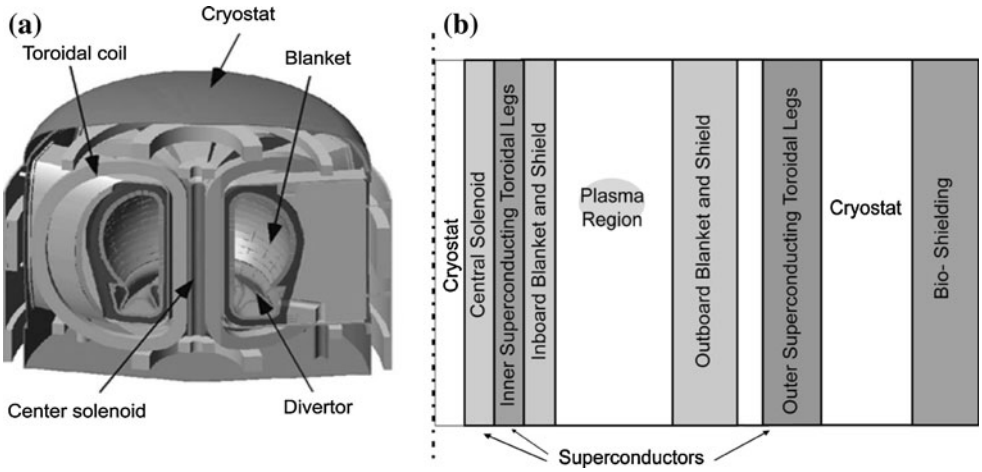

Fig. 1 DEMO concept [9] (**a**), illustration of DEMO cross-section [8] (**b**)

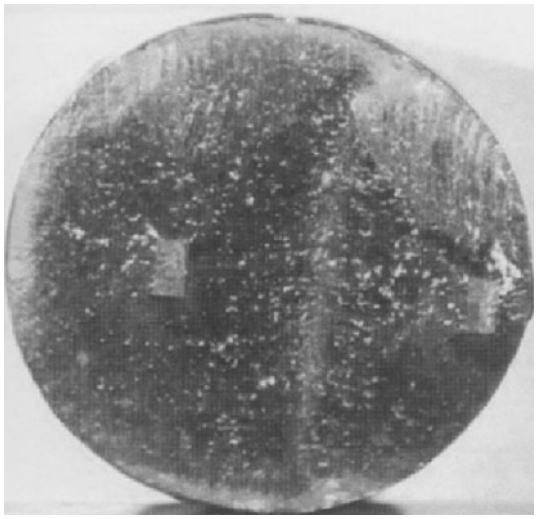

Fig. 3 MS2F: the *top* of the bulk

250 kW with a thermal/fast neutron flux density of about $4.2/5.3 \times 10^{16}$ m^{-2} s^{-1}. The temperature did not exceed 50°C during irradiation. The samples were sealed into a quartz-glass tube and then placed into the core (see Fig. 4) in an aluminum container. The first irradiation step was achieved by an exposure time of 7.5 h which corresponds to a fast neutron (>0.1 MeV) fluence of 1.2×10^{21} m^{-2}. The second irradiation step corresponds to a fluence of 6×10^{21} m^{-2} and was realized within 36.5 h.

The irradiation was performed in order to study the formation of structural defects. The introduced defects changed the superconducting properties of the samples. The enhancement of the critical current densities is expected to result mainly from defects of sizes between 1 and 5 nm, which have a spherical shape. The reduction in critical temperature can be due to a high concentration of small defects (with size $\sim 10^{-10}$ m), which can disorder the Cu–O sublattice, although they can contribute to pinning as well [11].

Finally, the irradiated samples were annealed at 250°C for 4 h in air after the measurement to investigate defect recombination and structure regeneration.

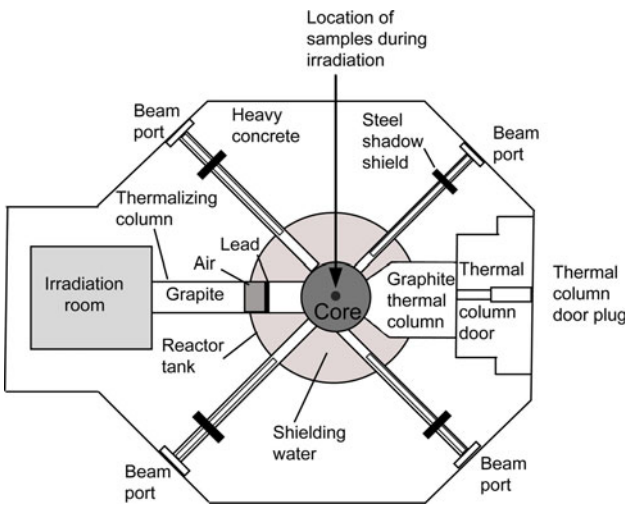

Fig. 4 Illustration of the sample position during irradiation in the experimental reactor

Experimental Techniques

The samples were investigated by applying three different experimental techniques for different properties. The first two techniques were used for the determination of the superconducting properties. The last one focused on the accumulation of defects during the irradiation and changes of the defect concentration in the microstructure.

Two important superconducting parameters were measured by the following methods:

- Measurements of the critical temperature (T_c) were performed in a 1 T *Superconducting Quantum Interference Device* (SQUID) magnetometer [16]. The transition temperature is defined as the temperature, below which the superconductor exhibits zero resistance and perfect diamagnetism in the limit of zero applied magnetic field and current.
- A *Vibrating Sample Magnetometer* (VSM) was used to determine the critical current density (J_c). The magnetic sweep rate was set to 0.5 T/min, which corresponds to an electric field criterion of about 0.2 μV/cm. The calculation of the critical current density was made by the Bean model [17], where J_c is expressed as a function of magnetic moment. The critical current density is the maximum loss free current.

The VSM (Oxford Instruments [18]) allows measuring the magnetic properties at fields of up to 5 T in the temperature range from 1.5 to 350 K. The sample oscillates typically with an amplitude between 0.1 and 1.5 mm at a frequency of 55 Hz [19].

Special sample sizes were needed for these magnetic measurements. A diamond saw was used to cut small samples (YBCO: $[2.5 \times 2.5 \times 1.7]$ mm^3, MS2F: $[2.8 \times 2.9 \times 0.7]$ mm^3) from the massive bulks described in the section "Samples". These small samples absolved the same irradiation and heat treatment procedures as the rests of the bulks.

The last experiment concerning the microstructure features was performed by positron annihilation lifetime spectroscopy (PALS) [20]. The defect size and concentration in both samples before and after the experimental treatment were observed.

In PALS, positrons are formed by $\beta+$ radioactive decay of ^{22}Na with a half-life of $\sim$2.6 years. This isotope emits a positron during its decay to ^{22}Ne, which is in an excited

state with a probability of 90.4%. It also emits a detectable gamma particle with a kinetic energy of about 1,274 keV practically immediately after the positron emission. Therefore, the information about the positron creation is obtained by registering the gamma radiation with this energy.

When the positron achieves thermal energy after slowing-down, it annihilates with an electron and two 2 quanta ($\sim$511 keV) are created. This can be detected as a signal of the positron annihilation.

The equipment used in this work consists of 2 BaF_2 scintillation detectors and two discriminators (see Fig. 5) recording the START (1,274 keV) and STOP signals (511 keV). Signals are treated in time to an amplitude converter (TAC) and stored in a multi-channel analyzer (MCA). The positron lifetime is given by the time difference between the START and STOP signal.

Every defect-free structure has its typical value of the positron lifetime called the bulk value. In a real material, there are one or more positron lifetimes in addition to the bulk value, which are describing defects. The total positron lifetime, so called "mean lifetime (MLT)", is increasing with defect size or defect concentration. Table 1 shows characteristic values for $YBa_2Cu_3O_7$ together with values for common defects within this structure.

The results from PALS measurements can be used for the identification of defects and the quantification of their concentration. For the interpretation we use the two components model, which assumes that only one type of defect will be taken into account (smaller ones). The bigger defects (e.g. pores, vacancy clusters, if existing) will be characterized by a much longer lifetime. Then the calculation of the defect group concentration can be performed according the following equations:

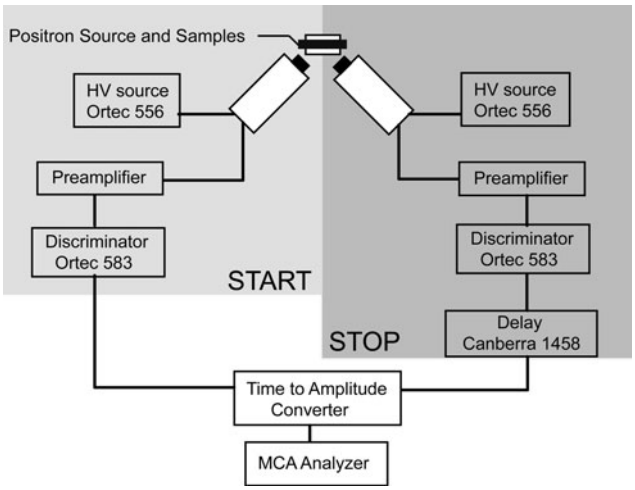

Fig. 5 Schematic of the PALS equipment at the Slovak University of Technology [21]

$$\kappa = \frac{I_2}{I_1} \cdot \left(\frac{1}{\tau_B} - \frac{1}{\tau_D} \right) \quad [25] \tag{3}$$

$$\kappa = \mu \cdot c_D \quad [26] \tag{4}$$

$$\mu = v_{th} \times r_o^2 \quad [27] \tag{5}$$

$$\mu\left[m^{-3}s^{-1}\right] = \frac{\mu[s^{-1}at.]}{N[m^{-3}at.]} \times 10^{-6} \quad [25] \tag{6}$$

where κ denotes the positron trapping rate [s^{-1}], μ the specific trapping coefficient [m^3 s^{-1} or s^{-1} at.], I_2 the positron intensity describing defects [%], I_1 the positron intensity of the bulk [%], τ_B and τ_D the lifetimes in the bulk and at defects [s], c_D the defect concentration [m^{-3} or at.$^{-1}$], v_{th} the mean thermal velocity of the positron [m s^{-1}], r_o the radius of a defect [m] and N the concentration of atoms in the investigated material [at.m^{-3}].

Results and Discussion

The results acquired by the magnetic measurements are presented in Figs. 6 and 7. They show the changes in critical current density caused by irradiation and annealing. The critical current density was higher in sample MS2F than in sample YBCO. It is important to mention, that a precise J_c estimation in the case of the YBCO sample (Fig. 6) is difficult due to the unclear ratio between intra- and intergranular supercurrents, a problem that occurs in granular superconductors. For simplicity, we assumed the sample geometry in the J_c evaluation and waive the absolute values, since we are mainly interested in the relative changes. We expect that the magnetic moment is dominated by intragranular currents, but the strong decrease in J_c after the second irradiation could be caused by a degradation of the grain connections.

The critical temperature also changed in both samples (see Table 2). Although the difference between YBCO and MS2F was small, the critical temperature is higher in YBCO, in the pristine sample, after both irradiation steps as well as after annealing.

The results after the irradiation show a small but undesirable T_c reduction as well as a favorable enhancement of the critical current density (J_c) in both samples. The increase is more significant in sample YBCO. This sample was not produced for high performance and does not contain any engineered pinning centers, which results in smaller values of J_c. Therefore, the introduction of the radiation induced defects caused a massive enhancement of the critical current density. Although the same effect is noted in sample MS2F, the enhancement is smaller. Further irradiation increases J_c of MS2F, but reduces J_c in sample YBCO. This could be a consequence of the missing texture and the corresponding weak link behavior of the grain

Table 1 Typical lifetime for bulk and defects [22–24]

	Lifetime (ps)	Binding energy (eV)
$YBa_2Cu_3O_7$ [22]	159	–
$YBa_2Cu_3O_7$ [23]	190	
O vacancy	~170	~0.2
O vacancy cluster (2–4 vacancies)	181–190	0.1–0.2
Cu (1) vacancy	207	1.1
Cu (2) vacancy	182	0.7
Y vacancy	206	2.7
Ba vacancy	263	3.5
Cu (1)–O (1) di-vacancy	236	1.5

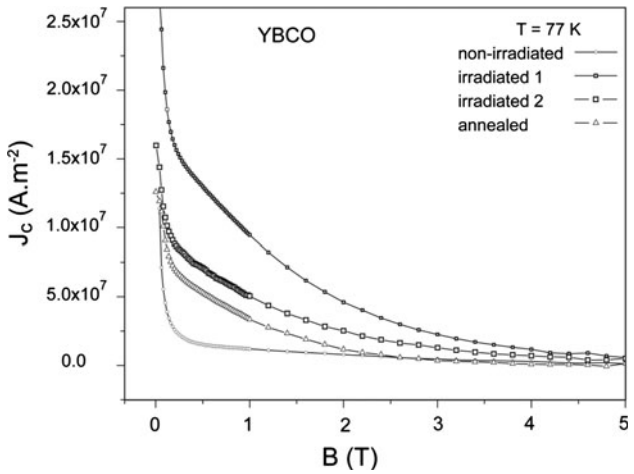

Fig. 6 Critical current density of sample YBCO as a function of the applied magnetic field

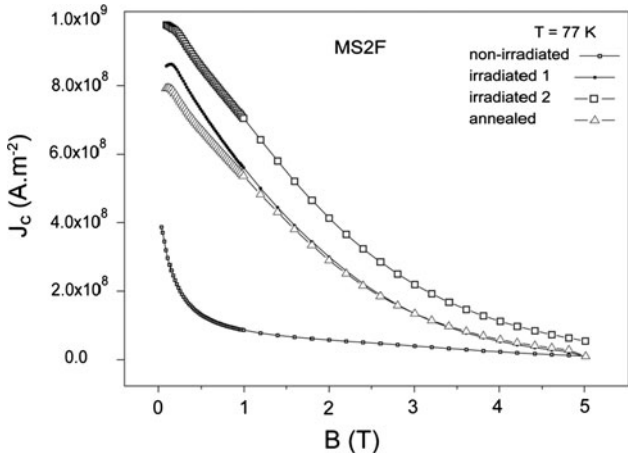

Fig. 7 Critical current density of sample MS2F as a function of the applied magnetic field

boundaries. A further reduction in J_c was found after the following heat treatment. This reduction occurs even though T_c was significantly enhanced (about 1 K in both cases, cf. Table 2), in good agreement with the results on single crystals reported by Sauerzopf [12].

Possible differences in microstructure and changes in defect size or defect concentration during irradiation and annealing can be observed and explained by positron annihilation lifetime spectroscopy. The data obtained from the PALS measurements were evaluated by the Lifetime 9 code [28]. The FWHM, which describes the sensitivity of the equipment, was up to 220 ps. The fit variant (FV—reduction of chi-square) has values in the range from below 1 to 1.1, which means that the quality of the fit is reasonable and the deviation is below 0.1% [29].

The shorter positron lifetime (LT1) describing the bulk, had values slightly above 160 ps for the YBCO sample, which is typical of very clean $YBa_2Cu_3O_{7-\delta}$ (theoretical value ~159 ps) [22]. For MS2F, LT1 was found in the region 180–190 ps, close to a typical value for the orthorhombic structure, 190 ps [23], containing small volume defects (O clusters, Y and Cu mono-vacancies). The difference of LT1 is caused by the different processing of the samples and in particular the existence of the Y211 phase in MS2F, which raises the lifetime 1.

The positron lifetime LT2, characterizing the defects, has values of 235 ps (YBCO) and 285 ps (MS2F) in the non-irradiated samples of $YBa_2Cu_3O_{7-\delta}$. The intensity of this positron lifetime (I2) ranges from 20 to 40%, i.e. MS2F (24.3%) and YBCO (38.6%) (see Fig. 8).

After irradiation to 1.2×10^{21} m^{-2}, the intensity I2 grows by more than 10% in both specimens, which demonstrates the defect accumulation in the samples during exposure to the neutrons. Sample MS2F with LT2 ~250 ps probably contains the same type of defects as sample YBCO (245 ps), but with a lower defect concentration related to the intensity difference of 3.2%.

The second irradiation (to 6×10^{21} m^{-2}) caused a further defect accumulation and the defect concentration increased again. The defect size seems to become constant corresponding to a lifetime of close to about 240 ps. The change in defect concentration is higher in sample YBCO this time ($\Delta I2 = 8.4\%$) in comparison to MS2F ($\Delta I2 = 2.5\%$), but the difference is within the experimental error.

The results on the annealed samples show a significant decrease in defect concentration. Small defects created during irradiation are able to recombine during annealing and the superconducting properties become closer to those of non-irradiated samples.

A similar behavior was found from the mean lifetime (MLT) analysis (see Table 3). The MLT increases much more in the irradiated YBCO sample (1st irradiation—$\Delta MLT = 15$ ps, 2nd irradiation—$\Delta MLT = 10$ ps) than for MS2F (8 ps and 6 ps) with the uncertainty being less than 2 ps. Therefore, these results indicate a significant

Table 2 Critical temperatures measured in a SQUID magnetometer

	Non-irradiated	Irradiated 1 (1.4×10^{21} m^{-2})	Irradiated 2 (7×10^{21} m^{-2})	Annealed (after 2nd irradiation)
YBCO	92.2	92.1	90.5	91.5
MS2F	92.0	91.5	90.0	91.0

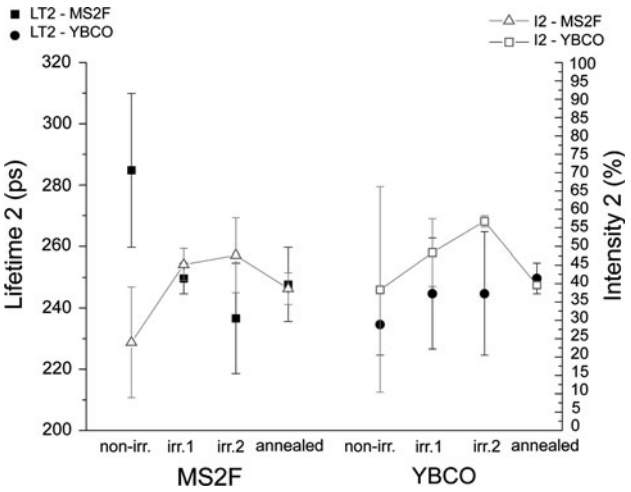

Fig. 8 PALS results for the pristine samples YBCO and MS2F, after both irradiation steps and following annealing

Table 3 Results on positron mean lifetimes (MLT) and intensities (I) for non-irradiated and irradiated samples

Sample		MLT [ps]
MS2F	Non-irradaiated	242
	Irradiated—2.10^{21} m^{-2}	250
	Irradiated—1.10^{22} m^{-2}	256
	Annealed—2 h at 400°C	234
YBCO	Non-irradaiated	214
	Irradiated—2.10^{21} m^{-2}	229
	Irradiated—1.10^{22} m^{-2}	239
	Annealed—2 h at 400°C	220

change in the defect volume, mainly in YBCO, although the MLT of MS2F is always higher (worse), which indicates that MS2F contains more defects in total (defects described by L2 and also included in LT1). Larger radiation damage can be assumed according to the MLT values in YBCO after both irradiation steps resulting in the generation of new pinning sites.

After annealing, the MLT decreases similarly in both samples. Sample YBCO shows a little higher MLT than in the non-irradiated state, which means that the structure of YBCO is not fully regenerated. On the contrary, the MLT in the annealed sample MS2F is smaller than in the pristine sample without treatment. This structure shows an almost complete regeneration of the microstructure in terms of the positron data.

The measured lifetime (LT2) in the non-irradiated sample MS2F indicates the presence of Ba mono-vacancies (~270 ps [22]), which are larger than the Cu–O di-vacancies (~240 ps [22]) found in all other measurements. In the irradiated as well as in the annealed sample MS2F, the number of di-vacancies dominates, although bigger defects might still be located there.

The defect concentration of the Ba mono-vacancies (in the non-irradiated sample MS2F) and Cu–O di-vacancies (in all other samples) was quantified according to 3–6 and is listed in Table 4. The calculated defect concentration was increasing after the irradiation and demonstrates decrease after annealing for both materials, YBCO and MS2F, as discussed above for MLT.

During irradiation small defects were accumulated in the structure. The defect concentration grows, although this growth is not linear with neutron fluence. The smaller increase in defect concentration upon further irradiation can be connected with the changing ratio between defect creation and recombination. The amount of these radiation induced defects may become saturated. However, a corresponding saturation in transition temperature is not observed.

Conclusions

High temperature superconductors possess a high potential for various applications and could effectively replace conventional superconductors in fusion facilities. $YBa_2Cu_3O_{7-\delta}$ is one of the most promising materials in view of its high critical temperature and critical current densities. These properties can be achieved or improved by using of an appropriate microstructure with a high defect concentration. This is not typical feature of other materials, where defects usually cause a degradation of structural and mechanical properties. Neverthless, a high defect concentration in superconductors improves the superconducting properties, particularly the critical current density. Studies of the influence of neutron and gama radiation indicate a pronounced change in the superconducting properties of $YBa_2Cu_3O_{7-\delta}$ after irradiation. The critical temperature decreases in both investigated samples, which were differently processed. At the same time, the results show an enhancement in critical current density at 77 K.

Table 4 Calculation of the defect (Cu–O divacancy) concentration

Sample		Defect concentration—c_D	
		(ppm/at.)	(10^{22}/m^3)
MS2F	Non-irradaiated (Ba mono-vacancies)	0.63	3.85
	Irradiated—2.10^{21} m^{-2} (Cu–O di-vacancies)	1.72	10.50
	Irradiated—1.10^{22} m^{-2} (Cu–O di-vacancies)	2.32	14.10
	Annealed—2 h at 400°C (Cu–O di-vacancies)	1.32	8.40
YBCO	Non-irradaiated (Cu–O di-vacancies)	1.59	7.94
	Irradiated—2.10^{21} m^{-2} (Cu–O di-vacancies)	2.39	12.00
	Irradiated—1.10^{22} m^{-2} (Cu–O di-vacancies)	3.37	16.50
	Annealed—2 h at 400°C (Cu–O di-vacancies)	1.68	8.37

In the pristine state, the sintered sample contains a lower concentration of impurities and probably smaller defects than the multi-seeded melt-textured sample. After irradiation, defects of the same size were found, probably Cu–O di-vacancies. The defects formed during neutron irradiation dominate in quantity over the defects, which were already present in the samples before the radiation treatment.

Annealing the samples at 250°C for 4 h leads to a defects recombination or combination of small defects to bigger ones. The $YBa_2Cu_3O_{7-\delta}$ lattice is partially regenerated by this process, which is confirmed by the enhancement in critical temperature. However, the decrease in the density of pinning centers (mostly small) causes a reduction in critical current density.

Acknowledgments N. Hari Babu, Brunel Centre for Advanced Solidification Technology (BCAST), Brunel University, and P. Diko from the Slovak Academy of Sciences (SAV) are acknowledged for the preparation of the investigated materials. The Nano Engineered Superconductors for Power Applications (NESPA) and VEGA 01/0129/09 grants are also acknowledged.

References

1. D. Maisonnier, I. Cook, S. Pierre, B. Lorenzo, D.P. Luigi, G. Luciano, N. Prachai, Fus. Eng. Des. **81**, 1123 (2006)
2. S.R. Foltyn, L. Civale, J.L. MacManus-Driscoll, Q.X. Jia, B. Maiorov, H. Wang, M. Maley, Nat. Mater. **6**, 631 (2007)
3. A. Xu, J.J. Jaroszynski, F. Kametani, Z. Chen, D.C. Larbalestier, Y.L. Viouchkov, Y. Chen, Y. Xie, V. Selvamanickam, Supercond. Sci. Technol. **23**, 014003 (2010)
4. F. Seitz, Rev. Mod. Phys. **34**, 656 (1962)
5. F.M. Sauerzopf, H.P. Wiesinger, W. Kritscha, H.W. Weber, G.W. Crabtree, J.Z. Liu, Phys. Rev. B **43**, 3091 (1991)
6. M. Eisterer, R. Fuger, M. Chudy, F. Hengstberger, H.W. Weber, Supercond. Sci. Technol. **23**, 014009 (2010)
7. R.T. Santoro, Y. Gohar, R.R. Parker, G. Shatalov, M.E. Sawan, H.Y. Khater, Fusion Eng. Des. **27**, 62 (1995)
8. R.T. Santoro, Radiation shielding for fusion reactors. in *Proceedings of the ICRS-9 conference*. (Tsukuba, Japan, Oct. 1999), pp. 17–22
9. JAEA R&D Review 2006, Report of Japan Atomic Energy Agency (JAEA). Available via http://jolisfukyu.tokai-sc.jaea.go.jp/fukyu/mirai-en/2006/index_set.html. Cited 12 May 2011
10. M.C. Frischherz, M.A. Kirk, J. Farmer, L.R. Greenwood, H.W. Weber, Physica C **232**, 309 (1994)
11. J. Giapintzakis, W.C. Lee, J.P. Rice, D.M. Ginsberg, I.M. Robertson, Phys. Rev. B **45**, 10677 (1992)
12. F.M. Sauerzopf, Phys. Rev. B **57**, 10959 (1998)
13. F.M. Saurezopf, M. Werner, H.W. Weber, R.A. Suris, D.V. Kulikov, Yu.V. Trushin, V.S. Kharlamov, Physica C **282**, 1333 (1997)
14. S. Jin, T.H. Tiefel, R.C. Sherwood, R.B. van Dover, M.E. Davis, G.W. Kammlot, R.A. Fastnacht, Appl. Phys. Lett. **52**, 2074 (1988)
15. J.C.L. Chow, P.C.W. Fung, J. Superconduct. **6**, 365 (1993)
16. O.F. de Lima, V.P.S. Awana, R.A. Ribeiro, M.A. Avila, Europhys. Lett. **51**, 174 (2000)
17. C.P. Bean, Phys. Rev. Lett. **8**, 250 (1962)
18. Oxford Instruments Superconductivity, Vibrating Sample Magnetometer Superconducting system with integral VTI, Version 1.0, July 2000
19. M. Chudy, *High Temperature Superconductors for Fusion Magnets*. Doctoral thesis (Atomic Institute, Vienna University of Technology, Vienna, Austria, 2011)
20. R. Kraus-Rehberg. S. H. Leipner, *Positron Annihilation in Semiconductors* (Springer, Berlin, Germany, 1998) ISBN 3-540-64371-0
21. M. Petriska, A. Zeman, V. Slugeň, V. Kršjak, S. Sojak, Phys. Stat. Solidi. C **60**, 2465 (2009)
22. K.O. Jensen, R.M. Nieminen, M.J. Puska, J.Phys. Condens. Matter **1**, 3727 (1989)
23. A. Bhahathi, C.S. Sundar, Y. Hariharan, J. Phys. Condens. Matter **1**, 1467 (1989)
24. S. Ishibashi, R. Yamamoto, M. Doyama, T. Matsumoto, J. Phys. Condens. Matter **3**, 9169 (1991)
25. K. Petersen, *Cystal Defects Studied by Positrons*. (Politeknik Forlag, Lyngby, Denmark 1978). ISBN 87 502 0488 2
26. P. Hautojarvi, C. Corbel, Positron spectroscopy of defects in metals and semiconductors, *in Positron Spectroscopy of Solids.* (Societa Italiana di Fisica, IOS Press, Amsterdam, Netherlands, 1995). ISBN 90 5199 203 3
27. J. Zhang, F. Liu, G. Cheng, J. Shang, J. Liu, S. Cao, Z. Liu, Phys. Lett. A **201**, 70 (1995)
28. J. Kansy, Nucl. Instr. Meth. Phys. Res. A **374**, 235 (1996)
29. C. F. Laub, T. L. Kuhl, How bad is good? A critical look at the fitting of reflectivity models using the reduced Chi-square statistic, *in SNS—HFIR Users Meeting 2005*, (ORNL Research Center, USA, Oct. 11–13, 2005)

Point defects in $YBa_2Cu_3O_{7-x}$ studied using positron annihilation

2012 Supercond. Sci. Technol. 25 075017

(http://iopscience.iop.org/0953-2048/25/7/075017)

Supercond. Sci. Technol. **25** (2012) 075017 (5pp) doi:10.1088/0953-2048/25/7/075017

Point defects in $YBa_2Cu_3O_{7-x}$ studied using positron annihilation

Michal Chudy[1], M Eisterer[1], H W Weber[1], J Veterníková[2], S Sojak[2] and V Slugeň[2]

[1] Vienna University of Technology—Atominstitut, Stadionallee 2, 1020 Vienna, Austria
[2] Institute of Nuclear and Physical Engineering, Faculty of Electrical Engineering and Information Technology, Slovak University of Technology, Ilkovičova 3, 812 19 Bratislava, Slovak Republic

E-mail: mchudy@ati.ac.at and mc672@cam.ac.uk (M Chudy)

Received 13 January 2012, in final form 17 May 2012
Published 15 June 2012
Online at stacks.iop.org/SUST/25/075017

Abstract
Fast neutron irradiation is a powerful technique for introducing additional pinning centers into high temperature superconductors. The spherical defects with sizes of a few nanometers are considered to be effective pinning centers, enhancing J_c. Their morphology is well-known and has already been investigated by several authors in great detail. However, only very little is known about the nature and density of smaller and point defects, which are invisible in transmission electron microscopy. Positron annihilation lifetime spectroscopy was applied to investigate the nature and the concentration of small point-like defects. In this work, the influence of small point defects, such as vacancies and vacancy clusters, on the superconducting properties of $YBa_2Cu_3O_{7-x}$ bulks was studied; these were introduced by irradiation in the TRIGA Mark II reactor in Vienna. J_c and T_c measurements were performed prior to and after each irradiation step. The samples were irradiated up to a fast neutron (>0.1 MeV) fluence of 6×10^{21} m^{-2}. The two kinds of defects—the large collision cascades and the small point-like defects—contribute to the decrease of T_c as well as to the J_c enhancement in astonishingly similar ways.

(Some figures may appear in colour only in the online journal)

1. Introduction

Recent research into high temperature superconductors (HTS) and the development of HTS conductors has been focused on flux pinning and on techniques for its improvement. The defects forming pinning centers are usually studied by transmission electron microscopy (TEM). However, not all defects which can act as effective pinning centers in high temperature superconductors can be observed by TEM. Several studies have shown that small point defects such as lattice vacancies, divacancies and small clusters of vacancies can also be effective pinning centers and significantly enhance the critical current densities in HTS [1]. In the cuprates, particularly in YBCO, small defects within the Cu–O sublattice cause a T_c reduction. A clear correlation between the defect concentration and T_c was found and studied in [2]. Fast neutron irradiation represents a very effective way of introducing effective pinning centers into high temperature superconductors [3, 4]. Various kinds of lattice defects can be introduced in this way. A fast neutron can initialize a cascade in the crystallographic lattice. In YBCO, the energy released in the cascade increases the local temperature of the surrounding material, eventually causing partial melting of the structure. Big amorphous defects of up to 10 nm in diameter [5] can be created in this way. However, numerous smaller defects, such as vacancies, divacancies and vacancy clusters, are created due to the various energies of the recoils and the neutrons in the reactor core [6]. Defects of 3–5 nm are considered as the most effective for flux pinning, since their size matches the coherence length in HTS at elevated temperatures. The density of these defects is $(1 \pm 0.5) \times 10^{22}$ m^{-3} [7] after irradiation to a fast neutron fluence of 2×10^{21} m^{-2}. They enhance J_c in $YBa_2Cu_3O_{7-x}$ and reduce the J_c anisotropy [3, 8]. The concentration of small defects is

expected to be at least one order of magnitude higher. These defects are of interest because their nature and effects have not been satisfactorily clarified until now. They are believed to be the main reason for the T_c reduction after neutron irradiation, but they might also enhance pinning due to their high density [1].

In this paper, we report on the changes of T_c and J_c following neutron irradiation and annealing of melt textured $YBa_2Cu_3O_{7-x}$. Similar experiments were carried out on single crystals [2], but the density of small defects was unknown at that time. Conclusions concerning small defects were only drawn on the basis of the observed changes of the superconducting properties. In this study, the density of small defects was assessed by positron annihilation lifetime spectroscopy (PALS), and the density of large defects estimated from the known relationship between the density of the collision cascade and the fast neutron fluence. The influences of the two kinds of defects can be separated and addressed in this way.

2. Experimental details

A multiseeded $YBa_2Cu_3O_{7-x}$ bulk with 0.1% of platinum addition was investigated in this work. The bulk was produced by the melt texture growth method at the University of Cambridge. The diameter of the bulk was 19–19.5 mm. A thin disk sample with a thickness of 0.7 mm was cut from the top of the bulk and the disk was then divided into two identical pieces (half-disks). A small sample of $3 \times 3 \times 0.7$ mm^3 was cut from one of them. The small sample was used for the magnetic J_c and T_c characterization. The rest was used for the PALS measurement, where thicker and bigger samples are desirable. The two half-disks were arranged into a sandwich together with the ^{22}Na positron source between them (figure 2).

The samples were studied by three different measurement techniques at two different laboratories. The point defects in the samples were investigated by a positron annihilation lifetime spectroscopy technique at the Institute of Nuclear and Physical Engineering, Faculty of Electrical Engineering, in Bratislava. The J_c and T_c characterizations were performed at the Atominsitiut in Vienna. A MagLab vibrating sample magnetometer (VSM) was employed for the J_c measurements due to its high speed and adequate accuracy. The VSM was operated with an amplitude of 0.2–0.5 mm at 55 Hz. The transition temperature, T_c, was obtained from ac susceptibility measurements in a 1 T SQUID magnetometer, with an applied field amplitude of 0.1 mT at 33 Hz.

The neutron irradiation was performed at the Central Irradiation Facility (CIF) of the TRIGA Mark II reactor in Vienna. The pristine samples were characterized by means of PALS, and J_c and T_c measurements. Afterwards, they were sequentially irradiated in the CIF up to a fast neutron fluence of 6×10^{21} m^{-2} ($E_n > 0.1$ MeV). An identical measurement procedure was performed after each irradiation step and also after the heat treatment. The heat treatment was performed after the last irradiation step under ambient pressure in air at a temperature of 250 °C for 2 h.

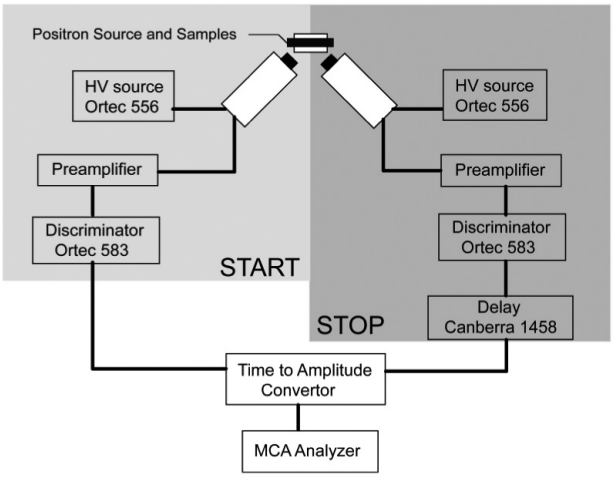

Figure 1. Schematic view of the PALS equipment (Slovak University of Technology—STU) [17].

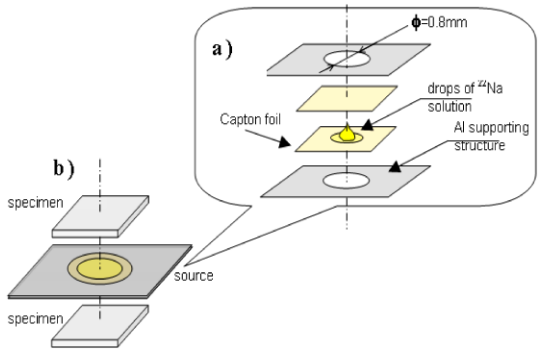

Figure 2. Positron source (a) and lay-out of the specimen (b).

The PALS measurements were performed at room temperature using the apparatus sketched in figure 1. The samples consisted of two half-disks, one above and the other below the positron source (figure 2). A detailed description of the PALS technique can be found in [9]. ^{22}Na with a half-lifetime of 2.6 years was used as the positron source. Sodium decays to ^{22}Ne with a probability of 90.4%. About 3.7 ps after the decay with the positron emission, an energy quantum of 1274 keV is emitted from the positron source. This is registered by a detector and provides information about the positron generation. The positron annihilation is detected by the emitted energy radiation of 511 keV.

As the next step, the positron lifetimes and intensities are measured. The positron lifetime increases with defect size. The positron intensity is proportional to the defect density; thus, these two quantities can be obtained from positron annihilation studies.

It is important to note that the PALS technique detects structural defects at the atomic level, i.e. monovacancies and divacancies, vacancy clusters and voids (order of 0.1 nm) are detected. The method is not sensitive to bigger defects such as microcracks, precipitates or clusters of amorphous material in the nanometer range.

Details of the positron annihilation spectroscopy measurements and the derived results have been presented

Table 1. Critical temperatures measured in a 1 T SQUID magnetometer.

Treatment	Unirradiated	Irradiated (1.2×10^{21} m^{-2})	Irradiated (6×10^{21} m^{-2})	Irradiated (6×10^{21} m^{-2})—after heat treatment
T_c (K)	92	91.5	90	91

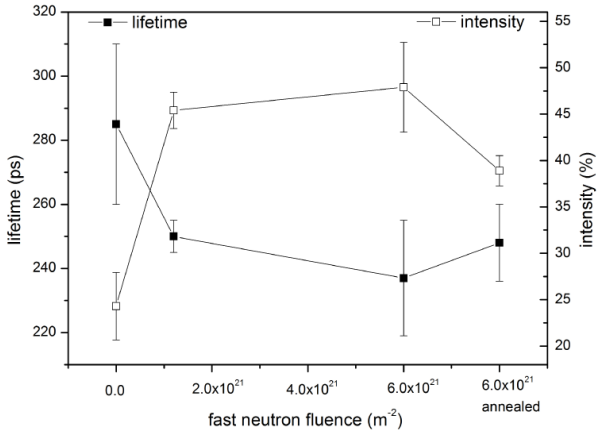

Figure 3. Lifetimes and intensities of the YBCO sample from PALS measurements.

elsewhere [11]. However, it is important to note some of the most relevant attributes of PALS characterization:

- A precise calculation of the densities of all kinds of vacancies (Y, Ba, Cu and O) is hardly possible and only the dominant vacancy type can be assessed by using the positron lifetime [12].
- The measured positron lifetimes fit best with expectations for Cu–O divacancies (and Ba vacancies in the unirradiated sample).
- Other kinds of vacancies (smaller ones or bigger clusters) are likely to exist in the samples.

3. Results and discussion

The superconducting transition temperatures of the sample after different treatments are listed in table 1. The effect of neutron irradiation and the resulting disorder in the YBCO lattice is monitored well by the drop in T_c. The heat treatment increased T_c, which was ascribed to the migration, clustering and recombination of small defects in [2].

The corresponding decrease in density of small defects is confirmed by the PALS measurements (figure 3). In figure 3, the lifetime represents the defect type and the intensity is a parameter reflecting the defect density. According to the lifetime values, Ba monovacancies were identified as the major kinds of defects in the pristine sample. The Cu–O divacancy was identified as the major defect after irradiation and annealing. All information about the PALS measurements performed is described in detail in [11].

Table 2 presents the calculated point defect concentrations, which were quantified and calculated according to [12–16]. The identified Cu–O divacancy can be understood

Table 2. Calculation of the point defect concentration (Cu–O divacancies).

	Small defects (10^{22} m^{-3})	Cascades (10^{22} m^{-3}) [7]
Non-irradiated	3.9[a]	0
Irradiated—1.2×10^{21} m^{-2}	10.5	0.6
Irradiated—6×10^{21} m^{-2}	14.1	3
Annealed—2 h at 400 °C	8.4	3

[a] Ba monovacancy.

as a very small cluster of defects within the Cu–O sublattice. The concentrations given in table 2 refer to this type of defect, except for in the unirradiated sample, where Ba monovacancies were identified as being dominant. This result confirms that the optimally doped sample does not contain many defects within the Cu–O sublattice as expected from the high T_c. The defect density can be calculated after identifying the dominant defect type in the sample from the positron lifetime. For this calculation, it was assumed that all the defects in the sample are identical—the identified dominant defect type. However, other defect types can be present in minor concentrations. This assumption results in an unavoidable error and prevents us from quoting error bars in table 2. The calculated values are considered as a good approximation, although they do not represent precise values of the total small defect concentration.

A marked increase in the density of small defects is found after the irradiation and a decrease after annealing. The concentration of small defects is more than one order of magnitude higher than the density of collision cascades (pinning centers of a few nm) after the first irradiation, but this ratio decreases upon further irradiation and annealing. The transition temperature clearly correlates with the defect density: the higher the defect density, the smaller T_c. Figure 4 shows the correlation between the fast neutron fluence and the defect concentration together with the critical temperature. It is interesting to note that the concentration of small defects does not scale linearly with the irradiation time (fluence), while the T_c reduction approximately does and the concentration of the collision cascades most likely does [2]. The generation and recombination of small defects during irradiation might cause this non-linearity.

Figure 5 presents the transition temperature as a function of the defect concentration. The squares represent the data if only the small defects are taken into account. According to the PALS measurements, the heat treatment did not anneal all the point defects, and thus their concentration remains higher than in the pristine sample. However, the corresponding transition temperature is smaller than one would expect from the

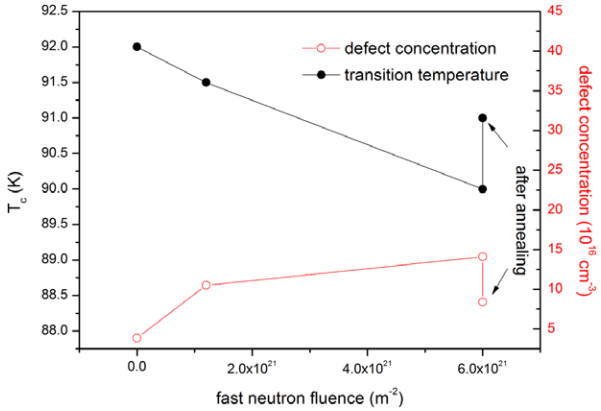

Figure 4. Concentration of point defects and T_c as a function of the fast neutron fluence.

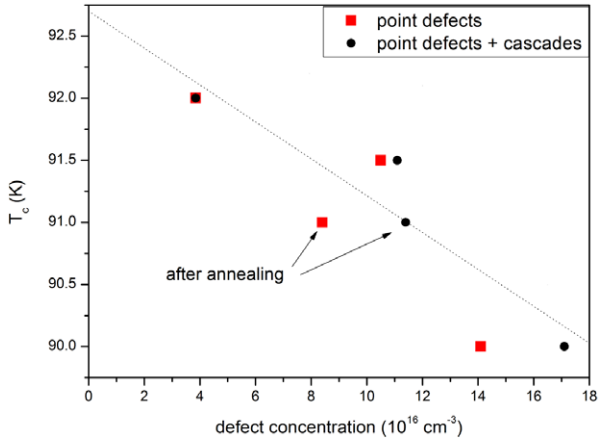

Figure 5. T_c as a function of the defect concentration.

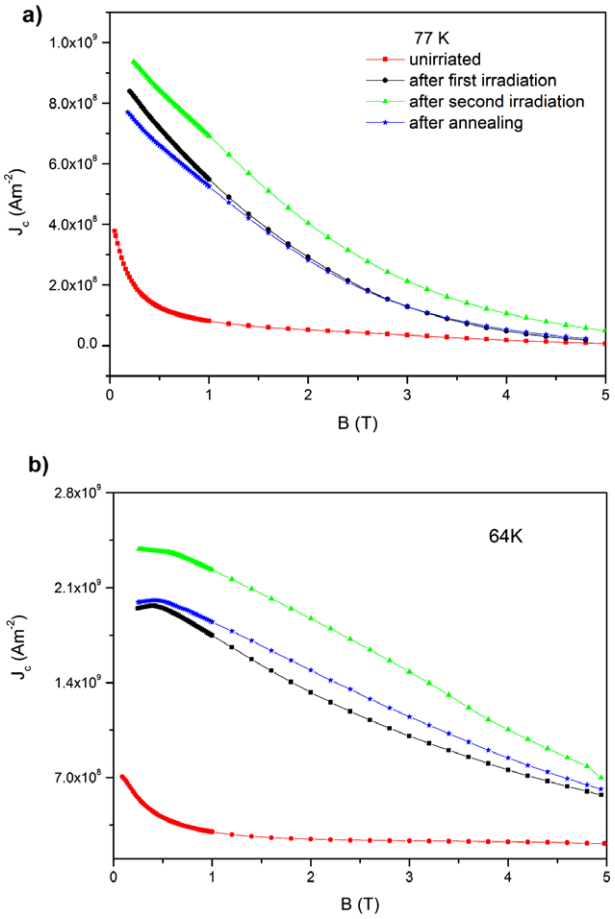

Figure 6. Critical current densities at 77 K (upper panel) and 64 K (lower panel) before and after various treatments.

actual concentration of small defects, since T_c after the first irradiation is higher, despite a higher density of small defects. This seems to be caused by the larger defects, which are stable during the heat treatment [17] and invisible in PALS. They might induce strain into the Cu–O lattice, thus decreasing the transition temperature. To support this explanation, the density of the collision cascades according to [7] was simply added to the density of the small defects (circles in figure 5). The dependence becomes monotonic and a linear fit (dotted line) to the data extrapolates to the highest reported values representing the limit of the very clean material. The transition temperature after the first irradiation still does not fit the linear behavior, but the addition of extremely different defects is obviously a quite serious oversimplification. In addition, the PALS analysis does not exclude further kinds of defects.

The J_c enhancement following fast neutron irradiation has already been investigated in YBCO single crystals [2, 4] and coated conductors [3]. The changes in J_c at 77 and 64 K of the present melt textured sample are shown in figure 6. J_c increases after both irradiations, becoming highest after the second irradiation step (6×10^{21} m^{-2}) as expected from previous results [2, 10]. The heat treatment reduced the number of (small) pinning centers and consequently also J_c, even though T_c increases. The drop of J_c is a direct consequence of point defect density reduction, which was precisely measured and calculated as reported in table 2. It is also interesting to compare J_c after the first irradiation and that after the final heat treatment, because the total defect densities are nearly the same in the two cases ($\sim 1.1 \times 10^{23}$ m^{-3}), but the ratio between collision cascades and Cu–O divacancies increases from about 0.06 to 0.36. In particular at 77 K, the critical currents are very similar. This was the motivation for plotting J_c as a function of the total defect density (figure 7). We also added the density of the barium vacancies found in the untreated sample, since the barium content could not have been changed by the treatments (only the type of dominant defect changed). Rather surprisingly, J_c turns out to be roughly proportional to the total defect density, despite the different kinds of defects, which add to the total pinning force. The highly non-linear increase of J_c with neutron fluence is caused by the pronounced non-linearity in the density of small defects. It has to be emphasized that we do not claim a rigorous proportionality between defect density and critical current. The critical currents are not identical at the same defect density at 64 K. The possibility that this difference arises from the rather large uncertainties in the determination of all kinds of defects can be excluded, since the critical currents are nearly identical at 77 K and fields above 1.5 T. This temperature dependence is an obvious

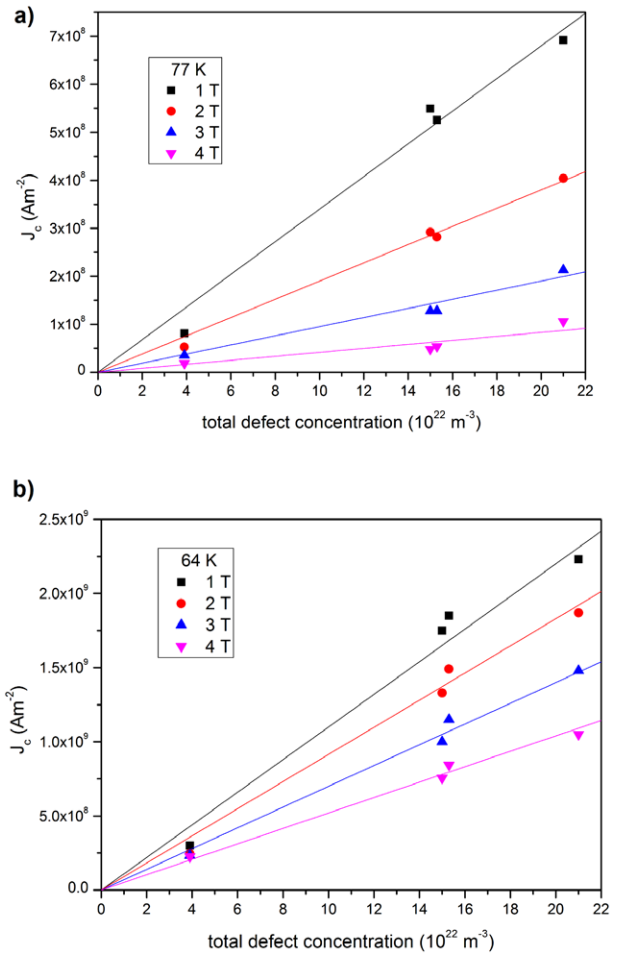

Figure 7. J_c at 77 K (a) and 64 K (b) as a function of the defect concentration.

manifestation of the different efficiencies of the different defect types at different temperatures. However, at least at the two temperatures investigated, the overall defect density seems to be the most important.

It is also worth noting that the critical currents in the unirradiated sample do not follow the linear trend at low fields, while they essentially do at high fields, which is closely related to the different field dependence of J_c in the pristine sample (cf figure 6). Although no fishtail (or second-peak) effect is observed in this sample, the critical current drops rapidly at low fields, followed by a much weaker (plateau-like) field dependence at higher fields, but no second peak occurs, which would be indicative of an order–disorder transition. However, the high critical currents in the sample after irradiation can only arise from strong pinning, leading to a highly disordered vortex lattice and the corresponding monotonic field dependence of J_c. J_c for the pristine sample might be reduced at low fields by the competition of the disordered state with the elastic forces (which causes a minimum of J_c if they 'win', i.e. fishtail effect), thus not following the same dependence on the magnetic field and defect density characteristic for a highly disordered vortex lattice.

4. Conclusions

The defect structure and changes of the transition temperature and critical currents in an YBCO bulk superconductor were investigated after sequential neutron irradiation and a heat treatment. The type and density of the small defects were assessed using positron annihilation spectroscopy (PALS). Barium vacancies in the pristine sample and Cu–O divacancies after irradiation were identified as the dominant point-like defects. Their density is not proportional to the neutron fluence and is higher by more than one order of magnitude than that of the well-known concentration of large defects (sizes of a few nm) at low fluences, but this ratio decreases upon further irradiation. The concentration of point defects is reduced after the heat treatment, but not all small defects anneal. The corresponding changes in J_c and T_c were investigated by means of magnetic measurement using VSM and SQUID magnetometers. Changes in J_c were described through precise value changes of point defect densities. The results demonstrate a surprisingly strong influence of point pinning centers on J_c and of collision cascades on T_c. The size of the defects turned out to be less important for J_c and T_c than their density.

References

[1] Giapintzakis J, Lee W C, Rice J P, Ginsberg D M and Robertson I M 1992 *Phys. Rev.* B **45** 10677–83
[2] Sauerzopf F M 1998 *Phys. Rev.* B **57** 10959–70
[3] Eisterer M, Fuger R, Chudy M, Hengstberger F and Weber H W 2010 *Supercond. Sci. Technol.* **23** 014009
[4] Sauerzopf F M, Wiesinger H P, Kritscha W, Weber H W, Crabtree G W and Liu J Z 1991 *Phys. Rev.* B **43** 3091
[5] Frischherz M C, Kirk M A, Zhang J P and Weber H W 1993 *Phil. Mag.* A **67** 1347
[6] Weber H W, Böck H, Unfried E and Greenwood L R 1986 *J. Nucl. Mater.* **137** 236–40
[7] Frischherz M C, Kirk M A, Farmer J, Greenwood L R and Weber H W 1994 *Physica* C **232** 309
[8] Chudy M, Eisterer M and Weber H W 2010 *Physica* C **470** 1300–3
[9] Krause-Rehberg R and Leipner H S 1999 *Positron Annihilation in Semiconductors: Defect Studies* (Berlin: Springer) ISBN 3-540-64371
[10] Chudy M, Fuger R, Eisterer M and Weber H W 2011 *IEEE Trans. Appl. Supercond.* **21** 3162–5
[11] Veterníková J, Chudy M, Eisterer M, Weber H W, Slugeň V, Sojak S, Petriska M and Sabelová V 2011 *J. Fusion Energy* **31** 89–95
[12] Jensen K O, Nieminen R M and Puska M J 1989 *J. Phys.: Condens. Matter* **1** 3727
[13] Petersen K 1978 *Crystal Defects Studied by Positrons* (Lyngby: Polyteknisk Forlag) ISBN 87 502 0488 2
[14] Hautojarvi P and Corbel C 1995 Positron spectroscopy of defects in metals and semiconductors *Positron Spectroscopy of Solids* (Amsterdam: Societa Italiana di Fisica, IOS Press) ISBN 90 5199 203 3
[15] Zhang J, Liu F, Cheng G, Shang J, Liu J, Cao S and Liu Z 1995 *Phys. Lett.* A **70** 201
[16] Petriska M, Zeman A, Slugeň V, Kršjak V and Sojak S 2009 *Phys. Status Solidi* c **60** 2465
[17] Vlcek B M *et al* 1992 *Phys. Rev.* B **46** 6441

n-Values of commercial YBCO tapes before and after irradiation by fast neutrons

2015 Supercond. Sci. Technol. 28 035008

(http://iopscience.iop.org/0953-2048/28/3/035008)

IOP Publishing Superconductor Science and Technology
Supercond. Sci. Technol. **28** (2015) 035008 (10pp) doi:10.1088/0953-2048/28/3/035008

n-Values of commercial YBCO tapes before and after irradiation by fast neutrons

M Chudy[1,2], Z Zhong[2], M Eisterer[3] and T Coombs[2]

[1] Graduate School of Technology Management, University of Pretoria, Lynnwood Road, Hatfield, Pretoria 0001, South Africa
[2] Department of Engineering, University of Cambridge, 9 JJ Thomson Avenue, Cambridge CB3 0FA, UK
[3] Vienna University of Technology—Atominstitut, Stadionallee 2, A-1020 Vienna, Austria

E-mail: michal.chudy@up.ac.za

Received 12 August 2014
Accepted for publication 26 November 2014
Published 28 January 2015

Abstract

The *n*-value is an important superconducting parameter, which represents the homogeneity of characterized superconductor as well as thermally activated depinning. In addition, *n*-values are important for the evaluation of pinning mechanisms and pinning forces. *n*-values are crucial input parameters for the numerical simulations of superconducting tapes, coils and other complicated superconducting applications where *E*–*J* power law applies. In this publication, complex measurement data of *n*-values from different 2nd generation of high temperature superconducting (2G HTS) tapes are presented and analysed. In addition, 2G HTS tapes were step-by-step irradiated by fast neutron fluences up to 1×10^{22} m^{-2}. *n*-values of the irradiated tapes, containing additional randomly distributed pinning centres, are presented, analysed and compared with unirradiated samples. Special attention is placed on the underlying physics resulting in the power-law part of the *I*–*V* curve and on the correlation between critical currents and *n*-values. The measurements are performed within the temperature range of 50–85 K and magnetic fields up to 15 T.

Keywords: *n*-value, neutron irradiation, inverse correlation, nonuniformity, YBCO 2G HTS

(Some figures may appear in colour only in the online journal)

1. Introduction

Each *I*–*V* curve of a superconducting sample contains a power-law part close to the transition to the dissipative state. This part of the *I*–*V* curve can be described by a simple equation:

$$V/V_c = \left(I/I_c\right)^n , \tag{1}$$

where V and I are the measured voltage and current, V_c is the voltage criterion, I_c is the critical current and the *n*-value the exponent n. Even though the *n*-value is an important superconducting parameter, results on 2nd generation of high temperature superconducting (2G HTS) tapes are available only in a few recent publications [1–5]. Therefore, a comprehensive overview of experimental *n*-value data would be beneficial when dealing with numerical modelling of superconductors. In low-temperature superconductors, the exponential relationship (power-law part) in *I*–*V* is usually explained by the J_c nonuniformity. Warnes and Larbalestier [6] and Plummer and Evetts [7] successfully developed models based on the J_c nonuniformity, but such a mechanism is not so successful in high temperature superconductors. Magnetic flux creep is a mechanism introduced by Anderson and Kim [8, 9] and describes a concept of thermally activated flux lines released from pinning centres. This phenomenon is mainly observed at higher temperatures where high temperature superconducting (HTS) operate. The rate of this process (R) is exponential, depending on the temperature of the superconductor according to the relation:

$$R \propto \exp\left(-\frac{U_e}{kT}\right), \tag{2}$$

where U_e represents activation energy, k is Boltzmann's constant and T is the absolute temperature. This process leads to the redistribution of flux lines resulting in a decrease of the magnetic moment of the superconductor, which is known as

magnetic relaxation. Magnetic relaxation in HTS was reviewed by Yeshurun *et al* [10], where the direct relation between flux creep and the power law relationship in the *I–V* curve was pointed out. Finally, studies by Sun *et al* [11] and Griessen [12] provided evidence that the power-law relationship is a consequence of the flux creep. However, both effects, nonuniformity and the flux creep, do not exclude each other and can collaboratively contribute to the exponential part of the *I–V* curve at the same time. Nowadays, flux creep is considered as the primary reason of the power-law relationship for high temperature superconductors even though some older publications suggested otherwise (i.e. nonuniformity or inhomogeneity) [13, 14]. It means that even a 'perfectly uniform' HTS would have the power law part of the *I–V* curve. The *n*-value of the 'perfectly uniform' HTS can be even relatively low in the case of efficient pinning centres with small activation energy. Nonuniformity is not necessarily present in large scale in modern 2G HTS tapes. Generally, the influence of the uniformity factor to the *n*-value is more important at lower temperatures. With increasing temperatures and magnetic fields the uniformity factor becomes less important and the importance of flux creep increases. As assumed by the uniformity based models [13, 14], critical currents are limited by grain boundaries and not grains. The transition between grain boundary and grain limited currents could be a threshold, where nonuniformity is not the main reason of the power-law relationship. In any case, the *n*-value always strongly depends on the efficient pinning mechanism in the superconductor.

Measurements of *n*-values after introducing additional pinning centres require special attention. Irradiation by fast neutrons introduces randomly distributed spherical pinning centres with diameters of a few nm [15–20] into a superconductor. It is a proven method of introducing efficient pinning centres into HTS, resulting in critical currents enhancements. Significant critical current enhancement was reported in rather stronger magnetic fields and lower temperatures for several types of tapes [20–22].

Regarding the HTS applications, high *n*-values reduce the losses by operation close to the J_c and are necessary to operate magnets in the persistence mode. At the same time, high *n*-values are also associated with unstable behaviour which can cause premature quenching in superconducting machines [23]. Usually, high *n*-values are considered as an asset of superconductors and rapid *n*-value reduction at higher magnetic fields can make them unsuitable for any applications. The *n*-value can vary significantly in different kinds of tapes as well as after irradiation. Therefore, measurements were performed on commercial 2G HTS tapes from three different manufacturers and also after irradiation by fast neutrons.

2. Samples

Standard tapes from three different manufacturers were used. The first is the 2G HTS SCS 4045 tape from SuperPower, which is made by metal organic chemical vapour deposition on an ion beam assisted deposition (IBAD) made MgO template [24]. The YBCO layer is 1 μm thick. Two sets of samples are characterized, both sets are the SCS 4045 tapes manufactured in 2008 and 2012 respectively. The size of YBCO grains in this kind of tape is ~1 μm. The second series of samples are from American Superconductor (AMSC). These tapes have RABiTS® (rolling assisted bi-axially textured substrates) substrate and metal organic deposited YBCO layer (~1 μm). The 4 mm wide tape is marked as 344 and the 12 mm wide tape as Amperium 8612, with a double HTS layer [25]. The usual size of YBCO grains in RABiTS® tapes is 20–50 μm [26]. The third series of samples is coming from Shanghai Superconductor Technology [27]. In these tapes, the MgO template is made by IBAD and pulsed laser deposition is used for 1 μm thick YBCO layer. The best tested 4 mm wide sample reached the highest value of critical current. More information about all the samples is listed in table 1. All the used 4 mm wide samples were 26 mm long and the 12 mm wide samples were 80 mm long.

Table 1. Critical currents and *n*-values of the samples at 77 K and self-field.

Sample	Critical current 77 K self-field	*n*-Value
SuperPower(2008) 4 mm	98 A	28.8
SuperPower(2012) 4 mm	114 A	30.5
SuperPower(2012) 12 mm	389 A	30.1
AMSC 4 mm	92.5 A	36
AMSC 12 mm	534 A	52.2
SHSC 4 mm	167.5 A	42.14

3. Instrumentation

All the presented instruments are adjusted for transport current characterization of short samples (approximately 3 cm length) by a standard 4 point method. As data for this study are obtained from several experiments performed by different devices in different laboratories (Low temperature and superconductivity laboratory at Vienna University of Technology, Atominstitut, and EPEC superconductivity laboratory at the University of Cambridge). Most of the samples were characterized by several experimental set-ups. A brief description of experimental instrumentation is given below.

3.1. The electromagnet set-ups

Two electromagnet measurement set-ups were employed for angle-resolved transport measurements, the first one was in Vienna (Atominstitut) and the second one in Cambridge (EPEC superconductivity group). The first set-up consisted of a 1.4 T water cooled electromagnet and the second of a 800 mT electromagnet where a larger area of homogenous field can be achieved. As for cryostats, a simple tubeshaped vacuum vessel (flask) and a polystyrene box were used. All

the measurements were performed in liquid nitrogen. Both set-ups are designed for angle-resolved transport measurements in the maximal Lorentz force configuration. The main difference between the two measurement set-ups is the rotation mechanism. While on the first set-up the holder is statically mounted between the rotating magnet poles, while the holder in the second set-up is rotating and the magnet poles are stable. Maximum achievable resolution on both systems is 0.5°. Both sample holders are equipped with Hall sensors and they produce identical results. The Cambridge was preferred for wider samples reaching very high currents and the irradiated samples were characterized exclusively in Vienna due to safety certificates.

3.2. 6 T measurement set-up

The 6 T measurement set-up is a helium gas flow cryostat equipped with a 6 T split coil. The main advantage of this cryostat is a wide temperature range of measurements from about 4.2–150 K. The horizontal magnetic field allows to perform angle-resolved transport measurements with a rotating sample holder. The rotating sample holder is equipped with a sensitive Hall probe, a Cernox temperature sensor and a fine rotating mechanism with a stepper motor (0.1° precision). Characterized samples can have lengths up to 30 mm. Indium press contacts are typically used for current and the conductive silver glue is used for the voltage contacts.

3.3. 17 T measurement set-up

The 17 T measurement set-up is a helium flow cryostat which is equipped with superconducting coils, generating magnetic field up to 17 T in vertical direction. The variable temperature inset has an inner diameter of about 3 cm and the magnetic field is homogeneous in a vertical length of about 30 mm. These parameters limit the maximum samples lengths to 30 mm. Two sample holders designed for short tapes characterization are available. One places the sample with the *ab* plane and the other with the *c*-axis parallel to the magnetic field. A 300 A current source was available for the transport characterization.

3.4. Triga (training, research isotope production general atomic) mark II reactor

The triga mark II was used as an irradiation facility in this work. It is a pool type research reactor that is used for TRIGA [28]. The reactor has a maximum continuous thermal power of 250 kW, though the power can be increased up to 250 MW for about 40 ms in the pulse regime. The fuel is in the form of an uniform mixture of 8 wt% uranium, 1 wt% hydrogen and 91 wt% zirconium, where the zirconium-hydride is being the main moderator. The maximum neutron flux density of $10^{17}\,\mathrm{m^{-2}\,s^{-1}}$ at 250 kW is reached in the central irradiation facility (CIF). The sample's temperature is estimated to remain below 50 °C during the irradiation procedure.

4. Results

4.1. Tapes in low magnetic fields

All the measurements in this section are performed by the electromagnetic measurement set-ups in liquid nitrogen in fields below or equal to 400 mT. As all studied commercial tapes have good grain alignment, the transition from grain boundary limited currents to grain limited currents must occur in this field range, according to [22, 29] even well below 400 mT. As at low fields the grain boundary limited currents may occur, both nonuniformity and flux creep must be taken into account as the reasons of the exponential part of the *I*–*V* curve. It is also important to mention that all the measurements are evaluated by a voltage criterion of 1 μV cm^{-1} as U_c is a locked parameter by fitting with equation (1). 4 mm tapes and wider 12 mm tapes from the three different manufacturers were characterized. In addition, two sets of 4 mm wide samples from SuperPower were characterized. Critical currents as well as *n*-values of all types of characterized tapes are listed in table 1. Results from both, newer (2012) and older (2008) tapes are available in figure 1. The results from 4 mm AMSC and SHSC tapes are shown in figures 2 and 3, respectively. All the angle-resolved measurements were performed in one of the introduced electromagnet measurement set-ups. The results of the *n*-values are shown together with figures of critical currents for a better illustration of critical current behaviour. Figures with *n*-values are generally noisier than the figures with critical currents as a consequence of fitting algorithm. *n*-values and critical currents were calculated from the power law fit of the exponential part of the IV curve. The beginning of the exponential part of the IV curve was determined by the first three points above the noise level. The same algorithm was applied for all the measurements from all used measurement set-ups.

By comparing of the result at 100 mT between SuperPower(2008) and SuperPower(2012), the increase in critical current is between 45% (at ∼90°) and 86% (at 0°). However *n*-values at 90° stayed practically unchanged (difference of ∼5%) and the difference at 0° is only about ∼33%.

Surprisingly, *n*-values of the AMSC tape are not dependent on the angle of magnetic field, even though some correlation between *n*-values and critical current exists also in RABiTS AMSC tape as presented in [2]. Figures 2 and 5 even show signs of inverse J_c–*n*-value correlation, which will be discussed later in this paper. In numerous experimental studies, it has been observed that *n*-values are usually correlated with critical currents [1, 2, 30], which causes that *n*-value varies also with external magnetic field. However, if the correlation is a consequence of relation presented by Zeldov *et al* [31], then:

$$U_e = U_0 \ln\left(\frac{J_{c0}}{J}\right), \tag{3}$$

where U_0 is the $J = 0$ activation energy (pinning energy), J is current density and J_{c0} is the critical current density in the

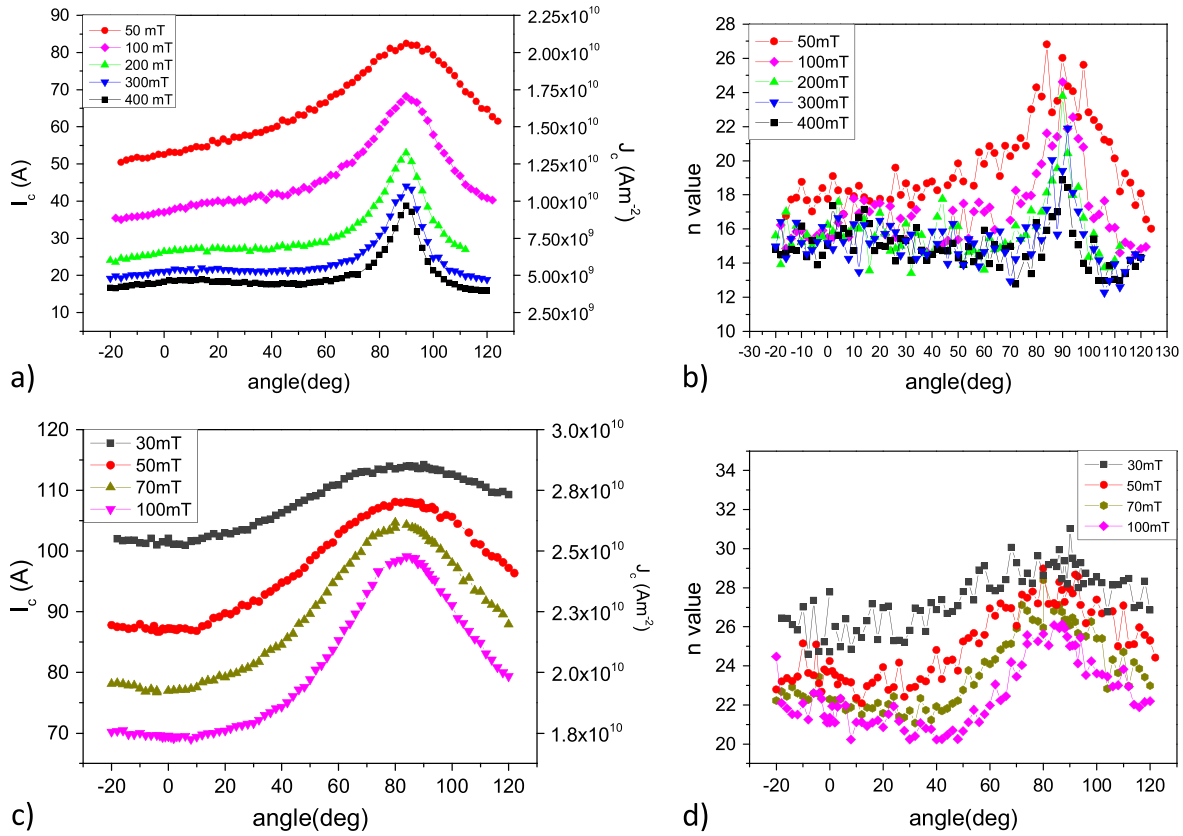

Figure 1. (a), (b) Critical current and *n*-values of the SuperPower tape (2008) at 77 K, (c), (d) critical current and *n*-values of the SuperPower tape (2012) at 77 K.

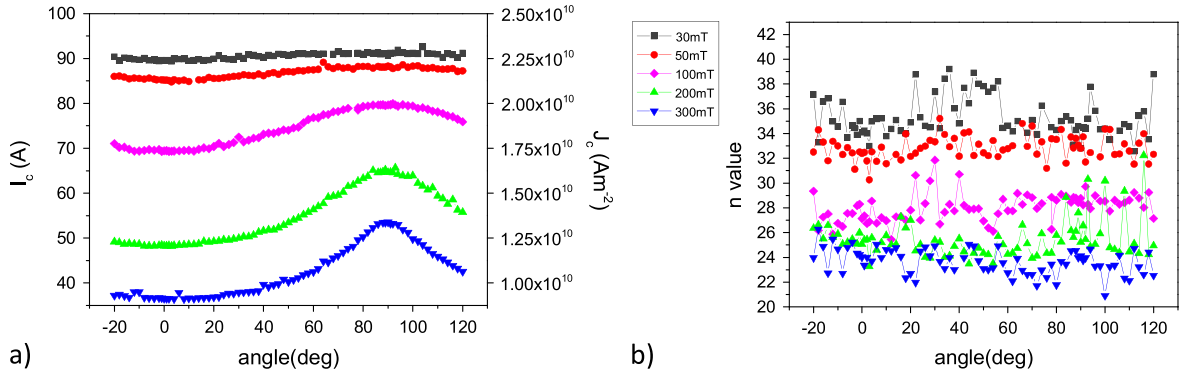

Figure 2. 4 mm AMSC tape at 77 K, (a) critical currents (b) *n*-values.

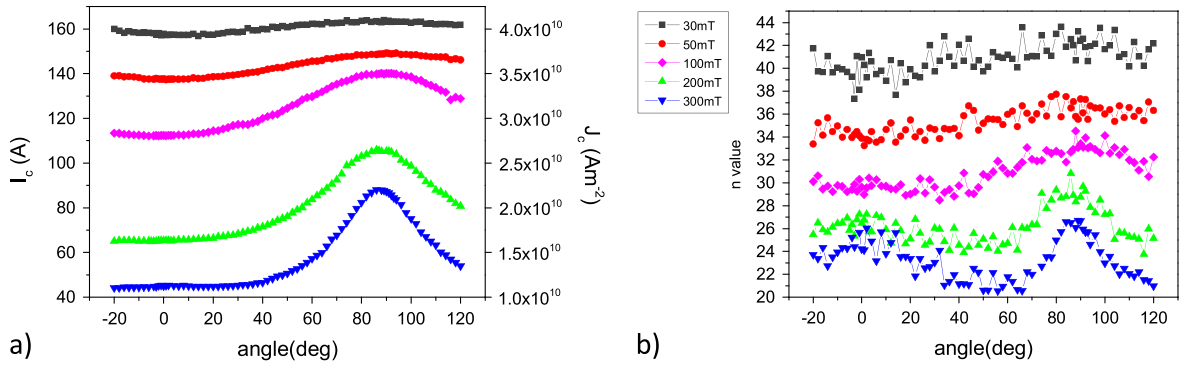

Figure 3. SHSC 4 mm wide tape at 77 K, (a) critical currents (b) *n*-values.

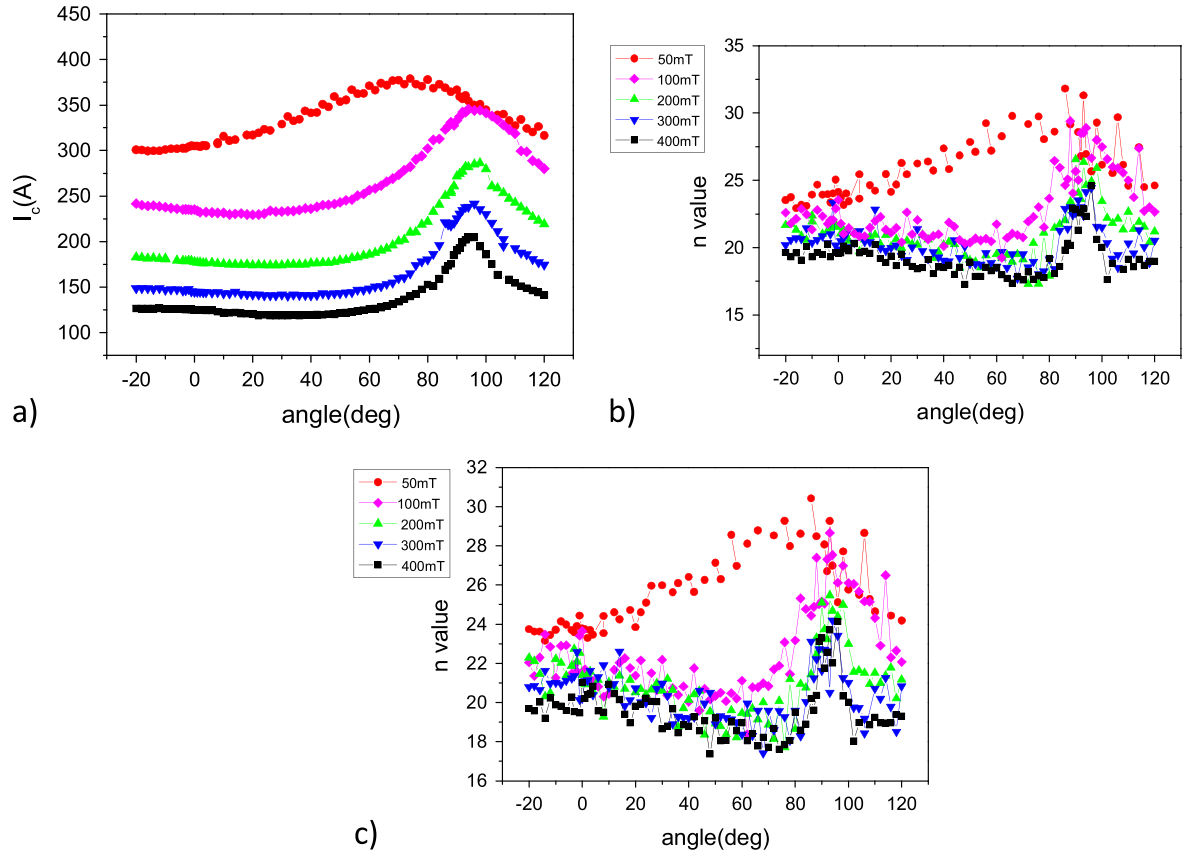

Figure 4. 12 mm wide SuperPower(2012) tape, (a) critical currents (b) n-values with criterion 1 μV cm^{-1} (c) n-values with criterion 3 μV cm^{-1}.

absence of thermal activation. From (2):

$$V \propto \frac{\mathrm{d}M}{\mathrm{d}t} \propto \exp\left(-\frac{U_\mathrm{e}}{kT}\right), \tag{4}$$

where $\mathrm{d}M/\mathrm{d}T$ is the rate of magnetization change. Thus, a simple substitution:

$$V \propto \frac{J_{c0}}{J}\exp\left(-\frac{U_0}{kT}\right) \propto \exp\left(\ln\left(\frac{J_{c0}}{J}\right)^{-\frac{U_0}{kT}}\right)$$

$$\propto \left(\frac{J_{c0}}{J}\right)^{-\frac{U_0}{kT}} \propto J^{\frac{U_0}{kT}}, \tag{5}$$

$$n \propto \frac{U_0}{kT},\ V \propto J^n \propto I^n\ . \tag{6}$$

It is shown that the n-value is directly proportional to the pinning energy of flux and not to the J_c. Thus $J_c = f\ (U_0)$, according to (3):

$$\ln\left(\frac{J_{c0}}{J_c}\right) = \frac{U_{ec}}{U_0}\ . \tag{7}$$

U_{ec} is activation energy at the critical current. It can be assumed that $(J_{c0} - J_c)$ is higher at higher temperatures and converging to zero at very low temperatures. If J_c is a function of (ϕ, H, T) according to (7), then U_0 is also a function of (ϕ, H, T), however, the angular dependence of U_0 in external magnetic field can be quite different than the one for the J_c. This can be a consequence of flux lines deformation e.g. into staircase like shapes [3, 4]. Nonuniformity might play a role in the uncorrelated dependence as well.

The SHSC sample has shown superior properties. Critical currents were significantly higher than in the other characterized tapes. Although n-values were very high at 30 mT, in higher fields they were comparable with tapes from other manufacturers. Anisotropy of the n-values is obvious only from fields above 200 mT.

In the next step, characterization of 12 mm wide tapes from SuperPower(2012) and AMSC was performed (figures 4, 5). According to the manufacturers [24, 25], the 12 mm tape from SuperPower should have identical structure as the 4 mm tape. Therefore, approximately three times higher critical currents and similar n-values would be expected compared to the 4 mm tape. The AMSC 12 mm tape contains two HTS layers. The additional layer causes that critical currents should be about six times higher than in the case of the 344, 4 mm wide tape. It is relatively difficult to predict the n-values of this tape according to the results of the 344 AMSC 4 mm wide tape. In the case of the SuperPower(2012) tape, n-values are slightly higher than for the 4mm tape. This difference seems to be insignificant and most likely it is just an effect of different voltage criterion. Wider tape creates

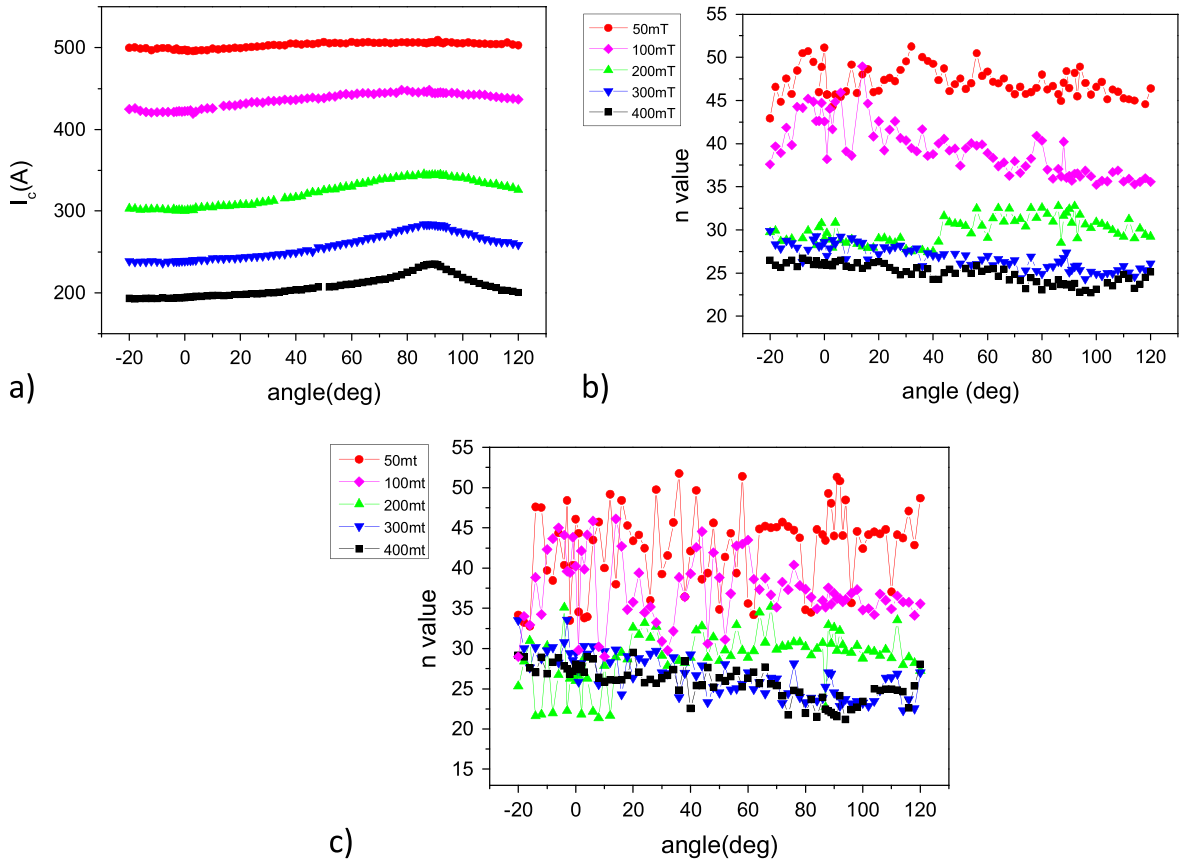

Figure 5. 12 mm wide double HTS layer Amperium tape, (a) critical currents (b) *n*-values with criterion 1 μV cm^{-1} (c) *n*-values with criterion 6 μV cm^{-1}.

more voltage for the same electric field E and therefore the critical electric field E_c, for the wider 12mm tape is smaller than the E_c of 4 mm tape at the same voltage criterion. For this reason, *n*-values were calculated for different voltage criteria [32]. The original 1 μV cm^{-1} criterion, but also higher 3 μV cm^{-1} and 6 μV cm^{-1} voltage criteria were used. Although, *n*-values calculated with higher criterion are slightly lower, no significant difference can be seen between figures 4(b) and (c). Even though *n*-values calculated by this enlarged voltage criterion are very similar to the 4 mm SuperPower(2012) tape, the used enlargement of the voltage criterion is not completely justified due to, for example, the edge effect of the tapes.

A clear *ab* peak shift can be observed in figure 4. This phenomenon was observed in [5, 33]. It is interesting to note that the shift of the *ab* peak is obvious also in the case of *n*-values (figure 4(b)). A change of the criterion seems to be without too much effect by the 12 mm wide AMSC tape with two YBCO layers. This tape has shown very high *n*-values for both voltage criteria. The measured *n*-values are significantly higher especially in low fields if compared to the 344 AMSC 4 mm wide tape (figure 5). Most likely, other more complex mechanisms are involved in this phenomenon, where identifying of these mechanisms would be a pure speculation at this stage.

4.2. Tapes in high magnetic fields and after irradiation

In this part, results in higher magnetic fields ($B \geqslant 1$ T) are presented. The tapes were irradiated several times by fast neutron fluences and re-measured. The presented graphs (figure 6) consist of results after each irradiation step. The type of artificial defects induced by neutron irradiation strongly depends on the kinetic energy of neutrons. Fast neutrons are neutrons with higher energies ($E \geqslant 0.1$ MeV) and they produce spherical defects of amorphous material with a diameter of a few nm (so called collision cascades) [15, 17–19]. The point defects and clusters of point defects are created by neutrons with lower energies and they can act as effective pinning as well [34]. The triga mark reactor II in Vienna (CIF) was used as an irradiation facility in this work. The irradiation levels of fast neutrons applied to the samples were up to fluences of 1×10^{22} m^{-2}. The other irradiation levels were: 2×10^{21} m^{-2} and 4×10^{2} m^{-2}. Since the irradiation procedure is a very time consuming process, only the 4 mm wide SuperPower(2008) tapes were characterized. The main time delays are caused by the fact that the samples are becoming radioactive emitters after the neutron irradiation procedure. In order to perform the measurements without any health and safety hazards, it is necessary to wait until the radioactivity of the sample is decayed to the acceptable limits.

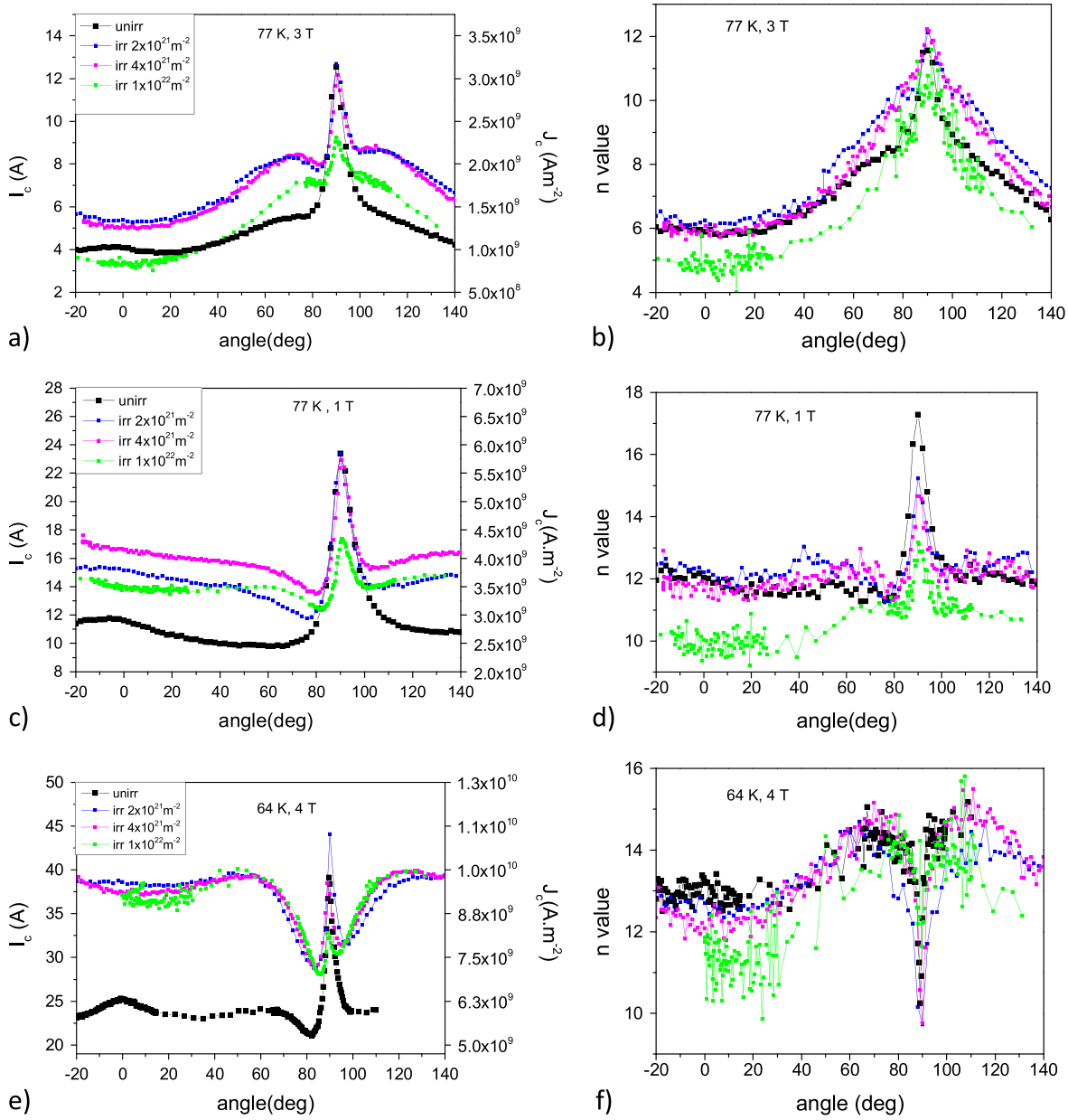

Figure 6. SuperPower(2008) tape characterized after fast neutron irradiation in the 6 T measurement set-up, (a) critical currents 77 K, 3 T (b) *n*-values 77 K, 1 T (c) critical currents 77 K, 1 T (d) *n*-values 77 K, 1 T (e) critical currents 64 K, 4 T (f) *n*- values 64 K, 4 T.

The measurements were performed in the 6 T and 17 T measurement set-ups at various temperatures from 50 K up to 85 K. Similar studies focused on only critical current enhancement/reduction of 2G HTS tapes after irradiation are already available [20–22]. In figure 6 the *n*-value results are shown together with corresponding critical currents.

A significant reduction of *n*-values over the whole scale of measured angles, fields and temperatures is observed at the highest fast neutron fluence (1×10^{22} m^{-2}). At the lower irradiation levels, there are some regions with increase and also with reduction of the *n*-values. At 64 K, the position of the J_c peak corresponds to the deep drop of the *n*-value curves which, in literature, is known as inverse correlation to the J_c (figure 6(f)) [3–5]. Despite this drop, the anisotropy of *n*-values at 64 K is rather low. The inverse correlation of the *n*-values by the J_c peak has also been observed at 50 K. The inverse *n*-value and J_c correlation is commonly related to the staircase flux lines in the superconductor [3, 4]. Staircase flux lines are usually created in periodic pinning structures of high densities. Intrinsic pinning could be considered as this pinning structure at certain temperatures. Intrinsic pinning is characteristic by the small activation energy of the pinned flux; however, the high density of these pinning centres makes them very efficient at low temperatures when thermal depinning becomes less important. The change of the *n*-value curve between 77 K and 64 K indicates some transition in the role of intrinsic pinning in this range. This transition could cause a change of parameters in relation (7), or even transition to a different relation. It was noticed in [31] that the relation between J_c and *n*-value can even be linear at certain low

current conditions. Nevertheless, it is important to note that all the presented measurements in this section are performed at high fields where critical currents are controlled by grains only and not the grain boundaries as shown in [22, 29]. This excludes models explaining *n*-values assuming grain boundary controlled currents and nonuniformity from [13, 14]. Even the explanation by the staircase flux lines theory is limited to the low fields, as the flux lines remain mostly straight due to their high numbers in fully penetrated superconductor in higher fields.

After the fast neutron irradiation, randomly distributed efficient pinning centres are introduced into superconducting grains. They are very efficient at wide range orientations of external magnetic fields except orientations where very high density of efficient pinning is present, e.g. close to the *ab* peak. The fast neutron introduced pinning centres can have higher activation energies than original pinning and can enhance *n*-values. This enhancement is observed in figure 6, especially at 77 K (figures 6(b) and (d)). A drop of *n*-values is observed at the fluence of 1×10^{22} m^{-2}. The drop of *n*-values looks like a consequence of very high density pinning centres. All the situations with very high density of efficient pinning centres (high neutron fluences, intrinsic pinning) have always shown smaller *n*-values. There is probably a threshold value of efficient pinning centres concentration after which the *n*-value starts to be reduced with increasing concentration. This threshold value is obviously strongly dependant on field and temperature. High irradiation fluences cause damage of the crystal structure which can be its reason of loss or partial loss of ability of flux pinning. The consequences are reduced J_c values close to the *ab* peak in all the presented measurements (figures 6(a), (c), (e)), especially at the highest fluence. The other consequence is probably partial *n*-value recovery at the *ab* peak at 64 K, 4 T, at the highest neutron fluence, where the flux pinning abilities of the intrinsic pinning centres could be significantly reduced.

None of the mentioned effects are a consequence of nonuniformity in the HTS, which is experimentally proven in the following section of the paragraph. It is well known that neutron irradiation introduces disorder into the YBCO crystals. The commonly observed consequence of this disorder, which is mostly a consequence of already mentioned point defects in the oxygen sublattice, is critical temperature reduction of irradiated samples [15, 33]. However if fast neutron irradiation creates nonuniformity in HTS, particular YBCO grains would have different T_c causing wider transition to the normal state. Therefore, fine T_c measurements after each irradiation step were performed. The result (figure 7) shows no influence of fast neutron irradiation on the broadening the transition. It means that the point defects caused by neutron irradiation are homogenously distributed and no additional nonuniformity is created. The homogenous distribution is possible due to their mobility and also relatively high neutron fluences.

The SuperPower(2008) tape was characterized also in high fields up to 15 T (17 T measurement set-up) in two main magnetic field directions. This measurement should confirm results from previous angle-resolved measurements with additional information of *n*-values in very high fields. Results of these measurements together with measurements after irradiation by fast neutron fluences of 4×10^{21} m^{-2} are shown in figure 8. It is worth noting that at lower temperatures such as 64 K and 50 K, at magnetic fields parallel to the *ab* planes (H ∥ ab represents 90° in figure 6), *n*-values are not reduced with increasing magnetic field (after the initial drop at low fields).

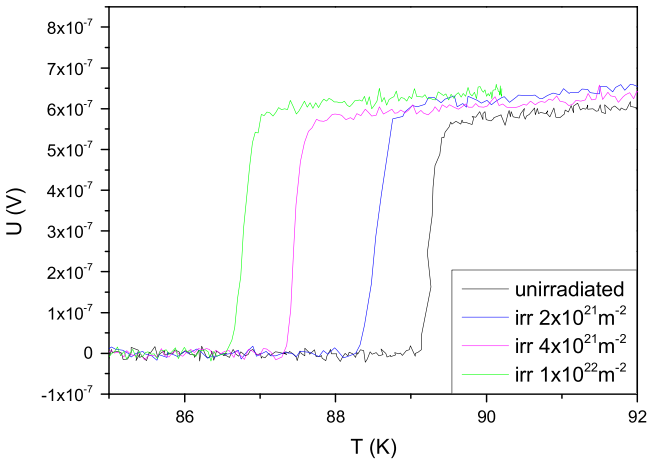

Figure 7. T_c transition transport measurements after each irradiation step performed in 17 T measurement set-up.

5. Summary and conclusions

n-values of different 4 mm and 12 mm wide commercial 2G HTS tapes at various magnetic fields and temperatures were presented. The performance of the HTS tapes characterized in higher fields is still relatively low. In addition, reduction of *n*-values would enforce them to be operated even at lower currents, which makes them not suitable for most of the possible applications where high fields are required.

Higher *n*-values and relatively low anisotropy of *n*-values (compared to J_c) was observed in recent 2G HTS tapes. *n*-values were studied also after fast neutron irradiation, which introduced randomly distributed spherical defects into the superconductor. Two main factors, nonuniformity and flux creep, are considered as a source of the exponential relationship of the *I*–*V* curve. Nonuniformity was excluded as the primary factor at higher temperatures and higher fields, where the currents are limited by grains and not by the grain boundaries. In addition, it was shown that all the *n*-value changes after fast neutron irradiation cannot be a consequence of nonuniformity, as irradiation defects were distributed homogenously. Another studied phenomenon was the correlation between *n*-values and J_c. It was shown that the *n*-value is proportional to pinning energy which usually results into correlation with J_c. However, inverse correlation between *n*-values and J_c was found under circumstances, where high densities of efficient pinning centres are present.

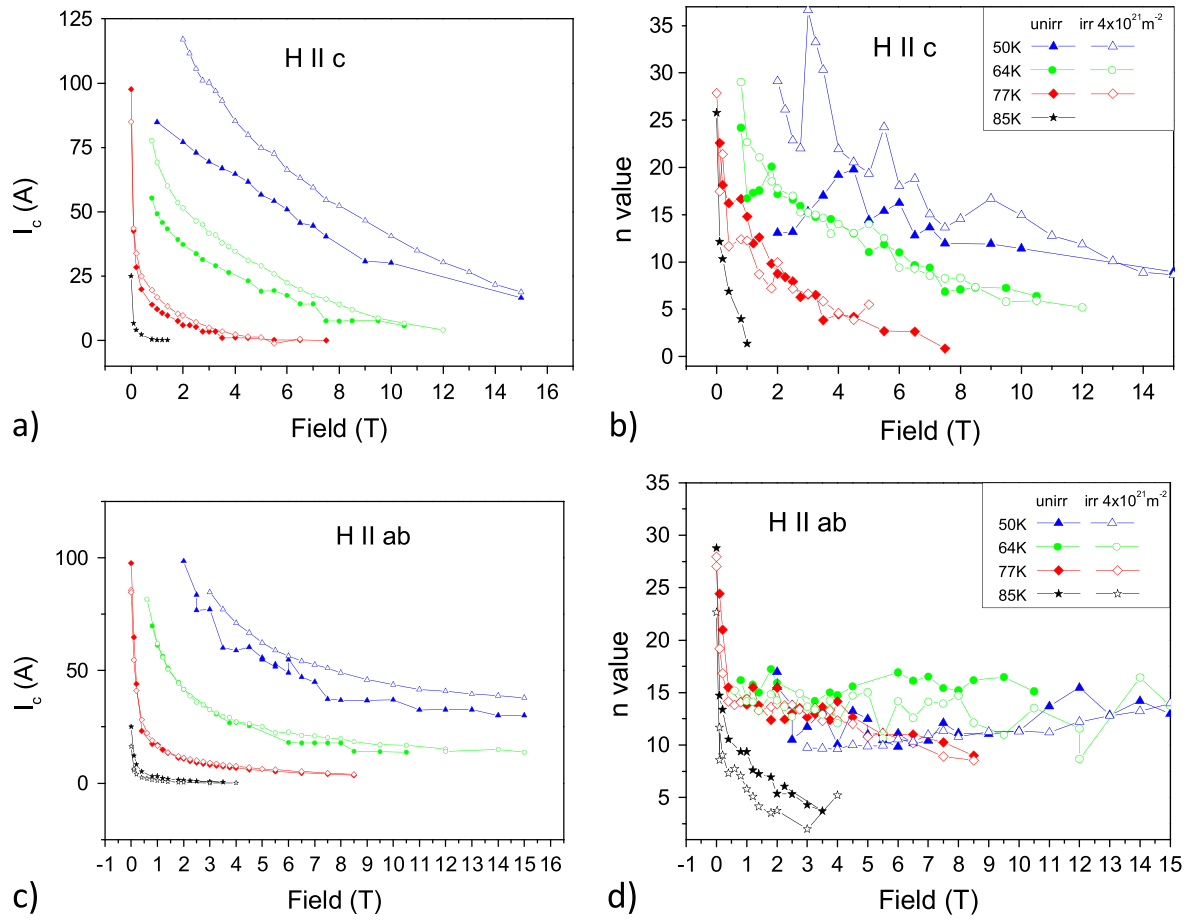

Figure 8. Critical currents and *n*-values at different external magnetic fields, temperatures and irradiation levels, (a), (b) H||ab, (c), (d) H||c.

References

[1] Willis J O, Coulter J Y and Rupich M W 2011 *n*-value analysis of position-dependent property variability in long-length coated conductors *IEEE Trans. Appl. Supercond* **21** 2988–91

[2] Coulter J Y, Holesinger T G, Kennison J A, Willis J O and Rupich M W 2009 Nondestructive investigation of position dependent I_c variations in multi-meter coated conductors *IEEE Trans. Appl. Supercond.* **19** 3609–13

[3] Sueyoshi T, Kotaki T, Fujiyoshi T, Mitsugi F, Ikegami T and Ishikawa N 2013 Angular dependence of critical current density and *n*-values in $BaZrO_3/YBa_2Cu_3O_y$ quasi-multilayered films with columnar defects *Physica* C **494** 153–7

[4] Civale L, Maiorov B, MacManus-Driscoll J L, Wang H, Holesinger T G, Foltyn S R, Serquis A and Arendt P N 2005 Identification of intrinsic *ab*-plane pinning in $YBa_2Cu_3O_7$ thin films and coated conductors *IEEE Trans. Appl. Supercond.* **15** 2808–11

[5] Chudy M, Eisterer M and Weber H W 2010 Asymmetric angular dependence of J_c in coated conductors prior to and after fast neutron irradiation *Physica* C **470** 1300–3

[6] Warnes W H and Larbalestier D C 1986 Analytical technique for deriving the distribution of critical currents in a superconducting wire *Appl. Phys. Lett.* **48** 1403

[7] Plummer C J G and Evetts J E 1987 Dependence of the shape of the resistive transition on composite inhomogeneity in multifilamentary wires *IEEE Trans. Magn.* **23** 1179

[8] Anderson P W 1962 Theory of flux creep in hard superconductors *Phys. Rev. Lett.* **9** 309

[9] Anderson P W and Kim Y B 1964 Hard superconductivity: theory of the motion of abrikosov flux lines *Rev. Mod. Phys.* **36** 39

[10] Yeshurun Y, Malozemoff A P and Shaulov A 1996 Magnetic relaxation in high-temperature superconductors *Rev. Mod. Phys.* **68** 911–49

[11] Sun J Z, Eom C B, Lairson B, Bravman J C and Geballe T H 1991 Magnetic relaxation, current-voltage characteristics, and possible dissipation mechanisms for high-T_c superconducting thin films of Y–Ba–Cu–O *Phys. Rev.* B **43** 3002

[12] Griessen R 1991 Relaxation effects, *I–V* curves and irreversibility lines in high T_c superconductors *Physica* C **175** 315

[13] Adamopoulos N and Evetts J E 1993 A model for the *V–I* characteristics in brick wall-like structures *IEEE Trans. Appl. Supercond.* **3** 1257

[14] Evetts E, Glowacki B A, Sampson P L, Blamire M G, Alford N McN and Harmer M A 1989 Relation of the *n*-value of the resistive transition to microstructure and inhomogeneity for YBCO wires *IEEE Trans. Magn.* **25** 2041–4

[15] Sauerzopf F M, Wiesinger H P, Weber H W and Crabtree G W 1995 Analysis of pinning effects in $YBa_2Cu_3O_{7-\delta}$ single crystals after fast neutron irradiation *Phys. Rev.* B **51** 6002

[16] Okada M and Kawakubo T 1989 *Radiat. Eff. Defects Solids* **108** 137–44

[17] Frischherz M C, Kirk M A, Zhang J P and Weber H W 1993 Transmission electron microscopy of defect cascades in $YBa_2Cu_3O_{7-\delta}$ produced by ion irradiation *Phil. Mag.* A **67** 1347
[18] Frischherz M C, Kirk M A, Farmer J, Greenwood L R and Weber H W 1994 Defect cascades produced by neutron irradiation in $YBa_2Cu_3O_{7-\delta}$ *Physica* C **232** 309–27
[19] Frischherz M C, Kirkl M A, Farmer J and Weber H W 1994 Defect cascades produced by neutron irradiation in in $YBa_2Cu_30_7$ *Superconductors, 7th Int. Workshop on Critical Currents in Superconductors (Alpbach, Tyrol/Austria)*
[20] Chudy M, Fuger R, Eisterer M and Weber H W 2011 Characterization of commercial YBCO coated conductors after neutron irradiation *IEEE Trans. Appl. Supercond.* **21** 3162–5
[21] Fuger R, Eisterer M and Weber H W 2009 YBCO coated conductors for fusion magnets *IEEE Trans. Appl. Supercond.* **19** 1532–5
[22] Eisterer M, Fuger R, Chudy M, Hengstberger F and Weber H W 2010 Neutron irradiation of coated conductors *Supercond. Sci. Technol.* **23** 014009
[23] Ghosh A K 2003 *V–I* transition and *n*-value of multifilamentary LTS and HTS wires and cables *ICMC'03 Topical Conf. (Enschede, The Netherlands, 25–28 May)*
[24] www.superpower-inc.com
[25] www.amsc.com
[26] Weigand M, Speller S C, Hughes G M, Rutter N A, Lozano-Perez S, Grovenor C R M and Durrell J H 2010 Individual grain boundary properties and overall performance of metal-organic deposition coated conductors *Phys. Rev.* B **81** 174537
[27] www.shsctec.com/en/index.asp
[28] Weber H W, Bock H, Unfried E and Greenwood L R 1986 Neutron dosimetry and damage calculations for the triga mark-II reactor in vienna *J. Nucl. Mater.* **137** 236–40
[29] Tonies S, Vostner A and Weber H W 2002 Determination of inter- and intragranular currents in high temperature superconducting tapes and coated conductors *J. Appl. Phys.* **92** 2628
[30] Hong Z, Hong W, Cong-Xin R and Guo-Liang C 1994 The anisotropy of the current-carrying characteristics of YBCO film fabricated by magnetron sputtering *Supercond. Sci. Technol.* **7** 354363
[31] Zedlov E, Amer N M, Krren G, Gupta A, Gambino R J and McElfresh M W 1989 Optical and electrical enhancement of flux creep in $YBa_2Cu_3O_7-\delta$ epitaxial films *Phys. Rev. Lett.* **62** 3093
[32] Pan A V, Golovchanskiy I A and Fedoseev S A 2013 Critical current density: measurements versus reality *Europhys. Lett.* **103** 17006
[33] Chen Z, Kametani F, Chen Y, Xie Y, Selvamanickam V and Larbalestier D C 2009 A high critical current density MOCVD coated conductor with strong vortex pinning centers suitable for very high field use *Supercond. Sci. Technol.* **22** 055013
[34] Chudy M, Eisterer M, Weber H W, Veternikova J, Sojak S and Slugen V 2012 Point defects in $YBa_2Cu_3O_{7x}$ studied using positron annihilation *Supercond. Sci. Technol.* **25** 075017

Full angular critical current characteristics of coated conductors studied using a two-axis high current goniometer

2011 Supercond. Sci. Technol. 24 075018

(http://iopscience.iop.org/0953-2048/24/7/075018)

Supercond. Sci. Technol. **24** (2011) 075018 (5pp) doi:10.1088/0953-2048/24/7/075018

Full angular critical current characteristics of coated conductors studied using a two-axis high current goniometer

M Chudý[1,2], S C Hopkins[1], M Woźniak[1], B A Glowacki[1,3], M Eisterer[2] and H W Weber[2]

[1] Department of Materials Science and Metallurgy, University of Cambridge, Pembroke Street, Cambridge CB2 3QZ, UK
[2] Vienna University of Technology-Atominstitut, Stadionallee 2, 1020 Vienna, Austria
[3] Institute of Power Engineering, ul Augustówka 6, 02-981 Warsaw, Poland

Received 28 January 2011, in final form 7 April 2011
Published 1 June 2011
Online at stacks.iop.org/SUST/24/075018

Abstract
Coated conductors are considered to be the most suitable candidates for applications in various devices. Recently, the critical current anisotropy of (RE)BCO (rare earth barium copper oxide) has become the focus of particular research interest, due to the changes in the angular dependence of the critical current density, $J_c(\varphi)$, resulting from different tape architectures and pinning landscapes. In this work, we present advanced anisotropy studies of coated conductors in low magnetic fields using a two-axis high current goniometer. Two different commercially available coated conductors were characterized and will be discussed: the first is based on an IBAD (ion beam assisted deposition) template with the YBCO (yttrium barium copper oxide) *ab* planes slightly tilted, and the second is highly symmetric with a template grown by the RABiTS (rolling assisted biaxially textured substrate) method. In addition, the requirements to be met by coated conductors for applications will be discussed.

(Some figures in this article are in colour only in the electronic version)

1. Introduction

In recent years, high temperature superconductors have increasingly been considered and selected for applications including as fault current limiters, as transformers and as high field electromagnets, and the competition between superconductor manufacturers has intensified. In most cases, a key requirement is the use of liquid nitrogen as the coolant, which suggests an operating temperature in the range ∼64–78 K. Coated conductors are widely considered to be the most suitable candidates because of the high critical temperature and high values of the B_{c2} of YBCO, but widespread use is deterred by the complicated and expensive manufacturing process and the natural critical current anisotropy of (RE)BCO. Measuring and controlling the anisotropy of YBCO thin films has become an important area of research. Anisotropy reduction or critical current density (J_c) enhancement in certain field directions is achieved by different methods. The addition of correlated pinning centres, such as BZO nanorods in the *c*-axis direction, can cause a broad and high *c*-axis peak [1] and irradiation by heavy ions leads to columnar defects enhancing J_c in a certain field direction [2]. Replacing the Y atoms in the crystal structure by other rare earth elements (e.g. Gd) causes significant changes in the angular dependence of J_c [3], as does irradiation with randomly oriented fast neutrons in a fission reactor [4, 5].

The coated conductors are often vicinal (*ab* planes are not parallel to the sample surface), which leads to an asymmetric $J_c(\varphi)$ dependence. The effects of misaligned *ab* planes and other correlated pinning centres were studied by for instance Chen *et al* [6] and Maiorov *et al* [7]. The *ab* peak in such tapes is not exactly aligned with the tape surface ($\varphi = 90°$) and its position is also not stable at low magnetic fields. All the aforementioned studies dealt with rotation-dependent

measurements under the maximal Lorentz force configuration. However, the differences between symmetric and asymmetric coated conductors can be particularly well studied by means of orientation-dependent measurements using a two-axis high current goniometer.

2. Samples

The samples were state-of-the-art commercially available coated conductors from SuperPower and American Superconductor (AMSC). The SuperPower coated conductor [8] exhibits properties very similar to those presented by Holesinger *et al* [9] and our XRD measurements also confirmed the *ab* planes to be tilted by an angle of $\alpha = -1.9°$ with respect to the sample surface. The tape is fully surrounded by an electroplated copper stabilizer. The substrate is non-magnetic, made of the high strength non-magnetic alloy Hastelloy C-276, which helps to keep hysteresis losses low in AC applications. The MgO buffer layer is made by ion beam assisted deposition (IBAD) and acts as a template for introducing biaxial texture for the superconductor material. The YBCO layer is 1 μm thick and prepared by a special metal–organic chemical vapour deposition technique (MOCVD). A 2 μm thick sputtered silver layer provides good electrical contact. The tape is 0.089 mm thick and 4 mm wide.

The second tape is made of 2G coated conductor from AMSC [10]. This coated conductor, called '344', has a laminar architecture: a three-ply structure 4.4 mm in width consisting of two stabilizing laminae enclosing the superconducting coated conductor (CC). This CC is based on production by the RABiTS route, in which the substrate is textured by rolling and forms the template for the buffer and superconducting layers. The substrate consists of a textured nickel–tungsten alloy (5 at.% W), followed by three epitaxial buffer layers: a thin yttrium oxide (Y_2O_3) layer, a layer of yttrium-stabilized zirconia (YSZ) and a layer of ceria (CeO_2). The Ni–W alloy has a thickness of 75 μm and forms a magnetic substrate for the tape. A 75 nm thick Y_2O_3 seed layer was deposited by electron beam evaporation. Both the 75 nm YSZ barrier and the 75 nm CeO_2 cap layer were subsequently deposited by RF sputtering. All the depositions were done by a continuous reel-to-reel process. The superconducting layer is formed by the decomposition of chemically deposited metal–organic precursors (MOD). The resulting YBCO thickness is 1–1.2 μm and the *ab* planes are parallel to the tape. A 3 μm thick silver cap layer protects the conductor. The tape is fully coated by a 50 μm thick copper strip, which ensures electrical, mechanical and environmental stabilization. Since the total breadth of the tape is 4.4 mm and the superconducting layer is only 4 mm wide, the remaining ~0.2 mm on the edges serves as corrosion protection and electrical stabilization. Both types of CC were cut into ~26 mm long samples and measured without slitting or pre-treatment.

3. The experimental set-up

The two-axis high current goniometer developed at ASCG in Cambridge [11, 12] (see figure 1) is designed for characterization of up to 14 mm wide superconducting tapes (coated conductors) with sample lengths of up to 36 mm. A standard four-point technique is employed for transport critical current measurement. This device is equipped with a sample holder with multiple sprung current contacts and large-diameter current leads, which allow transport currents of up to ~200 A to be applied routinely, which is significantly higher than commonly used goniometers can achieve [13, 14]. High currents in this range are needed for characterizing full-width commercial tapes without etching or other destructive sample preparation. The current contacts are soldered with indium at temperatures below 250 °C to minimize any degradation of the superconducting layer of the coated conductor. The sample holder is equipped with two perpendicular Hall probes, allowing the direction of the magnetic field to be verified for every sample orientation. The orientation is controlled using stepper motors, geared to achieve a step size of ~0.005° and delivering a positional accuracy of ~0.1°, with a position of zero repeatability of ~0.5°. As shown in figure 1(a), the sample holder can be rotated around its vertical axis (rotation, φ), and the platform on which the sample is mounted can be tilted around the line of centres of the magnet pole pieces (tilt, θ). For the work reported here, a full 360° scan range was available for rotation, and 110° in tilt. All the measurements were made in liquid nitrogen with a maximum external magnetic field of 0.5 T generated by a water-cooled electromagnet. The simple cryostat for liquid nitrogen used here can readily be replaced with a helium flow cryostat, if required.

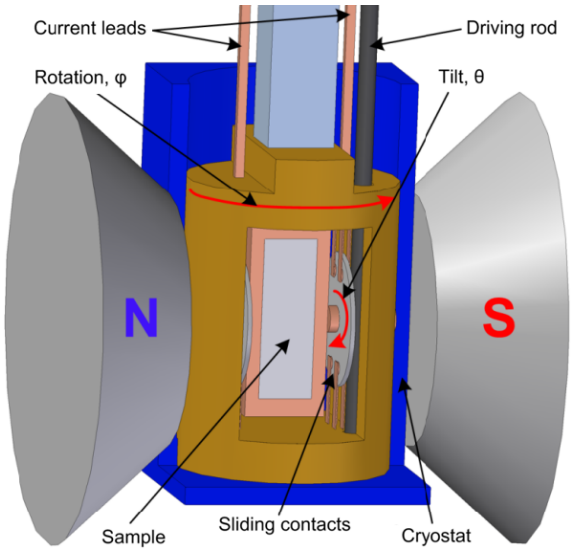

Figure 1. Experimental set-up of a two-axis high current goniometer developed at ASCG in Cambridge.

Custom-written software was used to control the sample orientation, perform the critical current measurements and analyse the results. Before each scan, the zero position was determined for both axes using the local extrema of the Hall sensor voltages, and the range and interval of rotation and tilt angles to be scanned were defined. For each orientation, the current was ramped at a rate of 1–5 A s^{-1} over the

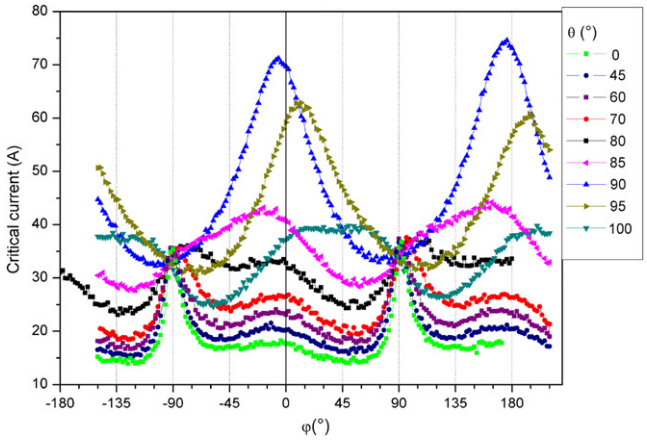

Figure 2. Two-axis orientation-dependent critical current measurements on SuperPower CC at a magnetic flux density of 500 mT.

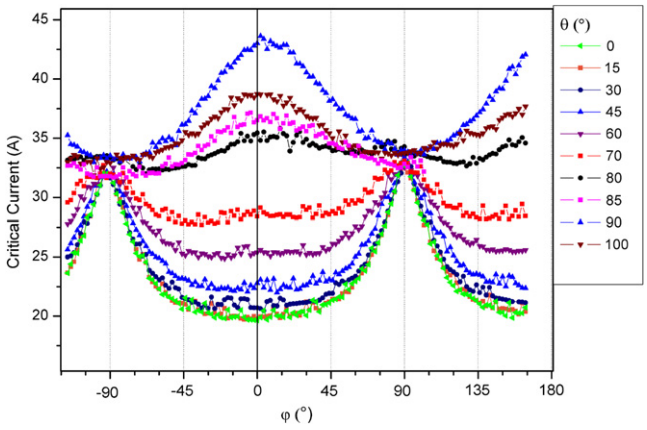

Figure 3. Two-axis orientation-dependent critical current measurements on AMSC CC at a magnetic flux density of 500 mT.

chosen range, with the ramp being automatically terminated at a sample voltage threshold. A power law function was automatically fitted to each voltage–current characteristic, and the critical current and n value calculated for the specified voltage criterion, chosen in this case to correspond to a 1 μV cm^{-1} electric field criterion. The transport measurements were performed in the full range of $0° \leqslant \varphi \leqslant 360°$ and $-10° \leqslant \theta \leqslant 100°$, mainly at a magnetic field of 500 mT. The step size for the φ scan was set to 2°. However, a fine 0.5°φ step size was used in additional measurements focused on small particular areas (around peaks). The tilt angle θ was stepped to the selected angles, and then the φ scan was performed.

4. Results and discussion

The resulting dependence of the critical current on the rotation angle φ, $I_c(\varphi)$, is plotted in figures 2 and 3 with a φ resolution of 2° for both CCs at a selection of θ (tilt) angles.

In the case of the symmetric AMSC tape (figure 3) all curves have a common crossover at $\varphi = 90°$, where the ab peak is located. In the case of the vicinal tape (SuperPower) the ab peak is shifted towards the c-axis peak at higher tilt angles. It is possible to determine the shift of the ab peak in a vicinal tape from elementary geometric relations. The parameterization of the system is shown in figure 4.

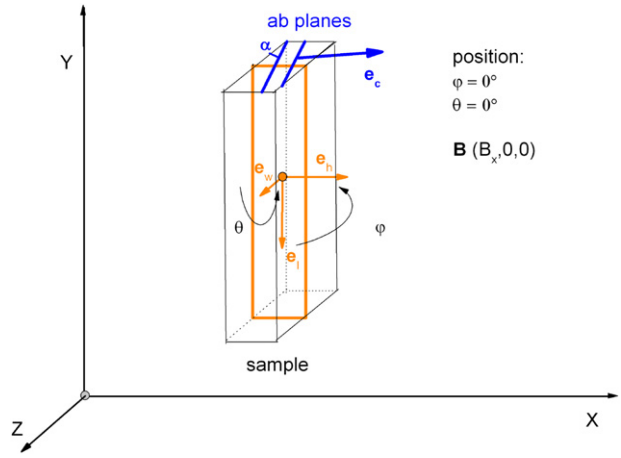

Figure 4. Sketch of a sample with tilted ab planes rotated in the magnetic flux of density B.

The sample surface normal vectors are

$$\mathbf{e_l} = \begin{pmatrix} \sin\theta\cos\varphi \\ -\cos\theta \\ -\sin\theta\sin\varphi \end{pmatrix}, \qquad \mathbf{e_h} = \begin{pmatrix} \cos\theta\cos\varphi \\ \sin\theta \\ -\cos\theta\sin\varphi \end{pmatrix},$$

$$\mathbf{e_w} = \begin{pmatrix} \sin\varphi \\ 0 \\ \cos\varphi \end{pmatrix}.$$

The vector $\mathbf{e_c}$ represents the c-axis of the YBCO layer ($\mathbf{e_c} \perp ab$ planes). It can be derived from $\mathbf{e_h}$ and $\mathbf{e_w}$ and from the misalignment angle α:

$$\mathbf{e_c} = \mathbf{e_h}\cos\alpha - \mathbf{e_w}\sin\alpha.$$

The ab peak is located at the angle φ, where the ab planes are parallel to B:

$$\begin{gathered} \mathbf{e_c}\vec{\mathbf{B}} = 0 \\ \cos\theta\cos\varphi\cos\alpha - \sin\varphi\sin\alpha = 0 \\ \varphi = \arctan\left(\cos\theta\frac{\cos\alpha}{\sin\alpha}\right). \end{gathered} \tag{1}$$

Figure 5 shows the function (equation (1)) for the tilt angle $\alpha = -1.9°$ determined by XRD and two other values for comparison, together with the ab peak positions presented in figure 2.

The correlation between calculated and measured ab peak positions is evident, although other effects, such as correlated pinning, may also play a role in the ab peak shift [15]. These effects are probably responsible for the peak deviation at $\theta = 85°$, where the peak maximum is unclear and placed at too low an angular position (figure 2). Moreover, the measurements were performed only with a φ resolution of 2°, which is too rough for distinguishing small shifts. Only negligible differences are observed at lower tilt angles. According to

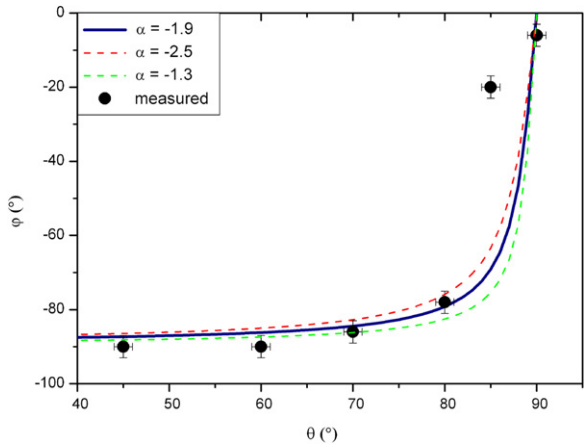

Figure 5. Calculated φ position of the ab peak as a function of the angle θ for three values of the angle α ($-1.9°$, as determined using XRD; $-2.5°$ and $-1.3°$), compared with experimental data.

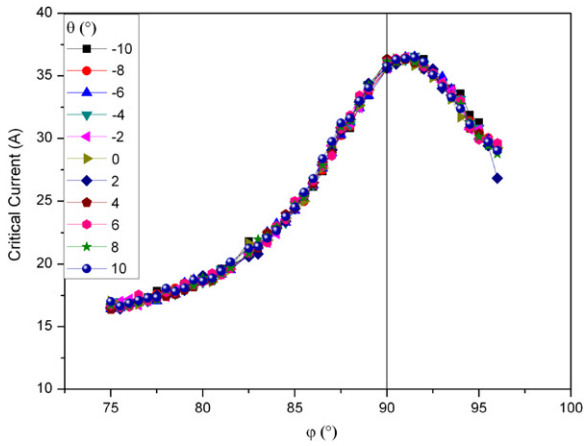

Figure 6. High resolution rotation dependence of the critical currents in the region of the ab peak for a range of tilt angles (SuperPower, $B = 500$ mT).

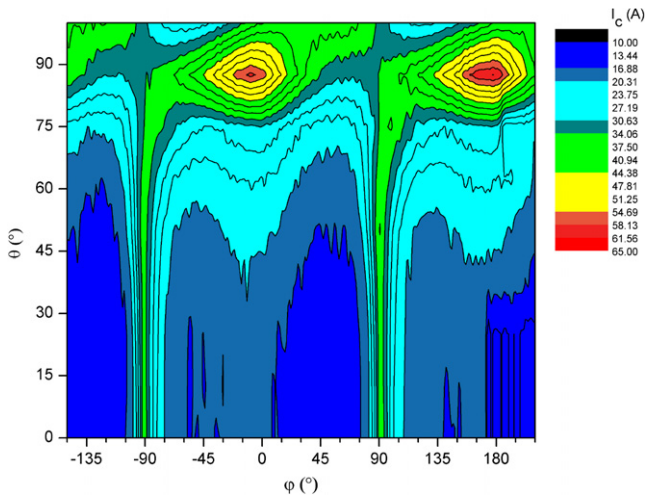

Figure 7. Contour diagram showing the critical current as a function of the tilt and rotation angles (SuperPower, $B = 500$ mT).

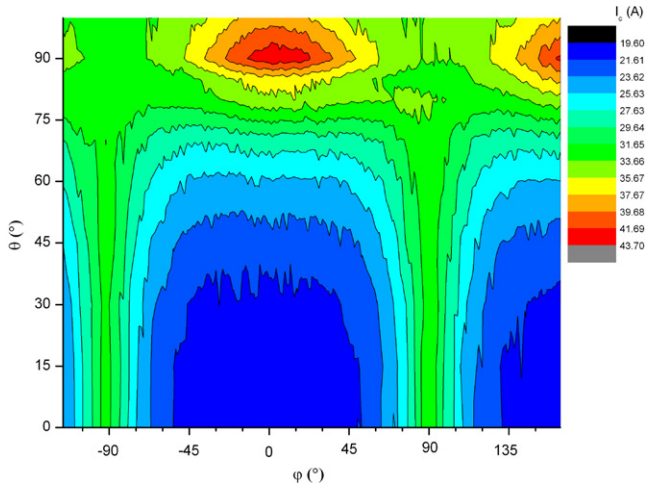

Figure 8. Contour diagram showing the critical current as a function of the tilt and rotation angles (AMSC, $B = 500$ mT).

equation (1), no measurable changes are expected close to the maximal Lorentz force configuration. Therefore, very fine scans with a φ angular step size of 0.5° and with a θ angular step size of 2° were performed. The measured tilt range was $-10° \leqslant \theta \leqslant 10°$ and no changes in $I_c(\varphi)$ were found (figure 6). This figure also presents the misalignment of the ab peak from the 90° axis which corresponds to the misalignment angle α.

It is important to note that the curves at 80° and 100° are not identical (figure 3), which would have been expected in the case of a symmetric tape. The effect of surface pinning [16] can be excluded as an explanation, since the two ab peaks measured at low tilt (θ) angles reach approximately identical I_c values. This difference is most probably caused by a small misalignment between the sample normal and the Hall probe, which would imply that the tilt (θ) angles presented in these experiments, i.e. as the samples were mounted, correspond to 'true' angles that are lower by ~2°.

In the following figures (figures 7 and 8), two-dimensional contour diagrams representing areas with identical critical currents (isocurrents) are presented. Again, a very high symmetry is found in the AMSC CC tape, whilst the diagram for the SuperPower tape is rather asymmetric.

The application relevance of the anisotropy measurements on 2G HTS tapes is demonstrated by the results presented here. The dependence of the critical current, I_c, on the direction of the external magnetic flux density, B_{ext}, should be known at the stage of design of superconducting devices in order to fully maximize the performance and reduce cost. The majority of applications operate (by necessity) in an orientation close to $\theta = 0°$ and $\varphi = 90°$; but the range of local field magnitudes and orientations depends on the device design. The maximum operating current is limited by the point of lowest critical current in operating conditions. As a result, the dependence of the critical current on both orientation and field should be measured for the application's range of interest when selecting the conductor or optimizing the design.

In high field insert coils, the magnetic field may be locally up to 10 degrees off the wide face of the tape ($H \parallel ab$)

in rotation (φ): for most YBCO CCs, including both ones reported on here, this causes a significant reduction in the critical current from a local maximum (e.g. see figure 6). An awareness of the exact behaviour of the tape is especially important when the tape is vicinal and the I_c (φ) dependence is asymmetric, as for the SuperPower sample here. Figure 6 also shows that the sensitivity of the critical current to the tilt angle (θ) is very low in the region of interest. 2G HTS tapes, thanks to their high resistivity in the normal state, also have very attractive fault current limiting properties. In this application, where the tape is used as an active component of a resistive SFCL device, there are several possible HTS tape configurations, including a bifilar winding to reduce self-inductance. In such a winding, the magnetic field can be very low and without a single orientation, but a detailed knowledge of the $I_c(\varphi)$ dependence can still help in optimizing the winding design. The dependence of the critical current on both θ and φ is also expected to have an influence on the performance in many cable configurations, for example Roebel cables and two-layer counter-wound power transmission cables, in which complex current flow and self-field geometries arise. The growing trend towards reducing the J_c anisotropy through, for example, Gd substitution, pinning centres and microstructural control highlights the need for a careful measurement of the field orientation dependence for rotations around all axes.

5. Conclusion

A two-axis goniometer was successfully tested and the characterization of two commercially available types of CC completed. The differences between vicinal and well-aligned coated conductors were studied at a magnetic flux density of 500 mT in liquid nitrogen (~77 K). The results explore the differences in J_c symmetry of the tapes. In contrast to the well-aligned AMSC CC, which shows a high symmetry of the $I_c(\varphi)$ curves and a precise alignment of the ab peaks at 90°, the vicinal CC from SuperPower is rather asymmetric. The ab peak of the SuperPower CC is shifted from the nominal 90° position as a function of the tilt angle θ and reasonably good agreement is found between the observed angular shift and the theoretical values calculated assuming a $-1.9°$ ab plane misalignment as determined by using XRD.

The strong differences between these two commercial coated conductors found by two-axis characterization indicate the importance of measurements with two-axis goniometers.

Acknowledgment

This work was supported by NESPA (Nano-Engineered Superconductors for Power Applications).

References

[1] Maiorov B, Baily S A, Zhou H, Ugurlu O, Kennison J A, Dowden P C, Holesinger T G, Foltyn S R and Civale L 2009 *Nat. Mater.* **8** 398–404
[2] Budhani R C, Zhu Y and Suenaga M 1992 *Phys. Rev. Lett.* **69** 3816–9
[3] Selvamanickam V *et al* 2010 *Supercond. Sci. Technol.* **23** 014014
[4] Eisterer M, Fuger R, Chudy M, Hengstberger F and Weber H W 2010 *Supercond. Sci. Technol.* **23** 014009
[5] Chudy M, Eisterer M and Weber H W 2010 *Physica* C **470** 1300–3
[6] Chen Y, Selvamanickam V, Zhang Y, Zuev Y, Cantoni C, Specht E, Paranthaman M P, Aytug T, Goyal A and Lee D 2009 *Appl. Phys. Lett.* **94** 062513
[7] Maiorov B, Gibbons B J, Kreiskott S, Matias V, Holesinger T G and Civale L 2005 *Appl. Phys. Lett.* **86** 13204
[8] Selvamanickam V *et al* 2007 *IEEE Trans. Appl. Supercond.* **17** 3231–4
[9] Holesinger T G, Maiorov B, Ugurlu O, Civale L, Chen Y, Xiong X, Xie Y and Selvamanickam V 2009 *Supercond. Sci. Technol.* **22** 045025
[10] Rupich M W *et al* 2003 *IEEE Trans. Appl. Supercond.* **13** 2458–61
[11] Janowski T, Glowacki B A, Wojtasiewicz G, Kozak S, Kozak J, Kondratowicz-Kucewicz B, Majka M and Woźniak M 2011 *IEEE Trans. Appl. Supercond.* at press
[12] http://www.msm.cam.ac.uk/ascg/lectures/fundamentals/ppms.php
[13] Herzog R and Evetts J E 1994 *Rev. Sci. Instrum.* **65** 3574–6
[14] Withnell T D, Schöppl K R, Durrell J H and Weber H W 2009 *IEEE Trans. Appl. Supercond.* **19** 2925–8
[15] Chen Z, Kametani F, Chen Y, Xie Y, Selvamanickam V and Larbalestier D C 2009 *Supercond. Sci. Technol.* **22** 055013
[16] Harrington S A, MacManus-Driscoll J L and Durrell J H 2009 *Appl. Phys. Lett.* **95** 022518

AIP | Journal of Applied Physics

Study of second generation, high-temperature superconducting coils: Determination of critical current

Min Zhang, Jae-Ho Kim, Sastry Pamidi, Michal Chudy, Weijia Yuan et al.

Citation: J. Appl. Phys. **111**, 083902 (2012); doi: 10.1063/1.3698317
View online: http://dx.doi.org/10.1063/1.3698317
View Table of Contents: http://jap.aip.org/resource/1/JAPIAU/v111/i8
Published by the American Institute of Physics.

Study of second generation, high-temperature superconducting coils: Determination of critical current

Min Zhang,[1,a)] Jae-Ho Kim,[2] Sastry Pamidi,[2] Michal Chudy,[1] Weijia Yuan,[1] and T. A. Coombs[1]
[1]*Department of Engineering, University of Cambridge, 9 JJ Thomson Avenue, Cambridge, CB3 0FA, United Kingdom*
[2]*Center for Advanced Power Systems, Florida State University, Tallahassee, Florida 32310, USA*

(Received 7 January 2012; accepted 23 February 2012; published online 16 April 2012)

This paper presents the modeling of second generation (2 G) high-temperature superconducting (HTS) pancake coils using finite element method. The axial symmetric model can be used to calculate current and magnetic field distribution inside the coil. The anisotropic characteristics of 2 G tapes are included in the model by direct interpolation. The model is validated by comparing to experimental results. We use the model to study critical currents of 2 G coils and find that 100 μV/m is too high a criterion to determine long-term operating current of the coils, because the innermost turns of a coil will, due to the effect of local magnetic field, reach their critical current much earlier than outer turns. Our modeling shows that an average voltage criterion of 20 μV/m over the coil corresponds to the point at which the innermost turns' electric field exceeds 100 μV/m. So 20 μV/m is suggested to be the critical current criterion of the HTS coil. The influence of background field on the coil critical current is also studied in the paper. © *2012 American Institute of Physics*. [http://dx.doi.org/10.1063/1.3698317]

I. INTRODUCTION

Second-generation (2 G), high temperature superconducting (HTS) coils have drawn a lot of attention in recent years, owing to the highly developed fabrication technology of 2 G, HTS, coated conductors. The potential operation at relatively high temperature makes them good candidates for power applications. Early experiments date back to 2006, when Polak *et al*. measured the field distribution and ac losses of a small YBCO pancake coil.[1] They came to the conclusion that the anisotropy characteristic of 2 G tapes makes the determination of field and current distribution in the coils less straightforward, as also reported by other authors in the case of first generation (1 G), HTS coils.[2,3]

Theoretically, to circumvent the challenge of tape anisotropy and to understand the coil properties, the critical state model solved by the finite element method is prevailing. Claassen proposes a method to quickly estimate the ac losses in the coil, assuming that the turns in the middle have constant critical current density, while the turns in the outer layer have decreasing critical current density toward the edge of the coil.[4] This work is followed by the assumption of Clem, Claassen, and Mawatari.[5] They assume that there are two regions in the coil known as critical region and subcritical region, the boundary of which can be depicted as a function of the height of the coil.[5] Yuan takes a further step by using a parabolic function to predict the boundary between the critical and subcritical region and calculates the current distribution by minimizing the magnetic field in the subcritical region.[6] Recently, Prigozhin proposed an efficient numerical scheme to simplify ac loss estimates for densely packed stacks of tapes in the infinitely thin approximation.[7] Souc and Pardo introduce the minimum magnetic energy variation method to model the pancakes' coils.[8,9] COMSOL[10] is popular to couple the smooth EJ power law to solve the current and field distribution, where E is electric field and J is current density.[11,12] Grilli compares the measured ac losses of stacks of YBCO-coated conductors with the results from H formulation,[13] Nguyen uses H formulation to study the ac loss of YBCO tape exposed to different background ac magnetic fields,[14,15] Gomory compares the ac losses of coated conductors with non-magnetic or magnetic substrate,[16] and Ainslie models stacks of infinitely long YBCO-coated conductors[17] and calculates the ferromagnetic substrate loss in a infinitely long stack of 2 G tapes.[18]

By far, most of the research focuses on model simplification and ac losses estimation. Normally, the DC current, which drives the terminal voltage to 100 μV/m, is chosen to define the critical current of the coil,[8,19] but the physical meaning underlying it is not clear. From the application point of view, to understand how the characteristics of 2 G tapes affect the critical currents of coils and how much current could a long-term operating coil carry are crucial. So in this paper, we study the critical current of 2 G, HTS coils and share our experience in coil modeling using finite element method. We have developed an axial symmetrical model of pancake coils to demonstrate our idea.

The objective of this paper is to study the critical current of HTS coils. The paper is organized as follows: In Sec. II, we describe the model in detail. In Sec. III, we validate the model by comparing the results of model and experiment. We also study the distribution of current and field inside the coil. In Sec. IV, we propose a method to estimate the critical current of the pancake coils. In Sec. V, we study the influence of background field on the coil critical current.

a)Electronic mail: mz279@cam.ac.uk.

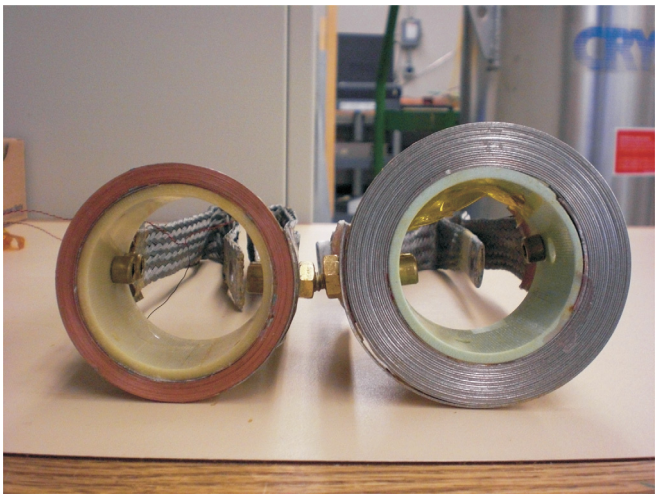

FIG. 1. Photos of pancake coils: coil S on the left hand side and coil A on the right hand side. They have identical inner diameter and turns.

II. THE EXPERIMENT

We made two pancake coils, called coil S and coil A, respectively, shown in Fig. 1. Coil S is made from 2 G tape S, which is manufactured by Superpower;[20] while coil A is made from 2 G tape A, which is manufactured by American Superconductor.[21] The pancake coils have 40 turns and an inner diameter of 59 mm. The detailed information is listed in Table I.

We measured the field dependency of critical currents for the tapes at 77 K, as shown in Fig. 2(a). Tape S is affected more by the external field comparing to tape A. Figure 2(b) shows the I-V curve measurements for the coils. According to the 100 μV/m criterion, coil S has 38 A critical current and coil A has 78 A critical current. The result can be roughly expected from the field dependency of critical currents from Fig. 2(a). The critical current of tape A is affected less by the magnetic field, so the critical current of coil A is higher.

III. THE FINITE ELEMENT MODEL

The YBCO pancake coil model is implemented in the finite element software COMSOL Multiphysics 4.2 a.[10]

A. Axial, symmetrical H formulation

2D axial symmetrical H formulation is applied to the model. The model contains two variables, defined as $H = [H_r, H_z]$. In 2D geometry, the induced or input current J_ϕ in the superconductor flows in the ϕ direction (shown in Fig. 3); so does the electric field $E_\theta = \rho J_\phi$, where ρ is the resistivity of the material.

TABLE I. Pancake coils.

	Coil S	Coil A
Tape type	Tape S	Tape A
Tape width	4 mm	4.35 mm
Tape thickness (insulation included)	0.15 mm	0.235 mm
Tape I_c	102 A	107 A
Total length	7.49 m	8.52 m

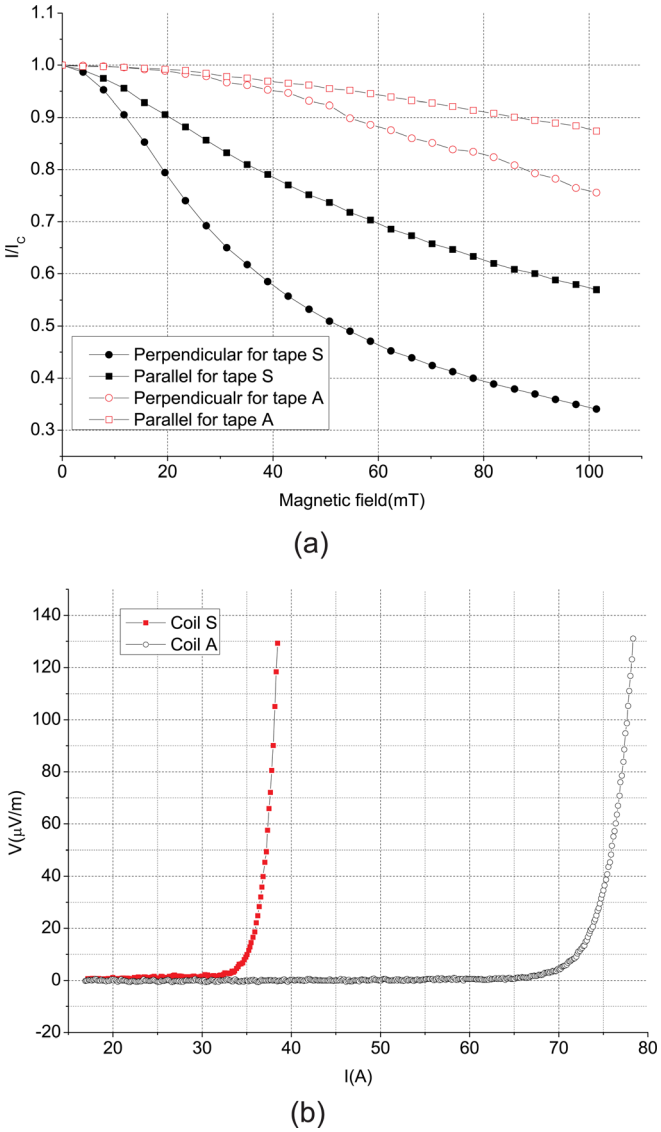

FIG. 2. Experimental data of coil S and coil A: (a) field dependency of normalized critical currents for tape S and tape A (perpendicular means that the field direction is normal to the tape surface; parallel means that the field direction is parallel to the tape surface). Reader should be reminded to use sufficient field range data to get accurate modeling results. Here, due to confidentiality, we only plot field range from 0 mT to 100 mT; (b) I-V curve measurements for coil S and coil A.

Ampere's law is written as

$$J_\phi = \frac{\partial H_z}{\partial r} - \frac{\partial H_r}{\partial z}. \tag{1}$$

Substitute $H = [H_r, H_z]^T$ and $E = E_\phi$ into Faraday's law for cylindrical coordinate

$$\begin{bmatrix} -\dfrac{\partial E_\phi}{\partial z} \\ \dfrac{1}{r}\dfrac{\partial (rE_\phi)}{\partial r} \end{bmatrix} = -\mu_0 \mu_r \begin{bmatrix} \dfrac{\partial H_r}{\partial t} \\ \dfrac{\partial H_z}{\partial t} \end{bmatrix}. \tag{2}$$

Combining the equations above, we can solve Eq. (3) by finite element software,

$$\mu_0 \mu_r \frac{\partial H}{\partial t} + \nabla \times (\rho \nabla \times H) = 0. \tag{3}$$

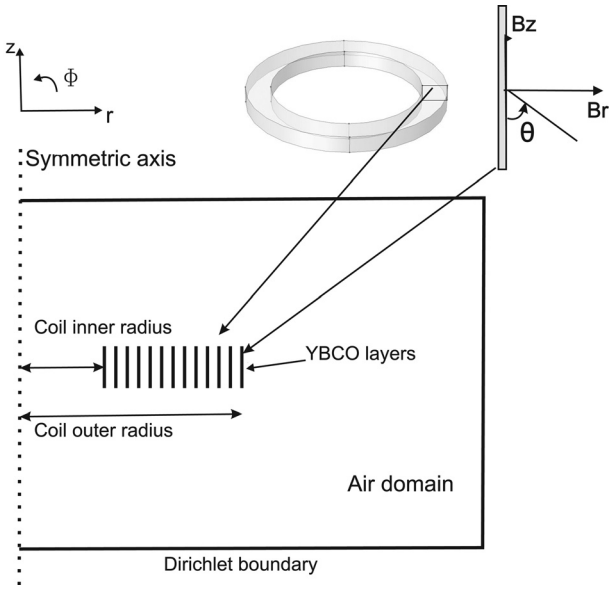

FIG. 3. Geometry of the axial symmetric model (r, Z, ϕ) showing the cross section of a pancake coil. θ defines the angle between the tape surface and local magnetic field.

We have to define resistivity for different materials in the model. For air, we use $\rho = 1000\ \Omega$m; for YBCO, we use the E-J power law:[22] $\rho = E_0/J_c(B) \times (J_\phi/J_c(B))^n$, where $n = 30$, $E_0 = 100\ \mu$V/m, and $J_c(B)$ is the field-dependent critical current of the 2 G tape.

B. Model setting

The coil geometry is shown in Fig. 3, assuming the air domain is so large that the magnetic field produced by applied current decays to zero on the boundary. So the Dirichlet boundary condition of the air domain is written as $H_r = 0$, $H_z = 0$. Only the 1-μm YBCO layer is modeled, with the distance between adjacent YBCO layers the tape thickness shown in Table I. Each YBCO layer represents one turn of the pancake coil; the innermost turn is turn 1, while the outmost turn is turn 40.

Applied current is assigned to each YBCO layer using Pointwise constraint of COMSOL. The integration of local J_ϕ in each YBCO layer gives the total current of one turn. The Pointwise constraint equals the total current to the predefined applied current.

Distributed mapped mesh is applied to the YBCO domains to control the total mesh size, and the free triangular mesh is applied to the air domain. Extra care must be taken to make sure that all YBCO domains have identical mapped meshes, because misaligned mesh elements in the nearby YBCO domain might lead to calculation error of the field angle, especially when the meshes along the z direction are coarse. Linear curl shape function is used in the model, and the other settings of COMSOL can be found in Ref. 29.

C. Anisotropy of 2 G tapes

Anisotropy of the YBCO tape under an external magnetic field would greatly influence the current and magnetic field distribution inside the coil.[1,9] Using constant, J_c, assumption or even Kim's model leads to results deviating from experiment.[2] So the $J_c(B)$ relationship must be treated with extra care in the modeling. Rostila *et al.*[25] introduce an ellipse fitting for the $J_c(B_\parallel, B_\perp)$ by taking into account the self-field at low magnetic fields. The ellipse fitting is also used in Refs. 26–28. Pardo *et al.* propose a good fitting for ReBCO tapes, with ten variables to determine.[24]

In this paper, we propose a simple method to consider anisotropy of YBCO tapes in FEM software. The method avoids the complicated optimization process of variables determination and uses experimental data directly. All the data we use are based on the measurement of tape S and tape A at 77 K.

As shown in Fig. 2(a), the critical currents of the tapes vary with both the magnitude of magnetic field and the angle of the magnetic field. For the θ defined in Fig. 3, $\theta = 90°$ stands for perpendicular field in Fig. 2, while $\theta = 180°$ stands for the parallel field. The angle dependency of critical currents of tape S and tape A under 100 mT is measured and the measurement is normalized so that $\theta = 180°$ corresponds to the value of 1 and $\theta = 90°$ corresponds to the value of 0. The results are illustrated in Fig. 4.

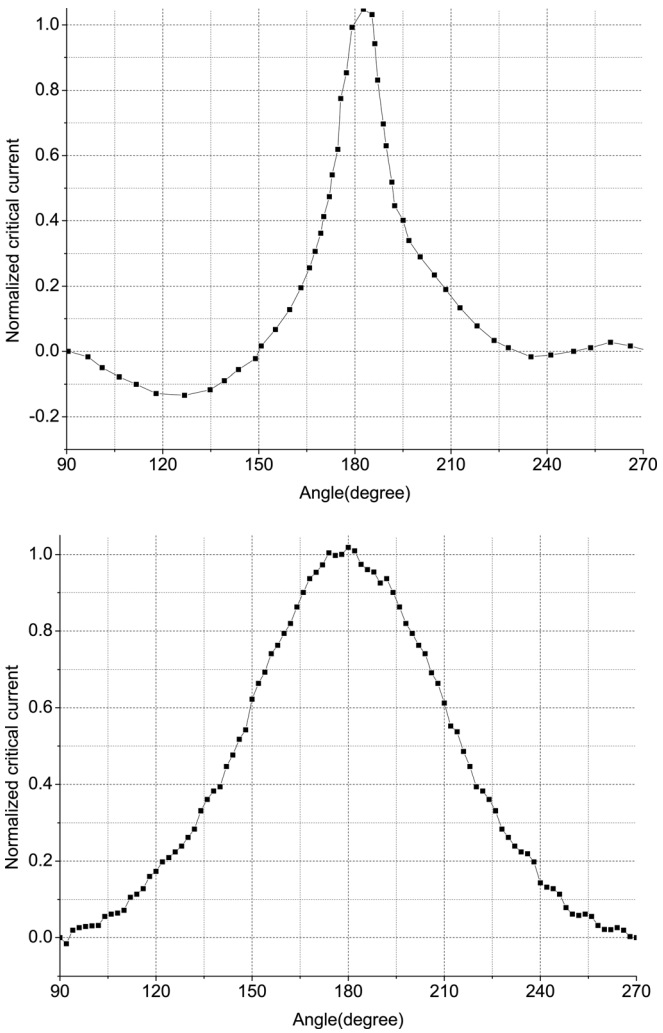

FIG. 4. Normalized experimental data of the tapes' critical currents under different field angles, which is also the definition of function $G(\theta)$ in Eq. (4): (a) data for tape S (Ref. 23); b) data for tape A.

TABLE II. Functions in Eq. (4).

	Definition
J_{c0}	Self-field critical current density calculated from Table I
P1(B)	Perpendicular field dependency: Circular curves in Fig. 2
P2(B)	Parallel field dependency: Square curves in Fig. 2
G(θ)	Normalized angle dependency for 100 mT: Curves in Fig. 4

The expression used in the model is written in Eq. (4), with the explanation of the functions listed in Table II.

$$J_c(B) = J_{c0} \times \{P1(B) + [P2(B) - P1(B)] \times G(\theta)\}. \quad (4)$$

When $\theta = 0°$, we have $G(\theta) = 0$, so $J_c(B) = J_{c0} \times P1(B)$ gives us the curve with circular symbols in Fig. 2; when $\theta = 180°$, we have $G(\theta) = 1$, so $J_c(B) = J_{c0} \times P2(B)$ gives us the curve with square symbols in Fig. 2. For the other θ value, the angle dependency of $J_c(B)$ is modulated by $G(\theta)$ and the magnitude dependency is modulated by $P1(B)$ and $P2(B)$. Figure 5 shows the results of Eq. (4) for tape S and tape A.

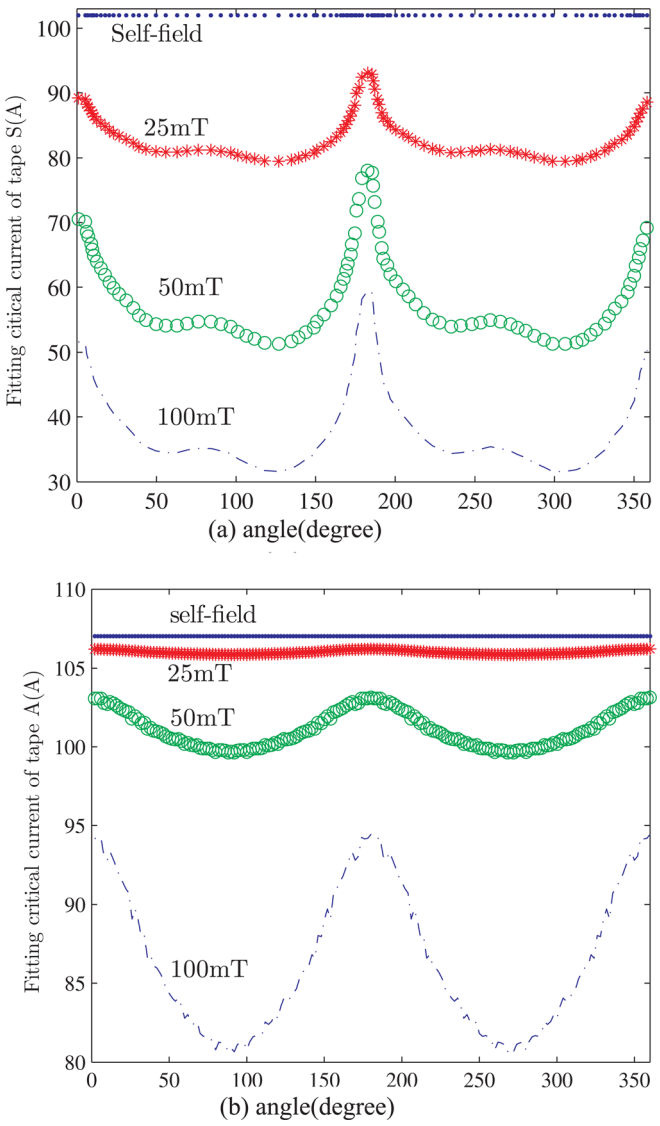

FIG. 5. Calculated tape critical current based on Eq. (4): (a) critical current of tape S vs field angle for self-field, 25 mT, 50 mT, and 100 mT; (b) critical current of tape A vs field angle for self-field, 25 mT, 50 mT, and 100 mT.

We employ the interpolation function of COMSOL to define functions of P1(B), P2(B), and $G(\theta)$ using the measurements in Fig. 2(a) and Fig. 4. Local magnetic field B is calculated by $B = \mu_0\sqrt{H_r^2 + H_z^2}$. This method enables accurate and convenient estimation of the critical currents of 2 G tapes. The parameters required are only critical currents under perpendicular and parallel field and normalized angle dependency of critical currents.

IV. VALIDATION OF THE FEM COIL

We compare the FEM results with experimental measurements to validate the model. The term "instant critical current" in this section stands for the critical current of each turn for each time step. The instant critical current of each turn is determined by the local field distribution (Eq. (4)) and it is changing instantaneously with the applied current. Readers must distinguish instant critical current from the intrinsic critical current of the tapes shown in Fig. 2, which is the characteristic of the material itself. Numerically, the instant critical current of each turn is given by surface integration of local $J_c(B)$ inside each turn.

To draw the I-V curve from the model, we need to calculate coil voltage from the integration of local electric field. Equation (5) shows how we do this,

$$Coilvoltage = \frac{\sum_{n=1}^{N} 2\pi r(\int_s E_\phi ds)}{s} V, \quad (5)$$

where N is the total turns, r is the radius of turn n, s is the cross sectional area of turn n. Dividing coil voltage by the total tape length of the coil both for experimental data and modeling data, we get the coil voltage in units of V/m.

For each calculated current I, we ramp up the applied current to I in 0.1 s and keep it constant for 1 s, and then calculate coil voltage by Eq. (5). Figure 6 compares the model results to the experimental measurement of coil S.

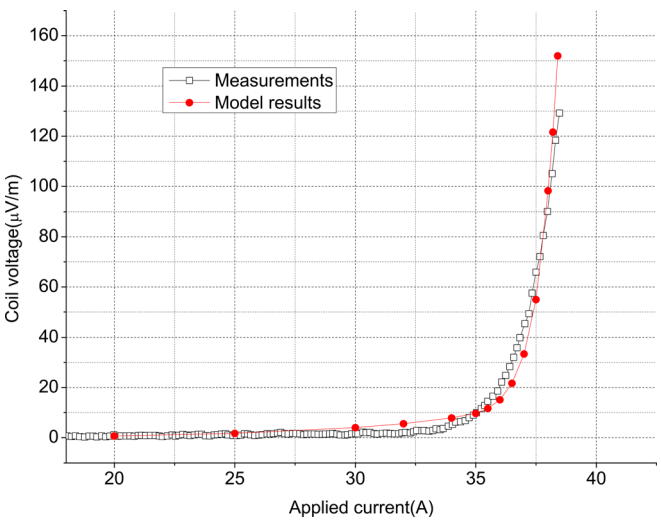

FIG. 6. Comparison of experimental and modeling I-V curve for coil S.

The modeling data are broadly consistent with experimental measurements, except that the modeling I-V curve is a little steeper than measurements. The discrepancy might come from the n value we choose or experimental error. Similar results are found in the model of coil A. So we conclude that the model simulates the pancake coil very well.

To understand what is happening inside the thin tapes, we take coil A as an example. We define such an applied current that it is ramped up from 0 to 100 A and ramped down from 100 A to 0 with the same rate of ramping. We plot the current distribution of the coil by zooming the x scale by a factor of 100 while keeping the y scale. Figure 7 shows the current distribution of coil A for four different time steps: ramping up to 20 A, ramping up to 74 A, ramping down to 74 A, and ramping down to 0.

Consistent with the assumption of Clem,[5] there are critical regions and subcritical regions in the coil. Critical current flows all over the critical region, while a smaller current follows in the subcritical region. The critical region penetrates from the bottom and top edges of the coils. When the applied current is large enough to penetrate most of the regions of the coil, the penetration depth varies largely with turns. The critical region penetrates deeper in the inner turns of the coil compared to outer turns. Currents in ϕ and $-\phi$ directions are existing simultaneously in the subcritical region. Moreover, there is a virgin region inside the subcritical region with no current flowing at all.

We plot the magnetic field and flux line of the same time steps in Fig. 8. We find that only B_z exists in the subcritical region (flux lines are parallel to the tape width), while virgin regions see no magnetic field at all. So the currents in the subcritical region are actually magnetization currents which shield the magnetic field B_z. We learn from Fig. 8(b) that the inner turns see relatively higher magnetic field and more perpendicular field compared to middle and outer turns. Equation (4) shows that higher magnetic field results in lower instant critical current, as does higher perpendicular field. So it is reasonable to suggest that the inner turns, especially the innermost turn, have lower instant critical current compared to the rest of the turns.

The net current in Fig. 8(d) is zero, so the flux line pattern is different from other time steps. Figures 8(b) and 8(c) have the same net current, but different current and magnetic distributions can be found due to the hysteresis effect of HTS.

V. THE DETERMINATION OF CRITICAL CURRENT

We learn from Sec. IV that anisotropy of the tape leads to nonuniform distribution of the current inside the coil. The inner turns are penetrated more by critical regions compared to the outer turns, and a higher magnetic field leads to lower instant critical currents. We apply 38 A to coil S and plot voltage (μV/m) for each turn in Fig. 9. To see the voltage variation clearly, we use LOG10 plot. The anisotropic current and field distribution results in a nonsymmetrical distribution of voltage inside the coil. Some inner turns clearly exceed 100 μV/m, with the innermost turn reaching 2000 μV/m, which means half of the terminal voltage drops at the innermost turn, because the applied current exceeds the instant critical current of the innermost turn, forcing it to enter the so-called flux flow region.[30] Although the transport loss (given by applied current times terminal voltage) is only 3.8 mW, half of the loss is generated by the innermost turn, which might lead to local heating. So the 100 μV/m is too high a criterion to define the coil critical current for long-term safe operation, in our point of view.

As we discussed in Sec. IV, the inner turns have lower instant critical currents compared to the rest of the turns. There must exist a single turn in the coil which has the lowest instant critical current. We define this turn as the weakest turn of the coil, which, in our experience, is always the innermost turn of the coil.

Instead of the 100 μV/m criterion, we suggest that the current at which the I-V curve becomes highly nonlinear is chosen as the long-term operating critical current of the coil. To be specific, when the applied current equals or exceeds the instant critical current of the weakest turn, the I-V curve starts to enter the highly nonlinear region, according to E-J power law. This applied current must be defined as our

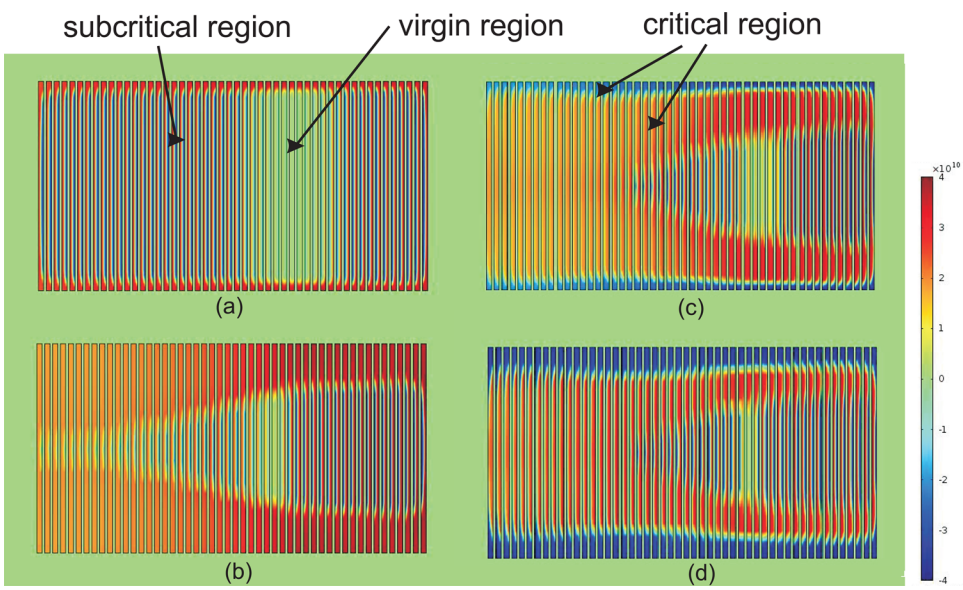

FIG. 7. Current distribution of coil A at: (a) ramping up to 20 A; (b) ramping up to 74 A; (c) ramping down to 74 A; (d) ramping down to 0.

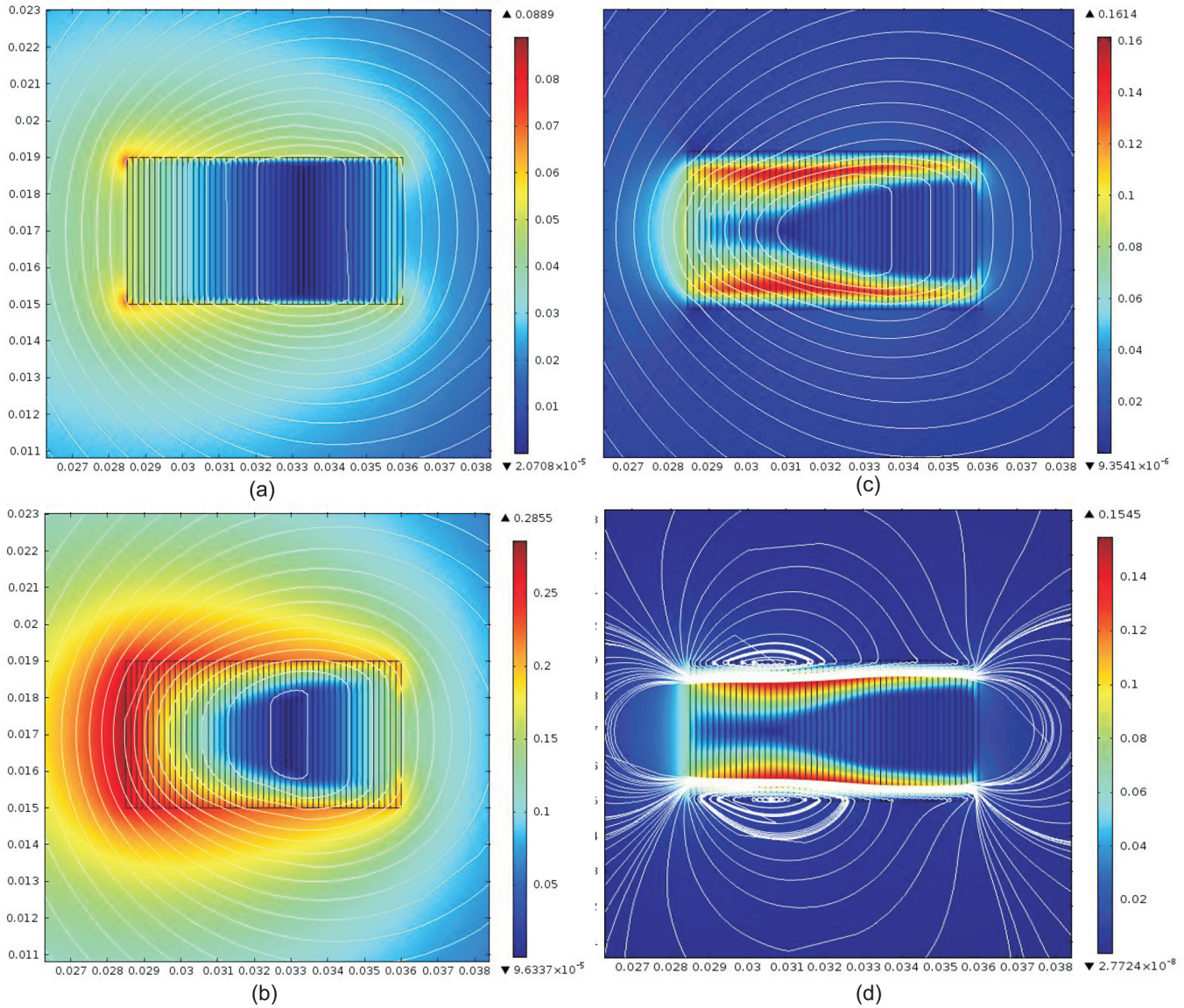

FIG. 8. Magnetic field distribution and flux line plot of coil A at: (a) ramping up to 20 A; (b) ramping up to 74 A; (c) ramping down to 74 A; (d) ramping down to 0.

critical current of the coil, because it effectively avoids the flux flow of the weakest turn and the resulting local heating.

To determine this criterion numerically, we employ the STOP function of the COMSOL solver. We assign a ramping-up current for the coil. Every time step, we look for the weakest turn, which has the lowest instant critical current. With the ramping up of the applied current, the magnetic field inside the coil increases, leading to decreasing instant critical current. Once the applied current equals or exceeds the instant critical current of the weakest turn, the STOP function will stop the solver and gives us the applied current at the last time step as the critical current. We use this method to check the new critical current for coil S and coil A, with results shown in Table III. Obviously, the new critical current determined by our new method is lower than the one determined by 100 μV/m. The terminal voltage is also below 100 μV/m. Accordingly, we suggest a coil voltage of 20 μV/m as the new criterion to determine long-term, safe operating current of the coil experimentally.

Figure 10 shows coil S's voltage plot for each turn with 36 A applied current. This time, the voltage variation among turns is not so large, so Log10 plot is no longer needed. As we expect, the new critical current restricts the turn voltage to well below 100 μV/m. Notably, the loss from the innermost turn is reduced by a factor of 20 when the coil carries the new critical current. The new criterion eliminates local flux flow and guarantees long-term, safe operation of the coil without apparent heating up inside the coil.

VI. CRITICAL CURRENT UNDER BACKGROUND FIELD

The potential application of the HTS coil involves a background field, such as windings of electrical machines and MRI machines. It is crucial to point out that, under background field, the critical currents of HTS coils reduce compared to non-background field circumstances. The reduction

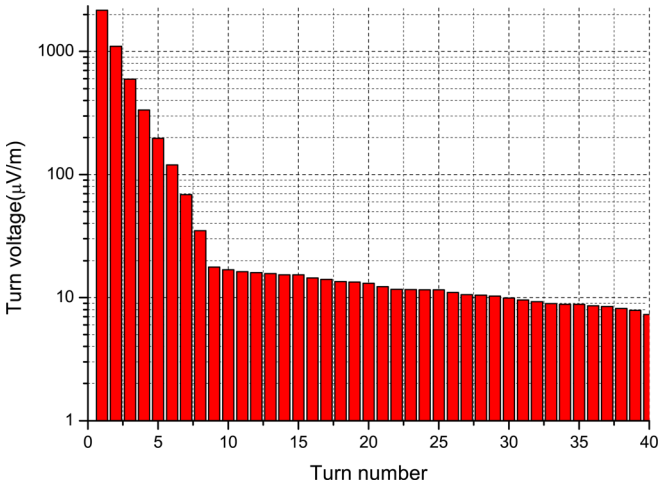

FIG. 9. Modeling results of voltage for each turn inside coil S when the applied current is 38 A.

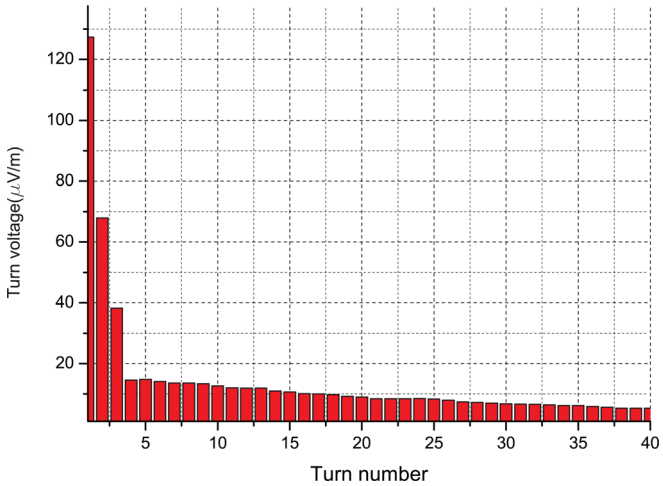

FIG. 10. Modeling results of voltage for each turn inside coil S when the applied current is 36 A.

of coil critical currents roots in the reduction of tape critical currents, which is illustrated in Fig. 2(a).

Limited by the geometry of the axial symmetrical model, we only study the influence of parallel field H_z on the coil critical current. We define in-phase field as while the background field H_z is in phase with the self-field inside the HTS pancakes and the anti-phase field $-H_z$ as while the background field is anti-phase, with the self-field inside the pancakes.

Results are shown in Fig. 11. When the background field is in phase and increasing, as we expect, the coil critical current is decreasing, because the background field enhances the local field of the innermost turn (or our weakest turn) and reduces its critical current. Interestingly, the coil critical current behaves differently when anti-phase background field is applied. While the anti-phase field is increasing, the coil critical current is first increasing and then decreasing, because the anti-phase field counteracts the self-field of the innermost turn so that the total field the innermost turn sees is lower compared to the self-field case and the in-phase case. And that is the reason why the coil critical current increases with the background field initially. However, the anti-phase background field enhances the field of the outermost turn, so while the anti-phase field increases the critical current of inner turns, it decreases the critical current of outer turns. When the background field magnitude exceeds 50 mT, the outermost turn replaces the innermost turn and becomes the weakest turn of the coil, so that the coil critical current is determined by the outermost, and that is why the coil critical current begins to decrease when the field exceeds 50 mT.

Normalized coil critical current reaches 0.934 when the in-phase field is 40 mT and the anti-phase field is 120 mT. There is 80 mT discrepancy due to the field direction. So when we consider the coil critical current under the background field, not only the magnitude, but also the direction should be considered.

TABLE III. Comparison of the two critical current criteria.

		Coil S	Coil A
100 μV/m criterion	Critical current	38 A	78 A
	Terminal voltage	100 μV/m	100 μV/m
	Total loss	3.8 mW	7.8 mW
	Innermost turn loss	1.9 mW	3.1 mW
New criterion	Critical current	36 A	74.9 A
	Terminal voltage	19 μV/m	26.4 μV/m
	Total loss	0.68 mW	1.98 mW
	Innermost turn loss	0.085 mW	0.24 mW

VII. CONCLUSIONS

Finite element modeling of 2 G, HTS pancakes is presented in this paper. We propose a new way to consider anisotropy of 2 G, HTS tapes by interpolating the measured data directly. The FEM model is validated by the measurement of the I-V curve. Transport current and magnetic field distribution inside the model are studied. We report that there are three regions inside the coil: critical region, subcritical region, and virgin region.

We use the model to study the critical current of 2 G, HTS pancake coils. We point out that the $E_0 = 100\ \mu$V/m criterion, which is commonly used in critical current

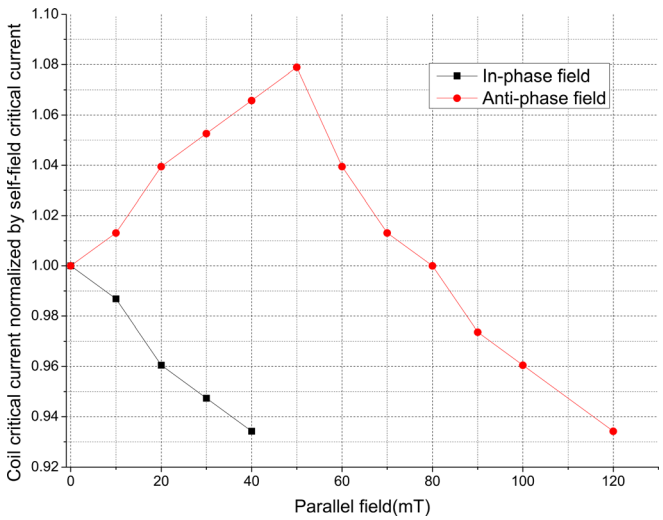

FIG. 11. Normalized coil critical current vs parallel field.

determination of HTS coils, tends to overestimate coil critical current. When the terminal voltage of the HTS coil reaches 100 μV/m, some inner turns have already entered the flux flow region due to the anisotropy of 2 G tapes. The local heat dissipation resulting from flux flow will lead to temperature increasing and drive the coil out of safe operation.

Instead, we suggest that the current at which the I-V curve becomes highly non-linear should be defined as the coil's critical current. To determine this critical current numerically, we propose a searching method. When the applied current equals or exceeds the critical current of the weakest turn, we set the applied current as the critical current of the coil. The new critical current definition effectively avoids potential flux flow inside HTS coils. For the experimental sake, we suggest a criterion of 20 μV/m, which can ensure a safely long-term operation of the coil.

We also study the influence of background field on the coil critical current. In-phase background field will drive the coil critical current down because of the enhancement of the weakest turn's field and critical current; the anti-phase background field will increase the coil critical current at first and then drive it down like the in-phase background field does. In real application, both the field magnitude and field direction need to be considered in the coil critical current estimation.

The FEM model we proposed in this paper predicts the critical currents of 2 G coils well. The model is also accurate in the AC loss estimation, and we will publish our study of AC loss in our following papers.

[1]M. Polak, E. Demencik, L. Jansak, P. Mozola, D. Aized, C. L. H. Thieme, G. A. Levin, and P. N. Barnes, Appl. Phys. Lett. **88**, 232501 (2006).
[2]K. Higashikawa, T. Nakamura, and T. Hoshino, Physica C **419**, 129140 (2005).
[3]J. Pitel and P. Kovac, Supercond. Sci. Technol. **10**, 847–852 (1997).
[4]J. H. Claassen, Appl. Phys. Lett. **88**, 122512 (2006).
[5]J. R. Clem, J. H. Claassen, and Y. Mawatari, Supercond. Sci. Technol. **20**, 1130 (2007).
[6]W. Yuan, A. M. Campbell, and T. A. Coombs, J. Appl. Phys. **107**, 093909 (2010).
[7]L. Prigozhin and V. Sokolovsky, Supercond. Sci. Technol. **24**, 075012 (2011).
[8]J. Souc, E. Pardo, M. Vojenciak, and F. Gomory, Supercond. Sci. Technol. **22**, 015006 (2009).
[9]E. Pardo, Supercond. Sci. Technol. **21**, 065014 (2008).
[10]See http://www.comsol.com for information about COMSOL software.
[11]Z. Hong, A. M. Campbell, and T. A. Coombs, Supercond. Sci. Technol. **20**, 331337 (2007).
[12]R. Brambilla, F. Grilli, and L. Martini, Supercond. Sci. Technol. **20**, 1624 (2007).
[13]F. Grilli and S. P. Ashworth, Supercond. Sci. Technol. **20**, 794–799 (2007).
[14]D. N. Nguyen, S. P. Ashworth, and J. O. Willis, J. Appl. Phys. **106**, 093913 (2009).
[15]D. N. Nguyen, P. Sastry, and J. Schwarts, J. Appl. Phys. **101**, 053905 (2007).
[16]F. Gomory, M. Vojenciak, E. Pardo, M. Solovyov, and J. Souc, Supercond. Sci. Technol. **23**, 034012 (2010).
[17]M. D. Ainslie, W. Yuan, Z. Hong, R. Pei, T. J. Flack, and T. A. Coombs, IEEE Trans. Appl. Supercond. **21**, 3 (2011).
[18]M. D. Ainslie, V. M. Rodriguez-Zermeno, Z. Hong, W. Yuan, T. J. Flack, and T. A. Coombs, Supercond. Sci. Technol. **24**, 045005 (2011).
[19]W. Yuan, M. D. Ainslie, W. Xian, Z. Hong, Y. Chen, Y. Yan, R. Pei, and T. A. Coombs, IEEE Trans. Appl. Supercond. **21**, 3 (2011).
[20]See http://www.superpower-inc.com/ for information about 2G tape.
[21]See http://www.amsc.com/ for information about 2G tape.
[22]J. Rhyner, Physica C **212**, 292300 (1993).
[23]E. Pardo, M. Vohenciak, F. Gomory, and J. Souc, Supercond. Sci. Technol. **24**, 065007 (2011).
[24]E. Pardo and F. Grilli, Supercond. Sci. Technol. **25**, 014008 (2012).
[25]L. Rostila, J. Lehtonen, R. Mikkonen, J. Souc, E. Seiler, T. Melisek and M. Vojenciak, Supercond. Sci. Technol. **20**, 1097 (2007).
[26]Z. Jiang, K. P. Thakur, M. Staines, R. A. Badcock, N. J. Long, R. G. Buckley, A. D. Caplin, and N. Amemiya, Supercond. Sci. Technol. **24**, 065005 (2011).
[27]M. Vojenciak, J. Souc, and F. Gomory, Supercond. Sci. Technol. **24**, 075001 (2011).
[28]K. P. Thakur, Supercond. Sci. Technol. **24**, 065024 (2011).
[29]M. Zhang and T. Coombs, Supercond. Sci. Technol. **25**, 015009 (2012).
[30]N. Schonborg and S. P. Hornfeldt, IEEE Trans. Appl. Supercond. **11**, 3 (2002).

Anisotropy of 2G HTS racetrack coils in external magnetic fields

2013 Supercond. Sci. Technol. 26 075012

(http://iopscience.iop.org/0953-2048/26/7/075012)

Supercond. Sci. Technol. **26** (2013) 075012 (7pp) doi:10.1088/0953-2048/26/7/075012

Anisotropy of 2G HTS racetrack coils in external magnetic fields

Michal Chudy, Yiran Chen, Min Zhang and T A Coombs

Department of Engineering, University of Cambridge, 9 JJ Thomson Avenue, Cambridge CB3 0FA, UK

E-mail: mc672@cam.ac.uk

Received 27 February 2013, in final form 16 April 2013
Published 20 May 2013
Online at stacks.iop.org/SUST/26/075012

Abstract
Pancake or racetrack coils wound with second generation high-temperature superconductors (2G HTSs) are important elements for numerous applications of HTS. The applications of these coils are primarily in rotating machines such as motors and generators where they must withstand external magnetic fields from various orientations. The characterization of 2G HTS coils is mostly focused on AC loss assessment, critical current and maximum magnetic field evaluation. In this study, racetrack coils will be placed in different orientations of external magnetic fields—J_c (I_c) versus angle measurements will be performed and interpreted. Full attention is paid to studies of anisotropy J_c versus angle curves for short samples of 2G HTS tapes. As will be shown, the shape of the J_c versus angle curves for tapes has a strong influence on the J_c (I_c) versus angle curves for coils. In this work, a unique and unpredicted behavior of the J_c versus angle curves for the 2G HTS racetrack coils was found. This will be analyzed and fully explained.

(Some figures may appear in colour only in the online journal)

1. Introduction

As high-temperature superconductors are being commercialized, several superconducting machines, such as fault current limiters [1–3] or superconducting motors [4, 5] are very close to commercial production. Obviously, devices such as superconducting magnetic energy storage (SMES) [6, 7], superconducting motors and generators have enormous potential in large scale machines. Second generation high-temperature superconductor (2G HTS) racetrack coils are elements which are present in most of the design concepts for superconducting rotating machines. Therefore, a lot of attention is paid to the study of the properties of these coils. One of the most interesting aspects for the case of rotating machines is AC and magnetization loss. Numerous excellent papers have been published which deal with the issue of AC losses in racetrack [8] or pancake [9, 10] coils. Another important focus of study is quenching in coils, with the work usually based on modeling [11], although for example the work of Lee *et al* [12] is based on real experiments.

Angular resolved measurements of critical current J_c versus angle characterization are especially important for 2G HTS characterization, as the anisotropy of YBCO is a phenomenon which makes all the HTS applications more problematic. This phenomenon also causes a great challenge for material scientists to engineer effective pinning centers in superconductors, which would reduce angular anisotropy while keeping the maximal critical currents unchanged. Many papers discuss the effects of different pinning features on the J_c versus angle curve in various magnetic fields [13–15]. IBAD MOCVD tape from SuperPower shows an extremely interesting J_c versus angle curve which has already been presented in numerous other publications. The features of the curve are shown in figure 1. For instance, the curve is asymmetric [16] with shoulders close to the ab-peaks [17] and the ab-peak is not parallel with the sample surface, its position varying according to the magnetic field [13]. In a standard YBCO tape, the YBCO ab-planes are parallel with the tape surface. Here, the ab-peak is shifted by about 2°, which has an obvious effect for ab-planes tilted by 2°. In previous work [18], this value was calculated by a sophisticated method from real experimental data. The shoulders, asymmetric shape and other features are consequences of various kinds of correlated pinning centers, which have various efficiencies.

Table 1. Racetrack coil parameters.

	SuperPower 4045 tape [19]	American superconductor (AMSC) 344 tape [20]
Tape type	4045	344
Tape width	4 mm	4.35 mm
Tape thickness	∼0.1 mm	∼0.2 mm
YBCO thickness	1 μm	∼1 μm
Substrate	Non-magnetic 50 μm	Ferromagnetic 50 μm
Number of turns	100	100
Inner radius	24 mm	24 mm
Outer radius	32 mm	36 mm
Length	250 mm	275 mm
Critical current	32.4 A	30.2 A

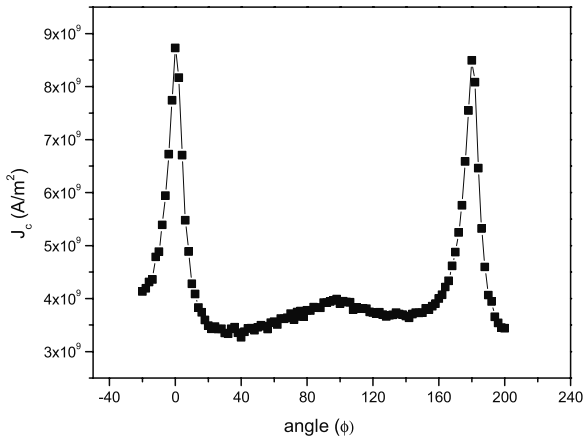

Figure 1. J_c versus angle measurement for IBAD MOCVD tape from SuperPower at 700 mT in liquid nitrogen (77 K).

An explanation of all the mechanisms is not the aim of this paper; however, most of the features have been satisfactorily explained and most of them can be found in [13–15]. It is important to know that the correlated pinning centers are not homogeneously distributed throughout the tape and that they are effective at different magnetic fields. Although the shape of the J_c versus angle curve for the case of tapes is more or less successfully elucidated, the J_c versus angle curves have never been really analyzed for 2G HTS racetrack coils. It is well known that tape anisotropy has a strong effect on the J_c versus angle curve for coils. Even though the applied field is uniform the total field includes a component from the coil itself and therefore we have constructed a finite element model (FEM) to explain our results.

2. Samples

Two types of 2G HTS racetrack coils have been evaluated. Both coils are double racetrack coils with 100 turns. The dimensions of the coils are very similar. The major difference is in the 2G HTS wire from which the coils were manufactured. One coil is made from a MOCVD 4045 coated conductor from SuperPower [19] and the other coil is made from a RABiTS MOD 344 coated conductor from American Superconductor (AMSC) [20]. A detailed list of parameters for both coils is shown in table 1.

3. Experimental set-up

A schematic view of the experimental set-up is shown in figure 2. A racetrack coil is simply rotated in the gap between two poles of a magnet. Rotation is manual; the current angle is measured using a protractor, which is attached to the rotating sample holder. The main challenge of the set-up is to ensure a homogeneous field in the rather large gap between the poles of the magnet. For this purpose, the magnet poles were modified. Mild steel blocks were added to the poles in order to enhance the homogeneity of the magnetic field. The field of the electromagnet at 25 A, which is the maximum permissible current, was reduced from 1.1 T in the unmodified magnet to 220 mT. The modified poles had a gap of 15 cm and measured 16 cm × 21 cm. The coils are 25–27.5 cm long with 15 cm of the length between the poles seeing a uniform magnetic field, with the remainder of the coil outside the pole pieces seeing an inhomogeneous and significantly weaker field (which was not expected to affect J_c).

The field above the mild steel poles was carefully evaluated, the maximum value reached only 50% of the homogeneous field and it was strongly reduced with increasing distance from the poles. Between the poles measurement showed a 10% difference between the field close to the steel poles and that in the middle of the gap. This result was sufficiently uniform for our experiments. The coils were immersed into a liquid nitrogen bath which was placed between the magnet poles. Critical currents were measured by a simple four-point method, where the voltage was measured through the full coils. An Agilent 6680 was used as a current source and the coil voltage was measured by a Keithley 2182 nanovoltmeter. The measurement set-up was controlled by a LabVIEW program from a PC.

4. Results and discussion

In figure 3, the results for J_c versus angle measurements performed on both tapes, AMSC and SuperPower, are shown. All the measurements were performed in liquid nitrogen by a standard four-point method with a voltage criterion of 1 μV cm^{-1}. The figures show differences in tape performance and the differences in shapes of the J_c versus angle curve, which as will be shown later are crucial to an explanation of the distinct behavior of the racetrack coils in a magnetic field.

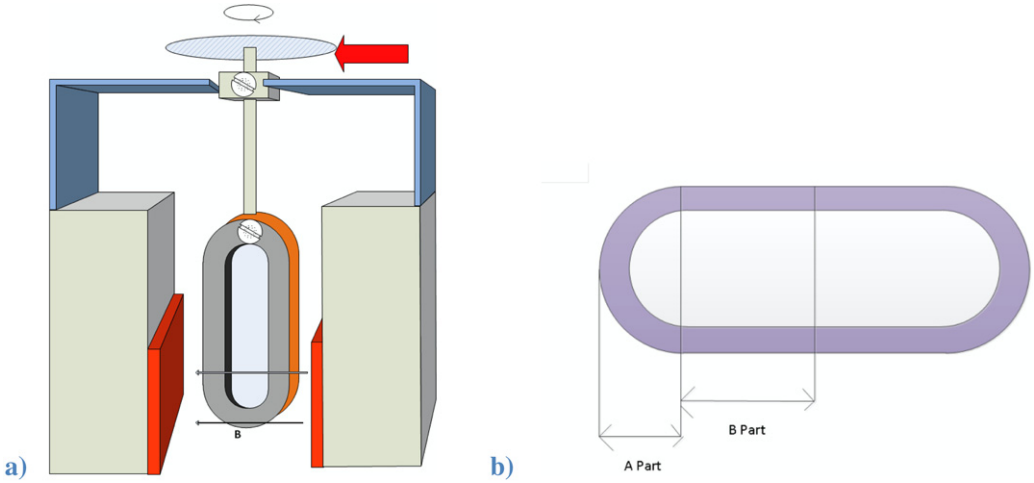

Figure 2. (a) Schematic view of experimental set-up. (b) Racetrack coil.

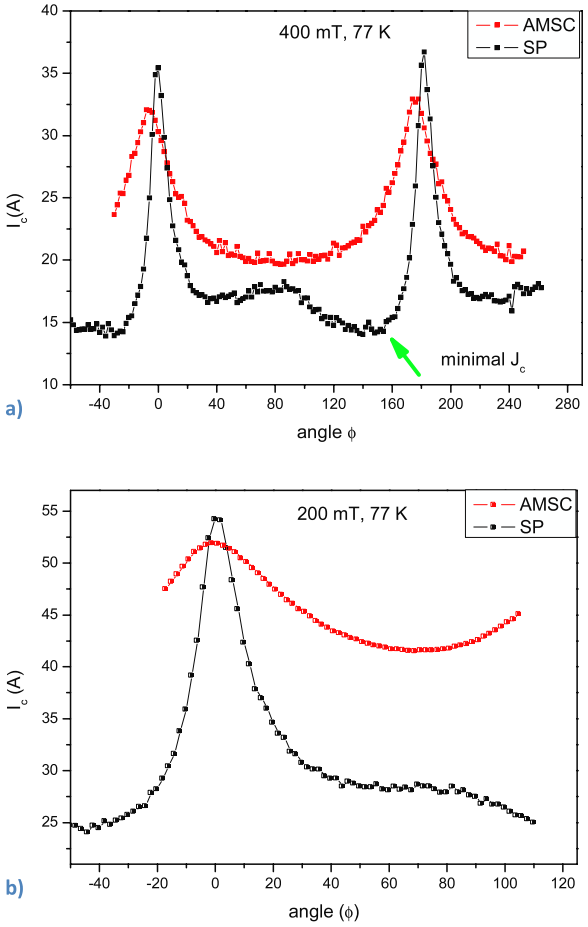

Figure 3. J_c versus angle measurements for AMSC and SuperPower short tapes, (a) 400 mT and (b) 200 mT.

From figure 3, two important phenomena can be observed. First: the shape of the curve (especially for the SuperPower tape) is changed by increasing magnetic field. Secondly: the SuperPower tape has a pronounced *c*-axis peak approximately at the orientation when $\mu\mathbf{H} \perp$ ab (90°). The peak is more pronounced in higher fields, however, it is not present in the AMSC tape. We should remember that the maximum J_c value is expected when the external magnetic field is parallel to the tape surface, which usually corresponds to $\mu\mathbf{H}$ II ab, which is approx. 0°.

One would expect a similar J_c (I_c) versus angle behavior for the racetrack coils rotated in external magnetic fields, but the experiments performed with coils manufactured from the same tapes, as presented in figure 3, show rather different results. The angular resolved measurements—J_c (I_c) versus angle—for the SuperPower and AMSC racetrack coils in a 120 mT external magnetic field are shown in figure 4. The behavior of the AMSC tape is not symmetric at 0° or 180°. The curve is shifted by approx. 25° resulting in the peak expected at 180° to be positioned at 155°. This is most likely caused by winding of the innermost layer where two pancakes of the double racetrack coil are joined. The crossing tape is slightly misoriented at this point and if the weak point is placed in this section, the J_c (I_c) versus angle curve could be shifted.

The angles in figure 4 correspond to the angles in the previous figures, where the angle $\varphi = 0°$ corresponds to $\mu\mathbf{H}$ II ab and $\varphi = 90°$ corresponds to $\mu\mathbf{H} \perp$ ab. Figure 5 illustrates the measurement configuration of the coils with regard to position and direction of rotation. As the coil geometries are very similar and the measurement conditions were identical, it is rather surprising that the shapes of the curves exhibit such huge differences. The reasons for these differences are most likely due to the microstructural differences of the tapes. Any effects connected with the coil geometries are unlikely, as these would be observed for both coils. Despite the same thickness of superconducting layer for both tapes, their structure and manufacturing processes are very different. In addition, the AMSC tape is based on a magnetic substrate.

The J_c versus angle curves could be understood as a direct consequence of the character and efficiency of the pinning centers present in the tape. This is the main reason why J_c versus angle curves are often studied [13–15, 21, 22]. However, this is not the case for coils, where the J_c versus angle curve is a consequence of several coil parameters such

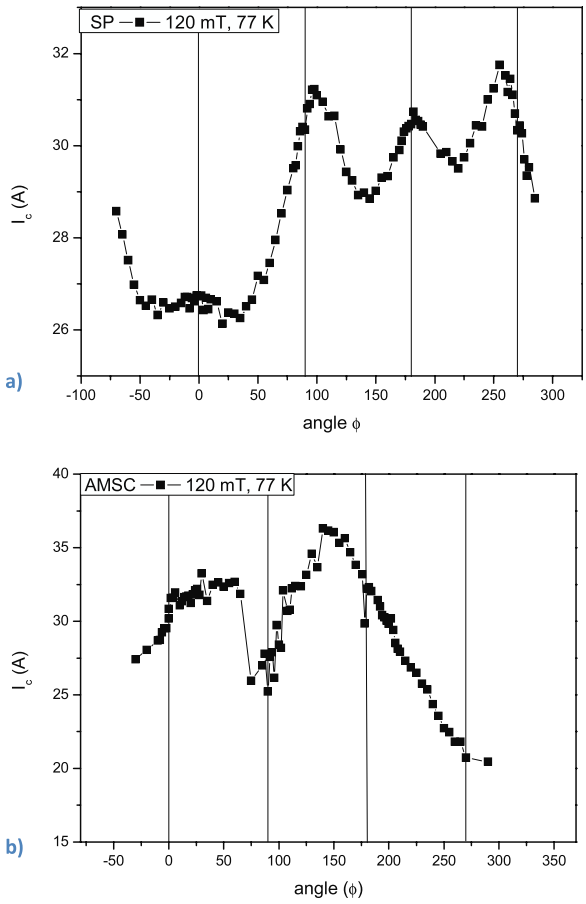

Figure 4. J_c versus angle measurement for (a) SuperPower racetrack coil and (b) AMSC racetrack coil.

as geometry, diameter, number of turns, etc. It is important to note that in general, the measured changes of critical current in coils are very small. According to the J_c versus angle curves for the coils (figure 4), their anisotropy is much reduced compared with that for the tapes. For instance the anisotropy coefficient ($I_{c,max}/I_{c,min}$) at 200 mT for the SuperPower tape was 2.26 (from figure 3(b)), but for the coil at 200 mT external field it was only 1.29, and 1.25 at 120 mT (figure 4(a)) which means a critical current difference ($I_{c,max} - I_{c,min}$) of only about 5.5 A. In the simulation an external field of 120 mT combines with the self-field of the coil when it is carrying 30 A to produce a maximum field on the tape close to 200 mT (about 160 mT) (figure 7(d)).

Every point of a racetrack coil carrying transport current in a magnetic field has its composite magnetic field vector **B**. **B** is the resulting vector from all contributions of the turns in the coil and external magnetic field. Vector **B** could be imagined as a vector resulting from two components: radial $\mathbf{B_r}$ and axial $\mathbf{B_a}$. In the following, the vector **B** will be referred to as $\mathbf{B}(B, \varphi)$, where B is the absolute value for vector **B** and φ is the angle to the tape surface which is identical to the value described in figure 3. The critical current of the coil is determined by the weakest point, which has a particular $\mathbf{B_w}(B_w, \varphi_w)$. The weakest point does not necessarily need to be the same in every field orientation. Most likely, the weakest point moves along the innermost turn, as this turn has to

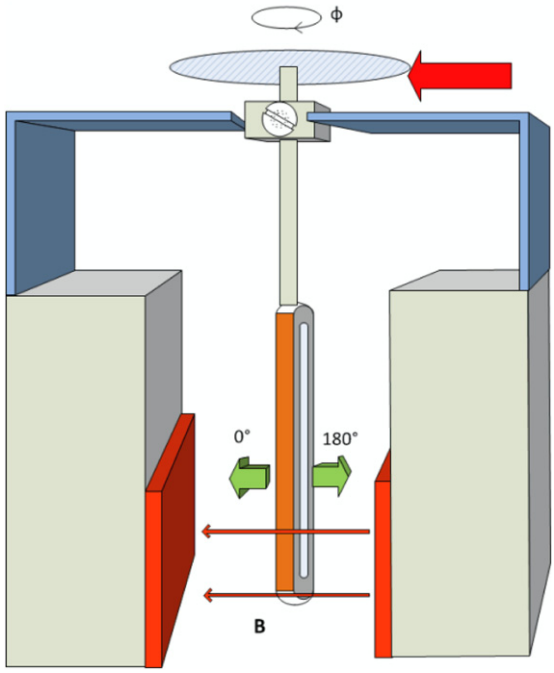

Figure 5. Measurement set-up configuration for racetrack coils. The (green) arrow indicates magnetic moment of the coil.

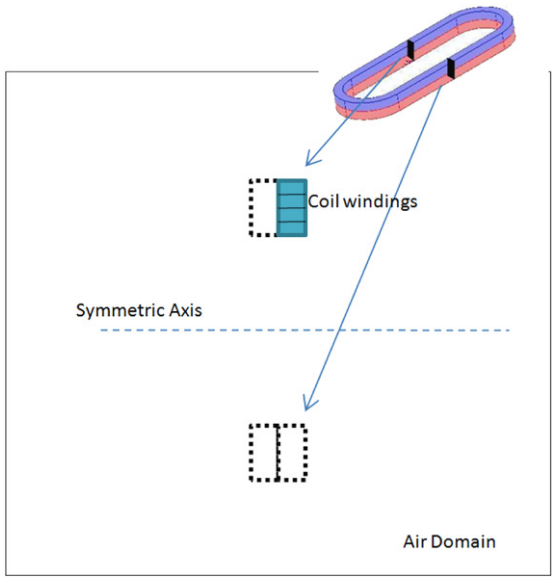

Figure 6. Cross section of a racetrack coil. The dark part represents windings which are reflected in the COMSOL model.

withstand the highest load of magnetic field. A 2D COMSOL model of the racetrack coil was employed. This kind of model is relatively easy to use for the calculation of magnetic fields in coil windings. During recent years, finite element modeling of 2G HTS coils, employing H-formulation and the E–J power law, has enjoyed a high level of popularity. In finite element software such as COMSOL, the H-formulation model has become a powerful tool to study HTSs. The models usually exhibit a high level of precision with very good agreement with experiment [23, 24]. The composition

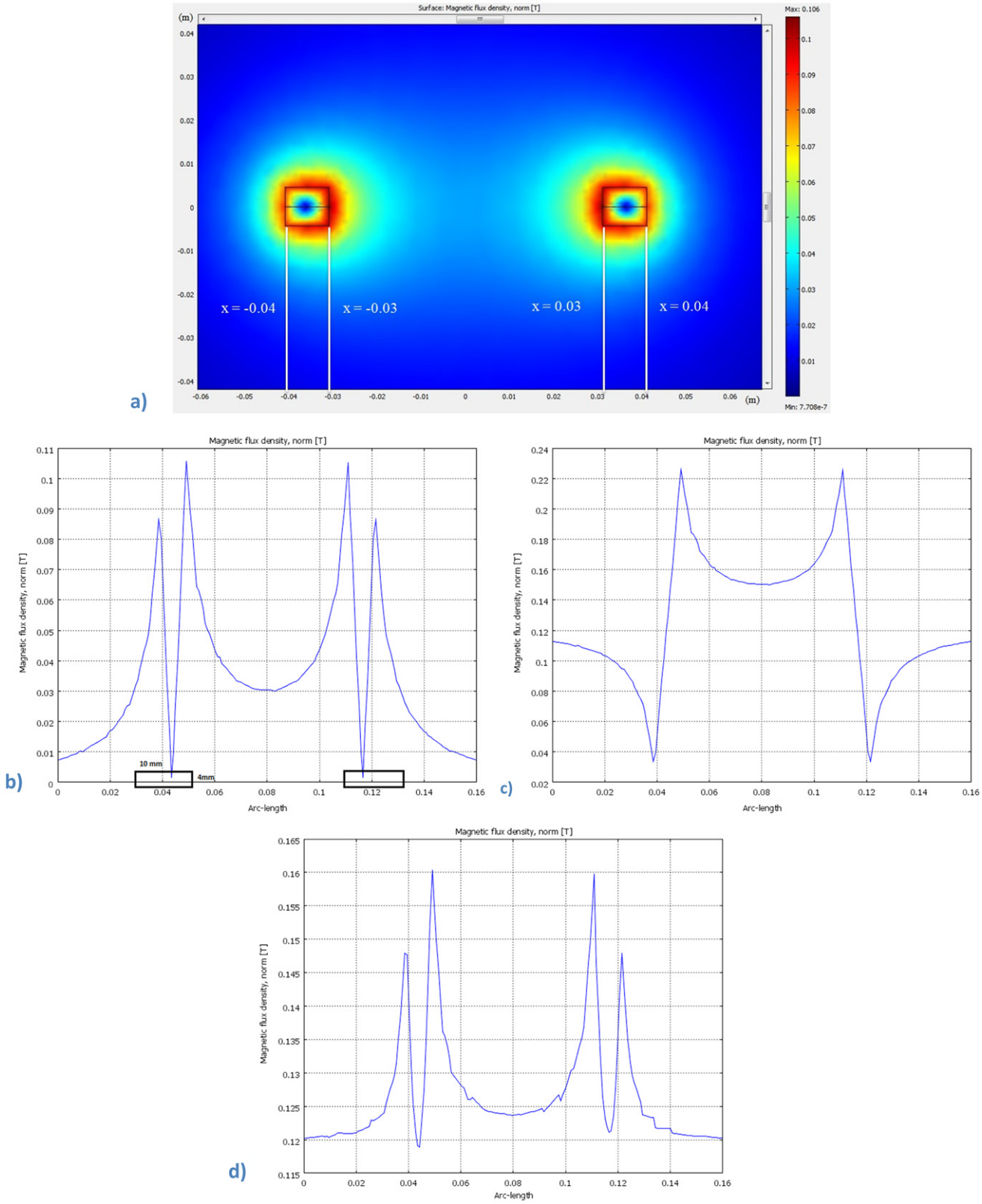

Figure 7. Distribution of magnetic field in the coil windings at 30 A. (a) without external magnetic field, contour diagram, (b) without external magnetic field, plot, (c) with external magnetic field of 120 mT at $\varphi = 0°$ and (d) with external magnetic field of 120 mT at $\varphi = 90°$.

of the model is introduced in figure 6. A current of 30 A, which is relatively close to the average I_c for both coils, was applied. The simulation was performed to learn approximate values for the magnetic fields affecting superconducting tapes at different turns. In this particular calculation a uniformly distributed transport current was assumed (not necessarily a

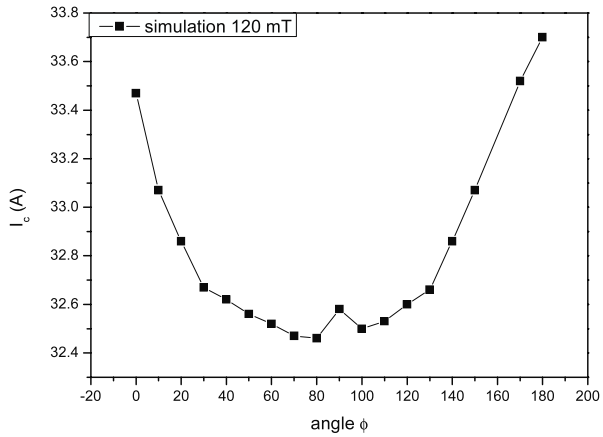

Figure 8. Simulation result for J_c (I_c) versus angle curve at 120 mT.

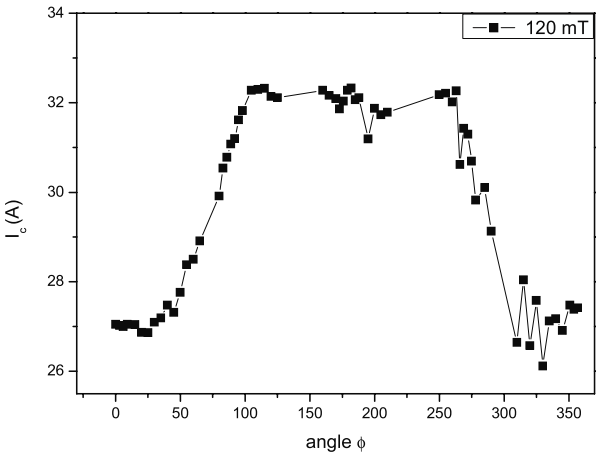

Figure 9. J_c versus angle measurement for SuperPower racetrack coil at 77 K—part A only.

superconducting tape). The resulting distribution of magnetic field is shown in figure 7. In addition, an external field of 120 mT was applied in the two main magnetic field orientations $\varphi = 0° = \mu\mathbf{H}$ II ab and $\varphi = 90° = \mu\mathbf{H} \perp$ ab.

From figures 7(b)–(d) it is clear that the innermost layer field load is highest at approx. 160–230 mT. As we cannot see the field orientations, the determination of the innermost layer as the weak point is not fully justified, though very probable. The same model, with the superconducting properties of the tapes included, could be used to calculate the critical currents under different orientations of the external magnetic field. Problems with the model are that it is only a 2D model, it does not consider part A of a coil nor the inputting J_c versus angle curve for the tape, which is usually taken in a reasonably small magnetic field (usually at 50 or 100 mT). As is shown in figure 3, the shape of the J_c versus angle curve could change significantly with magnetic field, especially in low fields, however, this is usually not reflected in the model. As an example, the J_c versus angle curve for the SuperPower tape contains no *c*-axis peak at 100 mT. The peak could be defined from about 150 mT and then is amplified with increasing magnetic field. Even though the model is a good approximation, some small changes in the critical current could not be precisely calculated. For instance, the calculated critical current for the SuperPower coil at $\varphi = 0°$, 120 mT external field is 33.7 A and at $\varphi = 90°$ is 32.6 A (figure 8). The values are in the opposite order compared to those from figure 4, where I_c ($\varphi = 0°$) < I_c ($\varphi = 90°$), which is in direct contradiction with the model and the experiment.

In order to find the weakest point on the coil, the following experiment was performed. As can be seen in figure 2(b), a racetrack coil consists of two parts, a curved part A and a linear part B. We measured a J_c versus angle curve for part A. In order to shield part B of the coil, we constructed a mu metal jacket over the A part of the coil. Mu metal is an alloy which exhibits very high permeability; it attracts magnetic flux lines into the metal. In this way, more than 50% of the magnetic field was trapped in the mu metal in our experiment. In addition, part B was already in the inhomogeneous weak magnetic field above the magnet's poles and so the effect on the critical current of the magnetic field applied to part B was reduced to a minimum. The J_c versus angle curve from this measurement is presented in figure 9. Here, the shape of the curve corresponds to theoretical expectations, as at 90° part of the external magnetic field is in the transport current direction, which induces no Lorentz force. All the measured I_c values are equal to or higher than those in figure 4(a). This suggests that the weak point might be located in part A at angles close to $\varphi = 0°$, $\varphi = 90°$, *and*$\varphi =$ 270°, but the rest of the weak points are probably located elsewhere.

The possible weak point has a current which is slightly smaller than the critical current and without any external magnetic field is defined by the vector $\mathbf{B_{wp}}(B_{wp}, \varphi_{wp})$. φ_{wp} is highly unlikely to be 0° or 180° as the radial component $\mathbf{B_r}$ is present at each point of the coil [25]. This component shifts φ further from 0° or 180° to angles with lower I_c. By applying an external magnetic field $\mathbf{B}_e(B_e, \varphi_e)$, the updated vector $\mathbf{B_w}$ for the weakest point will be $\mathbf{B_w} = \mathbf{B_{wp}} + \mathbf{B_e}$; $\mathbf{B_w}$ (B_w, φ_w). In general $B_w > B_{wp}$, as otherwise the weak point would be transferred somewhere else to a point with higher $\mathbf{B_w}$. The difference $\varphi_{wp} - \varphi_w$ is crucial, as the external field could shift φ_w closer to a local minimum at 90° or closer to a local maximum at 0°. External fields with $\varphi_e = 90°$ or 270° will increase the radial part of $\mathbf{B_w}$, which usually leads to a reduction of I_c. However, the SuperPower tape has a *c*-axis peak at ∼90° (figure 3) and any shift of φ_w towards the peak leads to an increase of I_c. In addition, external fields with $\varphi_e = 0°$ or 180° could shift the resulting φ_w to the locations beside the ab-peaks, where deep local minima are situated (arrow in figure 3(a)). The existence of the *c*-axis peak is a key answer to the mysterious maxima at 90° and 270°.

The presented analysis has shown that under special circumstances, an external magnetic field could increase I_c in the coil. This effect is very well described in the work of Pitel and Kovac, who studied BSCCO coils [25–27]. Reference [25] describes a method showing how to effectively increase the I_c of BSCCO coils by reducing the radial component of the vector $\mathbf{B_w}$ with additional coils, indeed producing an external magnetic field. Considering this fact, the assumption that part of the coil which is not in the

homogeneous magnetic field has no effect on the resulting I_c is incorrect. This assumption is not incorrect for the SuperPower coil, which has all its measured I_c in figure 4(a) lower than the critical current measured without any external field, which is 32.4 A. Since I_c in figure 4(b) for the AMSC coil is at some locations equal to or higher than the I_c for the coil in zero field (30.2 A), the measured J_c versus angle curve is deformed at those places. This means that the weak point is located in an area of inhomogeneous magnetic field, which affects the critical current value.

5. Conclusions

2G HTS racetrack coils in external magnetic fields have been studied. The external field was set to 120 mT in most measurements, as this field is achievable in real applications. Two 2G HTS coils with very similar geometries, but manufactured from different coated conductors were characterized. 4045 MOCVD tape from SuperPower and 344 MOD RABiTS tape from AMSC show rather different characteristics for J_c versus angle measurements performed on short samples (figure 3). Due to the different properties of the tapes such as pinning or magnetic, non-magnetic substrate, the coils have defined different weak points, which are responsible for critical currents under external magnetic fields. It was found that an external magnetic field applied to the coil changes the value and also the angle of the resulting field acting on the weakest point of the coil. The change of the angle increasing the radial component ($\varphi = 90°$ or 270°) leads to a critical current reduction in the AMSC tape whereas it leads to a small increase of the critical current in the SuperPower coil, where a more complicated J_c versus angle curve was measured on a short tape sample. The existence of a *c*-axis peak and local minima near the ab-peaks in the J_c versus angle curve for the SuperPower tape is a key explanation for the minima and maxima of the coil J_c versus angle curve, which occurred in reversed locations according to the short sample measurements. Looking further to the microstructure of the tapes, the different characters of the pinning centers, especially those oriented in the *c*-axis of YBCO are responsible for the coil J_c versus angle curve. The tape substrates might play a role as well. Reported changes in I_c for the coils are rather small compared to those for the tapes. In addition, I_c could even be improved by certain sizes and orientations of the external magnetic field. However, it is important to know about all the features of the behavior of racetrack coils in external magnetic fields in order to design a good rotating machine. Described phenomena could cause a slight capacity extension for SMES or slight weight and size reductions for specially designed rotating machines.

Acknowledgments

This work was supported by EPRSC grant RG56741. Thanks to Magnetic Shields Limited for providing high quality mu metal for the experiments. We wish to thank F Spaven, W Wang J Zou and D Hu for help and support with the experiments.

References

[1] Maguire J, Folts D, Yuan J, Lindsay D, Knoll D, Bratt S, Wolff Z and Kurtz S 2009 *IEEE Trans. Appl. Supercond.* **19** 1740–3
[2] Velichko A V, Zeimetz B and Coombs T A 2007 *IEEE Trans. Appl. Supercond.* **17** 1780–3
[3] Ye Lin, Majoros M, Coombs T A and Campbell A 2007 *IEEE Trans. Appl. Supercond.* **17** 2339–42
[4] Gubser D U 2003 *Physica* C **392–396** 1192–5
[5] Jiang Y, Pei R, Hong Z, Jiang Q and Coombs T A 2008 *J. Phys.: Conf. Ser.* **97** 012123
[6] Yuan W, Xian W, Ainslie M, Hong Z, Yan Y, Pei R, Jiang Y and Coombs T A 2010 *IEEE Trans. Appl. Supercond.* **20** 1379–82
[7] Kozak J, Majka M, Jaroszyñski L, Janowski T, Kozak S, Kondratowicz-Kucewicz B and Wojtasiewicz G 2010 *J. Phys.: Conf. Ser.* **234** 032034
[8] Hong Z, Yuan W, Ainslie M, Yan Y, Pei R and Coombs T A 2011 *IEEE Trans. Appl. Supercond.* **21** 2466–9
[9] Pardo E, Šouc J and Kováč J 2012 *Supercond. Sci. Technol.* **25** 035003
[10] Pardo E 2008 *Supercond. Sci. Technol.* **21** 065014
[11] Zhang M, Matsuda K and Coombs T A 2012 *J. Appl. Phys.* **112** 043912
[12] Lee J-D *et al* 2007 *IEEE Trans. Appl. Supercond.* **17** 1603–6
[13] Chen Z, Kametani F, Chen Y, Xie Y, Selvamanickam V and Larbalestier D C 2009 *Supercond. Sci. Technol.* **22** 055013
[14] Maiorov B, Gibbons B J, Kreiskott S, Matias V, Holesinger T G and Civale L 2005 *Appl. Phys. Lett.* **86** 132504
[15] Holesinger T G, Maiorov B, Ugurlu O, Civale L, Chen Y, Xiong X, Xie Y and Selvamanickam V 2009 *Supercond. Sci. Technol.* **22** 045025
[16] Chudy M, Eisterer M and Weber H W 2010 *Physica* C **470** 1300–3
[17] Chudy M, Fuger R, Eisterer M and Weber H W 2011 *IEEE Trans. Appl. Supercond.* **21** 3162–5
[18] Chudy M, Hopkins S C, Wozniak M, Glowacki B A, Eisterer M and Weber H W 2011 *Supercond. Sci. Technol.* **24** 075018
[19] www.superpower-inc.com/content/products-services
[20] www.amsc.com/solutions-products/hts_wire.html
[21] Maiorov B *et al* 2007 *IEEE Trans. Appl. Supercond.* **17** 3697–700
[22] Maiorov B, Wang H, Foltyn S R, Li Y, DePaula R, Stan L, Arendt P N and Civale L 2006 *Supercond. Sci. Technol.* **19** 891–5
[23] Chen Y, Zhang M, Chudy M, Matsuda K and Coombs T A 2013 *Physica* C **487** 31–6
[24] Hong Z and Coombs T A 2010 *J. Supercond. Novel Magn.* **23** 1551–62
[25] Pitel J and Kovac P 2011 *Physica* C **471** 1680–8
[26] Pitel J and Kovac P 1997 *Supercond. Sci. Technol.* **10** 847–52
[27] Pitel J and Kovac P 1997 *Supercond. Sci. Technol.* **10** 7–16

Physica C 487 (2013) 31–36

Contents lists available at SciVerse ScienceDirect

Physica C

journal homepage: www.elsevier.com/locate/physc

Complex study of transport AC loss in various 2G HTS racetrack coils

Yiran Chen *, Min Zhang, Michal Chudy, Koichi Matsuda, Tim Coombs

University of Cambridge, 9 JJ Thomson Avenue, Cambridge CB3 0FA, United Kingdom

ARTICLE INFO

Article history:
Received 19 April 2012
Received in revised form 30 October 2012
Accepted 6 February 2013
Available online 26 February 2013

Keywords:
AC losses
HTS
Substrate

ABSTRACT

HTS racetrack coils are becoming important elements of an emerging number of superconducting devices such as generators or motors. In these devices the issue of AC loss is crucial, as performance and cooling power are derived from this quantity. This paper presents a comparative study of transport AC loss in two different types of 2G HTS racetrack coils. In this study, both experimental measurements and computer simulation approaches were employed. All the experiments were performed using classical AC electrical method. The finite-element computer model was used to estimate electromagnetic properties and calculate transport AC loss. The main difference between the characterized coils is covered inside tape architectures. While one coil uses tape based on RABITS magnetic substrate, the second coil uses a non-magnetic tape. Ferromagnetic loss caused by a magnetic substrate is an important issue involved in the total AC loss. As a result, the coil with the magnetic substrate surprised with high AC loss and rather low performance.

1. Introduction

High temperature superconductors have strong potential to be used in a wide range of engineering applications. One of the crucial factors which prevents industry from widely adopting high temperature superconductors is AC loss [1–3]. Numerous studies deal with this problem and several methods of reducing AC loss have been developed, both experimentally and theoretically. Claassen, Clem, and Yuan developed with critical state method to estimate AC loss in HTS coils [4,5], Šouc and Pardo used a minimum magnetic energy variation method to estimate the AC loss [6,7]. Grilli and Ashworth developed a model based on edge elements to estimate the transport AC loss in the HTS coils [8]. Prigozhin and Sokolovsky used an efficient numerical scheme based on a variation formulation of the Kim critical-state model to solve the transport AC loss for a stack of YBCO tapes [9]. The measurements of the transport AC loss were explored and clarified in [6,8,10]. There are also several simulation methods on the interaction between superconductors and magnetic materials have been proposed and developed in [11–14]. However, few papers were focused on comparative studies of different 2G HTS tapes. In 2G HTS YBCO coated conductors, the tape architecture has been proven to be an important issue, which directly influences AC loss. This work is focused on exploring the transport AC loss behavior between two 2G HTS racetrack coils, manufactured from different types of 2G HTS tapes. The first coil – denoted as MAG RABITS is made of YBCO coated conductor which is based on the RABITS™ template. This template creates a basis for a textured substrate along with a metal organic deposited (MOD) YBCO layer. The substrate consists of a textured nickel tungsten alloy, which is magnetic. The second coil – denoted as NON MAG has a non-magnetic substrate. The tape consists of several buffer layers i.e. IBAD MgO template. The YBCO layer is made by metal organic chemical vapour deposition (MOCVD).

2. Experimental

2.1. Samples

Both, MAG RABITS and NON MAG HTS racetrack coils were manufactured from thin ~4 mm wide tapes, which were arranged in two stacks – double racetrack coil. The total length of the tape used in the coils is ~50 m creating 50 turns in the pancake. Both racetrack coils have very similar geometry. All the specifications are listed in Tables 1 and 2. The main difference of the outer radius results from different thickness of used 2G HTS tapes. Photographs of the coils are presented in Figs. 1 and 2. It can be seen that, despite of rather different coil shells, the tape arrangement is almost identical.

2.2. Experimental set-up

The AC transport loss was measured by the electrical method, which is the simplest standard method used for AC loss estimation. A full detail description of this method is published elsewhere [15–18]. A sketch of the experimental setup is shown in Fig. 3. The current leads configuration plays a crucial role as it determines accuracy of the measurement results. The design of voltage leads

* Corresponding author. Tel.: +44 7885240662.
E-mail address: yc315@cam.ac.uk (Y. Chen).

0921-4534/$ - see front matter © 2013 Elsevier B.V. All rights reserved.
http://dx.doi.org/10.1016/j.physc.2013.02.003

Table 1
Specification of the MAG RABITS coil.

Tape manufacturer	American superconductor (344)
Critical current of the tape, I_c (self-field, 77 K)	100 A
Critical current of the coil (self-field, 77 K)	50 A
Coil length	50.6 m
Tape width, w	4.35 mm
Tape thickness, d_c	0.2 mm
YBCO layer thickness, d_{sc}	1 μm
Number of turns	50
Inner radius	2.4 cm
Outer radius	3.6 cm
Ferromagnetic substrate thickness, d_{mag}	50 μm

Table 2
Specification of the NON MAG coil.

Tape manufacturer	Superpower (SCS4050)
Critical current of the tape, I_c (self-field, 77 K)	80 A and higher
Critical current of the coil, (self-field, 77 K)	46 A
Coil length	49.7 m
Tape width, w	4 mm
Tape thickness, d_c	0.1 mm
Number of turns	50
YBCO layer thickness, d_{sc}	1 μm
Inner radius	2.4 cm
Outer radius	3.2 cm
Non-magnetic substrate thickness, d_{mag}	50 μm

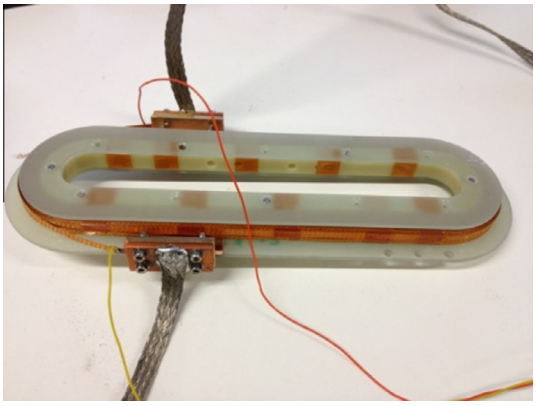

Fig. 1. The NON MAG superconducting racetrack coil with non-magnetic substrate.

in both types of coils is shown in Figs. 1 and 2. Two voltage probes, made of chromel wire, were soldered onto the tape surface with a low-temperature solder. To reduce the out-of-phase component of the voltage measured at the tape surface, the voltage probes were twisted together at a distance as close to the surface of the superconductor coil as possible.

The power was supplied via two 400 W KEPCO power supplies connected in parallel. They are able to supply current up to 40 A. A lock-in amplifier provided reference voltage signal to the power supply. It was used to measure voltage signals. The current flow in the circuit was measured by a current transducer which was connected to an oscilloscope. The critical current of the MAG RABITS coil is approximately 50 A [19] and the critical current of NON MAG coil was measured to be 46 A. As, in the YBCO racetrack coils, the loss voltage is the in-phase voltage signal with respect to the current source. The difficulty is that there is a large out-of-phase inductive voltage, induced by the voltage loop. In this experiment, a compensation coil was employed to bypass this problem. It was achieved by using variable mutual inductances between the voltage measurement circuit and the transport current circuit. A 4000 turns of copper windings (diameter: 0.3 mm) were positioned close to the loop made in the ac current cable and the relative orientation of these two loops can be adjusted to get the mutual inductance value. The compensation process can be divided into two steps: first, a low transport current was applied (less than 1 A), the superconducting coil was assumed to be totally inductive, the compensation coil was adjusted to minimize the measurement voltage; secondly, a higher transport current was applied (more than 20 A), the superconducting coil was assumed to be totally resistive and the lock-in amplifier was used to minimize the inductive part. As the compensation coil is not able to compensate the entire inductive component in the HTS coil, there is still some inductive component remaining in the consequent voltage signal. To completely remove the inductive part from the superconducting coil, a pure resistance signal was taken from the shunt resistor and the lock-in amplifier was employed to measure the resistance phase angle of the shunt resistor, then the phase angle of the consequent voltage signal was compared and subtracted from the pure resistance signal phase angle, the resulted angle θ is the actual phase angle between inductive and resistive components of the consequent voltage signal voltage as the resistive component is in-phase with the pure shunt resistor signal. Even though, there existing a small inductive component in the pure resistor signal, it is assumed to be negligible as comparing with the large resistive part. Meanwhile, the resistance in the compensation coil can be neglected due to the large input impedance in the lock-in amplifier.

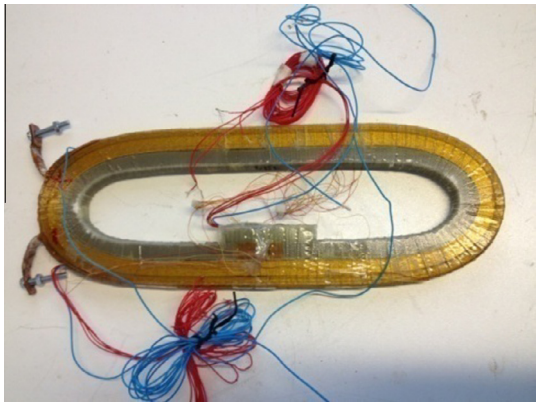

Fig. 2. The MAG RABITS superconducting racetrack coil with RABITS substrate.

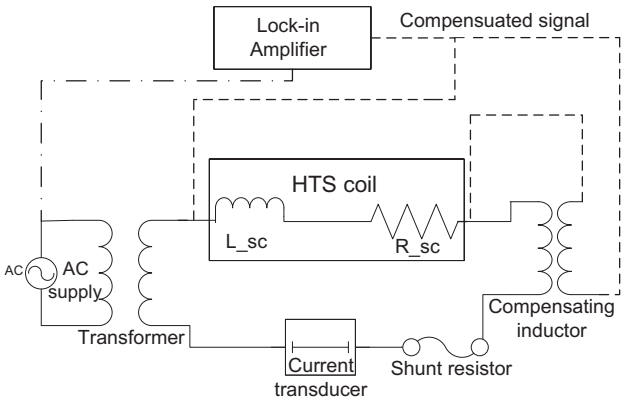

Fig. 3. AC loss electrical method experiment setup.

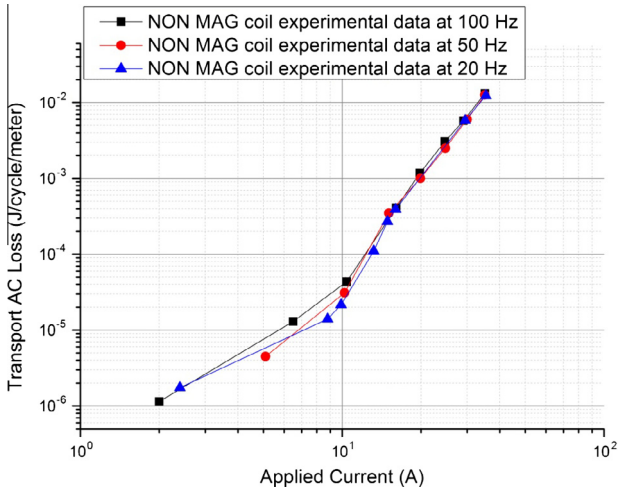

Fig. 4. Self-field AC loss as a function of the transport current for NON MAG coil without magnetic substrate.

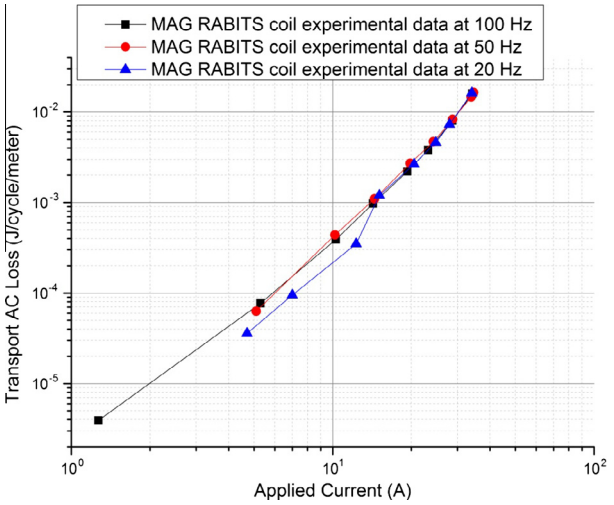

Fig. 5. Self-field AC loss as a function of the transport current for MAG RABITS coil with magnetic substrate.

2.3. Experimental results

The experiments were performed at 20 Hz, 50 Hz and 100 Hz for currents from 5 A to 35 A. The values of the transport current applied are all listed as the RMS value I_{rms}. The results for the NON MAG coil and the MAG RABITS coil are presented in Figs. 4 and 5 respectively. A slight frequency dependence of the losses at applied current less than 12 A in these two figures can be explained by an eddy current loss contribution from the Cu stabilizing layer. After 12 A, it shows that the transport AC loss per cycle is practically independent of the AC frequency. This observation confirms the assumption that the AC loss in the both coils could be well described as a hysteretic loss and that the effect of the eddy currents in all the metallic parts are negligible.

AC loss comparison between NON MAG and MAG RABITS is shown in Fig. 6. Only the results measured at 50 Hz were selected for this comparison. In Fig. 6, we also included the Norris' formula for a strip [20], using the respective measured critical current. The measured values are roughly 6 times higher for the MAG RABITS coil and 3 times higher for the NON MAG coil than the corresponding Norris Strip Calculations. It is well known that the Norris equations are derived based on the critical state model, and more effective for the low temperature superconductors. For high temperature superconductors such as YBCO tapes, some giant creep that significantly affects the AC loss in the coil and results in going beyond the explanation of the Norris equation [21]. According to the experimental results, the MAG RABITS coil generated higher AC loss than that the NON MAG coil. However, the difference was reduced as the current reaches the maximum measured value of 35 A. This effect could be caused by the magnetic substrate – a magnetization loss, which significantly increases AC loss at rather lower currents. At higher currents the magnetization loss is saturated. In this way, its share on the total loss is reduced. To better understand AC loss origins in both coils, computer simulations were performed. As will be discussed in the next paragraphs, the effect of the magnetic substrate is more complex.

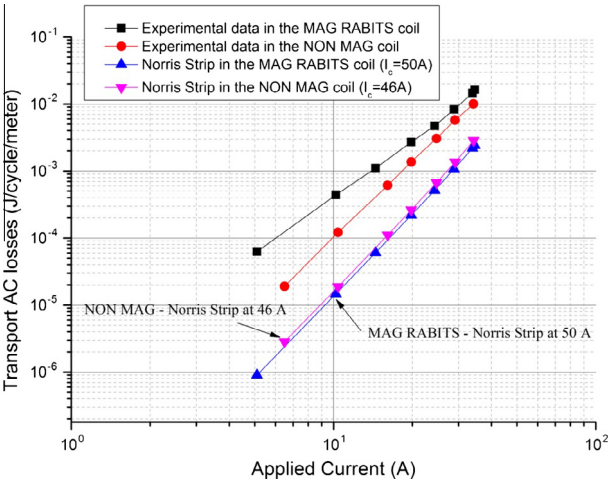

Fig. 6. Experimental transport AC loss comparison between MAG RABITS and NON MAG coils at 50 Hz.

3. Computer modelling

3.1. Model description

2D axial symmetrical H formulation was applied to the simple models of both coils. The racetrack geometry was simplified to an infinitely long model in the z direction. In this way, it represents the cross-section of the coil in x, y projection. The H_x and H_y represent the magnetic fields in x and y directions respectively. In 2D geometry, the induced or input current J_z in the superconductor flows in the z direction. Resulting in electric field of $E_z = \rho J_z$.

Two elementary equations are taken. Faraday's law:

$$\mu_0 \frac{\partial H}{\partial t} + \nabla \times \rho J_z = 0 \tag{1}$$

Ampere's law:

$$J_z = \frac{\partial Hy}{\partial x} - \frac{\partial Hx}{\partial y} \tag{2}$$

The resistivity of different sub-domains in this model has to be defined. The electric properties of superconductors can be described by the E–J power law:

$$\rho = \frac{E0}{Jc} \cdot \left(\frac{Jz}{Jc}\right)^{n-1} \tag{3}$$

In order to calculate AC loss, $E_z \cdot J_z$ was integrated over all the YBCO domains (J/cycle/m) of the model and it was then divided it by the total number of turns. The coil geometry as represented

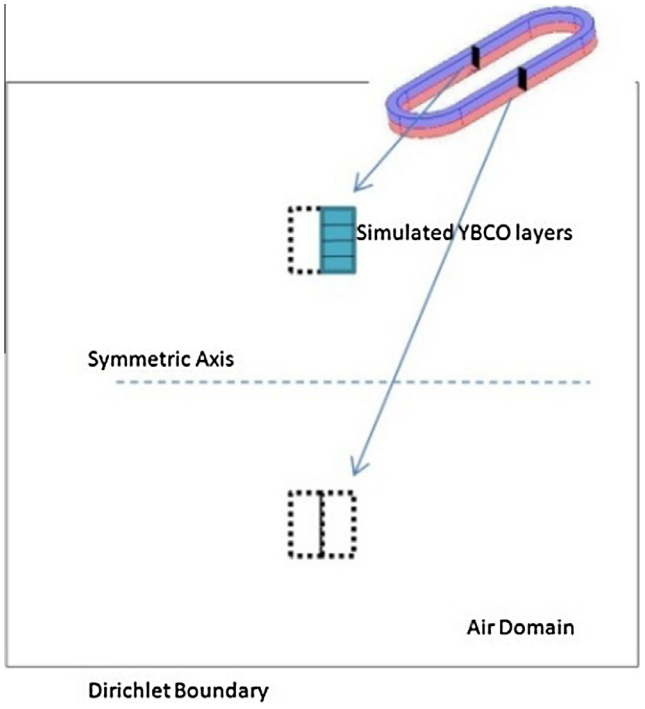

Fig. 7. Geometry of the axial symmetric model showing the cross-section of a pancake coil.

in the model is shown in Fig. 7. It was assumed that the air domain is large enough for the magnetic field to decay to zero on the boundary. Dirichlet boundary condition was applied in the air sub-domain with $H_y = 0$ for the y axis boundary of the symmetric line. Neumann boundary condition was applied to the boundaries of the superconductor and ferromagnetic substrate sub-domain. The linear curl shape function was employed in the electromagnetic simulation.

Applied current was assigned to each YBCO layer using the Pointwise constraint of COMSOL. The integration of local J_z in each YBCO layer gave the total current of one turn. The Pointwise constraint equalled the total current to the predefined applied current. A distributed mapped mesh was applied to the YBCO domains to control the total mesh size. The free triangular mesh was applied to the air domain [22]. Extra care was taken to ensure that all YBCO domains have identically mapped meshes.

The n value was defined from DC measurements of the superconductor's highly nonlinear I–V characteristic and usually ranged from 5 to 130 for type-II superconductors [23]. In this model, $n = 21$ is used. This value is reasonable from other studies on similar HTS tapes [24]. $E_0 = 1\ \mu V\ cm^{-1}$voltage criterion was used.

3.2. Tape anisotropy

Angular anisotropy of the 2G HTS tapes in external magnetic field is well known and more-less satisfactory explained phenomenon. However, the NON MAG tape expresses unusual asymmetric angular J_c dependence, which is reported in several publications [24–26]. It would be very complicated to find a simple fitting function for such an asymmetric J_c dependence. Therefore, a simple method based on the experimental data for the normalized critical current dependence was used. The experimental data were used directly in a single variable as $G(\theta)$. The anisotropy dependence of critical current density $J_c(B)$ is then illustrated by the following expression proposed by Zhang et al. [27]:

$$J_c(B) = J_{c0} \times \{P1(B) + [P2(B) - P1(B)] \times G(\theta)\} \quad (4)$$

The $G(\theta)$ parameter of Eq. (5) was estimated according to angular resolved measurements, which were applied on both types of tapes The measurements were performed at an external magnetic field of 2 mT. When $\theta = 9°$, we have $G(\theta) = 1$, $J_c(B) = J_c * P1(B)$; when $\theta = 18°$, we have $G(\theta) = 1$, $J_c(B)$ 8 $J_c * P2(B)$ For other θ values, the angle dependency of $J_c(B)$ is modulated by $G(\theta)$, and the magnitude dependency is modulated by $P1(B)$ and $P2(B)$.

We use the linear interpolation method to define $P1(B)$, $P2(B)$ and $G(\theta)$ which is based on the measurement results in [28]. The explanations of parameters used in Eq. (4) are shown in Table 3. It is an accurate and simple method to estimate the critical current properties of 2G YBCO tapes as it only require the values measured within perpendicular and parallel directions.

3.3. Ferromagnetic substrate definition

In the coated conductors with ferromagnetic substrate, the total AC loss is mainly due to the superconductor layer and the ferromagnetic substrate. The ferromagnetic effect on the superconductor substrate in a single tape or stack configurations was investigated by [6,29,30]. In this paper we modified the model by adding the ferromagnetic substrate according to the paper [28]. The eddy current loss in the metal stabilizer layer of coated conductor was assumed to be negligible.

In the MAG RABITS coated conductor model, the relative permeability μ_r is a function of magnetic field $\mu_r(H)$, which is represented in Eq. (5) [29]:

$$\mu_r(H) = 1 + 30600\left(1 - \exp\left(-\left(\frac{H}{295}\right)^{2.5}\right)\right)H^{-0.81} + 45 \times \exp\left(-\left(\frac{H}{120}\right)^{2.5}\right) \quad (5)$$

where H represents the amplitude of the magnetic field, $H = \sqrt{H_x^2 + H_y^2}$. With this fitting function, $\mu_r(H)$ tends to 46 when H goes to zero and $\mu_r(H)$ tends to 1 when H goes to infinity. The fitting function shows good agreement with the experimental data which was determined and published in [12].

According to Maxwell's equations (Eqs. (1) and (2)), the governing equations can be written [29]:

$$\frac{\partial E_z}{\partial x} = \mu_0\left[\frac{\partial \mu_r(H)}{\partial t}H_y + \mu_r(H)\frac{\partial H_y}{\partial t}\right] \quad (6)$$

$$\frac{\partial E_z}{\partial y} = \mu_0\left[\frac{\partial \mu_r(H)}{\partial t}H_x + \mu_r(H)\frac{\partial H_x}{\partial t}\right] \quad (7)$$

H_x and H_y represent the components of the magnetic field in the x and y directions. The induced electric field and current density have only single z-component. They are denoted as E_z and J_z. The total AC loss generated in the MAG RABITS coil is the sum of the hysteresis loss from the superconducting layers and the ferromagnetic loss from the magnetic substrate layers. The superconducting hysteresis loss was calculated by integrating the current density and electric field over the cross-section of the overall HTS layer. For the ferro-

Table 3
Eq. (4) parameters definition.

Parameters	Definition
J_{c0}	Self-field critical current density
$P1(B)$	Perpendicular field dependency
$P2(B)$	Parallel field dependency
$G(\theta)$	Normalized angle dependency under 200 mT

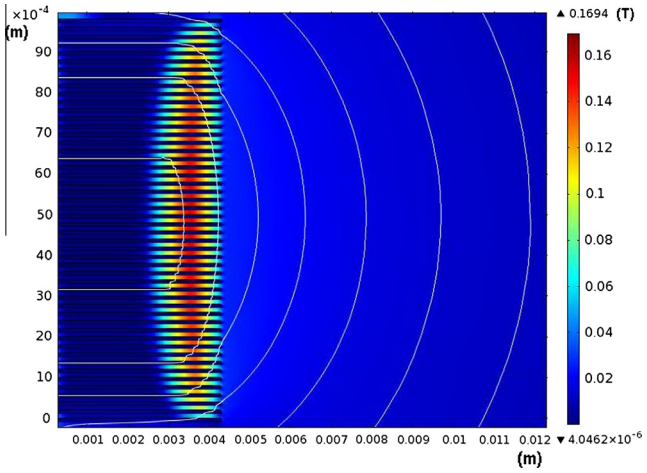

Fig. 8. Magnetic flux density of MAG RABITS racetrack coils with applied current at 35 A.

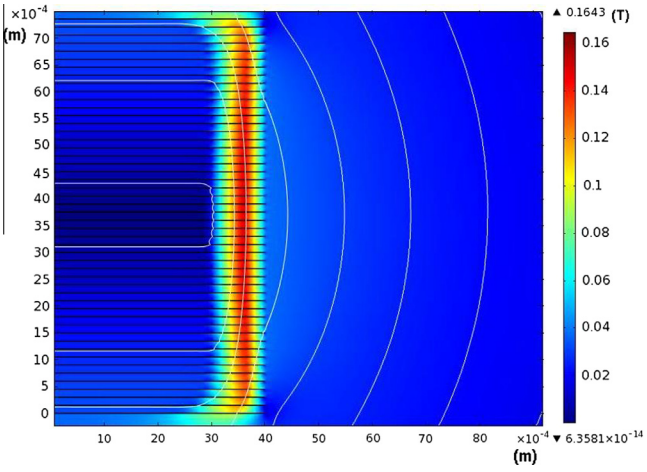

Fig. 9. Magnetic flux density of NON MAG racetrack coils with applied current at 35 A.

magnetic loss Q_{fe}, it is the area of the B–H loop in the magnetic substrate and is a function of the B_{max}, the maximum magnetic field of the loop. A fitting function of Q_{fe} based on the experimental data [12] is represented in the following equation [29]:

$$Q_{fe}(B_{max}) = \begin{cases} 4611.4B_{max}^{1.884} & B_{max} \le 0.164 \\ 210\left(1 - \exp\left(-(6.5B_{max})^4\right)\right) & B_{max} \ge 0.164 \end{cases} \quad (8)$$

As shown in Eq. (8), $Q_{fe}(B_{max})$ represents the ferromagnetic loss and B_{max} represents the maximum magnetic field which is seen in the substrate rather than the maximum magnetic field in the whole coil. As B_{max} tends to infinity, the ferromagnetic loss in the substrate gets saturated at the value of 210 J/m^3/cycle. The total ferromagnetic loss dissipated in the substrate is the integral of the loss distribution over substrate cross-section.

3.4. Results and validation

Fig. 8 shows the magnetic flux density at an AC transport current at 35 A. The flux lines change to a triangular shape and get the deepest penetration in the middle of the stack and become shallow in the top and bottom. The dark[1] blue area in the middle

[1] For interpretation of color in Fig. 8, the reader is referred to the web version of this article.

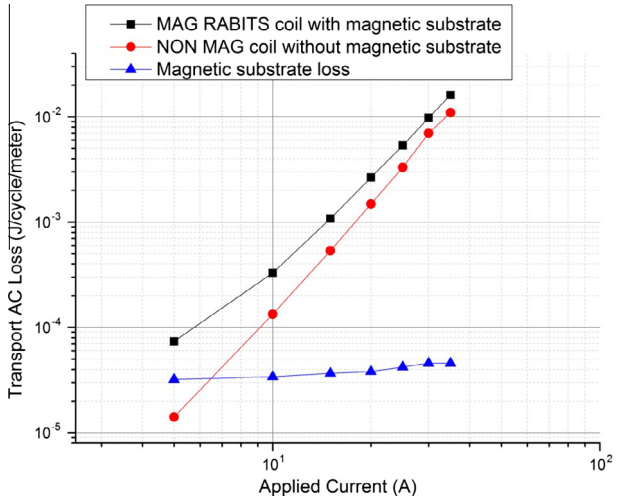

Fig. 10. Comparison of simulated transport AC loss for YBCO coils with and without magnetic substrate.

of the coil appeared to be the low magnetic field according to the colour index line on the right side, alternatively, the bright red area referred to the high magnetic field region. Fig. 9 represents the same case in the NON MAG coil. In this case, the flux lines and the shape line are identical and very consistent from the top to the bottom. The black horizontal lines within the region of the coil represent each layer of the superconducting coil. Based on these two figures, the MAG RABITS coil has higher magnetic flux penetration to the middle of the coil which can be explained as the presence of the magnetic substrate and an increase of permeability around each superconductor tape within the whole stack of coil. These attributors would consequently increase the total AC loss in the MAG RABITS coil.

Fig. 10 summarizes calculated AC loss from the models. The figure shows an interesting discovery, as magnetic loss completely saturates at 30 A. While magnetization loss plays an important role at low currents, at higher currents the magnetization loss is completely negligible. The proportion of this loss at 25 A is only 0.8%. It also shows that the total transport AC loss in the coil with the magnetic substrate (MAG RABITS) is always higher than that in the coil without magnetic substrate (NON MAG) which validates the results that published in [14].

Experimental and simulation results are in very good agreement. This is expressed in Fig. 11 where the experimental and simulation results are plotted in a single graph. To be mentioned here, at 35 A, there is still a small difference of 1.2% for the MAG RABITS coil and 2.2% for the NON MAG coil between the measurements and simulations. In addition, the graph contains the line with magnetization loss of the MAG RABITS coil.

It is important to understand that total loss in the MAG RABITS magnetic substrate is negligible. It saturates at currents of about 30 A. At 25 A, it contributes only 0.8% of total AC loss in the coil. According to the presented data at 35 A, total AC loss of the MAG RABITS coil is 36% higher than of the NON MAG coil. Although, the magnetic substrate is the main factor effecting transport AC loss in the superconducting layer, it is obvious that the difference is not coming from loss within the substrate. To prove this statement a new simulation of the MAG RABITS coil was done. In this simulation, μ_r of the substrate was defined as 1, which made the substrate non-magnetic. All the other parameters remained the same, which is academic rather than a realistic situation. However, this kind of simulation can very well describe the effect of the magnetic substrate. As shown in

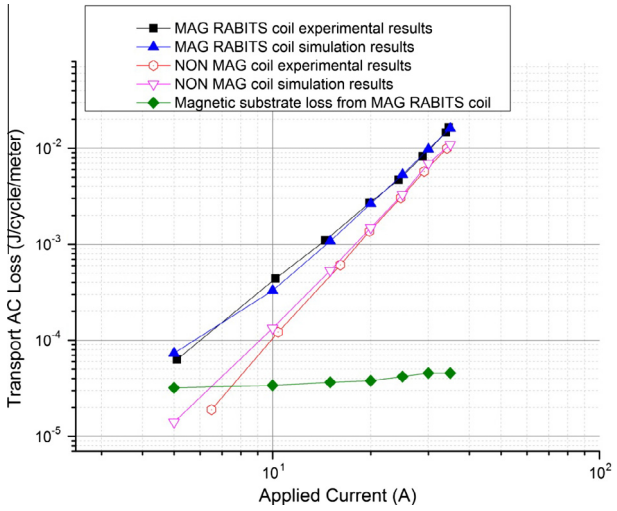

Fig. 11. Comparison of simulation and experimental data at 35 A and 50 Hz.

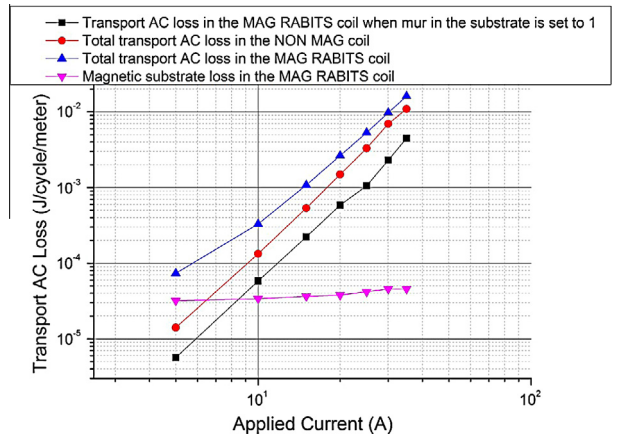

Fig. 12. The contributions of transport AC loss in MAG RABITS coil from magnetic substrate and superconducting layer.

Fig. 12, AC loss decreased significantly. They are even lower than the losses of the NON MAG coil; however, this was expected as measured critical current of the MAG RABITS coil was higher. According to the results, the total AC loss of the MAG RABITS tape could be divided into two parts: transport AC loss in the superconducting layer and magnetic loss in the substrate. The transport AC loss in the superconductor could be divided into the part caused by the magnetic substrate and the part caused by other effects. All those fractions can be seen in Fig. 12. It is relatively easy to assume that additional magnetic field introduced into the superconductor by the magnetic substrate will create additional AC loss.

4. Conclusion

In this paper, a comparative study of AC loss of two 2G HTS racetrack coils was presented. A MAG RABITS coil with magnetic substrate and a NON MAG coil with a non-magnetic substrate were used as samples. Both, experiments and simulations were successfully performed. An agreement between both methods was reported. The new simple method to describe YBCO angular anisotropy in magnetic field [27], developed by the EPEC Superconductivity group in Cambridge, was successfully applied. Analysis shows that the transport AC loss in the MAG RABITS coil is about 36% higher than that in the NON MAG coil. It was found that, despite losses inside the magnetic substrate being negligible, the substrate is responsible for a higher AC loss. It is an important message for 2G HTS tape manufacturers to avoid using magnetic materials. In conclusion, by keeping all the substrate properties with non-magnetic materials, coil performance and AC loss could be significantly improved.

References

[1] J.R. Hull, Rep. Prog. Phys. 66 (2003) 1865.
[2] D. Larbalestier, M. Feldmann, A. Polyanskii, Nature 414 (2001).
[3] M.P. Oomen, R. Nanke, M. Leghissa, Supercond. Sci. Technol. 16 (2003) 339.
[4] J.R. Clem, J.H. Claassen, Y. Mawatari, Supercond. Sci. Technol. 20 (2007) 1130.
[5] W. Yuan, A.M. Campbell, T.A. Coombs, Supercond. Sci. Technol. 22 (2009) 075028.
[6] E. Pardo, J. Šouc, J. Kováč, Supercond. Sci. Technol. 25 (2012) 035003.
[7] E. Pardo, Supercond. Sci. Technol. 21 (2008) 065014.
[8] F. Grilli, S.P. Ashworth, Supercond. Sci. Technol. 20 (2007) 794.
[9] L. Prigozhin, V. Sokolovsky, Supercond. Sci. Technol. 24 (2011) 075012.
[10] M. Polak, E. Demencik, L. Jansak, P. Mozola, D. Aized, C.L.H. Thieme, G.A. Levin, P.N. Barnes, Appl. Phys. Lett. 88 (2006) 23.
[11] F. Gömöry, M. Vojenčiak, E. Pardo, M. Solovyov, J. Šouc, Supercond. Sci. Technol. 23 (2010) 034012.
[12] D. Miyagi, Y. Yunoki, M. Umabuchi, N. Takahashi, O. Tsukamoto, Phys. C: Supercond. 468 (2008) 15.
[13] Y. Genenko, H. Rauh, P. Kruger, Appl. Phys. Lett. 98 (2011) 15.
[14] M. Ainslie, V. Rodriguez-Zermeno, W. Yuan, T. Flack, T. Coombs, Supercond. Sci. Technol. 24 (2011) 045005.
[15] S.P. Ashworth, M. Suenaga, Phys. C: Supercond. 329 (2000) 149159.
[16] N. Amemiya, Y. Iijima, K. Kakimoto, Supercond. Sci. Technol. 17 (2004) 983988.
[17] M. Ciszek, A.M. Campbell, Phys. C: Supercond. 233 (1994) 203208.
[18] E. Martínez, C. Beduz, Y.B. Huang, Physica C 331 (2000) 216226.
[19] Y. Jiang, W. Xian, Z. Hong, T.A. Coombs, Supercond. Sci. Technol. 21 (2008) 065011.
[20] W.T. Norris, J. Phys. D: Appl. Phys. 3 (1970) 489507.
[21] H. Luo, J.W. Lin, S.Y. Ding, Phys. C: Supercond. 386 (2003) 81.
[22] V.M. Rodriguez-Zermeno, C. Træholt, T. Zirngibl, E. Seiler, A.B. Abrahamsen, M.P. Sørensen, IEEE Trans. Appl. Supercond. 21 (2010) 3.
[23] F. Grilli, Y.L. Floch, M.C. Bouzo, E. Vinot, I. Klutsch, G. Meunier, P. Tixador, B. Dutoit, IEEE Trans. Appl. Supercond. 15 (2005) 1725.
[24] M. Chudy, M. Eisterer, H.W. Weber, Phys. C: Supercond. 470 (2010) 1300–1303.
[25] T.G. Holesinger, O. Ugurlu, L. Civale, Y. Chen, X. Xiong, Y. Xie, V. Selvamanickam, Supercond. Sci. Technol. 22 (2009) 045025.
[26] Z. Chen, Y. Chen, Y. Xie, V. Selvamanickam, D.C. Larbalestier, Supercond. Sci. Technol. 22 (2009) 055013.
[27] M. Zhang, J. Kim, S. Pamidi, M. Chudy, W. Yuan, T. Coombs, J. Appl. Phys. 111 (2012) 083902.
[28] E. Pardo, M. Vojenčiak, F. Gömöry, J. Šouc, Supercond. Sci. Technol. 24 (2011) 065007.
[29] D.N. Nguyen, J.O. Willis, F. Sirois, F. Grilli, Supercond. Sci. Technol. 23 (2010) 025001.
[30] M. Majoros, L. Ye, A.V. Velichko, T.A. Coombs, M.D. Sumption, E.W. Collings, Supercond. Sci. Technol. 20 (2007) 299.

Theoretical and Experimental Magnetization Loss Comparison Between IBAD Coils and RABiTS Coils

Yiran Chen, *Member, IEEE*, Min Zhang, *Member, IEEE*, Michal Chudy, *Member, IEEE*, Wei Wang, *Member, IEEE*, Zhaoyang Zhong, Zhen Huang, and Tim Coombs, *Member, IEEE*

***Abstract*—This paper presents a comparative study of ac magnetization losses in two types of 2 G HTS racetrack coils. The magnetic substrate made by RABiTS is the main difference between the two types, because ferromagnetic loss caused by magnetic substrate is accounted into the total ac losses. IBAD and RABiTS tapes were successfully wound into racetrack shape with identical geometry. The measurements were carried out by using electromagnetic method with pick-up coils under a sinusoidally varying external magnetic field, with amplitudes up to 27 mT, ranging from 10 Hz to 100 Hz at a temperature of 77 K. The field was oriented perpendicularly to the surface of the tapes. Experimental measurements were validated by applying theoretical models and the results showed that the magnetization loss in the MAG RABiTS coil is always higher than that in the NON MAG coil due to the presence of the magnetic substrate, which increases the magnetic field penetration into the coil and causes higher magnetic flux density within the penetrated region.**

***Index Terms*—AC magnetization loss, YBCO racetrack coil.**

I. Introduction

DISSIPATION appears in different kinds of materials when they are exposed to AC magnetic field. This phenomenon, called magnetization AC loss, is of particular importance for superconducting coils considered for electrical power applications. It has direct consequences for the rated cooling power of cryogenic machines and thus the installation cost. It is therefore important to be able to measure the losses on HTS coils under appropriate conditions of magnetic field. The electrical method for measuring magnetization loss due to an applied oscillating magnetic field is now well established [1]. Using a pick-up coil technique the magnetic losses can be obtained with good accuracy—the voltage from the pick-up coil is multiplied by the field value and the integral over an ac cycle can be shown to be the same as $\int M\partial H$. A number of groups have published data on losses with changing magnetic field [2]–[4] and great efforts have been applied on reducing AC losses of 2G HTS tapes [5], [6]. However, not many papers have focused on comparative studies of AC magnetization loss in 2G tapes which is mainly different from the substrate. In 2G HTS YBCO coated conductors, the tape architecture was proven to be an important issue, which directly influences AC losses. This work is focused on exploring the AC magnetization loss behavior of two types of HTS racetrack coils. The first coil—denoted as MAG RABiTS is made of YBCO coated conductor which is based on the RABiTS template.

Manuscript received October 4, 2012; accepted December 20, 2012. Date of publication December 28, 2012; date of current version February 6, 2013. This work was supported in part by the EPSRC and Rolls Royce Funding.

The authors are with the Engineering Department, Cambridge University, Cambridge, CB2 1PZ, U.K. (e-mail: yc315@cam.ac.uk; mz279@cam.ac.uk; mc672@cam.ac.uk; ww283@cam.ac.uk; zz272@cam.ac.uk; zh252@cam.ac.uk; tac1000@cam.ac.uk).

Color versions of one or more of the figures in this paper are available online at http://ieeexplore.ieee.org.

Digital Object Identifier 10.1109/TASC.2012.2236592

TABLE I
SPECIFICATION OF THE MAG RABiTS COIL AND NON MAG COIL

Parameters	MAG RABiTS	NON MAG (IBAD)
Critical current of the tape, I_c	100 A	120 A and higher
Tape width, w	4.35 mm	4 mm
Tape thickness	0.2 mm	0.1 mm
YBCO layer thickness	1 μm	1 μm
Number of turns	50	50
Inner radius	2.4 cm	2.4 cm
Outer radius	3.3 cm	3.25 cm
Substrate thickness	50 μm	50 μm

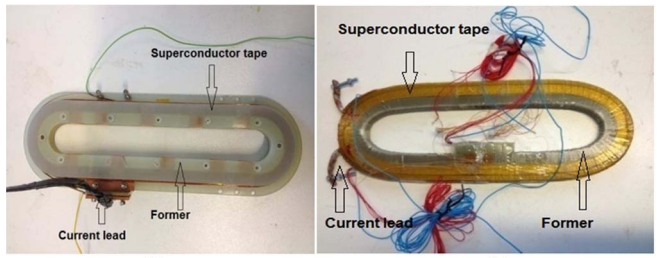

(a) (b)

Fig. 1. (a) NON MAG superconducting racetrack coil with nonmagnetic substrate. (b) MAG RABiTS superconducting racetrack coil with RABiTS substrate.

This template creates a basis for a textured substrate along with a metal organic deposited (MOD) YBCO layer. The substrate consists of a textured nickel tungsten alloy, which is magnetic. The second coil—denoted as NON MAG has a nonmagnetic substrate. The tape consists of several buffer layers i.e. IBAD MgO template.

II. Experimental

A. Samples

Both, MAG RABiTS and NON MAG (IBAD) HTS racetrack coils were manufactured from thin ∼4 mm wide tapes, which were arranged in two stacks—double racetrack pancake coils. The total length of the tape used in the coils is ∼50 m creating 50 turns in the pancake. Both racetrack coils have very similar geometry. All the specifications are listed in Table I. The main difference of the outer radius results from different thickness of the 2G HTS tapes. Photographs of the coils are presented in Figs. 1(a) and (b). It can be seen, that despite of rather different coil shells, the tape arrangement is almost identical.

B. Experimental Set-Up

The magnetization loss was measured using a pick-up coil method. The schematic experimental configuration for measurement of magnetization loss generated in the sample coils is shown in Fig. 2. The field was applied perpendicular to the tape face by a solenoid with an iron core of 15 cm diameter and 22 cm length. It was wound with 2300 turns of Cu wire

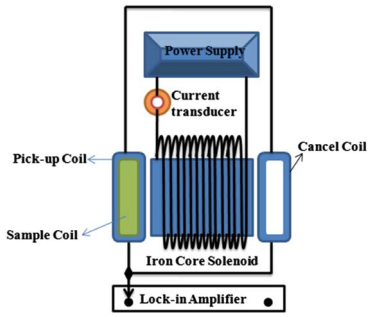

Fig. 2. Experimental set-up configuration.

(diameter: 2.5 mm). The applied frequency ranged from 10 Hz–100 Hz with maximum amplitude of 27 mT. Due to limited experimental conditions, the magnet generated a magnetic field with restricted effecting regions which can only cover $\sim(1/3)$ of the entire surface of the coil.

The pick-up coil consisted of a single layer racetrack shape winding with 300 turns of Cu wire (diameter: 0.7 mm). In order to make the measurement results more accurate, the pick-up coil was wound to nominally match the dimensions of the sample coil. The compensation coil was placed at a position symmetrically along the axial direction of the solenoid. Calibration was performed by measuring the loss of a Cu racetrack shape coil with known properties. The wire diameter was 0.5 mm. The 77 K resistance of the Cu sample was measured using four-point technique which results in 0.26 $\mu\Omega$/cm and the resistance $R_{\mathrm{Cu}} = 0.29$ mΩ. The loss values were then employed to extract a proportionality ratio to be compared to the directly measured value.

The magnetization loss per cycle per unit volume generated in HTS coil under a changing magnetic field can be obtained from the Poynting vector expressed as:

$$Q = -\int_0^T \oint (\vec{E} \times \vec{H}) \cdot d\vec{S}\, dt. \tag{1}$$

Where, V_S is the sample volume, T is one cycle period and S is the sample volume. E and H are the electric field and external magnetic field in the circuit respectively. The power loss was measured by detecting the subtracted voltage between the pick-up coil and compensation coil connecting in anti-series and the current from the feeding line to magnetic source as shown in Fig. 2. Therefore, (1) can be rewritten as (2) by replacing electric field E and magnetic field H with voltage $v(t)$ and current $i(t)$.

$$Q = C_p K \int_0^T v(t) \cdot i(t) dt. \tag{2}$$

Where, k is the magnetic constant which is the magnetic flux density created at the sample coil per background magnet current, and C_p is the pick—up coil calibration factor.

C. Experimental Results

The experiments were performed at 10 Hz, 50 Hz and 100 Hz. The results for the NON MAG coil and the MAG RABiTS coil are presented in Figs. 3 and 4, respectively. A slight frequency dependence of the losses at field less than 15 mT can be explained by an eddy current loss contribution from the

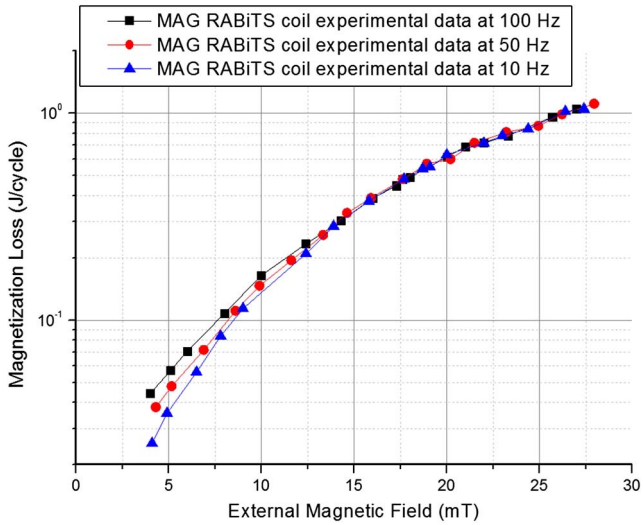

Fig. 3. Magnetization loss as a function of external magnetic field for NON MAG coil without magnetic substrate.

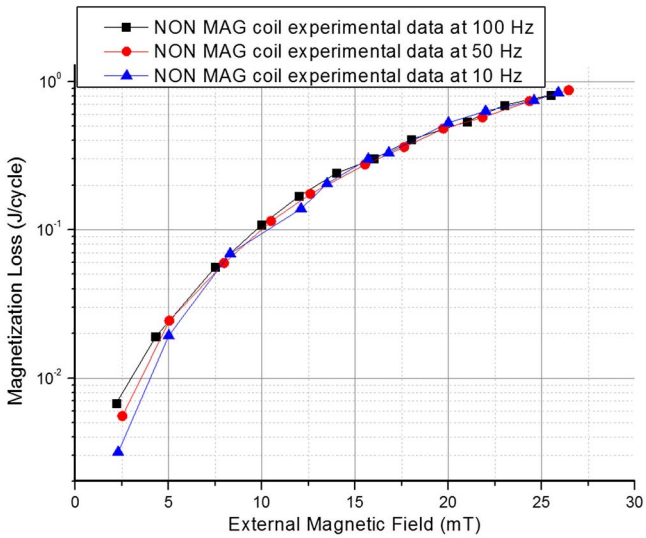

Fig. 4. Magnetization loss as a function of external magnetic field for MAG RABiTS coil with magnetic substrate.

Cu stabilizing layer. This layer covers the entire YBCO film, enabling the closing of the eddy currents at the edges.

Magnetization loss comparison between NON MAG and MAG RABiTS is shown in Fig. 5. Only results measured at 50 Hz were selected for this comparison. According to the experimental results, MAG RABiTS coil generated higher magnetization losses than that in the NON MAG coil. This effect could be caused by the magnetic substrate, which significantly enhances AC losses at rather low external magnetic field. Since the magnet is not able to provide uniform magnetic flux cross the entire area of the coil, the experimental data in Fig. 5 is not sufficient proof of this effect in general. For a better understanding of magnetization loss origins in both coils, computer simulations were performed.

III. Computer Modeling

A. Model Description

The numerical analysis was performed with finite element method (FEM) in 2D to prove the reliability of the loss measurement in previous section. The racetrack geometry was

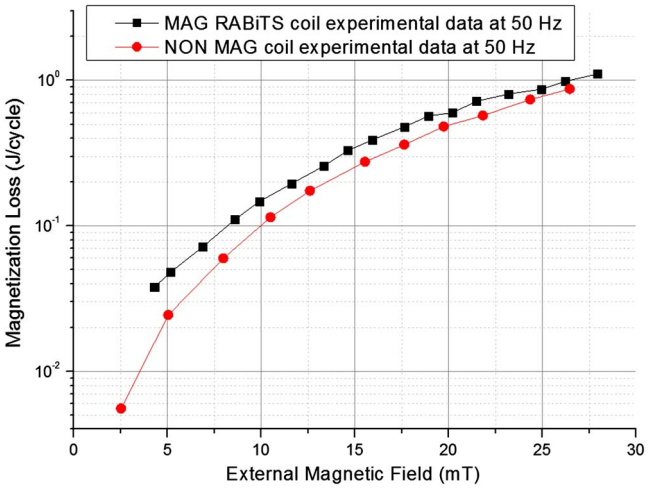

Fig. 5. Experimental magnetization loss between MAG RABiTS and NON MAG coils at 50 Hz.

simplified to an infinitely long model in the z direction. H_x and H_y represent the magnetic fields in the x and y directions respectively. In 2D geometry, the induced or input current J_z in the superconductor flows in the z direction. Resulting in an electric field of $E_z = \rho J_z$. The resistivity of different sub-domains in this model has to be defined. The electric properties of superconductors can be described by E–J power law:

$$\rho = \frac{E_0}{Jc} \cdot \left(\frac{J_Z}{J_c}\right)^{n-1}. \tag{3}$$

In order to calculate magnetization loss, $E_z \cdot J_z$ was integrated over all the YBCO domains (J/cycle/m) of the model and then divided by total turns. Neumann boundary condition was applied to the boundaries of the superconductor and ferromagnetic substrate sub-domain.

The over-layer and buffer stack were ignored as it is assumed they would not affect the calculation. The n value was defined from *DC* measurements of the superconductor's highly nonlinear I–V characteristic and usually ranged from 5–130 for type-II superconductors [7]. In this model, $n = 21$ is used. This value is considered reasonable based on other studies on similar HTS tapes [8]–[10]. $E_0 = 1\ \mu\text{Vcm}^{-1}$ voltage criterion was used.

B. Tape Anisotropy

Anisotropy of the YBCO tape under an external magnetic field would greatly influence the current and magnetic distribution inside the coil [11], [12]. A simple method avoiding complicated optimization of variables determination was used. The experimental data were used directly in a single variable as $G(\theta)$. The anisotropy dependence of critical current density $J_c(B)$ is then illustrated by the following expression (4) [13]:

$$J_c(B) = J_{c0} \times \{P1(B) + [P2(B) - P1(B)] \times G(\theta). \tag{4}$$

The $G(\theta)$ parameter of the Equation (8) was estimated according to angular resolved measurements, which were applied on both types of tapes. The measurements were performed at an external magnetic field of 200 mT. When $\theta = 90°$, we have $G(\theta) = 0$, $Jc(B) = Jc0 * P1(B)$; when $\theta = 180°$, we have $G(\theta) = 1$, $Jc(B) = Jc0 * P2(B)$. For other θ values, the angle dependency of $Jc(B)$ is modulated by $G(\theta)$, and the magnitude dependency is modulated by $P1(B)$ and $P2(B)$. We use the linear interpolation method to define $P1(B)$, $P2(B)$ and $G(\theta)$ which is based on the measurement results in new [14]. The explanations of parameters used in (8) are shown in Table II.

TABLE II
EQUATION (6) PARAMETERS DEFINITION

Parameters	Definition
J_{c0}	Self-field critical current density
P1(B)	Perpendicular field dependency
P2(B)	Parallel field dependency
G(θ)	Normalized angle dependency under 100 mT

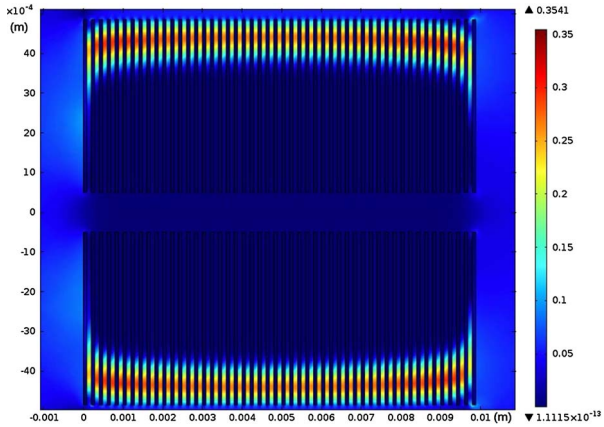

Fig. 6. Magnetic field distribution of MAG RABiTS racetrack coils.

C. Ferromagnetic Substrate Definition

In the conductors coated with ferromagnetic substrate, the total AC losses come mainly from the superconductor layer and the ferromagnetic substrate. The ferromagnetic effect on the superconductor substrate in a single tape or stack configurations was investigated by [15]–[17]. In this paper we modified the model by adding the ferromagnetic substrate according to the paper [15]. The eddy current loss in the metal stabilizer layer of coated conductor was assumed to be negligible. The heat losses from the ferromagnetic substrate Q_{fe} were calculated by the magnetic field distribution in this layer.

$$Q_{fe}(B_m) = \begin{cases} 4611.4 B_{max}^{1.884} & B_{max} \le 0.164 \\ 210\left(1 - \exp\left(-(6.5 B_{max})^4\right)\right) & B_{max} \ge 0.164 \end{cases}. \tag{5}$$

D. Results and Validation

We accomplished numerical calculations for two types of coils results shown in Figs. 6 and 7 with the magnetic field distribution at 50 mT external magnetic field.

The magnetic field is lower in inner tape than outer tape due to magnetic shielding by diamagnetism of the superconductors. Fig. 8 summarizes calculated magnetization losses from the models. The figure shows an interesting story, as the magnetic substrate in the MAG RABiTS coil completely saturates at 20 mT. While ferromagnetic loss plays an important role under low external magnetic field (< 20 mT), at higher changing field the superconductor hysteretic loss tends to dominate the ferromagnetic loss. It also shows that the total magnetization loss in the coil with the magnetic substrate (MAG RABiTS) is about 30% higher than that in the coil without magnetic substrate (NON MAG) at an external magnetic field of 100 mT

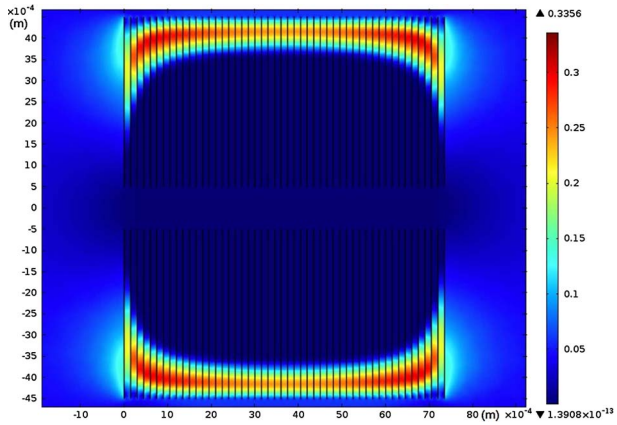

Fig. 7. Magnetic field distribution of NON MAG racetrack coils.

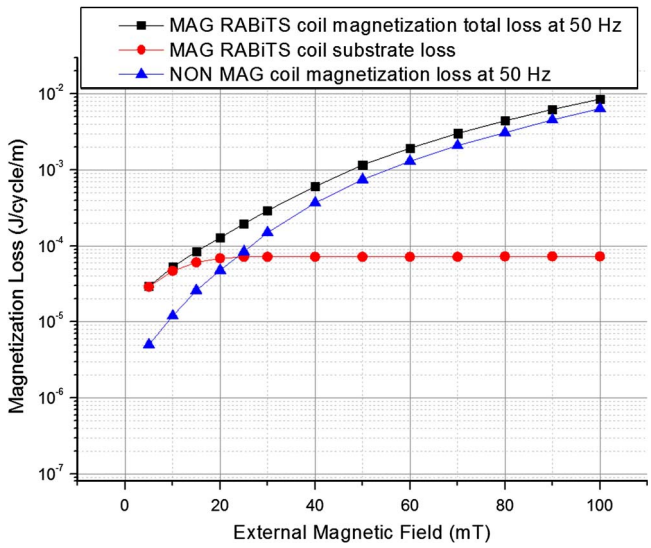

Fig. 8. Comparison of simulated magnetization losses between MAG RABiTS and NON MAG coils.

due to increased penetration of the magnetic field into the coil and higher magnetic flux density within the penetrated region.

While the calculated results in Fig. 8 validated the conclusion deduced from the experiment in Section II, however the substrate usually has a strong effect on pinning center template of a superconductor. By FEM simulations, it is not possible to find a new $J_c(B)$ function of the superconductor, as $J_c(B)$ is a function of microscopic vortex pinning behavior. In special cases or field angles, the magnetic substrate could even enhance properties, as ferromagnetic pinning centers within superconductors were proven to be effective pinning centers [18]. By using FEM simulations, the negative effect of the magnetic substrate was explored. Nevertheless, the microscopic effect of the vortex pinning could be positive. For practical applications, where exposed under a varying magnetic field, superconducting coils should be wound where possible using coated conductors with a non-magnetic substrate to reduce the total AC losses in the coil.

IV. Conclusion

In this paper, a complex comparative study of the magnetization loss of two 2G HTS racetrack coils was presented. Both experiments and simulations were successfully performed. Although the experimental results only presented the magnetization loss of coils where $\sim(1/3)$ of the entire surface were under a uniform changing magnetic flux, these limitations due to the experimental conditions were compensated for by using well established models and validated the conclusion of the experimental measurement.

The new simple method to describe YBCO angular anisotropy in magnetic field was successfully applied. Analysis shows that the magnetization loss in the MAG RABiTS coil is always higher than that in the NON MAG coil due to the presence of the magnetic substrate that increases penetration of the magnetic field into the coil and higher magnetic flux density within the penetrated region. The ferromagnetic loss of the substrate itself is found to be negligible in most cases, except for small magnitudes of external varied magnetic field where the substrate is not yet saturated. In conclusion, by keeping all the substrate properties with non-magnetic materials, coil performance and magnetization losses could be significantly improved.

References

[1] H. Eckelmann, M. Quilitz, and W. Goldacker, "AC transport current losses of multifilamentary Bi(2223) tapes with varying filament geometries," *Phys. C*, vol. 78, p. 4584, 1995.

[2] J. K. Lee, M. J. Park, and G. Cha, "Magnetization loss in HTS stacked tapes by various directional external magnetic fields," *IEEE Trans. Appl. Supercond.*, vol. 14, no. 2, 2004.

[3] J. Kim, P. Patil, J. Kvitkovic, and S. Pamidi, "Electrical characteristics of stacks of YBCO tapes in applied magnetic field," *IEEE Trans. Appl. Supercond.*, vol. 21, no. 3, 2001.

[4] M. D. Sumption, "AC loss in YBCO coated conductors exposed to external magentic field at 50–200 Hz," *Phys. C*, vol. 466, pp. 29–36, 2007.

[5] O. Tsukamoto, M. Liu, S. Odaka, D. Miyagi, and K. Ohmatsu, "AC magnetization loss characteristics of HTS coated-conductors with magnetic substrates," *Phys. C*, vol. 463, pp. 766–769, 2007.

[6] O. Tsukamoto, S. Sekizawa, A. K. M. Alamgir, and D. Miyagi, "Methods to reduce AC losses in HTS coated conductors with magnetic substrates," *Phys. C*, vol. 463, pp. 770–774, 2007.

[7] F. Grilli, Y. L. Floch, M. Costa-Bouzo, E. Vinot, I. Klutsch, G. Meunier, P. Tixador, and B. Dutoit, "Finite-element method modeling of superconductors: From 2-D to 3-D," *IEEE Trans. Appl. Supercond.*, vol. 15, no. 1, pp. 17–25, 2005.

[8] M. Chudy and H. W. Weber, "Asymmetric angular dependence of Jc in coated conductors prior to and after fast neutron irradiation," *Phys. C*, vol. 470, pp. 1300–1303, 2001.

[9] Z. Hong, Q. Jiang, R. Pei, A. M. Campbell, and T. A. Coombs, "A numerical method to estimate AC loss in superconducting coated conductors by finite element modelling," *Supercond. Sci. Technol.*, vol. 20, pp. 331–337, 2007.

[10] Z. Hong, A. M. Campbell, and T. A. Coombs, "Numerical solution of critical state in superconductivity by finite element software," *Supercond. Sci. Technol.*, vol. 19, pp. 1246–1252, 2006.

[11] M. Polak, L. Jansak, P. Mozola, D. Aized, C. L. H. Thieme, G. A. Levin, and P. N. Barnes, "AC losses in a YBa2Cu3O7 coil," *Appl. Phy. Lett.*, vol. 88, pp. 232–501, 2001.

[12] E. Pardo, "Modeling of coated conductor pancake coils with a large number of turns," *Supercond. Sci. Technol.*, vol. 21, p. 065014, 2008.

[13] M. Zhang, S. Pamidi, M. Chudy, W. Yuan, and T. A. Coombs, "Study of second generation, high-temperature superconducting coils: Determination of critical current," *J. Appl. Phys.*, vol. 111, no. 8, p. 083902, 2012.

[14] E. Pardo, M. Vojenciak, F. Gomory, and J. Soul, "Low-magnetic-field dependence and anisotropy of the critical current density in coated conductors," *Supercond. Sci. Technol.*, vol. 24, p. 065007, 2011.

[15] F. Gomory, E. Pardo, M. Solovyov, and J. Sorc, "AC losses in coated conductors," *Supercond. Sci. Technol.*, vol. 23, p. 034012, 2010.

[16] D. N. Nguyen, J. O. Willis, F. Sirois, and F. Grilli, "A new finite-element method simulation model for computing AC loss in roll assisted biaxially textured substrate YBCO tapes," *Supercond. Sci. Technol.*, vol. 23, no. 2, p. 025001, 2010.

[17] M. Majoros, A. V. Velichko, T. A. Coombs, M. D. Sumption, and E. W. Collings, "Transport AC losses in YBCO coated conductors," *Supercond. Sci. Technol.*, vol. 20, no. 9, p. S299, 2007.

[18] S. A. Harrington, "Practical vortex diodes from pinning enhanced YBa2Cu3O7-delta," *Appl. Phy. Lett.*, vol. 95, p. 022518, 2009.

Power Losses of 2G HTS Coils Measured in External Magnetic DC and Ripple Fields

M. Chudy, Y. Chen, M. Zhang, M. Baghdadi, J. Lalk, T. Pretorius, and T. Coombs

***Abstract*—Power losses are an important phenomenon in type-2 superconductors. Precise evaluation of power losses in superconducting coils is crucial for designing novel machines such as superconducting motors or generators. Although ac losses are relatively easy to measure with electrical methods, it is more difficult to measure power losses in the dc mode, which is induced by varying external magnetic fields, such as in a real operating environment. In particular, the problematic one could be the direct-drive wind generator, where several elements introduce nonsynchronous disturbances to the magnetic fields. Modeling had been carried out to estimate the power losses in second-generation high-temperature superconducting coils under various external dc or ripple fields; however, experimental work in the area is less common due to the difficulty of conducting experiments and special equipment requirements. In this paper, power losses under various magnetic fields are experimentally measured by the calorimetric method.**

***Index Terms*—Alternating-current losses, calorimetric method, ripple fields.**

I. Introduction

In RECENT years, high-temperature superconducting (HTS) applications such as motors and generators have been the subject of a high level of interest. Among all the possible applications of HTS devices, applications in renewable energy have very strong potential. Recent developments in wind energy generators are strongly focused on direct-drive wind turbines due to higher reliability, lower maintenance costs, and a lower noise profile. To remove the requirement for gearboxes, which are responsible for long periods of outages [1], bigger and heavier direct-drive generators are necessary. Since there are some weight and size limits for constructing and operating wind turbines, it seems that, for further wind-turbine performance upscaling, employment of superconductors is essential. Superconductors could significantly reduce the size and weight of wind generators. There are numerous studies dealing with the design of direct-drive synchronous superconducting wind generators with power rates of up to 10 MW [2]–[6]. Terao *et al.* [3] has presented a fully superconducting generator design with an MgB_2 stator and rotor made of YBCO second-generation (2G) HTS racetrack coils. Ohsaki *et al.* [4] presented a fully superconducting concept based on HTS tapes and Re(BCO) bulks. Stacks of 2G HTS tapes have shown superior magnetic properties [7] and represent real alternatives to the bulks. Therefore, a conceptual design of a generator (motor) based on magnets made from stacks of tapes will probably be available very soon. Nevertheless, design concepts with a superconducting rotor and a conventional stator are the most common and the most likely to be constructed first [2], [5]. The main reasons for keeping the stator nonsuperconducting are the ac losses. In a synchronous machine, the rotor (bulks or coils) operates in the dc mode, which is in general without any losses. Stator windings must produce ac fields, which mean power losses even in superconductors. It is widely known that ac losses in the stator of a fully superconducting machine are still too high for a feasible design; however, there are methods available to reduce them. One of them is to reduce the number of turns of armature coils and increase the number of poles, as suggested by Zhang *et al.* [8].

There remain many issues to be solved before superconducting generators and motors can achieve commercial production. Prices of 2G HTS tapes are still relatively high, and the world 2G HTS production capacities are insufficient to supply mass production, e.g., conceptual machines presented in [2] and [3], which require hundreds of kilometers of 2G HTS tapes. The other problem is power losses, which reduce the efficiency of the machine. Therefore, comprehensive studies of the power losses of the 2G HTS coils are crucial. Numerous outstanding publications deal with ac losses in 2G HTS tapes [9], [10]. Other researchers are focused on ac losses in racetrack or pancake coils [11]–[13] or in HTS generators as a whole [14]. The most important factor for superconducting generator or motor applications is to know ac losses (stator) and power losses in the rotor. Although the rotor superconducting coils are in the dc mode, power losses are introduced due to alternating ripple fields. In a synchronous motor or a generator, the magnetic field of the superconducting coil is phase-locked with the stator field as the coils are under balanced conditions and they experience a dc field from the armature; however, in real machines, some ripples in the field do occur. Ripple fields are also present in generators; however, dc fields are produced only by other rotor coils. Nonsynchronous disturbances resulting in unbalanced fields in the armature will create power losses in the superconducting rotor coils. In particular, in direct-drive wind

Manuscript received October 1, 2013; revised October 30, 2013 and November 7, 2013; accepted November 7, 2013. Date of publication November 14, 2013; date of current version December 12, 2013. This work was supported by the Engineering and Physical Sciences Research Council under Grant EPRSC EP/H019294/1. This paper was recommended by Associate Editor M. Parizh.

M. Chudy is with the Department of Engineering, University of Cambridge, Cambridge CB3 0FA, U.K., and also with the Graduate School of Technology Management, Department of Engineering and Technology Management, University of Pretoria, Pretoria 0001, South Africa (e-mail: mc672@cam.ac.uk).

Y. Chen, M. Zhang, M. Baghdadi, and T. Coombs are with the Department of Engineering, University of Cambridge, Cambridge CB3 0FA, U.K.

J. Lalk and T. Pretorius are with the Graduate School of Technology Management, Department of Engineering and Technology Management, University of Pretoria, Pretoria 0001, South Africa.

Color versions of one or more of the figures in this paper are available online at http://ieeexplore.ieee.org.

Digital Object Identifier 10.1109/TASC.2013.2291072

generators where the disturbances could be much higher as they are caused by nonconstant wind speeds and the tower shadow effect [15], [16]. Sources of power losses in wind generators and a rough estimation for particular design was presented by Mijatovic *et al.* [6]. Some computer modeling work, which analyzes losses caused by ripple fields, was presented in [17]–[19], even if there is an electrical experimental method available, which was presented by Pardo *et al.* [20] and Šouc *et al.* [21], that is not calorimetric and can deliver power-loss results under dc and certain ripple fields. Other papers describe ac losses of HTS tapes or coils measured under certain kinds of external magnetic fields by electrical methods [22], [23]. These measurements are theoretically possible, although they may be very difficult in practice for bigger samples, such as HTS coils for generators, under certain types of magnetic fields. Measuring power losses of a rather big coil under simultaneous dc and ripple fields seems to be much simpler by the calorimetric method. This method has strong benefits in theoretical simplicity, and no additional compensating coils are needed. Nevertheless, quench studies could be easily performed by this method. On the other hand, there are some drawbacks of the calorimetric method such as challenging construction of a reliable measurement setup [24]–[27]. Relatively lower sensitivity and precision compared with the electrical methods are added challenges of the calorimetric method. Using the calorimetric method limits the boiling point of liquid nitrogen (LN) to $\sim$77 K.

II. Measurement Setup

The conceptual design of the measurement setup has already been presented by Chen *et al.* [24]. The calorimetric measurement setup consists of two vessels, both filled with LN. The smaller inner vessel is placed inside the bigger outer vessel that is insulated by a vacuum chamber. The outer vessel is filled to the top with LN and provides perfectly stable thermal insulation for the inner vessel. In addition, all the coils producing background fields are in the outer vessel immersed in LN. In this way, all the heat produced by the copper coils are transferred into LN, ensuring higher performance. Any heat losses in the inner vessel will transform LN from the vessel into gas, which is then measured by a precise gas flow meter. The losses in the outer vessel are not measured, and the nitrogen gas can leave through several valves on the top of the cryostat. The inner vessel is designed particularly for characterization of racetrack coils; however, measuring other kinds of coils or even tapes would be possible after small modifications of the central core assembly (see Fig. 1). In the measurement setup, the superconducting sample coil is placed in the inner vessel between coils producing external dc or ripple fields. The position of the superconducting sample coil in the relation of the cryostat coils is shown in Fig. 2. The dc coils are able to produce homogeneous field of up to 250 mT in the sample area. This field is perpendicular to the face of the sample coil. These coils could be eventually connected to an ac power supply and produce a perpendicular ripple field. Due to the limited power of current supply and the relatively high impedance of the coils, the maximum achievable magnetic field is 130 mT peak at 10 Hz.

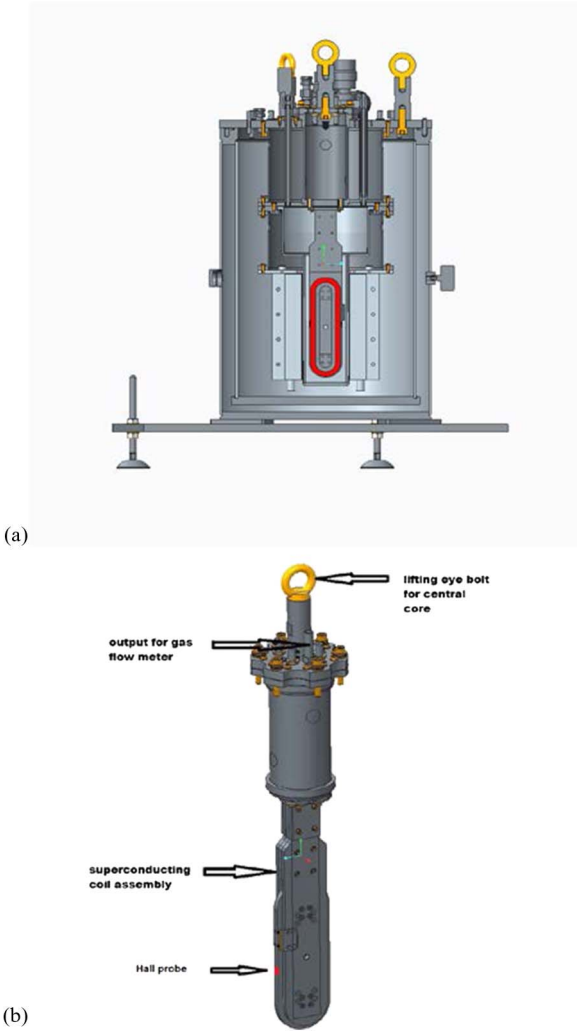

Fig. 1. Calorimetric measurement setup and the central core assembly.

Six other coils produce a ripple field perpendicular to the sample coil axis. They are designed to produce ripples fields of amplitude of up to 40 mT, and they are connected in three phases shifted by 120°, The values were measured by a Hall probe placed on the coil turns. The calibration of the losses was done up to 40 W using a resistive heater installed inside the inner vessel. The calibration curve was $\sim$0.225 SLPM/W (standard liters per minute/watt) which is within 10% of the theoretical value of 0.25 SLPM/W [26]. The difference is caused by nitrogen gas in the flow meter being less than room temperature $(\sim -20\ ^{\circ}\mathrm{C})$ and by possible microcracks in the sealing of the inner vessel. For these reasons, a second-order polynomial equation was used as the best calibration fit to estimate the loss in watts (see Fig. 3). For better precision, an offset heater power of 10 W was used. Nucleation of nitrogen gas results in variable heat transfer from the superconductor and, hence, the resolution is limited to $+/-0.5$ W, which also means that the minimal detectable loss is 0.5 W. Unfortunately, this is lower than the resolution of electrical methods, and it would be insufficient for characterizing of tapes, where the losses are rather small. Nevertheless, the resolution is satisfactory for coils consisting of long lengths of tapes, e.g., 50 m.

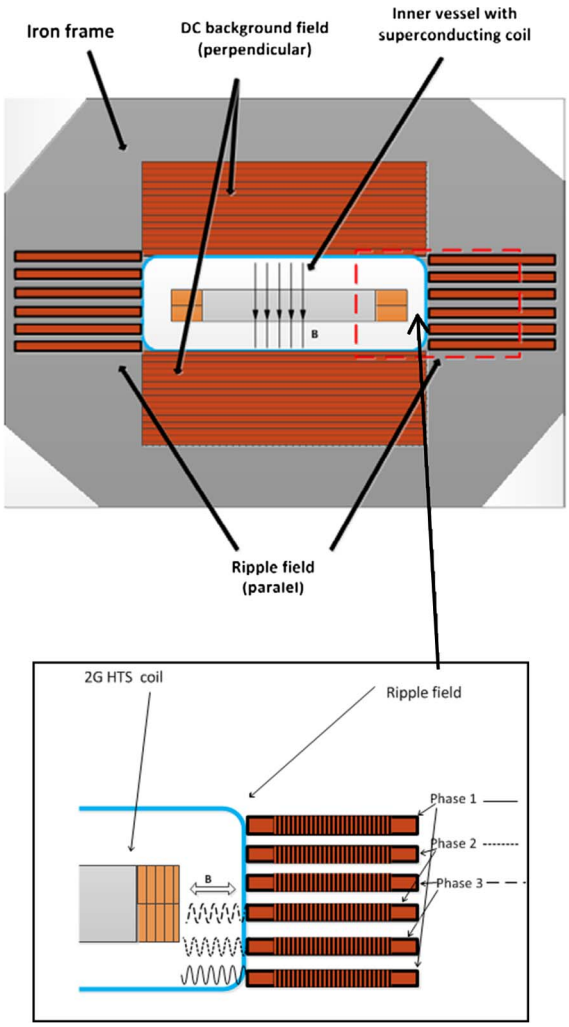

Fig. 2. (Top) Cross-sectional view of the magnets and the superconducting sample in the cryostat. (Bottom) Detailed view of the ripple-field coils and fields.

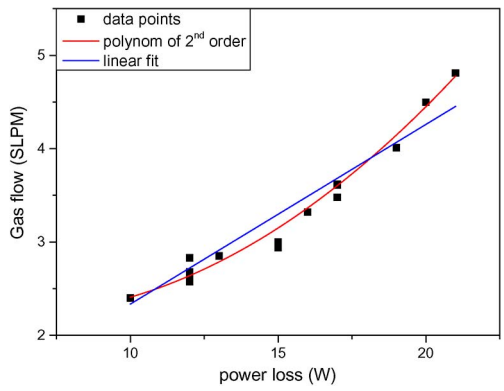

Fig. 3. Calibration data points with linear and quadratic fits.

III. Sample

A superconducting double racetrack coil made from 2G HTS superconducting tape manufactured by SuperPower was used as a sample. The parameters for this sample are listed in Table I. The critical current of the coil was measured as 36.3 A.

TABLE I
PARAMETERS OF THE SAMPLE 2G HTS RACETRACK COIL

	SuperPower 4045 tape [28]
Tape type	4045
Tape width	4 mm
Tape thickness	~0.1 mm
Tape critical current	130 A
YBCO thickness	1 μm
substrate	Non-magnetic 50 μm
Number of turns	100
Inner width	24 mm
Outer width	32 mm
Length	250 mm
Coil critical current	36.3 A

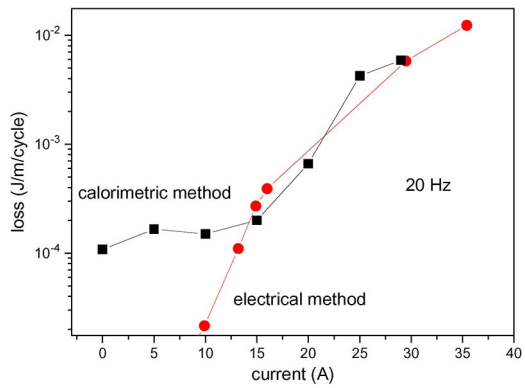

Fig. 4. Comparison of results from the electrical and calorimetric methods at zero external dc field.

IV. Results and Discussion

In this paper, power losses were measured in three different scenarios. The first scenario corresponds to a typical ac loss measurement where the 2G HTS coil was connected to an ac source with a perpendicular dc field. The second scenario was the 2G HTS coil in dc mode, in perpendicular ripple field. In the final scenario, the 2G HTS coil was in the dc mode and subjected to a range of dc background fields (perpendicular to the tape) and ripple fields (parallel to the tape).

A. AC, DC Field

The main reason for measurements at these settings is to evaluate the reliability of the measurement setup. The results can be compared with results obtained from the electric method described by Chen *et al.* [13]. The comparison was done at zero external magnetic field at 20-Hz ac in the sample coil. The results are shown in Fig. 4, and they are in very good agreement with the calculations of Zhang *et al.* [8] As loss is almost independent of frequency [13] (hysteresis losses), the

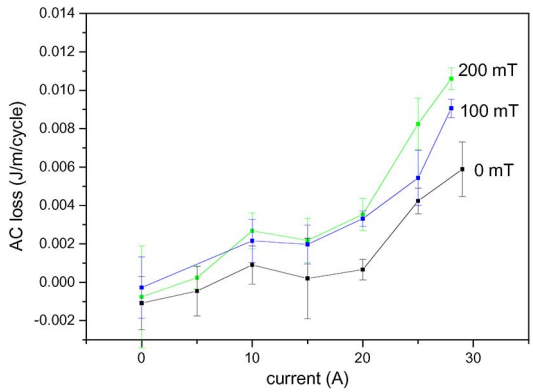

Fig. 5. AC losses in different dc magnetic fields (10 Hz).

plot would be very similar at different frequencies. Results from the calorimetric method at lower currents (under 10 A) are below the resolution of the measurement setup, and the points do not represent the real ac loss of the 2G HTS coil. The resolution could be improved by employing more powerful ac source, which would be able to provide the same currents under higher frequencies (up to 100 Hz). It might be interesting to note that, during the calorimetric measurements, the power losses of the nonsuperconducting current leads supplying the sample with ac were up to 90% of the measured power losses within the inner vessel of the cryostat.

In Fig. 5, the ac loss measurements at 10 Hz in various background dc magnetic fields are presented. As expected, ac losses increase with an increasing background dc magnetic field due to critical current reduction. It is important to note that this is not a rule for every HTS coil. Coils manufactured from certain anisotropic tapes can increase critical current under certain background magnetic fields [29]–[31]. Although it is not the case here, an identical coil was characterized under different magnetic fields of different sizes and orientations in [29], and critical currents were always smaller than compared with the self-field critical current.

B. 2G HTS Coil in DC Mode + Ripple Fields

As the 2G HTS rotor coils of a superconducting generator or motor operate in dc mode, these measurements are the most important results of the paper. The ripple field was produced by the dc background field coils while they were connected in an ac mode, as shown in Fig. 6. It was noted before that, if a superconducting coil with a trapped field in persistent mode is exposed to an ac or relatively small ripple field, the current will decay [32]. For very small amplitudes of ripple field, changes in the superconductor and losses are limited to the small edge areas of the superconducting tape, and the loss is independent of the transport current. However, as the ac fields become larger, currents further penetrate the coil, and local currents in the coil turns could even reverse. At this point, a discontinuous change of the flux in the sample occurs as the flux moves right across the sample from one side to the other and power losses increase rapidly. This effect could cause serious problems in the operation of superconducting rotating machines. Power losses as an effect of ripple fields in HTS generators were studied by Sivasubramaniam *et al.* [18], whereas MgB_2 superconductors

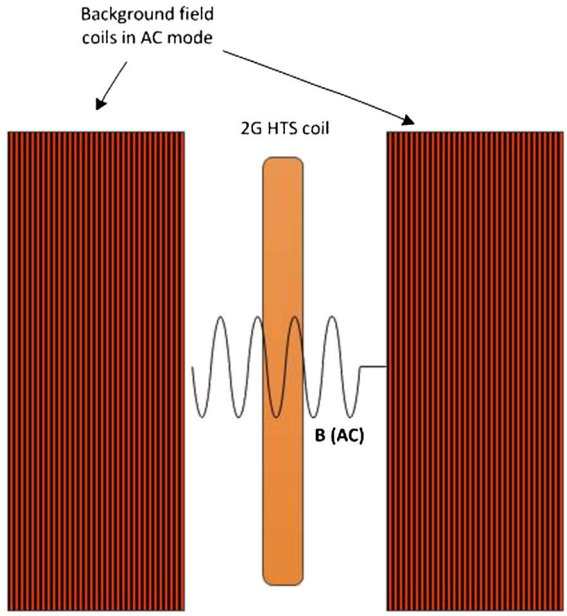

Fig. 6. 2G HTS coil in ac field.

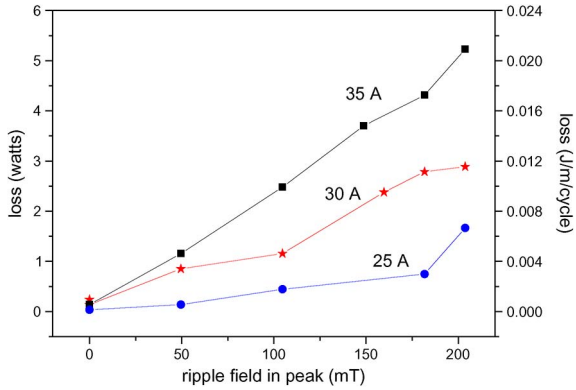

Fig. 7. Magnetization losses at 5 Hz in two different scales (in watts and in J/m/cycle).

was studied by Lahtinen and Stenvall [17]. Power losses introduced by ripple fields are considered a serious issue; however; both works were based purely on computer simulations.

In the experiments, perpendicular ripple fields were applied up to ∼200 mT. As the coils are surrounded by an iron frame, the magnetic fields produced in ac mode were carefully measured by hall probes. Fig. 7(a) and (b) presents experimental results at different currents. They represent the same measurements in two various scales. The maximum measured current is 35 A, which is very close to the critical current value (36.3 A). Relatively high losses (up to 5.5 W) were measured at 35 A, which represents 0.02 J/m/cycle. Power losses escalate with applied dc in the superconducting coil. At 25 A, power loss of about 1.5 W was measured under the maximum applied field. At 20 A, which represents 55% of the critical current, all measured losses were under the resolution of the measurement setup. Again, power loss is expected to be independent on the field frequency, and some of the results were remeasured at different frequencies with very similar results. Disadvantages of measurements at higher frequencies are limitations of the ac source for magnets with relatively high coil impedance.

Detectable losses of the measurement setup are 0.001 J/m/cycle at 10 Hz and 0.002 J/m/cycle at 5 Hz.

C. Perpendicular DC Background Fields and Parallel Ripple Fields

In the last part of the experiment, a ripple field was applied perpendicular to the coil axis, as shown in Fig. 2 (bottom). Ripple fields of up to 30 mT peak were produced by 12 ripple-field solenoid coils (arranged on both sides of the cryostat in the perpendicular direction to the face of the 2G HTS coil). A standard single-phase motor inverter (Omron MX2 0.75 kW) was used as a current source for the ripple-field coils. The inverter had three-phase output, and six ripple-field coils were connected according to Fig. 7. The produced magnetic field was varying as a moving wave. The field was examined with a Hall probe placed on the 2G HTS coil outer turn, where maximum value of 30 mT was measured. In this case, the field was not homogeneous, and it was weakening toward the middle of the inner vessel. Nevertheless, nonuniform field is the case of real machines. The ripple frequencies applied during the experiment were from 0.5 to 50 Hz. An external dc field up to 250 mT was also applied together with the ripple field. Under all these circumstances, no power loss was measured. Any loss higher than 0.5 W or 2×10^{-4} J/m/cycle for the particular coil would be reliably detected. An applied ripple field with 30 mT peak is probably too low to cause flux movement from one side of the superconductor to the other. In addition, the outermost turn, which is operating far below its critical current, is able to shield the field for the other turns. Consequently, any losses from more inner turns are avoided, resulting that the losses in the outermost turn represent the majority of all the power losses generated in the coil. This is a very small number per meter of the tape indeed. In addition, the losses in the outermost turn by itself are relatively low because of relatively small current in the tape.

V. Conclusion

Measurements of power losses at various external magnetic fields using the calorimetric method were carried out. The equipment was validated in the first part of the experiment. The sensitivity of the calorimetric method is lower than the electrical methods; however, several types of measurements cannot be easily carried out using the electrical methods. Superconducting coils in rotors of superconducting rotating machines have to withstand ripple fields in both perpendicular and parallel directions. The power losses were measured in the parallel direction at different currents. The measurements have shown very small losses at currents of about $\sim$50% of the critical current, up to relatively high losses close to critical of the current value. Whereas in the case of ripple fields parallel to the coil axis, power losses are relatively high; in the perpendicular direction, no losses were detected, even under dc background fields of up to 250 mT. The experiment has proven that any losses caused by ripple fields in the perpendicular direction could be neglected by superconducting generator designs, and further work should be focused on losses caused by ripples in the parallel direction. This fact was theoretically expected but never experimentally proven.

Acknowledgment

The authors would like to thank Prof. A. Campbell and F. Saven of the Department of Engineering, University of Cambridge, Cambridge, U.K., and Prof. R. Bansal of the Faculty of Engineering, University of Pretoria, Pretoria, South Africa, for their valuable advices on this work.

References

[1] D. Robb, "The gearbox challenge–The role of bearings in gearbox failure," *Windpower Monthly Mag.*, pp. 53–60, Nov. 2005.

[2] A. B. Abrahamsen, N. Mijatovic, E. Seiler, T. Zirngibl, C. Trholt, P. B. Nrgard, N. F. Pedersen, N. H. Andersen, and J. stergard, "Superconducting wind turbine generators," *Supercond. Sci. Technol.*, vol. 23, no. 3, pp. 034019-1–034019-8, Mar. 2010.

[3] Y. Terao, M. Sekino, and H. Ohsaki, "Comparison of conventional and superconducting generator concepts for offshore wind turbines," *IEEE Trans. Appl. Supercond.*, vol. 23, no. 3, p. 5200904, Jun. 2013.

[4] H. Ohsaki, M. Sekino, T. Suzuki, and Y. Terao, "Design study of wind turbine generators using superconducting coils and bulks," in *Proc. Int.Conf. Clean Elect. Power*, 2009, pp. 479–484.

[5] O. Keysan and M. A. Mueller, "Superconducting generators for renewable energy applications," in *Proc. IET Conf. Renew. Power Gener.*, 2011, pp. 1–6.

[6] N. Mijatovic, A. B. Abrahamsen, C. Trholt, E. Seiler, M. Henriksen, V. M. Rodriguez-Zermeno, and N. F. Pedersen, "Superconducting generators for wind turbines: Design considerations," *J. Phys., Conf. Series*, vol. 234, p. 032038, 2010.

[7] A. Patel, S. C. Hopkins, and B. A. Glowacki, "Trapped fields up to 2 T in a 12 mm square stack of commercial superconducting tape using pulsed field magnetization," *Supercond. Sci. Technol.*, vol. 26, pp. 032001-1–032001-7, 2013.

[8] M. Zhang, M. Chudy, W. Wang, Y. Chen, Z. Huang, Z. Zhong, W. Yuan, J. Kvitkovic, S. V. Pamidi, and T. A. Coombs, "AC loss estimation of HTS armature windings for electric machines," *IEEE Trans. Appl. Supercond.*, vol. 23, no. 3, p. 5900604, Jun. 2013.

[9] R. Pei, A. Velichko, M. Majoros, Y. Jiang, R. Viznichenko, Z. Hong, R. Marchant, A. M. Campbell, and T. A. Coombs, "IC and AC loss of 2G YBCO tape measurement for designing and fabrication of an HTS motor," *IEEE Trans. Appl. Supercond.*, vol. 18, no. 2, pp. 1236–1239, Jun. 2008.

[10] S. H. Rupp, A. D. Caplin, and M. P. Staines, "Magnetisation ac-loss measurements on YBa2Cu3O7 tapes with weakly-ferromagnetic NiW substrates," *Proc. J. Phys., Conf. Series*, vol. 97, p. 012078, 2008.

[11] J. H. Claassen, "An approximate method to estimate AC loss in tape-wound superconducting coils," *Appl. Phys. Lett.*, vol. 88, no. 12, pp. 122512-1–122512-3, Mar. 2006.

[12] J. Souc, E. Pardo, M. Vojenciak, and F. Gomory, "Theoretical and experimental study of ac loss in high temperature superconductor single pancake coils," *Supercond. Sci. Technol.*, vol. 22, no. 1, p. 015006, Jan. 2009.

[13] Y. Chen, M. Zhang, M. Chudy, K. Matsuda, and T. Coombs, "Complex study of transport AC loss in various 2G HTS racetrack coils," *Physica C*, vol. 489, no. 15, pp. 1–7, 2013.

[14] L. Quéval and H. Ohsaki, "AC losses of a grid-connected superconducting wind turbine generator," *IEEE Trans. Appl. Supercond.*, vol. 23, no. 3, p. 5201905, Jun. 2013.

[15] S. Das, N. Karnik, and S. Santoso, "Time-domain modelling of tower shadow and wind shear in wind turbines," *ISRN Renew. Energy*, vol. 2011, pp. 890582-1–890582-11, 2011.

[16] D. S. L. Dolan and P. W. Lehn, "Simulation model of wind turbine 3p torque oscillations due to wind shear and tower shadow," in *Proc. IEEE PSCE/PES*, 2006, pp. 2050–2057.

[17] V. Lahtinen and A. Stenvall, "The difficulty of modeling ripple field losses in superconductors using the eddy current model," *IEEE Trans. Appl. Supercond.*, vol. 23, no. 3, p. 4900505, Jun. 2013.

[18] K. Sivasubramaniam, X. Huang, D. Ryan, K. Weeber, J. W. Bray, E. T. Laskaris, L. Tomaino, J. M. Fogarty, and S. Ashworth, "AC losses in a high temperature superconducting generator," *IEEE Trans. Appl. Supercond.*, vol. 15, no. 2, pp. 2162–2165, Jun. 2005.

[19] F. Grilli, E. Pardo, A. Stenvall, D. N. Nguyen, W. Yuan, and F. Gömöry, "Computation of losses in HTS under the action of varying magnetic fields and currents," *IEEE Trans. Appl. Supercond.*, vol. 24, no. 1, p. 8200433, Feb. 2014.

[20] E. Pardo, J. Kováè, and J. Souc, "Power loss in ReBCO racetrack coils under AC applied magnetic field and DC current," *IEEE Trans. Appl. Supercond.*, vol. 23, no. 3, p. 4701305, Jun. 2013.
[21] J. Šouc, F. Gömöry, and M. Vojenèiak, "Calibration free method for measurementof the ac magnetization loss," *Supercond. Sci. Technol.*, vol. 18, p. 592, 2005.
[22] J.-K. Lee, S.-W. Lee, M.-J. Park, and G. Cha, "Magnetization loss in HTS stacked tapes by various directional external magnetic fields," *IEEE Trans. Appl. Supercond.*, vol. 14, no. 2, pp. 630–633, Jun. 2004.
[23] Y. Chen, M. Zhang, M. Chudy, W. Wang, Z. Zhong, Z. Huang, and T. Coombs, "Theoretical and experimental magnetization loss comparison between IBAD coils and RABiTS coils," *IEEE Trans. Appl. Supercond*, vol. 23, no. 3, p. 8201504, Jun. 2013.
[24] Y. Chen, W. Yuan, M. Zhang, and T. A. Coombs, "The experiment to evaluate the AC loss of 2G HTS windings in the application of rotating electric machines," *IEEE Trans. Appl. Supercond.*, vol. 22, no. 3, p. 4705204, Jun. 2012.
[25] N. Magnusson and S. Hörnfeldt, "Calorimetric apparatus for alternating current loss measurements on high-temperature superconductors," *Rev. Sci. Instrum.*, vol. 69, no. 9, p. 3320, Sep. 1998
[26] J. Ekin, *Experimental Techniques: Cryostat Design, Material Properties and Superconductor Critical-Current Testing*. New York, NY, USA: Oxford Univ. Press, 2006.
[27] J.-H. Kim, C. H. Kim, G. Iyyani, J. Kvitkovic, and S. Pamidi, "Transport AC loss measurements in superconducting coils," *IEEE Trans. Appl. Supercond.*, vol. 21, no. 3, pp. 3269–3272, Jun. 2011.
[28] [Online]. Available: http://www.superpower-inc.com/content/products-services
[29] M. Chudy, Y. Chen, M. Zhang, and T. A. Coombs, "Anisotropy of 2G HTS racetrack coils in external magnetic fields," *Supercond. Sci. Technol.*, vol. 26, no. 7, pp. 075012-1–075012-7, Jul. 2013.
[30] J. Pitel and P. Kováè, "Influence of external magnetic fields on critical currents of solenoids wound with anisotropic HTS tapes–Theoretical analysis," *Supercond. Sci. Technol.*, vol. 10, no. 1, pp. 7–16, Jan. 1997.
[31] J. Pitel and P. Kováè, "Compensation of the radial magnetic field component of solenoids wound with anisotropic Bi(2223)Ag tape," *Supercond. Sci. Technol.*, vol. 10, no. 11, pp. 847–852, Nov. 1997.
[32] S. Jeong, J. V. Minervini, J. R. Hale, and Y. J. Chen, "Persistent current decay of a superconducting coil in an AC field," *Adv. Cryogenic Eng.*, vol. 39, pp. 17–24, 1994.

Authors' biographies not available at the time of publication.

AC Loss Estimation of HTS Armature Windings for Electric Machines

Min Zhang, M. Chudy, Wei Wang, Yiran Chen, Zhen Huang, Zhaoyang Zhong, Weijia Yuan, J. Kvitkovic, S. V. Pamidi, and T. A. Coombs

***Abstract*—This paper studies 2G high-temperature superconducting (HTS) coils for electric machine armature windings, using finite element method (FEM) and H formulation. A FEM model for 2G HTS racetrack coil is built in COMSOL, and is well validated by comparing calculated ac loss with experimental measurements. The FEM model is used to calculate transport loss in HTS armature windings, using air-cored design. We find that distributed winding used in conventional machine design is an effective way to reduce transport loss of HTS armature winding, in terms of air-cored design. Based on our study, we give suggestions on the design of low loss HTS armature winding.**

***Index Terms*—AC loss, high-temperature superconducting (HTS), machine, YBCO.**

I. Introduction

SUPERCONDUCTING ARMATURE winding was once deemed as unpractical due to the high AC loss and unfeasible cooling capacity [2]. So most of the machine projects focus on superconducting machines with superconducting rotor and conventional copper armature winding [3], [4]. The major drawback of this kind of machine is that the thick cryogenic shell between "cold" rotor and "warm" stator greatly increases the air gap so it reduces the magnetic field in armature windings. Full superconducting machine, enabled by superconducting armature winding, is a much better solution in terms of coupling rotor and stator to produce strong magnetic field [2]. So along with the development of high temperature superconducting (HTS) coils, the idea of superconducting armature winding has flourished again. Economic liquid nitrogen cooling gives hope to HTS armature winding, with projects ongoing all over the world. Our laboratory in University of Cambridge has demonstrated a synchronous motor using 2G HTS racetrack coils as armature winding [5]; Kyoto University has successfully built and tested a fully HTS induction motor with BSCCO as distributed armature winding [6], and is challenging the fabrication of a fully induction motor using M_gB_2 wires [7].

Manuscript received September 28, 2012; accepted January 6, 2013. Date of publication January 11, 2013; date of current version February 27, 2013.

M. Zhang, M. Chudy, W. Wang, Y. Chen, Z. Huang, Z. Zhong, and T. Coombs are with the Engineering Department, Cambridge University, CB3 0FA, U.K. (e-mail: mz279@cam.ac.uk).

J. Kvitkovic and S. V. Pamidi are with Center for Advanced Power Systems, Florida State University, Tallahassee, FL 32310 USA.

W. Yuan is with the Department of Electronics and Electrical Engineering, University of Bath, BA2 7A1, U.K.

Color versions of one or more of the figures in this paper are available online at http://ieeexplore.ieee.org.

Digital Object Identifier 10.1109/TASC.2013.2239341

TABLE I
DOUBLE RACETRACK PARAMETERS

Symbol	Quantity	Value
n	Turns per layer	38
L	Total tape length	39 m
w	Tape width	4 mm
R_1	Inner radius	68 mm
R_2	Outer radius	93 mm

While the projects of HTS winding are prevailing, the need to estimate AC loss of HTS armature winding is urgent and challenging. Numerically, finite element software is extremely popular in calculating AC loss of HTS. Initially, the modeling is focused on single tape: Z. Hong and R. Brambilla *et al.* take the lead in using H formulation for single tape AC loss computation [1], [8], [9]; D. N. Nguyen *et al.* calculate the transport AC loss of YBCO tape with ferromagnetic substrate [10], and magnetization loss when the tape is exposed to a parallel AC magnetic field [11]. Recently, the modeling is more focused on the interaction between tapes such as the modeling of HTS coils. F. Grilli *et al.* use vector potential to simulate stacks of YBCO coated conductors [12]; M. Ainslie *et al.* use H formulation to calculate AC loss for a HTS racetrack coil [16]. We also build an axial symmetrical FEM model for 2G HTS pancakes [13], [14], and find the model consist with experiments.

In this paper, we extend the FEM model in paper [13] to estimate AC loss of 2G HTS racetrack coils used as motor armature windings. The paper is organized as follows: The second section of the paper introduces the FEM model, and validates the FEM model by experimental measurements; the third section studies the transport loss for HTS armature winding; the fourth section discusses the influence of 2G HTS tape performance on their AC loss.

II. The FEM Model and Validation

Double racetrack coil is suitable for making machine armature winding, as shown in Table I the parameters of the racetrack coil we made and used in a synchronous motor [5].

H formulation is applied to the 2D infinite-long model. We have to simplify the racetrack geometry to infinite-long model; we will show below that the infinite-long model simulates the racetrack coil very well. The model contains two variables, defined as $\boldsymbol{H} = [H_x; H_y]$. In 2D geometry, the induced or input current J_z in the superconductor flows in the z direction, so

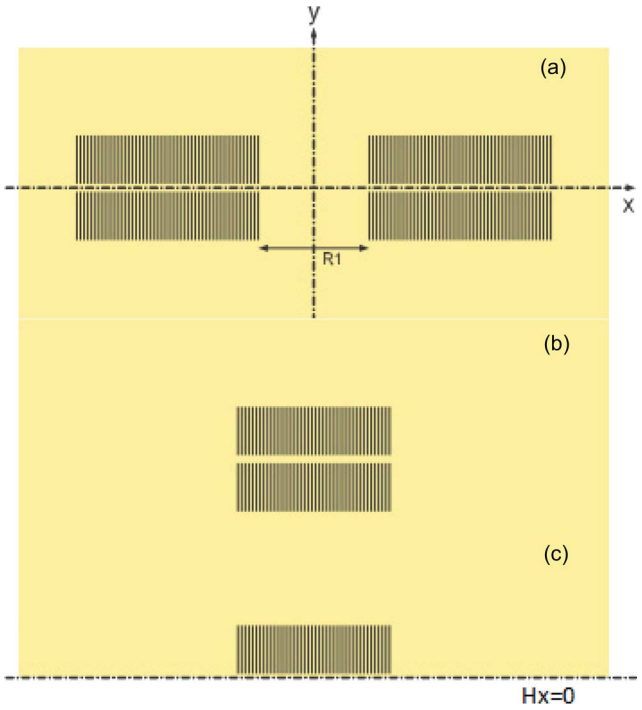

Fig. 1. Cross-section view of the racetrack: (a) whole model and (b) quarter model.

does the electric field $E_z = \rho J_z$, with ρ as the resistivity of the sub-domain.

Ampere's law is written as:

$$J_z = \nabla \times \boldsymbol{H}. \tag{1}$$

Faraday's law is written as:

$$\nabla \times E_z = -\mu_0 \mu_r \, \partial \boldsymbol{H} / \partial t. \tag{2}$$

Combining the equations above, we can solve (3) by finite element software:

$$\mu_0 \mu_r \frac{\partial \boldsymbol{H}}{\partial t} + \nabla \times (\rho \, \nabla \times \boldsymbol{H}) = 0 \tag{3}$$

We have to define resistivity for different materials in the model. For air, we use $\rho = 1000$ Ωm. For YBCO, we use the E-J power law: $\rho = E_0 / J_c(B) \; (J_z / J_c(B))^{n-1}$. Other details of the model can be found in our paper [13]–[15].

Fig. 1(a) shows the cross section of the racetrack coil. In the AC loss calculation, we only model the YBCO layer of each turn, which is 1 μm thick in this case. We find from the modeling that $R_1 = 68$ mm of the coil is large enough to decouple the left and right bar of the coil, and ignoring the electromagnetic interaction between them only leads to an error of 2% when the coil is carrying 30 A current. So we manage to simplify the full model from Fig. 1(a) to (b). Without x directional background field, Fig. 1(b) can be further reduced to Fig. 1(c), with only the upper half of the right bar modeled, due to symmetry. Without background field, the boundary conditions are $H_x = 0$ and $H_y = 0$; with background field, the conditions become $H_x = H_{appx}$ and $H_y = H_{appy}$.

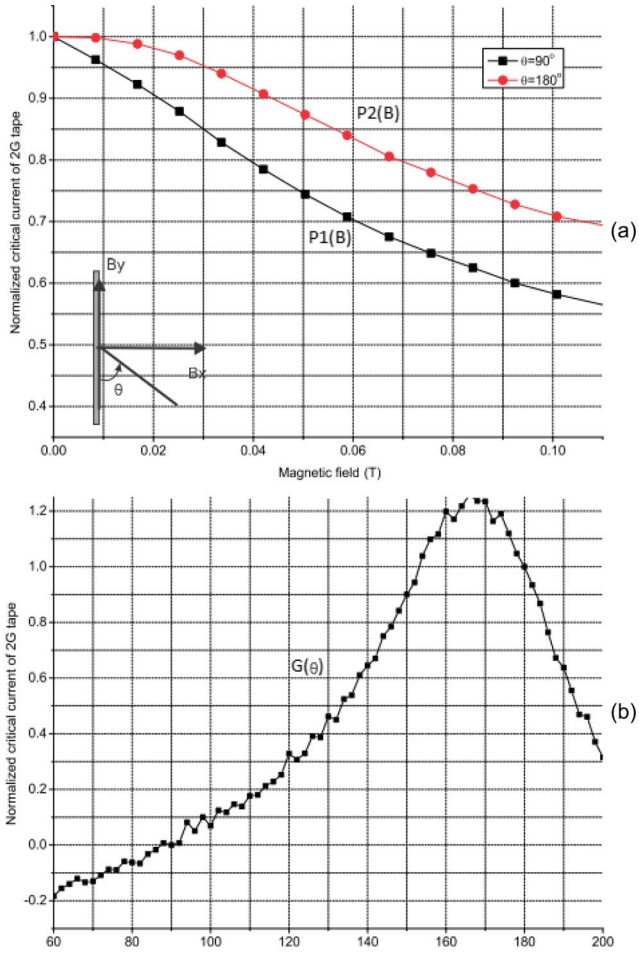

Fig. 2. Normalized experimental data of the tapes' critical currents under (a) perpendicular and parallel field and (b) different field angles of 100 mT.

The influence of magnetic field on the critical current of 2G HTS tape $J_c(B)$ is of paramount importance in the FEM model. We have proposed a well validated method to implement tape anisotropy in COMSOL. Here we briefly introduce the main idea. More details about how to model anisotropic 2G tapes can be found in paper [13].

We measured the magnetic field dependency of 2G tape, with part of the normalized results illustrated in Fig. 2(a). We also measured the angle dependency of critical currents under 100 mT, and normalized the measurement so that $\theta = 180°$ corresponds to the value of 1 and $\theta = 90°$ corresponds to the value of 0. The normalized results are illustrated in Fig. 2(b). The expression used in the model is written in (4), with the explanation of the functions illustrated in Fig. 2.

$$J_c(B) = J_{c0} * \{P1(B) + [P2(B) - P1(B)] * G(\theta)\} \tag{4}$$

when $\theta = 90°$, we have $G(\theta) = 0$, so $J_c(B) = J_{c0} * P1(B)$ gives us the curve with square symbol in Fig. 2(a); when $\theta = 180°$, we have $G(\theta) = 1$, so $J_c(B) = J_{c0} * P2(B)$ gives us the curve with circular symbol in Fig. 2(a). For other θ values, the angle dependency of $J_c(B)$ is modulated by $G(\theta)$, and the magnitude dependency is modulated by $P1(B)$ and $P2(B)$.

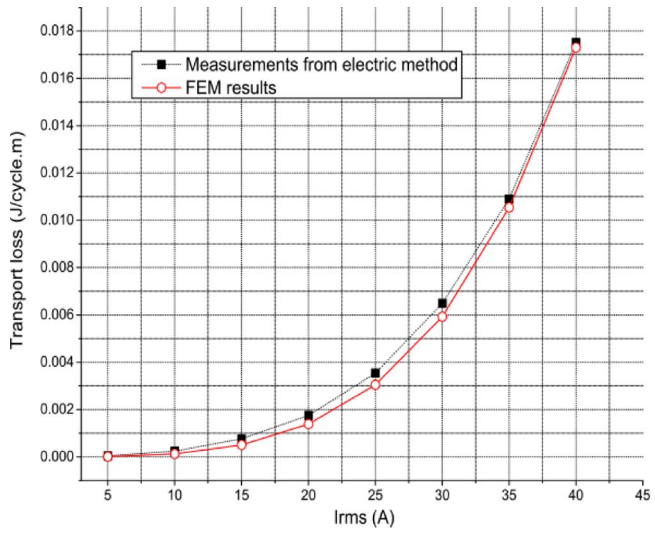

Fig. 3. AC loss of the racetrack coil: comparison of measurements and model results.

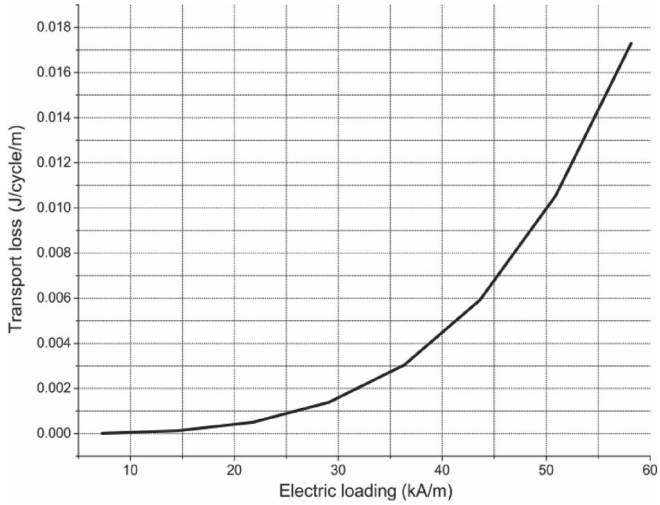

Fig. 4. Electric loading versus transport loss.

The measurements are interpolated into COMSOL directly and used as the functions of (4).

To calculate AC loss ($\mathrm{J}\cdot\mathrm{cycle}^{-1}\cdot\mathrm{m}^{-1}$) from Fig. 3, we integrate $E_z \cdot J_z$ over all the YBCO domains, and then divide it by total turns. We perform loss calculation for 50 Hz AC current, and compare the model results with measurements in Fig. 3. Fig. 3 shows that the model results are consistent with measurements. The experimental results are slightly higher than measurements, which might due to geometry discrepancy, because the end-effect of the racetrack coil cannot be considered in the model. We suggest that the end-effect is the reason for higher measured loss, but further study is required to confirm it. Generally speaking, the FEM model is very accurate in AC loss estimation.

III. Transport Loss Estimation for Armature Winding

Transport loss is closely related to machine electric loading and the arrangement of armature winding. The apparent power output of a machine can be standardly expressed in terms of electric and magnetic loading [2]

$$s = \frac{\pi^2}{\sqrt{2}} k_w B A_s L R^2 \frac{\omega}{p} \quad [\mathrm{VA}] \tag{5}$$

where k_w is the winding factor, B is the average magnetic field density (T), A_s is electric loading (kA/m), L is effective length (m), R is the radius of the machine (m), ω is speed rad/s, and p is the pole pair number. From (5) we learn that the increase of electric loading directly leads to the increase of machine output, and that is exactly the merit of HTS armature winding, to increase machine outputs. Electric loading can vary from 10 kA/m to hundreds of kA/m according to machine size and cooling method. We intend to provide a general idea of the relationship between electric loading and transport loss.

The machine studied has an air-cored armature winding, which suggests that there is no iron in the stator side. 3D

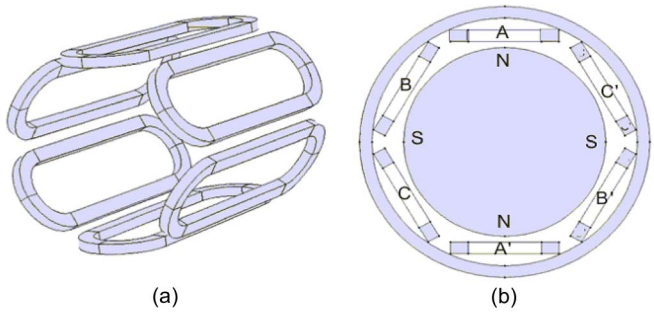

Fig. 5. Armature of the synchronous motor: (a) 3-D geometry of the six racetrack-coils of the armature winding and (b) cross-section view of the motor, with gray area indicating rotor and stator yoke. The mean perimeter of the armature winding is 660 mm, leading to the armature radius $R = 0.105$ m.

and cross-sectional illustrations of such an armature winding is shown in Fig. 5. Assuming that the double racetrack coil mentioned above is used in the armature winding with a pole pitch of 3/4 (which suggests the distance between adjacent coils is 1/4 that of the width of the coil, 68 mm). Based on the design, we are able to plot the loss data in Fig. 3 versus the electric loading, with results shown in Fig. 4. Total transport loss can easily be calculated by multiplying the results in Fig. 4 with the total length of 2G tapes. The tape length of a single coil is 39 m, which gives the total tape length of the armature winding as 234 m. So if the electric loading is designed to be 58 kA/m (corresponding to 40 A AC current) and 50 Hz, the transport loss of the armature winding will be $Q = 0.0173\ \mathrm{J}\cdot\mathrm{cycle}^{-1}\cdot\mathrm{m}^{-1}\cdot 234\ \mathrm{m}\cdot 50\ \mathrm{Hz} = 0.2\ \mathrm{kW}$.

The value of Q is the total transport loss of the machine, giving a general idea of how much loss there is regardless of rotor. However, the magnetic field from the rotor will greatly affect the magnetic field of the armature winding. In real applications of estimating the total loss of the armature winding, the existence of rotor windings cannot be ignored. It can be estimated by applying a background field to the racetrack coil model. The magnitude and direction of magnetic field varies, depending on the rotor design and the air gap length.

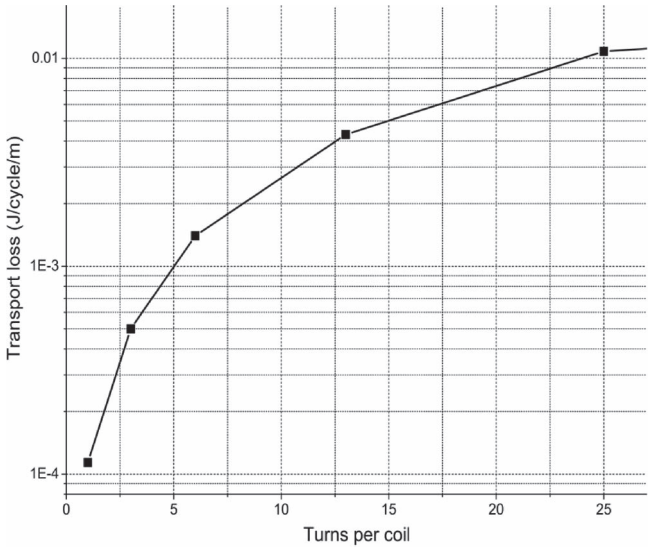

Fig. 6. Transport loss of coils with varied total turns

Specific studies need to be carried out for different machine design.

IV. Armature Loss Reduction

Conventional armature design employs distributed winding to approximate sinusoidal waveforms. So we study the influence of distributed armature winding. We still take electric loading 58 kA/m and 50 Hz as an example. If we divide our 6 racetrack coils into 12, so each coil has 20 turns. Assuming that 12 coils distributed equally along the circumference of the stator, we redesign the motor shown in Fig. 6. The total turn remains unchanged, so the current should be the same to give the same electric loading. We perform transport loss calculation for 20 turns coil carrying $I_{rms} = 40$ A. This time the transport loss reduces to 0.00767 $\mathrm{J \cdot cycle^{-1} \cdot m^{-1}}$, and the total transport loss of the armature winding is 0.09 kW. Comparing to 0.2 kW loss of the concentrated design, the reduction of transport loss reaches 55%. We also test 25, 12, 6, 3, and 1 turn per coil, and the transport losses $(\mathrm{J \cdot cycle^{-1} \cdot m^{-1}})$ are illustrated in Fig. 6. The loss keeps decreasing while we reduce the turns per coil. Given that the total length of the armature winding is fixed to 234 m, we get to the conclusion that fewer turns per coil leads to lower transport loss. In other words, distributed winding helps to reduce AC loss. The reason is that distributed winding reduces the total turns in one coil, as well as the self-field of the coil. The magnetic field affects the critical current density of HTS, as shown in Fig. 2. Lower self-field coil has higher critical current, so for the same applied current, it has lower AC loss.

However, too many distributed coils increase the difficulty and cost of armature manufacture. In this case, 12 coil armature windings would be a good strategy to reduce loss. And also readers should be reminded that we ignore the overlapping of end winding in the case of distributed winding, which might lead to certain amount of loss increase. As long as the coils are long enough and the contribution from end winding can be ignored, our conclusion stands.

V. Conclusion

This paper studied 2G HTS racetrack coil, used as armature winding for electric machine. We built FEM model to simulate 2G HTS coils, with the consideration of 2G tape anisotropy. We well validated the model by comparing transport loss results with experimental measurements by both electric method and calorimetric method. We calculated the transport loss of HTS armature winding in terms of electrical loading of the machine, and we pointed out the distributed winding would be a feasible way to reduce transport loss.

References

[1] Z. Y. Hong, A. M. Campbell, and T. A. Coombs, "Numerical solution of critical state in superconductivity by finite element software," *Supercond. Sci. Technol.*, vol. 19, no. 12, pp. 1246–1252, Dec. 2006.

[2] J. R. Bumby, *Superconducting Rotating Electrical Machines*. New York: Oxford Univ. Press, 1983.

[3] H. W. Neumuller, W. Nick, B. Wacker, M. Frank, G. Nerowski, J. Frauenhofer, W. Rzadki, and R. Hartig, "Advances in and prospects for development of high-temperature superconductor rotating machines at Siemens," *Supercond. Sci. Technol.*, vol. 19, no. 3, pp. S114–S117, Mar. 2006.

[4] R. Ackermann, J. Alexander, A. Gadre, T. Laskaris, K. Sivasubramanium, J. Urbahn, R. Nold, and L. Tomaino, "Testing of a 1.8 MVA high temperature superconducting generator," in *Proc. IEEE Power Eng. Soc. Annu. Meeting*, Toronto, ON, Canada, 2003.

[5] Y. Jiang, R. Pei, W. Xian, Z. Hong, and T. A. Coombs, "The design, magnetisation, control of a superconducting permanent magnetic synchronous motor," *Supercond. Sci. Technol.*, vol. 21, no. 6, pp. 065011-1–065011-6, Jun. 2008.

[6] D. Sekiguchi, T. Nakamura, S. Misawa, H. Kitano, T. Matsuo, N. Amemiya, Y. Ito, M. Yoshikawa, T. Terazawa, K. Osamura, Y. Ohashi, and N. Okumura, "Trial test of fully HTS induction/synchronous machine for next generation electric vehicle," *IEEE Trans. Appl. Supercond.*, vol. 22, no. 3, p. 5 200 904, Jun. 2012.

[7] T. Nakamura, Y. Yamada, H. Nishio, K. Kajikawa, M. Sugano, N. Amemiya, T. Wakuda, M. Takahashi, and M. Okada, "Development and fundamental study on a superconducting induction/synchronous motor incorporated with MgB2 cage windings," *Supercond. Sci. Technol.*, vol. 25, no. 1, pp. 014004-1–014004-7, Jan. 2012.

[8] R. Brambilla, F. Grilli, and L. Martini, "Development of an edge-element model for AC loss computation of high-temperature superconductors," *Supercond. Sci. Technol.*, vol. 20, no. 1, pp. 16–24, Jan. 2007.

[9] Z. Hong, A. Campbell, and T. A. Coombs, "A numerical method to estimate AC loss in superconducting coated conductors by finite element modelling," *Supercond. Sci. Technol.*, vol. 20, no. 4, pp. 331–337, Apr. 2007.

[10] S. P. Ashworth, J. O. Willis, F. Sirois, and F. Grilli, "A new finite-element method simulation model for computing AC loss in roll assisted biaxially textured substrate YBCO tapes," *Supercond. Sci. Technol.*, vol. 23, no. 2, pp. 025001-1–025001-5, Feb. 2010.

[11] D. N. Nguyen, S. P. Ashworth, and J. O. Willis, "Experimental and finite-element method studies of the effects of ferromagnetic substrate on the total ac loss in a rolling-assisted biaxially textured substrat YBCO tape exposed to a parallel ac magnetic field," *J. Appl. Phys.*, vol. 106, no. 9, pp. 093913-1–093913-7, Nov. 2009.

[12] F. Grilli, S. P. Ashworth, and S. Stavrev, "Magnetization AC losses of stacks of YBCO coated conductors," *Phys. C, Supercond.*, vol. 434, no. 2, pp. 185–190, Feb. 2006.

[13] M. Zhang, J.-H. Kim, S. Pamidi, M. Chudy, W. Yuan, and T. A. Coombs, "Study of 2G high temperature superconducting coils: Determination of critical current," *J. Appl. Phys.*, vol. 111, no. 8, pp. 083902-1–083902-8, Apr. 2012.

[14] M. Zhang, J. Kvitkovic, J.-H. Kim, C. H. Kim, S. V. Pamidi, and T. A. Coombs, "Alternating current loss of second-generation high-temperature superconducting coils with magnetic and non-magnetic substrate," *Appl. Phys. Lett.*, vol. 101, no. 10, pp. 102 602-1–102 602-4, Sep. 2012.

[15] M. Zhang, J. Kvitkovic, S. V. Pamidi, and T. A. Coombs, "Experiment and numerical study of YBCO pancake coil with magnetic substrate," *Supercond. Sci. Technol.*, vol. 25, no. 12, pp. 125 020–125 025, Dec. 2012.

[16] M. Ainslie, V. M. Rodriguez-Zermeno, Z. Hong, W. Yuan, T. J. Flack, and T. A. Coombs, "An improved FEM model for computing transport AC loss in coils made of RABiTS YBCO coated conductors for electric machines," *Supercond. Sci. Technol.*, vol. 24, no. 4, p. 045005, Apr. 2011.

Control and Operation of a High Temperature Superconducting Synchronous Motor

Zhen Huang, Wei Xian, Min Zhang, Michal Chudy, Yiran Chen, Zhaoyang Zhong, Mehdi Baghdadi, Wei Wang, Fred Spaven, Koichi Matsuda, and T. A. Coombs

***Abstract*—We have built a four-pole high temperature superconducting (HTS) permanent magnet synchronous motor (PMSM) in our lab. At this stage, the HTS PMSM uses two 2G HTS racetrack coils, which are YBCO wires, type 344 from AMSC, and four conventional copper coils as stator windings. 75 YBCO bulks are mounted on the surface of the rotor. After the pulsed field magnetization system had been developed and tested in our lab in 2011, the rotor can trap a four-pole magnetic field. This makes HTS bulks possible for motor application, other than HTS coils. The HTS PMSM can successfully run at a low speed of around 150 rpm for an initial test. This paper states theoretical and practical works on the HTS PMSM's operation including HTS motor drive development and its application.**

***Index Terms*—High temperature superconducting (HTS), machine control, YBCO.**

I. Introduction

A SUPERCONDUCTING machine is an ideal device for power generation, ship propulsion, and electric vehicles, for it would be many times smaller, lighter, and more efficient than an equivalent copper wound machine. Also, compared with conventional machines, a superconducting machine can achieve cost competitiveness owing to its high efficiency, high power density, high torque density, etc. In the last few years, an increasing number of research groups have concentrated on the development of a new generation of motors and generators whose rated power is from some kilowatts up to several hundred megawatts, such as Ohsaki Laboratory from University of Tokyo [1], Amemiya's group from Kyoto University [2], Masson's group from University of Houston [3], etc. However, most of the designs mainly focus on the application of the second generation (2G) high temperature superconducting (HTS) coils rather than that of HTS bulks. From 2005, a project of a fully HTS motor has been carried on in Superconductivity Group of Department of Engineering, University of Cambridge [4]. The HTS motor was designed as a non-salient pole, surface-mounted, permanent magnet synchronous motor (PMSM). In 2011, the success of pulsed field magnetization (PFM) makes it possible for the bulk-based HTS PMSM to run successfully [5].

Manuscript received October 8, 2012; accepted November 29, 2012. Date of publication December 11, 2012; date of current version January 12, 2013.

Z. Huang, W. Xian, M. Zhang, M. Chudy, Y. Chen, Z. Zhong, M. Baghdadi, W. Wang, F. Spaven, and T. A. Coombs are with the Department of Engineering, University of Cambridge, Cambridge CB3 0FA, U.K. (e-mail: huangzhen418@hotmail.com).

K. Matsuda is with the Department of Mechanical Engineering, Kyushu University, Fukuoka 812-8581, Japan (e-mail: zh252@cam.ac.uk).

Color versions of one or more of the figures in this paper are available online at http://ieeexplore.ieee.org.

Digital Object Identifier 10.1109/TASC.2012.2233262

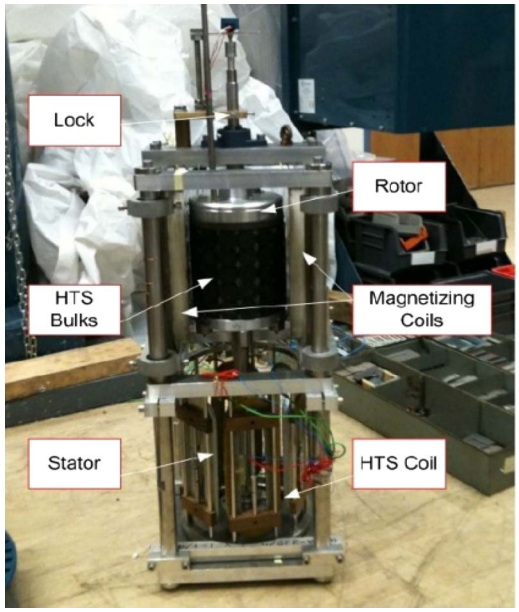

Fig. 1. Photograph of the HTS PMSM prototype.

The significantly improvement was made after modified V/F control successfully implemented on a DSP to start up the HTS PMSM. Finally, the prototype of the HTS PMSM in our lab can run at no load operation.

This paper is organized as follows: in Section II, we provide the structure of the HTS PMSM. In Section III, we detail the theoretical works of modified open-loop variable-voltage, variable-frequency (VVVF or V/F) control for the HTS PMSM. Section IV provides the method of practical implementation of modified V/F control on a DSP to start up the HTS PMSM for an initial test and also present some operation results.

II. Structure of the HTS PMSM

The prototype of the HTS PMSM is shown in Fig. 1. The HTS PMSM consists of two parts—magnetization part and operation part. The upside of the rig, which is the magnetization part, has two magnetizing copper coils used for magnetizing HTS bulks on the rotor. The lock installed on the top of the shaft is to stabilize the motor during the PFM process. The stator is located on the bottom of the rig. Prior to starting the motor, the rotor is fixed in the magnetization part where PFM is processed. After PFM, the rotor is moved down to the operation part. The total rig is immersed into a bath filled up with liquid nitrogen during the experiment.

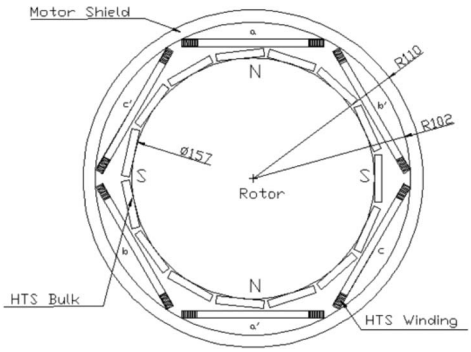

Fig. 2. Cross-sectional drawing of the HTS PMSM.

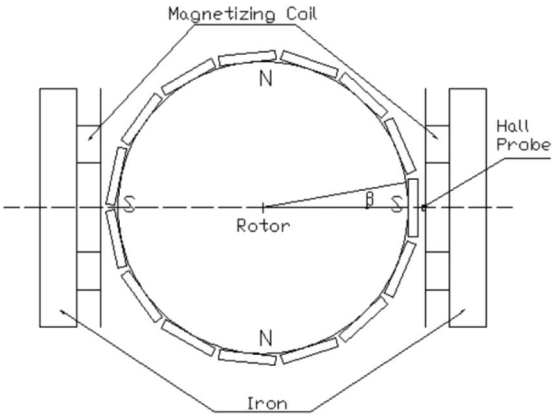

Fig. 3. Schematic diagram of PFM [5].

A. Structure of Rotor

75 YBCO bulks (15 columns, 5 pieces per column) are mounted on the rotor to make a four-pole permanent magnet after magnetization. Fig. 2 provides the cross-sectional view of the HTS PMSM.

Generally, there are four typical ways to magnetize a bulk superconductor: field cooling (FC) magnetization, zero field cooling (ZFC) magnetization, pulsed field magnetization (PFM), and flux pumping [6]. After exploring the magnetization process of superconducting bulks [7], the PFM method was chosen, as it facilitates the assembling of the devices and allows an easy recovery of partial demagnetization following a fault event. By using YBCO bulks, a practical PFM system which can produce a pulsed field with 0.9 T (peak) was built to let the rotor trap four poles and then produce a magnetic flux density of 375 mT at 77 K [5]. In the PFM method, the field has a pulsed waveform that lasts for a time of the order of the milliseconds and is generally produced by the discharge of a capacitor bank into a small copper coil. Fig. 3 shows a schematic diagram of PFM. It indicates that a pair of magnetization copper coils is installed on the motor rig in series and a rotor with 15 columns of YBCO bulks are in the middle of the coils. The processes of the magnetization contain two steps: first discharge the pulse to a certain place of the rotor to produce a pair of north (N) poles and then rotate the rotor by 90° to carry out the second magnetization to produce a pair of south (S) poles. Consequently, a four-pole permanent magnet is obtained. A hall probe which is used to monitor trapped magnetic field by bulk after magnetization is attached to the center of magnetizing coil and the distance between the bulk and the magnetizing coil is 3 mm.

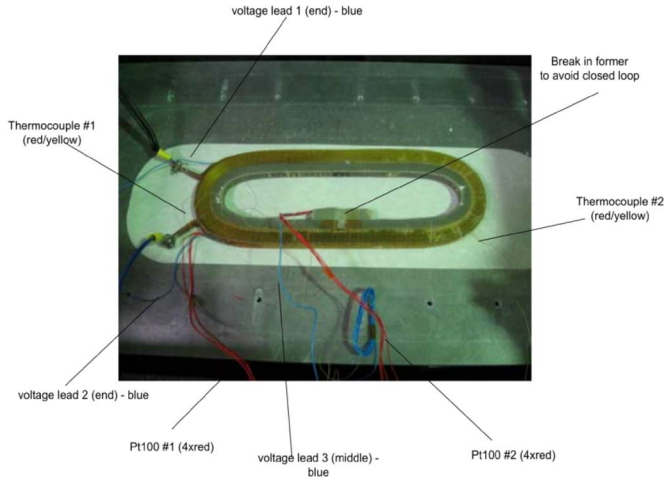

Fig. 4. Photograph of 2G HTS coil.

B. Structure of HTS Winding

The coils for the HTS stator windings demonstrated in Fig. 2 are 2G HTS YBCO wire, type 344 from AMSC. They were manufactured by Zenergy Power GmbH, Germany. In Fig. 4, it shows the photograph of the 2G HTS coil.

The straight length and the inner width of 2G HTS coils are 180 mm and 68 mm respectively. The thickness of the coils is about 10 mm and both the corners of the coils are round to avoid sharp bending of 2G HTS wires. At the same time, one insulated cut is in the former and is bridged by a G10 piece to avoid the current flow in the former. There are two layers of 2G HTS coils which are stacked together to make one racetrack coil. This configuration maximizes the inductance of the 2G HTS coil within the limited geometry. The total number of turns per phase of the armature windings is 200. Since there are two coils for each phase and each coil has two layers, each layer will have 50 turns. The 2G HTS coils work at an operating temperature of 77 K. The coil contains two halves of 2G HTS wires, which are internally connected. At both ends, copper contacts are integrated for current connections by screws. Three voltage leads (blue) are integrated—one at each end, one in the middle of the coil. Two thermocouple (red/yellow) wires are placed between the two halves of the coils. Two Pt100 sensors are integrated. The coil has been completely impregnated with epoxy resin.

III. Control Theory

The HTS PMSM designed in our lab is a non-salient pole PMSM. The one phase stator equation is:

$$\dot{U} = -\dot{E}_0 + \dot{I}_a(R_s + jX_s) \tag{1}$$

where E_0 is the field generated excitation voltage; U is the terminal voltage; I_a is the stator current and R_s, X_s are the stator resistance and reactance respectively.

The field generated excitation voltage E_0 and the stator reactance X_s can be expressed as follows:

$$E_0 = -N\frac{d\phi}{dt} = -\frac{d\lambda_f}{dt} = j\omega\lambda_f \tag{2}$$

$$X_s = \omega L_s \tag{3}$$

where N is the number of turns for armature winding; ϕ is the rotor flux; λ_f is the rotor flux linkage; ω is the frequency of supply voltage and L_s is the stator inductance. Substitute (2) and (3) into (1) becomes

$$\dot{U} = j\omega\dot{\lambda}_f + \dot{I}_a(R_s + j\omega L_s). \tag{4}$$

As the field oriented control is applied, I_a has the same direction as λ_f. Hence, the amplitude of the stator voltage is

$$U = \sqrt{I_a^2 R_s^2 + \omega^2(\lambda_f + I_a L_s)^2}. \tag{5}$$

On the other hand, if six stator coils are all HTS, since the equivalent resistance of superconductor is proportional to frequency of applied AC current, then (5) can be simplified as follows

$$U = \omega\sqrt{I_a^2 R_{sf}^2 + (\lambda_f + I_a L_s)^2} = kf \tag{6}$$

where

$$k = 2\pi\sqrt{I_a^2 R_{sf}^2 + (\lambda_f + I_a L_s)^2} \tag{7}$$

$$R_{sf} = \frac{R_s}{\omega}. \tag{8}$$

Here, R_{sf} is the fundamental resistance of the HTS winding.

According to (6), the amplitude of the terminal voltage U is proportional to the speed f. The input of this control system is a ramp function which represents the frequency f at the HTS PMSM start-up. The output is the amplitude of stator voltage U which will generate pulse width modulation (PWM) signals to the insulated-gate bipolar transistors (IGBTs) in the voltage source inverter (VSI) in one phase. PWM is applied to generate the desired voltage by selecting the switches' states of VSI. The above situation is under the condition that all the six windings are 2G HTS coils. However, at the moment, there are only two 2G HTS windings in our HTS PMSM's stator. It means that the stator resistance could not be neglected at a low speed. The motor speed is not linear with the voltage on the stator for copper winding when the HTS PMSM starts up. The stator voltage in HTS winding is negligible, since the equivalent resistance R_{sf} of 2G HTS windings at 1 Hz is close to zero. Although the stator resistance in 2G HTS windings can be ignored, the conventional V/F control is still not suitable for this HTS PMSM due to two phases of copper windings. Currently, the open-loop V/F control for the HTS PMSM is based on (5) rather than (6).

IV. Experiment and Results

Digital signal processors (DSPs) and xPC target are usually used to execute Simulink models on a target computer for a real-time testing application. In our project, a DSP kit TMS320F2812 eZdsp manufactured by Texas Instruments was chosen for implementation of the modified V/F control algorithm for the HTS PMSM. Fig. 5 depicts the overall system for execution of V/F control on the HTS PMSM. The program is first built in Simulink and then transferred from a computer into the DSP chip through an emulator SIGNUM JTAGJET. There are six output PWM signals from DSP, which are directly connected to the six IGBTs in the inverter. The modified V/F

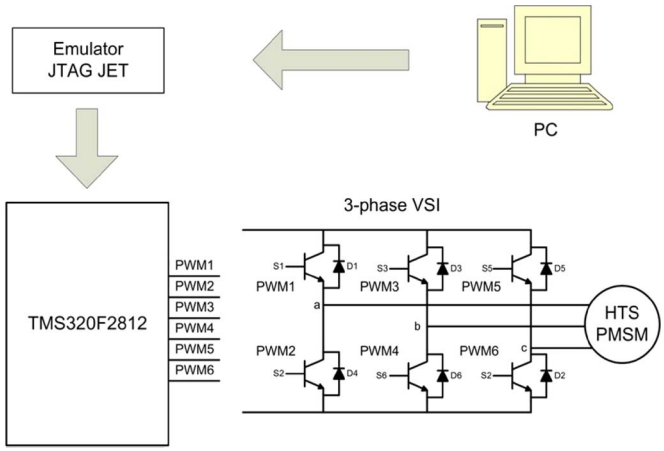

Fig. 5. Schematic diagram for execution of V/F control on a DSP.

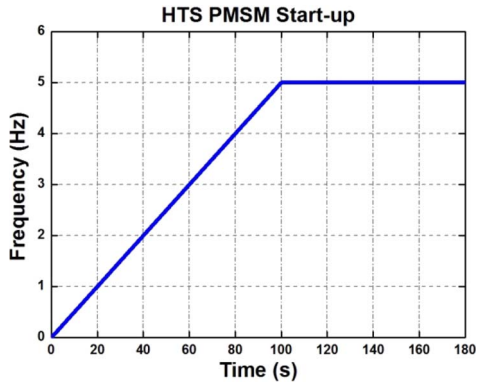

Fig. 6. Start up the HTS PMSM.

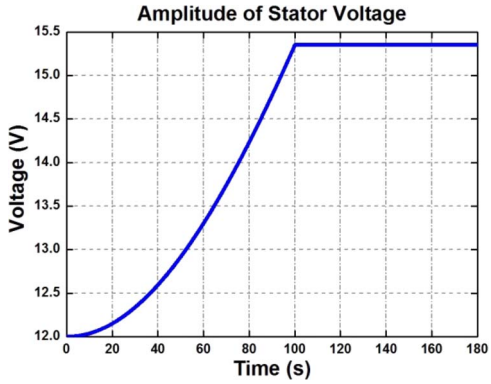

Fig. 7. Change of amplitude of stator voltage.

control program has been developed in Simulink by using target support package which contains Texas Instruments C2000 configuration. There is a discrete rate limiter, which is used to determine the increasing rate of frequency activated by a discrete timer. Its increasing frequency represents how fast the HTS PMSM acceleration is at start-up. The saturation block is applied for setting upper limit of frequency which equals to the final frequency of motor at start-up. Fig. 6. indicates that the frequency rises from 0 Hz to 5 Hz at the rate of 0.05 Hz/s when the HTS PMSM starts up. Fig. 7 shows the change of amplitude of voltage on the stator. It takes 100 s to let the voltage on the stator change from 12 V to 15.3 V under the V/F control.

The amplitude of PWM output is around 3.28 V and the frequency is about 31.25 kHz. Since the practical IGBTs have

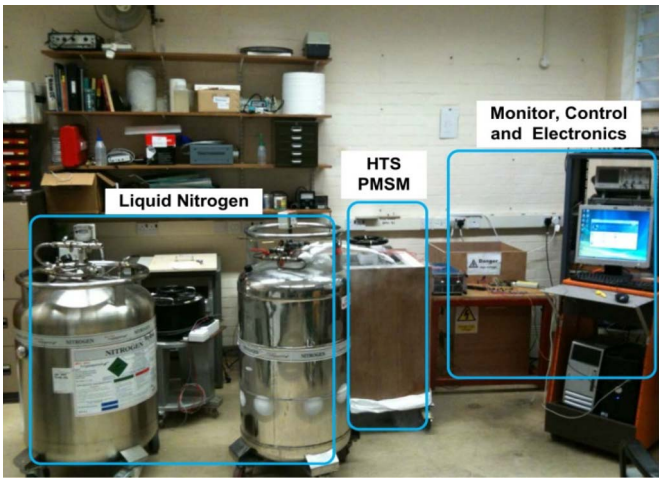

Fig. 8. Photograph of the overall experiment system.

turn on and turn off time, two IGBTs in one bridge of VSI may switch on or off simultaneously. In order to avoid either making a short circuit (on) or resulting an undefined AC output line (off), a deadband which should longer than the sum of turn on and turn off time of the IGBTs between two gate signals in one bridge of VSI is set to 2.16 μs.

The overall operation system for the HTS PMSM is displayed in Fig. 8. The experiment system contains the following main parts: the control and monitor, which are used to control the PFM magnetization process, start up the HTS PMSM and record all the results from the PFM process and motor operation; the power electronics which contain the VSI, rectifier, etc.; the motor rig which will fill with the liquid nitrogen by using two Dewar bottles (280 L) at the beginning of the experiment. The HTS PMSM can accelerate from 0 rpm to 150 rpm with the rising rate of frequency at around 0.05 Hz/s in no-load operation. Depending on the critical current and AC losses of 2G HTS coils, the amplitude of the currents through the 2G HTS windings and copper windings are set to 10 A and 5 A, respectively. The values in 2G HTS winding is set twice bigger than the copper winding, since the resistance in 2G HTS winding is much lower than that in copper winding at a low speed of running. Because of safety reasons such as liquid nitrogen splash, mechanical limitation on the motor rig, etc., the HTS PMSM cannot run at a high speed at this stage. The phase currents in 2G HTS winding (peak 9.9 A) and copper winding (peak 5.1 A) are recorded in Figs. 9 and 10 respectively. These current values are almost the same as the values set in the program. The peak-to-peak one phase line voltage is 40 V when the HTS PMSM runs at 150 rpm at no load operation.

V. Conclusion

This paper has given a detailed description of the modified V/F control algorithm implemented in the HTS PMSM both theoretically and practically. The stator of the HTS PMSM consists of two 2G HTS windings and four copper windings. The rotor was constructed by 75 YBCO bulks. These YBCO bulks are magnetized by PFM, in order to make them into a four-pole permanent magnet. Currently, the HTS PMSM can run at 150 rpm at no load operation. The efficiency will be

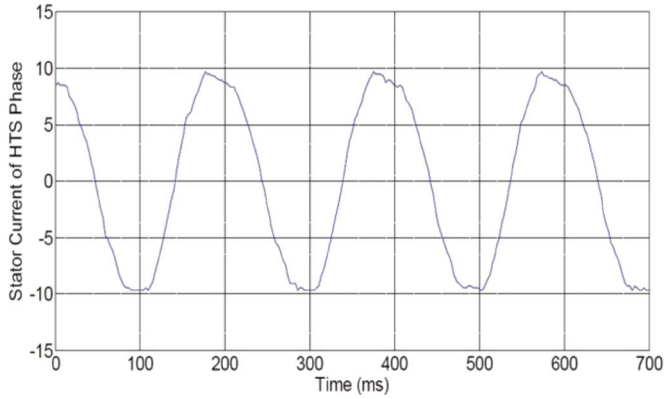

Fig. 9. Stator current of the HTS PMSM in 2G HTS winding.

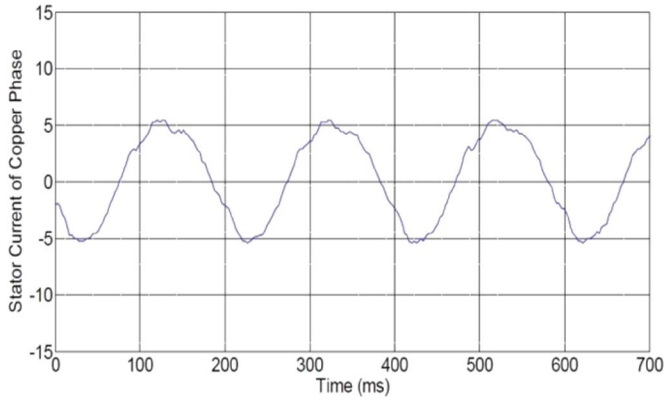

Fig. 10. Stator current of the HTS PMSM in copper winding.

estimated after four copper windings are replaced by four 2G HTS windings and a detectable load will be set up on the HTS PMSM in the future.

Acknowledgment

The authors thank Y. Jiang, D. Hasko, and J. Grundy for their gracious help. They also thank A. Dennis from the Bulk Superconductivity Group, University of Cambridge, for providing their YBCO bulks.

References

[1] H. Ohsaki and Y. Tsuboi, "Study on electric motors with bulk superconductors in the rotor," *J. Mater. Process. Technol.*, vol. 108, pp. 148–151, 2001.

[2] D. Sekiguchi *et al.*, "Trial test of fully HTS induction/synchronous machine for next generation electric vehicle," *IEEE Trans. Appl. Supercond.*, vol. 22, no. 3, p. 5200904, Jun. 2012.

[3] S. Ishmael, C. Goodzeit, P. Masson, R. Meinke, and R. Sullivan, "Flux pump excited double-helix rotor for use in synchronous machines," *IEEE Trans. Appl. Supercond.*, vol. 18, no. 2, pp. 693–696, Jun. 2008.

[4] Y. Jiang, R. Pei, W. Xian, Z. Hong, and T. A. Coombs, "The design, magnetization and control of a superconducting permanent magnetic synchronous motor," *Supercond. Sci. Technol.*, vol. 21, p. 065011, 2008.

[5] W. Xian, Y. Yan, W. Yuan, R. Pei, and T. A. Coombs, "Pulsed field magnetization of a high temperature superconducting motor," *IEEE Trans. Appl. Supercond.*, vol. 21, no. 3, pp. 1171–1174, Jun. 2011.

[6] T. A. Coombs, Z. Hong, and X. Zhu, "A thermally actuated superconducting flux pump," *Phys. C*, vol. 468, p. 153, 2007.

[7] M. Fabbri, A. Morandi, F. Negrini, and P. L. Ribani, "Sensitivity of the field trapped by superconducting bulks on the parameters of the magnetization process," *IEEE Trans. Appl. Supercond.*, vol. 16, pp. 1570–1573, 2006.

Wind farms associated with flywheel energy storage plants

Michal Chudy, Lynette Herbst, Jörg Lalk

The Department of Engineering and Technology Management, The Graduate School of Technology Management, University of Pretoria , South Africa
michal.chudy@up.ac.za

***Abstract*—Recent developments in flywheel technology opens new possible applications. Connecting flywheels and wind generators is not a new idea. However, flywheels were always considered as a short time compensation of stochastic output variations of wind generators instead of fully fledged means of energy storage. In this study connecting a wind farm with a flywheel system containing a number of flywheel units is proposed. Actual wind speed data from a wind farm location in South Africa is used in the study. The analysis of this system is based on algebraic optimization models of systems containing both kinds of devices. The outcome of the study illustrates the feasibility of using a flywheel plant as fully fledged energy storage solution.**

***Index Terms*—wind turbine, flywheel, energy storage**

I. INTRODUCTION

Stochastic output viability of wind generators is a problem which prevents higher penetration of this type of renewable energy source. When approaching a high ratio of wind power capacity in a power grid, the grid has less capacity to compensate for output variations which are caused by renewables and which in turn can lead to grid instabilities and failures. The danger is especially high for poorly interconnected national grids. The maximal penetration of renewables is then dependent on the flexibility of the grid. This flexibility can be enhanced by commissioning of inherently more flexible conventional power generators such as hydro plants, combined gas cycle turbines (CCGTs) or diesel generators. Another option is to install compensations plants such as flywheel plants [1, 2].

A high penetration of renewable power sources also is problematic due to difficulties in energy forecasting [3]. Longer term variations are relatively well predictable due to progress made in wind meteorological modeling [4]. However, short term prediction up to 48 hours, [5], will always bring some uncertainties despite increased efforts attempting to improve precision. The situation in solar power can be much simpler during a sunny day, however, the problem are cloudy days, which make predictions much more difficult and challenging. [6]. Well known solutions for stochastic availability of renewable power are high capacity energy storage, smart grids or both together.

According to a study by Darrelmann, [7], power failures (also known as "brown outs") where the voltage drops below 80 % of the standard voltage level for a duration of less than 0.1s, generate more than half of all grid failures. Due to their fast response times and ability to achieve very high power outputs in limited time periods (usually in the order of a few seconds), flywheel plants are a very suitable solution for power quality applications. Among numerous flywheel applications e.g. from the automotive industry, a flywheel in synergy with a wind turbine was proposed by K. Vespremi et.al and G. O. Cimuca et al., [8-10]. It was shown that a flywheel and a wind turbine can be linked together in order to reduce the turbine power output oscillations. The question now is how much flywheel energy storage capacity would be required for the flywheel to also qualify flywheel as a fully-fledged energy storage device.

During recent years the development of high speed flywheels with superconducting magnetic bearings pushed up both power and capacity of these machines. For examples 35 kg rotor has been constructed by A.Cansiz et al. in 2002 [11], 132 kg rotor by Boeing in 2010 [12] and 600kg rotor by ATZ in 2012 [13]. With further enhancement in performance of high temperature superconductors (HTS) and superconducting bearings [14, 15] it is reasonable to expect further capacity enhancements. Progress was also made in research of second generation of HTS tapes. It was shown that stacks of HTS tapes have strong potential to replace superconducting bulks [16] in several applications, e.g. in superconducting bearings.

Stored energy in a flywheel (solid cylinder rotor) is given by the relationship:

$$E = \frac{1}{4} m r^2 \omega^2$$

978-1-4799-7720-8/14/$31.00 ©2014 IEEE

,where E – stored energy, m – weight of the rotor, r-diameter of the rotor, ω – rotational speed. Due to the quadratic relation of the rotational speed ω, it is more efficient to increase speed of rotation rather than the weight of the rotor, which is a linear relationship. Further increasing both rotational speed and weight of the rotor is also possible. In this study, flywheel plants are examined to determine whether they can be used as energy storage systems and power quality control devices at the same time. The possible performance enhancements are considered as well.

II. FEATURES OF THE STUDY

In this study, a special optimization model simulating time dependent operation of a system with linked wind turbines in a wind farm and flywheels in a flywheel plant. Research is performed as a case study at an actual location in South Africa, which is a strong candidate for a potential new wind farm construction project. Comprehensive wind speed data are available for this location. The model calculates with a selected type of a wind turbine and a flywheel.

A. *Wind speed map of the location*

The selected wind farm location is situated on South Africa's West Coast close to the town of Vredendal. The coordinates of the location where the wind data were measured are E°18.419916 S°31.730507. Detailed information about the location, wind data attributes and wind data acquisition can be found in the comprehensive WASA (Wind Atlas of South Africa) report, [17]. This particular location was selected due to good wind conditions, but also because the closest town Vredendal has population of 20 000 inhabitants, which can be reasonable to be supplied by the studied wind farm.

B. *Energy consumption data*

Energy consumption was estimated using data published by the major South African energy utility Eskom [18]. From these data, daily electricity demand for 20 000 average South African electricity consumers in Vredendal was calculated. (Fig. 1). No special features of industry or business in the location, which could change the overall electricity demand in the area was included. The variation between winter and summer months are considered though.

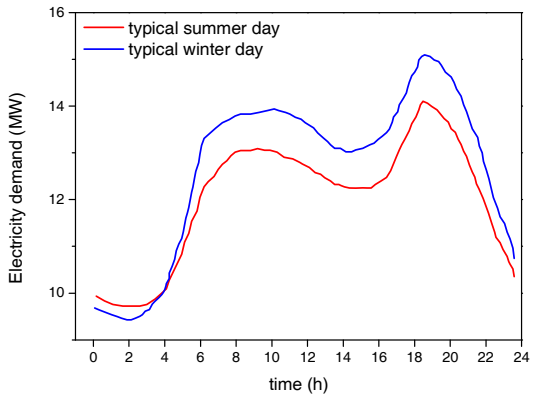

Figure 1: Hourly based electricity consumption for average 20 000 citizens calculated from overall South African Figs 2012[18].

C. *Flywheel and wind turbine specifications*

For the purpose of this study, properties of a 100 kWh Superconducting Flywheel Energy Storage from Kepco are taken. This machine is presented in detail by the work of J. Lee et al, [19]. It is assumed that the machine is able to release all its stored energy in time lower than 10 minutes, which is the resolution of GAMS model. It is important to mention, this flywheel is equipped with superconducting magnetic bearings, which ensure extremely low rotational losses. The major losses of the device are caused by a cryocooler, required for cooling of superconducting parts, which is about 14 MJ/h. Rotational and other losses are significantly smaller and therefor can be neglected. Loss reduction by solid nitrogen production which is an asset of this device, however is not considered in this work.

A Vestas V90 2MW [20] wind turbine is used in the model. Performance characteristics such as power output dependence on wind speed are calculated accordingly WAsP^{TM} software [21]

D. *Optimization model*

GAMS (General Algebraic Modeling System) was used as the modeling optimization software. The model time resolution is 10 minutes, which is the resolution of available wind speed data at WASA [17]. The study is performed in three stages:

1) Modeling of an independent system without any grid connection was performed in this stage. The system contains only Vestas V90 2MW wind generators, unlimited "ideal" energy storage and 20 000 electricity consumers in the Vredendal location. The "ideal" energy storage is defined as unlimited and without any losses. The results from this stage are giving valuable information about minimal required capacity of the "ideal" energy storage required for such an independent (off grid) system. Amount of electricity wasted due to disconnection from the grid is calculated as well.

2) In this stage, energy storage of the independent system from stage 1 is supplied by Kepco superconducting flywheels. The model considers flywheel plant and the wind farm as two separated, however interconnected units. (Not a direct connection wind turbine – flywheel like presented in [8]). The optimal number of flywheels and wind turbines for the system is calculated. The study is performed in carefully selected longer time periods, where extremes such as long windless periods can occur.

3) The system of linked wind farm and flywheel plant is connected to the grid in this stage. The most efficient number of flywheels in the system is found. The operation of the flywheel plant is analyzed. The results

III. RESULTS AND DISCUSSION

It is well known that independent power systems are not feasible without high capacity energy storage. According to WASA [17] and daily demand in the Vredendal location presented above (Fig. 1), minimal required energy storage capacities of "ideal" energy storage were calculated. (Table 1). The data is calculated for separate months and it is possible to see some variations. It is clear that the minimal required energy storage capacity is strongly dependent on the number of wind generators in the system. In this model it was assumed that a price to commission of 17000 kWh of energy storage is equivalent to commission price of a single wind turbine (This ration is realistic in the case of pumped hydro energy storage). The model was minimizing wasted energy as well, however the minimizing of waste energy had 100 times lower priority than minimizing of the storage capacity. Different weighting of objective variables can still slightly change the results in Table 1, however, the fact that the system requires very high capacity of energy storage remains the same. In addition, a significant amount of produced electrical energy is wasted. Clearly, connecting such a system to the grid, if possible, seems to be a much more reasonable option.

Table 1: Minimum and optimal required stored energy in "ideal" energy storage.

	No. wind generators	Min. req. capacity of energy storage (MWh)	Energy wasted (MWh)
December 2012	23	180.5	6315
January 2012	26	177.5	7046
July 2012	61	243	19908
June 2012	29	370	4274

The study of a flywheel or any other energy storage in the independent systems has a strong advantage as no deep knowledge of a grid characteristic is needed. A GAMS model of such an independent system including the wind farm, the 20 000 consumers and a flywheel plant was developed. This model is able to determine the minimal required amount of wind turbines and flywheels by algebraic optimization. The main feature of the model is that the final optimization results are always determined by critical time periods where no or almost no output from wind farm is produced. This is a typical case with no wind or strong wind requiring one to stop wind turbine operation in order to prevent any damage. Such long periods with no power output can lead to the situation where the calculated most optimal solution is containing thousands of wind turbines and flywheels, which is a completely unrealistic solution. Since the Kepco flywheels have relatively limited capacity and constant losses due to cooling (even when they are discharged, but ready for operation), longer windless periods can even cause infeasibility of the problem. The infeasibility case happens also by searching for optimal solutions in a time period of a full month. For this reason, finding an optimal time period for the calculation is crucial in order to get reasonable optimization results. Obviously this kind of "optimal" solution will not allow an operation of a completely off-grid system. Although such a "semi optimal" solution would require a grid connection, the grid will be employed only in certain critical time periods.

In order to choose the most suitable time period for the model, a closer study of the wind speed data is performed. Wind speed data at a height of 62m (relevant for Vestas V90 2MW wind turbines) is shown in Fig. 2. A time period of six days is shown for different months in the year 2012. According to the date, pronounced daily wind speed patterns were observed in summer months. Therefore, to find representative days for all summer months as an input into the optimization algorithm is not a problem. By choosing the most suitable time period, no fitting or any other simple statistical methods can be used. Such methods would reduce sudden changes and extremes which are crucial for determining the number of flywheels and turbines, which will be reduced.

Different situations are observed during winter months, where wind speed variation is much less predictable. From overall WASA 2012 wind atlas data for 17.9 % of the time the wind speed is below 3.5 m/s which means that wind turbines are not turning. Selected appropriate representative days for optimization are as follows: summer: 5-7th January, winter: 12-14th July.

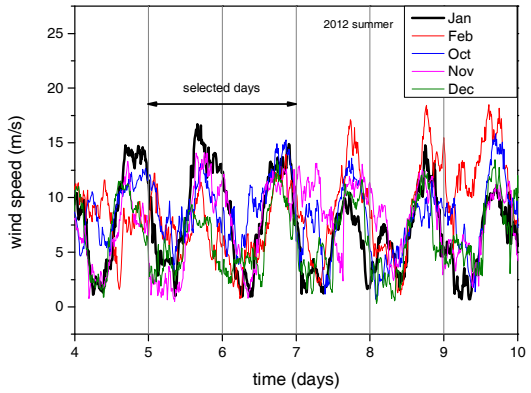

a)

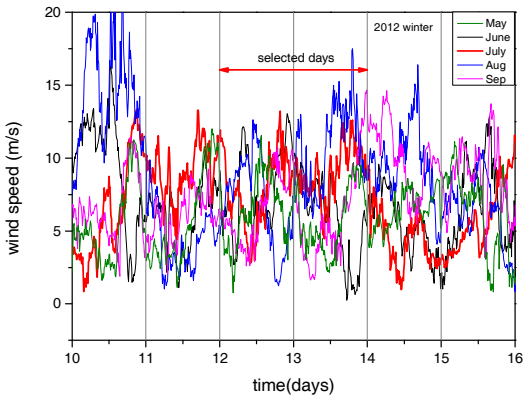

b)

Figure 2: Wind speeds in Vredendal location according WASA[14] a) Summer months b)Winter months

The calculated results are presented in Fig. 3. In the model, cost of a single wind turbine is considered to be one order of magnitude higher than the cost of a single flywheel in the plant. The calculation was performed for a Kepco 100 kWh flywheel, [19], and also for similar flywheels with an extended storage capacity up to 1200 kWh. Such a capacity enhancement is reasonable to expect in the future.

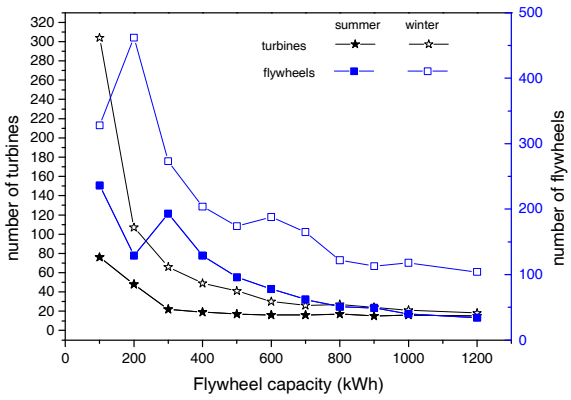

Figure 3: Calculated minimal numbers of wind turbines and flywheels in selected representative time periods

As was indicated before, winter months are more problematic due to higher wind speed variations (Fig. 2b) and higher electricity demand (Fig. 1). Selecting a reasonable number of wind turbines and flywheels in the flywheel energy storage plant, the number of turbines will be in the range of 25 +/-10 and the number of flywheels (100 kWh) will be in the range of 150+/-50.

In the last stage of this study, the identical model as used in previous stages was connected to the grid. The number of wind turbines for this calculation was fixed to 30. An interesting information regarding this number is that overall energy produced (according to January 2012 wind speed data) by 15 wind turbines could satisfy overall monthly demand of the assumed population in the Vredendal location. The optimization algorithm searches for the number of required flywheels in order to minimize the amount of electrical energy supplied to the system by the grid. The results are shown in Fig. 4. The results for flywheels of lower capacities such as 100 kWh and 200 kWh are showing zero, which means that flywheels with such a small energy storage capacity cannot be used as high capacity-fully fledged energy storage devices.

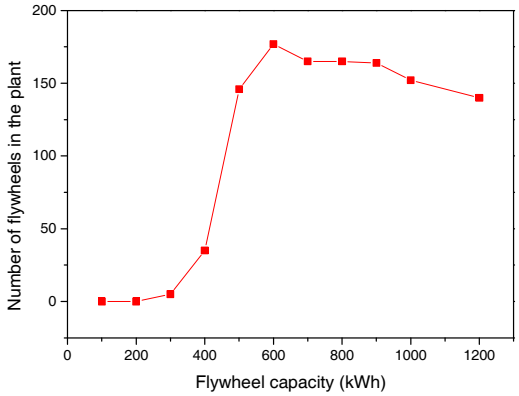

Figure 4: Most efficient number of flywheels in the flywheel plant. as result of minimizing amount of energy supplied from external sources (power grid). The considered wind farm consists of 30 wind turbines.

The flywheel plants containing such flywheels can have a significant role as compensation plants, however, energy losses caused by the plant operation will be higher than benefits gained by energy storage. It is important to note that the dependency converges to 1, which means that after reaching a certain capacity of a flywheel, all energy storage can be serviced by a single flywheel.

By enhancing storage capacity of the flywheels by factor 3 (300 kWh), but with identical losses, the flywheel plant starts to be beneficial as an energy storage device. Thus the flywheel plants consisting from flywheels with capacities from 300 kWh – 400 kWh can be already used as energy storage, but cannot offer sufficient energy capacity to have a real impact on the grid as compensation plant. The number of such flywheels in an efficient flywheel plant must remain low. More flywheels would cause inefficiency (because was shown that superconducting flywheels have constant losses regardless of stored energy) as it is shown in Fig. 5 on an example of 500 kWh flywheel.

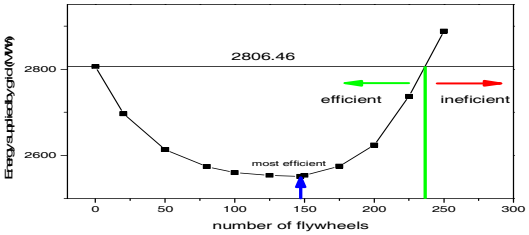

Figure 5: Number of 500 kWh flywheel in the system of 30 wind turbines. Too high number of flywheels is inefficient.

The flywheel plant starts effectively fulfilling both functions if the energy storage capacity of a single flywheel reaches more than 400 kWh.

In Fig. 6, the operation of a 500 kWh flywheel plant consisting of 147 flywheels is shown (the most efficient configuration according to Fig. 4). Fig. 7 is representing the anount of energy stored in the flywheel plant for varying time periods. It is possible to see that the flywheel plant is fully charged during most of the time, which ensures the capability of operation as a compensation plant. Considering the energy storage function this flywheel plant would save 9% of energy compared to the case without the flywheel plant (Fig 5). However if the flywheel plant of 167 x 1000kWh flywheels is operating, it would save up to 66% of power consumed from the grid.

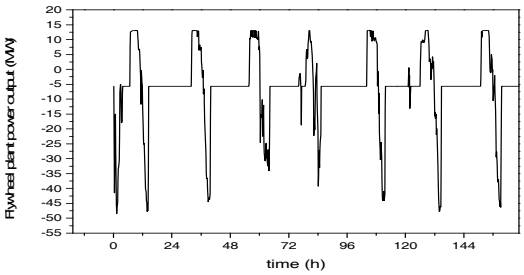

Figure 6: Flywheel plant charging-discharging operation. Positive output means discharging-supplying system with energy, negative is charging the flywheel plant and consuming electricity. Shown power output is average power output of the flywheel plant in time of 10 minutes.

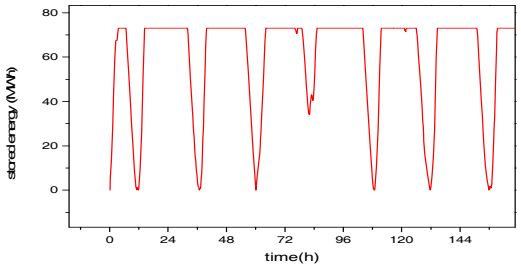

Figure 7: Stored energy in the flywheel plant. Zero means that the flywheel plant is completely discharged. The plant consist of 147x500kWh flywheels with total capacity of 73.5 MWh.

IV. CONCLUSIONS

In this study flywheel plants as a full-fledged energy storage linked to the wind farm were studied. In the first stage of the work, it was shown that independent energy systems require high capacities of energy storage with high amount of energy waste. Avoiding this energy waste, required energy storage would be even one order of magnitude higher. For this reason, it is always reasonable for wind farms, even if they are equipped with some sort of energy storage, to be connected to the grid. Finding an optimal size of a windfarm and attached energy storage, e.g. flywheel plant, is a difficult process requiring detailed knowledge of wind patterns in the region as well as grid performance and flexibility in the area. In this work, the size of the wind farm (Vredendal location in South Africa) and flywheel plant were calculated according to flywheel maximal stored energy capacity and wind speed data in the location. In the last stage, defined sizes of wind farms and flywheel plants were analyzed. It was found that flywheel with current available capacities and losses would not be feasible for a flywheel plant which would operate as a fully-fledged energy storage. However, it can be used as a compensation plant. The fully fledged energy storage application linked to the wind farm starts to be interesting in case of enhancing the flywheel energy storage capacity by factor of 4. If flywheel's available capacity reaches 1000 kWh with no significant increase of losses, flywheel plants would be perfectly justifiable as compensation plants and fully- fledged energy storage with saving up to 66% of energy otherwise necessary to be supplied from the grid.

REFERENCES

[1] Hazle Spindle, Beacon Power 20 M W Flywheel Frequency Regulation Plant,Beacon Power report

[2] H. J.Bomemann, M. Sander, "Conceptual System Design Of a 5MWh/100 MW Superconducting Flywheel Energy Storage Plant for Power Utility Applications", IEEE Trans. Appl. Sup. 7, No. 2, 1997 N. G.

[3] F. Bouffard,and F. D. Galiana, "Stochastic Security for Operations Planning with Significant Wind Power Generation", Power and Energy Society General Meeting - Conversion and Delivery of Electrical Energy in the 21st Century, 2008 IEEE

[4] P. Louka, G. Galanis, N. Siebert, G. Kariniotakis, P.Katsafados, I. Pytharoulis, G. Kallos[a,] Improvements in wind speed forecasts for wind power prediction purposes using Kalman filtering, Journal of Wind Engineering and Industrial Aerodynamics, Vol. 96, Issue 12, 2008, pp 2348–2362

[5] Ismael Sánchez, "Short-term prediction of wind energy production", International Journal of Forecasting 22 (2006) 43–56

[6] S. Pelland,J. Remund,J. Kleissl,T. Oozeki,K. De Brabandere, "Photovoltaic and Solar Forecasting: State of the Art ", IEA PVPS Task 14, Subtask 3.1 Report IEA-PVPS T14-01:

[7] H. Darrelmann, "Comparison of High Power Short Time Flywheel Storage Systems", Telecommunication Energy Conference, 1999. INTELEC '99. The 21st International

[8] K. Veszpremi and I. Schmidt, "Flywheel Energy Storage Drive for Wind Turbines", Power Electronics and Drive Systems, 2007. PEDS '07. 7th International Conference on

[9] K. Veszprémi and István Schmidt, "Different Flywheel Energy Storage Drives for Renewables – Limits and Optimization", Power Electronics and Motion Control Conference (EPE/PEMC), 2010 14th International

[10] Gabriel O. Cimuca, Christophe Saudemont, Benoît Robyns, and Mircea M. Radulescu, "Control and Performance Evaluation of a Flywheel Energy-Storage System Associated to a Variable-Speed Wind Generator", IEEE Trans. Ind. Electron. 53, No. 4, 2006

[11] A. Cansiz, A.M. Campbell and T.A. Coombs, "An Evershed type superconducting flywheel bearing", Physica C, 390, 305, (2003)

[12] M. Strasik, J. R. Hull, J. A. Mittleider, J. F. Gonder, P. E. Johnson, K. E. McCrary and C. R. McIver, An overview of Boeing flywheel energy storage systems with high-temperature superconducting bearings, Supercond. Sci. Technol. 23, 034021, (2010)

[13] F. N. Werfel, U. Floegel-Delor, R. Rothfeld, T. Riedel, B. Goebel, D. Wippich and P. Schirrmeister, "Superconducting bearings, flywheels and transportation", Supercond. Sci. Technol. 25, 014007, (2012)

[14] T. Coombs, A. M. Campbell, R. Storey, R Weller," Superconducting Magnetic Bearings for Energy Storage Flywheels IEEE Trans. Appl. Sup. 9, No. 2, 1999

[15] A. Patel, R. Pałka, B. A. Glowacki, G. Giunchi, A. Figini Albisetti, Y. Shi, D. A. Cardwell, S. C. Hopkins, Permanent Magnet Enhancement of Fully Superconducting MgB_2-$YBa_2Cu_3O_{7-x}$ Bearing", Journal of Superconductivity and Novel Magnetism April 2013, Vol. 26, Issue 4, pp 923-929

[16] A. Patel, S C Hopkins and B A Glowacki, "Trapped fields up to 2 T in a 12 mm square stack of commercial superconducting tape using pulsed field magnetization" ,Supercond. Sci. Technol.26 032001 (2013)

[17] Mortensen, J. Carsten Hansen, M. C. Kelly, E. Prinsloo, E. Mabille and S. Szewczuk, "Wind Atlas for South Africa (WASA)" 2012

[18] http://www.financialresults.co.za/eskom_ar2009/ar_2009/info_sheets/energy_02.htm

[19] J. Lee, S. Jeong,, Y. Hee Han, and B. Jun Park, "Concept of Cold Energy Storage for Superconducting Flywheel Energy Storage System", IEEE Trans. Appl. Sup. 21, No. 3, 2011

[20] http://www.vestas.com/

[21] http://www.wasp.dk/download/power-curves/vestasPowerCurves